



FACULTY OF MEDICAL SCIENCES

Biosciences Institute

**Three-dimensional Mapping of the Retinal Neurovascular Unit in Health and
Diabetes**

by

Mona J. Albargothy

Thesis for the degree of Doctor of Philosophy

2024

ABSTRACT

Diabetic Retinopathy (DR), a leading cause of adult blindness, is a progressive development of microvascular and neurovascular damage in the retina which leads to vision-threatening complications. The disruption of the neurovascular unit (NVU) is a primary factor in the pathogenesis of DR. The NVU is an interdependent unit made up of many cell types including pericytes, endothelium, glial cells and neurons, which work synergistically to maintain the function of the retina and allows adaptation to change in the physiological environment; for example, by regulating blood flow and by maintaining the blood retinal barrier (BRB). To assist with improving our understanding of retinal biology, and developing strategies to correct NVU dysfunction, detailed knowledge of the heterocellular interactions of the NVU is required. To address this issue, I have used serial block face scanning electron microscopy (SBF-SEM), and computational image reconstruction, which has enabled the first three-dimensional ultrastructural analysis of the NVU in retinal capillaries. Examination of the data in the x-, y- and z-planes was performed with the use of semi-automated computational image analysis tools including segmentation, 3D image reconstruction and quantitation of cell proximities to provide visualisation and analysis of the data. Heterocellular relationships within the retina were assessed in mouse and human tissues in health and diabetes. Prominent features of the capillary arrangements in 3D were the extensive sheath-like coverage by singular pericytes. They appeared in close register to the basement membrane (BM) with which they interwove in a complex mesh-like appearance. Breaks in the basement membrane appeared to facilitate pericyte interactions with other NVU cell types. There were frequent, close (<10 nm) pericyte to endothelial interactions with direct contact points and peg-and-socket-like morphology, usually appearing 2-4 times per micron with each formation spanning across several sections. Macroglia typically intervened between neurons and capillary structures; however, regions were identified where neurons came into closer contact with the BM. With the onset of diabetes, endothelial cells and pericytes showed areas of detachment from the BM, leaving intermittent gaps between their plasma membranes and the BM. These separations spanned a minimum depth of 200 nm in the z-dimension and exhibited a minimum width of 20 nm. Pericyte-endothelial cell interactions via peg and socket formations in non-diabetic capillaries show both cell membranes in close apposition, however, there appeared to be space surrounding the peg in the socket area of diabetic capillaries. Similar electron lucent gaps were present in the endothelium of diabetic capillaries. Moreover, showed electron-lucent tubules traversing its structure. These tubules,

appearing as white, electron-lucent holes, varied in size and did not open on either side, suggesting they do not form conventional channels within the endothelium. An increase in the number of leukocytes were present in the luminal space of diabetic capillaries, which were found to make direct communication with endothelial projections. This work provides new information on the ultrastructural changes in the murine retinal NVU during the onset and progression of diabetes, which in turn can serve as a platform to inform future studies aimed at delaying or preventing the progression of retinopathy.

Table of Contents

Table of Contents	i
List of Tables	v
List of Figure	vii
Academic Thesis: Declaration of Authorship	xxi
Acknowledgements	xxii
Abbreviations	1
Chapter 1 Introduction	6
1.1 The Eye	6
1.2 Retina	7
1.2.1 Function of the Retina	7
1.2.2 Structure of the Retina	8
1.2.3 Neurons	10
1.2.3.1 Photoreceptors.....	10
1.2.3.2 Bipolar cells.....	11
1.2.3.3 Horizontal cells	12
1.2.3.4 Amacrine cells.....	13
1.2.3.5 Retinal Ganglion cells	14
1.2.4 Macroglia.....	15
1.2.4.1 Müller cells	15
1.2.4.2 Astrocytes	16
1.2.5 Microglia.....	18
1.2.1 Blood supply within retina	19
1.3 Retinal Metabolic Demand	22
1.4 The Retinal Neurovascular Unit	24
1.4.1 Vasculature.....	25
1.4.1.1 BM function	26
1.4.1.2 Endothelial cell	26
1.4.1.3 Pericytes	27
1.4.2 Comparison of Retinal NVU to Other Tissues	29
1.5 Diabetic Retinopathy	30
1.5.1 Epidemiology	33
1.5.1 Animal models for Diabetes	33

1.5.2	Pathophysiology	36
1.5.2.1	Chronic hyperglycaemia and retinal microvasculopathy	36
1.5.2.2	Angiogenesis.....	38
1.5.2.3	Retinal neurodegeneration	38
1.5.2.4	Glial changes in DR	39
1.5.2.5	Inflammation	40
1.5.3	Treatments	41
1.6	Electron Microscopy	42
1.6.1	Examination of NVU by TEM	43
1.6.2	SBF-SEM.....	43
1.6.3	Other Imaging Modalities for Studying the Retinal NVU	45
1.7	Hypothesis	46
1.8	Aims and objectives.....	46
Chapter 2	Materials and methods	48
2.1	Sample Preparation.....	48
2.1.1	Fixation and microdissection.....	48
2.1.2	Diabetes-induced mouse samples	49
2.1.2.1	HbA1c measurements	49
2.1.3	Diabetic mouse sample preparation	50
2.1.4	Human samples	50
2.2	Electron Microscopy	51
2.2.1	Serial Block Face Scanning Electron Microscopy	51
2.2.2	Sample preparation for EM.....	52
2.2.2.1	TEM.....	53
2.2.3	Immunogold EM	53
2.2.3.1	Immunostaining.....	53
2.2.3.2	Pre-embedding Immunoelectron Microscopy:	53
2.3	Immunofluorescent labelling	54
2.3.1	Immunohistochemistry of mouse retinal flatmounts	54
2.3.2	STED and Confocal Microscopy	55
2.4	Image processing.....	55
2.4.1	Segmentation	55
2.4.2	3D Image Reconstruction	57
2.4.2.1	AMIRA.....	57
2.4.2.2	ARIVIS	57
2.4.2.2.1	Pipeline Creation	58
2.5	MATLAB.....	59

2.5.1	Morphological analysis.....	59
2.5.2	Pairwise distance analysis	60
2.6	Identification of features of interest	62
2.6.1	Peg-and-socket formations	62
2.6.2	Qualitative assessment of NVU changes.....	62
2.6.2.1	Separation of basement membrane criterion.....	63
2.6.2.1.1	Basement membrane separation from endothelium	63
2.6.2.1.2	Basement membrane separation from pericytes	63
2.6.2.2	Endothelial tubules criterion.....	64
2.6.3	Quantitative assessment of NVU changes	64
2.6.3.1	Basement membrane thickening	64
2.6.3.2	Distances from basement membrane.....	65
2.7	Statistics	69
2.7.1	T-test (unpaired).....	69
2.7.2	Standard deviations.....	70
Chapter 3	Mouse Retinal Neurovascular Unit	71
3.1	Introduction.....	71
3.2	Retinal Ultrastructure.....	72
3.2.1	Ultrastructural Features of the NVU	76
3.2.1.1	Endothelial projections.....	80
3.2.1.2	Endothelial tubules.....	82
3.3	Pericyte-endothelial interactions	83
3.4	Glial cells.....	88
3.4.1	Astrocytes and Müller Cells.....	88
3.4.2	Glial cell coverage.....	91
3.4.3	Glial closeness to pericytes	93
3.4.1	Microglia.....	94
3.5	Neurons	97
3.5.1	Quantitative assessment of NVU components	98
3.5.1.1	Proximity of NVU components to pericytes.....	98
3.5.1.2	Morphological analysis of NVU components	101
3.6	6-month-old mouse ultrastructure.....	102
3.6.1	Ultrastructural Consistency.....	102
3.7	Discussion	109
3.8	Conclusion	112
Chapter 4	Diabetic Mouse Neurovascular Unit	114

4.1	NVU changes in DR	114
4.2	Results	115
4.2.1	Ultrastructure.....	115
4.2.1	Basement membrane irregularity and thickening	120
4.2.2	Separation of cells from BM.....	122
4.2.3	Pericyte-endothelial interactions.....	125
4.2.4	Endothelial tubules.....	129
4.2.5	Leukocytes.....	132
4.3	Discussion	135
4.4	Conclusion	139
Chapter 5	The Human Neurovascular Unit in Health and Diabetes	141
5.1	Introduction	141
5.1.1	Differences between human and mouse retina	141
5.2	Results	143
5.2.1	Ultrastructure	143
5.2.2	Basement membrane.....	145
5.2.2.1	Lipid-like deposits	146
5.2.3	Pericyte to endothelial interactions.....	147
5.2.3.1	Pericyte-endothelial interactions in diabetes	148
5.2.3.2	Pericyte-endothelial complexes	149
5.2.4	Human neurovascular unit with diabetes	152
5.2.4.1	Basement membrane changes.....	153
5.2.4.1.1	Thickening.....	153
5.2.4.1.2	Separation from basement membrane.....	155
5.3	Discussion	160
5.4	Conclusion	165
Chapter 6	General Discussion	166
Chapter 7	Conclusion	171
	List of References	178

List of Tables

- Table 2-1 Experimental samples and corresponding glycosylated haemoglobin (HbA1c) levels.** This table presents data on experimental samples, each identified by a unique number, along with their respective weights in grams, HbA1c ranges in mmol/mol, and the percentage of glycosylated HbA1c. The HbA1c values offer insights into the glycaemic control of each sample, providing valuable information for assessing diabetes severity in the experimental cohort.50
- Table 2-2 Details on human samples.** This table provides a comprehensive overview of the human retinal samples, including gender, age, diabetes status (DM), and the presence of age-related macular degeneration (AMD).51
- Table 2-3 Details of antibodies for immunohistochemistry.** Details of all primary and secondary antibodies are listed in the table. The type of serum and primary antibody used based on the species in which the primary and secondary antibodies were raised and the protein of interest (target protein). The company and product code for all antibodies are provided. 54
- Table 3-1 Summary of the proximity analyses for the selected NVU feature pairs.** Means and standard deviations of the cumulative distribution functions at increasing distances up to 1000nm are provided for the intercellular and cellular-BM pairs. BM, basement membrane; P, pericyte; E, endothelium; M, macroglia; N, neurons.....101
- Table 4-3 Leukocyte count in diabetic and non-diabetic capillaries.** The table provides a comprehensive listing of diabetic and non-diabetic samples, indicating the respective counts of leukocytes observed within each sample. Entries highlighted in green denote samples where leukocytes were identified.....132
- Table 5-1 Summary of TEM analysis of peg-and-socket junctions results.** This table provides a comprehensive summary of TEM analysis results for pericyte-endothelial interactions in non-diabetic human samples. The data includes the number of human samples analysed, total sections examined from each sample, count of observed peg and socket formations, and the number of pericyte-endothelial junctions identified.150
- Table 5-2 Total occurrences of BM separation in diabetic human capillaries.** This table summarises the counts of basement membrane (BM) separation occurrences in three different diabetic human capillaries. The occurrences are categorised into BM-Endothelium, BM-Pericyte,

and BM-Neuroglia, providing insights into the distribution of BM separation types across the examined capillaries.159

Table 4-1 Basement membrane separation occurrences in non-diabetic capillaries. The table provides a comprehensive listing of diabetic samples, indicating respective number of total occurrences of basement membrane (BM) separation in all analysed capillaries and a detailed distribution of these occurrences across specific sections. Endothelium (Endo), Pericytes (Peri), Macroglia and Neurons (Neuroglia).175

Table 4-2 Basement membrane separation occurrences in diabetic capillaries. The table provides a comprehensive listing of diabetic samples, indicating respective number of total occurrences of basement membrane (BM) separation in all analysed capillaries and a detailed distribution of these occurrences across specific sections (i.e 1 indicated section 1, 1-5 indicated the separation was analysed on section 1 through to section 5). Endothelium (Endo), Pericytes (Peri), Macroglia and Neurons (Neuroglia).....176

List of Figure

- Figure 1-1 Macrostructure and microstructure of the Human Eye.** Panel **a** depicts a sagittal section of the human eye, highlighting its major anatomical features, including the sclera, cornea, pupil, iris, lens, retina, retinal vessels, choroid, and the optic nerve. A red square indicates a magnified area within the retina. Panel **b** is a magnified view of the retinal structure, detailing the cellular layers and components. It shows the arrangement of retinal cells and their interconnections, from the photoreceptor layer containing rods and cones at the bottom to the ganglion cell layer at the top. The various types of cells such as horizontal cells, bipolar cells, amacrine cells, and Müller glia are depicted. Blood vessels are also shown servicing the retinal layers. The cellular layers are labelled as follows: ganglion cell layer (GCL), inner plexiform layer (IPL), inner nuclear layer (Schafer et al.), outer plexiform layer (OPL), outer nuclear layer (ONL), and the retinal pigment epithelium (RPE). Modified from (Fu *et al.*, 2020).9
- Figure 1-2 Vascular organisation of the retina.** (a) Diagram illustrating the blood supply to the eye. The central retinal artery and its branches, along with the short posterior ciliary arteries, supply blood to the retina. These vessels originate from the ophthalmic artery, which branches off the internal carotid artery. The optic nerve sheath and pial vessels are also shown as part of the eye's vascular structure. (b) Cross-sectional schematic of the retina showing the internal blood-retinal barrier (iBRB) and outer blood-retinal barrier (oBRB). The iBRB is formed by the superficial, intermediate, and deep vascular plexuses, which nourish the inner retinal layers. The oBRB is formed by the retinal pigment epithelium (RPE) and Bruch's membrane, which separate the outer retina from the choroid vessels.22
- Figure 1-3 TEM vs SBF-SEM a normal retinal capillary.** a. TEM of 2D slice of retinal NVU from a human non-diabetic capillary 20,000 X. (Bianchi, Enrica. 2015). b. SBF-SEM serial stack of NVU from a human non-diabetic capillary 1, (for this study, see **Figure 5-1** for fuller description of this dataset). Endothelium (e) basement membrane (bm), lumen (L) and pericytes (p). Scale bar 5 μm45
- Figure 2-1 Pictographic summary of morphological analysis features.** A schematic of intracellular feature morphological assessments to recapitulate from the methods, The area (A) of each object was determined by counting the number of pixels comprising it. The perimeter (P) of each object was measured by first using MATLAB `bwperim` to determine boundary pixels, and then estimating P by analysis of its Freeman chain code. Convex hull areas (CA) and perimeters (CP) (MATLAB `bwconvhull`), which enclose the smallest convex area about each

object, were calculated equivalently. Radii were measured by determining the central coordinate of the subject area and calculating the 2D Euclidean distance (i.e. $r = \sqrt{\Delta x^2 + \Delta y^2}$) from it to each of the pixels composing the boundary (MATLAB pdist2), taking the mean of this distribution. The ratios of these key metrics (A, A:P, and the convex hull equivalents) were calculated for additional interpretation of object shape and compactness. The steps followed for convexity, solidity, and sphericity calculations are further illustrated in the workflow, which shows how each of these measures is applied to provide a comprehensive analysis of object morphology.61

Figure 2-2 Analysis of maximum BM thickness dynamics. A detailed representation of BM thickness variation serves as an illustrative example to elucidate the methodology employed. a. Raw data image highlighting an area of BM thickening (BM segmented in brown). B. Colour graph illustrating the thickness variation across the analysed region. The colour intensity reflects the thickness, with more intense colouring, and cooler tones (yellow-white) indicating thicker basement membrane region. Scale bar 4 μm65

Figure 2-3 Spatial analysis of basement membrane proximity to endothelium and pericytes. This figure presents a comprehensive analysis of the BM in relation to endothelium. a. raw data segmentation highlights the manual delineation of the BM (brown) and endothelium (aqua), capturing the intricacies of their spatial interactions. b. provides a pre-analysis snapshot of the materials, offering a baseline view before undergoing proximity analysis. c. depicts the results of the analysis with coloured lines, representing points in the materials that are closest (warmer colours) and furthest (cooler colours) from each other. 66

Figure 2-4 SBF-SEM Workflow for Retinal Tissue Imaging and Analysis. The figure illustrates the key steps involved in the SBF-SEM process used for retinal tissue preparation, imaging, and data analysis. Sample preparation - Fixation and EM staining: Retinal tissue is extracted through enucleation, followed by fixation using 4% paraformaldehyde (PFA). The tissue is then subjected to heavy metal staining with osmium tetroxide (Os) and uranyl acetate (U) to enhance contrast for electron microscopy. Embedding: The stained retinal samples are embedded in resin and heated to 60°C to harden. This step ensures that the sample is preserved for imaging and can be sectioned without damage. Imaging and image post-processing - Trimming and mounting: The embedded sample blocks are trimmed and mounted for imaging. Serial sectioning is performed using a diamond knife to create thin sections for electron microscopy. Imaging and sectioning: The tissue block is imaged using SBF-SEM, where each slice is sequentially sectioned and imaged. This generates a stack of high-resolution images. Segmentation and 3D rendering: The image stack undergoes

segmentation, where individual structures of interest (e.g., pericytes, BM, endothelium) are identified and delineated. This data is then used to generate 3D reconstructions of the tissue's microarchitecture. Data analysis - Qualitative analysis: The segmented 3D structures are analysed qualitatively, allowing for detailed examination of the heterocellular components. Regions of interest are highlighted, facilitating comparison of different structural features. Quantitative analysis: Quantitative analysis is conducted using computational tools including MATLAB. Parameters such as pairwise distance and sphericity including machine learning techniques, are used to assess structural features and quantify key metrics for further analysis.69

Figure 3-1 SBF-SEM micrographs displaying cross-sections taken at different depths along a mouse retinal capillary. A series of SBF-SEM micrographs illustrating cross-sectional images taken from specific depths along a mouse retinal capillary. The schematic at the bottom highlights the locations from which each section (a–d) was obtained along the capillary's length. (a): Section 1 (0.12 μm), representing the surface of the capillary. (b): Section 50 (6 μm), taken from deeper within the capillary. (c): Section 100 (12 μm), showing a mid-depth cross-section. (d): Section 120 (15.6 μm), taken from a deeper section towards the base of the capillary.73

Figure 3-2 Ultrastructure of 3-month old mouse capillary 1. A collection of SBF-SEM micrographs taken from a mouse retinal capillary to display the morphological changes along the capillary length. a, slice 1 (0.12 μm), b, slice 50 (6 μm), c, slice 100 (12 μm) and d, slice 120 (14.4 μm), Lumen: L, Pericytes: P, Endothelium: E, Macrogia: MG, Neurons: N. Scale bar 3 μm . Full dataset can be found here: <https://figshare.com/s/20fbbd90d386a8938a4f>.74

Figure 3--2 Ultrastructure of 3-month old mouse capillary 2. A collection of SBF-SEM micrographs taken from a mouse retinal capillary to display the morphological changes along the capillary length. a, slice 1 (0.10 μm), b, slice 50 (5 μm), c, slice 100 (10 μm) and d, slice 150 (15 μm). Lumen: L, Pericytes: P, Endothelium: E, Macrogia: MG, Neurons: N. Scale bar 2 μm . Full dataset can be found here: <https://figshare.com/s/b8b2f33da20ab5688768>75

Figure 3-4 Ultrastructure of 3-month old mouse capillary 3. A collection of SBF-SEM micrographs taken from a mouse retinal capillary to display the morphological changes along the capillary length. a, slice 1 (0.12 μm), b, slice 50 (6 μm), c, slice 100 (12 μm) and d, slice 150 (18 μm). Lumen: L, Pericytes: P, Endothelium: E, Macrogia: MG, Neurons: N. Scale bar 2 μm . Full dataset can be found here: <https://figshare.com/s/885aea53a0a501803620>76

- Figure 3-5 Identification of cells from plasma membrane outlines.** White arrows indicate plasma membrane outline separating the different cell types.78
- Figure 3-6 Segmented vasculature of 3-month old mouse.** The vasculature was identified, and each component was assigned a colour for segmentation through the data stack and subsequent visualisation in 3D reconstructions. a, endothelium, E (aqua), b, basement membrane, BM (brown), c, pericytes, P (blue) d, complete vasculature. RBC, red blood cell. Scale bar 3 μm79
- Figure 3-7 3D reconstruction of 3-month-old mouse capillary vasculature.** Displayed are features associated with a 3D reconstruction of the vasculature of capillary 1. Column a: endothelium (aqua); column b: basement membrane (brown); column c: pericytes (blue); and column d: combined vasculature.(a)(b)(c)(d). Full 3D animation can be found here: <https://figshare.com/s/43603b11f3fa1bab9886>80
- Figure 3-8 3D reconstruction of endothelial projections.** Illustration of endothelial projections within a capillary. a. presents the raw data of a section 1 of the dataset, capturing the intricate details of the endothelial structure. b. the segmentation of section 1, highlights the endothelial projections. c. deeper along the capillary to section 50, displays the raw data, providing insights into variations along the capillary length but consist observations of endothelial projections. d. segmentation of section 50. For a holistic perspective, panels e. and f. present 3D reconstructions of the endothelium, providing a 3D visualisation of the endothelial structure and projections. Red arrows indicate endothelial projections, yellow arrows indicate double stranded projection. Scale bar 4 μm81
- Figure 3-9 Endothelial tubules from non-diabetic mouse capillary.** a. Presents an overview of the capillary with a focus area highlighted in red. b – e. provide magnified views of the specified region as consecutive slices 1 -4, showcasing the presence of electron-lucent tubules (indicated by red arrows).83
- Figure 3-10 Pericyte-endothelial interaction via direct contact.** Close contacts of a pericyte (blue) and endothelial cell (aqua) in absence of a bordering BM (brown) are indicated for the raw data (a and c) and segmented data (b and d) of two sections 1.2 μm apart.85
- Figure 3-11 Peg-and-socket, pericyte-endothelial formation spanning across multiple sections.** a, Peg-and-socket formation identified on a capillary (magnified area evident on right hand side bounded by box). b-d, This peg and socket spanned across three sections (minimum 360 nm). e, displays the 3D nature of peg and sockets. Full 3D animation can be found: <https://figshare.com/s/238d32953dde668ac862>86

- Figure 3-12 Semi-automated detection of pericyte-endothelial interactions.** Capillaries were analysed under the Arivis analysis pipeline, which semi-automatically detected endothelial-pericyte closeness via endothelial/pericyte intersect and depicted such occasions in green highlights. Data shown from capillary 1 from which the pipeline assessed all 150 sections. One section (corresponding to section 36) is shown in panels a-d. a) segmented features are endothelium: aqua; basement membrane: brown; pericyte: royal blue. (b)-(d) close contacts are displayed with green elements as quantified in Arivis with user instructed minimal distances of (b) 5 pixels, c) 3 pixels and (d) 1 pixel. Scale bar 3 μm . .87
- Figure 3-13 Distribution of peg and sockets across 3-month-old mouse capillaries.** The distribution of peg-and sockets evident across 150 sections examined in 3 capillaries. Note more than one peg-and-socket may appear in the same sections (i.e. at different points of pericyte-endothelial membrane interaction in the same z-plane).88
- Figure 3-14 SBF-SEM electron micrographs showcasing three distinct electron density categories.** Panel a. presents the overall micrograph with a capillary cross-section. Panel b is a magnified view of the highlighted area in panel a, displaying regions of low density (Yildirim et al.), intermediate density (ID), and high density (Timpl et al.).....89
- Figure 3-15 Identification of astrocytes via astrocyte nucleus presence within stack of data.** Astrocytes indicated in shade of purple. White arrow indicates astrocyte nucleus.90
- Figure 3-16 3D reconstruction of astrocyte.** Panel a shows the astrocytes (purple) enveloping the vasculature, with the basement membrane (brown), pericytes (blue), and endothelium (aqua) clearly distinguished. Panels b, c, and d represent different orientations of the same astrocyte, illustrating the star-like morphology and the extensive connections with the surrounding vasculature.....91
- Figure 3-17 Segmented data and 3D reconstruction of macroglia surrounding the vasculature.** (a, b) Glial cells a in (red and purple shades) can be seen to wrap around the vasculature across different sections along capillary depth. Purple shading depicts a cell identified as an astrocyte. Displayed in a and b are sections 6 μm apart. 3D reconstruction views (c, d) show the complexity of the wrapping along 18 μm of vessel. Full 3D animation can be found: <https://figshare.com/s/05be25f5f4da056d5cdf>92
- Figure 3-18 Immunostaining of astrocytes surrounding the capillary.** Astrocyte stained with GFAP (Reddy et al.) shown to surround the capillary (marked by endothelial cells, stained with Isolectin B4, green and staining pericytes in purple with NG2) and extend its processes in directions distant from capillary. a. Z-stack of entire vessel b.c.d. STED image of astrocytes (Reddy et

al.) wrapping around the capillary (b), endothelium (green) forming the capillary wall (d) and combined stains of astrocytes, endothelial cells, and pericytes showing the proximity and interactions of the astrocytic processes with the capillary structure.93

Figure 3-19 Macroglia-pericyte direct contact. Top slide, raw data. Bottom slide, segmented features. Of the two macroglia evident in this image, represented in the bottom panel by red features, one comes within close proximity of the pericytes (blue) by breaking through the BM (brown). Endothelial (aqua) and macroglia (purple and red shades).....94

Figure 3-20 CLEM of microglia using P2Y12R in 6-month mouse capillary. a. lectin blue, an endothelial stain, for identification of sample b. P2Y12 stained green for microglia, visualised in the green channel and AQP4 in red, Müller cell stain c. identification of microglia in OPL by indication of gold nanoparticles, shown as black dots, indicated as by red arrow d. example 2 of microglia in IPL e. identification of microglia near vascular capillaries in IPL f. example of microglia close to vascular capillary in OPL j. example 2 of microglia close to vasculature in OPL. Green arrows indicate capillaries. (Figures from Experimental Institute Budapest).96

Figure 3-21 Segmented data and 3D reconstruction of neurons surrounding the vasculature. (a, b) neurons in (green shades) can be seen to surround the vasculature across different sections along capillary depth. Displayed in a and b are sections 12 μ m apart. 3D reconstruction views (c, d) show the complexity of the wrapping along 18 μ m of vessel. Scale bar 3 μ m. 97

Figure 3-22 Neuron coming into close contact with vasculature. Raw (a and c) and segmented (b and d) data from consecutive sections (120 nm apart) illustrating a neuron in proximity with the vasculature. e and f, 3D arrangements from 6 consecutive sections: neurons: green shades, macroglia: red shades, endothelium: aqua; basement membrane: brown; pericytes: blue. Full 3D animation can be found: <https://figshare.com/s/37a0f2a3d62b1838b413> 98

Figure 3-23 Quantitative assessment of intercellular and cellular-BM proximities for 3 month old capillary 1. a, The stack mean population histogram of pericyte to endothelium distances. b, The cumulative distribution function obtained from a. Panel c, 10nm readings of the cumulative distribution functions obtained from selected intercellular and cellular-BM feature pairs to assess the degree of direct contact. CDF, cumulative distribution function; BM, basement membrane; P, pericyte; E, endothelium; M, macroglia; N, neurons.100

Figure 3-24 Column scatter graphs for convexity, solidity and sphericity of NVU cellular components and the BM for 3 month old mouse capillary 1. All 150 slices were analysed with each dot representing the area weighted mean obtained for all segmented features within each slice.

Panels a-c convexities (convex perimeter:perimeter, CP:P), solidities (area:convex area, A:CA) and sphericities (Rmin:Rmax) of NVU component cells and the BM. .102

Figure 3-25 Ultrastructure of 6-month-old mouse capillary 1. A collection of SBF-SEM micrographs taken from a mouse retinal capillary to display the morphological changes along the capillary length. a, slice 1 (0.1 μm), b, slice 25 (2.5 μm), c, slice 50 (5 μm) and d, slice 100 (10 μm). Lumen: L, Pericytes: P, Endothelium: E, Macroglia: MG, Neurons: N. Scale bar 2 μm . Full dataset can be found here: <https://figshare.com/s/43917a967b535710cef6>.103

Figure 3-26 Ultrastructure of 6-month-old mouse capillary 2. A collection of SBF-SEM micrographs taken from a mouse retinal capillary to display the morphological changes along the capillary length. a, slice 1 (0.1 μm), b, slice 25 (2.5 μm), c, slice 50 (5 μm) and d, slice 100 (10 μm). Lumen: L, Pericytes: P, Endothelium: E, Macroglia: MG, Neurons: N. Scale bar 3 μm . Full dataset can be found here: <https://figshare.com/s/3dc00501955f6b40b96b>.104

Figure 3-27 Ultrastructure of 6-month-old mouse capillary 3. A collection of SBF-SEM micrographs taken from a mouse retinal capillary to display the morphological changes along the capillary length. a, slice 1 (0.1 μm), b, slice 25 (2.5 μm), c, slice 50 (5 μm) and d, slice 100 (10 μm). Lumen: L, Pericytes: P, Endothelium: E, Macroglia: MG, Neurons: N. Scale bar 3 μm . <https://figshare.com/s/56c634fcab321ac6cf24>105

Figure 3-28 Segmented vasculature of 6-month-old mouse. The vasculature was identified, and each component was assigned a colour for segmentation through the data stack and subsequent visualisation in 3D reconstructions. a, endothelium (aqua), b, basement membrane (brown), c, pericytes (blue), d, complete vasculature. Scale bar 2 μm106

Figure 3-29 3D reconstruction of 6-month-old mouse capillary 1 vasculature. Displayed are features associated with a 3D reconstruction of the vasculature of capillary 1. Column a: endothelium (aqua); column b: basement membrane (brown); column c: pericytes (blue); and column d: combined vasculature.(a)(b)(c)(d)107

Figure 3-30 Distribution of peg and sockets across 6-month-old mouse capillaries. The distribution of peg and sockets evident across 130 sections examined in 9 capillaries. Note more than one peg and socket may appear in the same sections (i.e. at different points of pericyte-endothelial membrane interaction in the same z-plane).108

Figure 3-31 Analysis of peg and socket distributions in 3-month and 6-month-old mouse capillaries. a. Number of pegs in capillaries at 3 months and 6 months. b. Percentage of peg coverage per capillary depth in capillaries at 3 and 6 months. Bars indicate mean coverage, with individual

data points as black dots. No significant differences were found between age groups. Error bars represent standard deviations.108

Figure 4-1 Ultrastructure of diabetic 6-month-old mouse capillary, sample 1. A collection of SBF-SEM micrographs taken from a mouse retinal capillary to display the morphological changes along the capillary length. a, slice 1 (0.1 μm), b, slice 25 (2.5 μm), c, slice 50 (5 μm) and d, slice 100 (10 μm). Lumen: L, Pericytes: P, Endothelium: E, Macroglia: MG, Neurons: N. Scale bar 4 μm . Full dataset can be found here: <https://figshare.com/s/f06d367d6da9cc6d1198>.116

Figure 4-2 Ultrastructure of diabetic 6-month-old mouse capillary, sample 2. A collection of SBF-SEM micrographs taken from a mouse retinal capillary to display the morphological changes along the capillary length. a, slice 100 (10 μm), b, slice 125 (12.5 μm), c, slice 150 (15 μm) and d, slice 200 (20 μm). Lumen: L, Pericytes: P, Endothelium: E, Macroglia: MG, Neurons: N. Scale bar 3 μm . Full dataset can be found here: <https://figshare.com/s/9e650a62724ced4fb585>.117

Figure 4-3 Ultrastructure of diabetic 6-month-old mouse capillary, sample 3. A collection of SBF-SEM micrographs taken from a mouse retinal capillary to display the morphological changes along the capillary length. a, slice 100 (10 μm), b, slice 125 (12.5 μm), c, slice 150 (15 μm) and d, slice 200 (20 μm). Lumen: L, Pericytes: P, Endothelium: E, Macroglia: MG, Neurons: N. Scale bar 3 μm . Full dataset can be found: <https://figshare.com/s/43917a967b535710cef6>.118

Figure 4-4 Segmented vasculature of diabetic 6 month old mouse capillary 1. A collection of SBF-SEM micrographs taken from a mouse retinal capillary to display the morphological changes of along the capillary length. a, raw image slice 1 (0.1 μm), b, basement membrane (brown), slice 25 (2.5 μm), c, endothelium (aqua), slice 50 (5 μm) and d, pericytes (blue), slice 100 (10 μm). Scale bar 4 μm119

Figure 4-5 3D reconstruction of diabetic 6 month old mouse capillary 1 vasculature. Displayed are features associated with a 3D reconstruction of the vasculature of capillary 2. Column a: endothelium (aqua); column b: basement membrane (brown); column c: pericytes (blue); and column d: combined vasculature.120

Figure 4-6 Segmented BM showing convoluted nature of diabetic 6 month old mouse capillary 1. A collection of SBF-SEM micrographs taken from a mouse retinal capillary to display the morphological changes of BM (brown) along the capillary length. a, slice 1 (0.1 μm), b, slice 25 (2.5 μm), c, slice 50 (5 μm) and d, slice 100 (10 μm). Scale bar 4 μm121

Figure 4-7 Maximum and mean BM thickening of mouse diabetic vs non-diabetic. Every 10th section through the depth of the stack, and the thickest sections were analysed consecutively, represented as coloured dots, each colour depicts a separate capillary. Specifically, BM thickness was calculated by analysing every 10th section (e.g., sections 1, 10, 20, 30, up to section 100). After identifying the section with the thickest BM, the thickness for five sections before and five sections after that thickest slice were calculated. These consecutive sections, representing the region around the thickest BM, are shown as coloured dots. Analysis was conducted on three capillaries each state including three diabetic mice and three non-diabetic mice. Error bars represent standard deviations.122

Figure 4-8 BM separating from cells in the NVU. a. and b. 6-month-old non-diabetic capillary 1 displaying the direct contact nature of endothelium and pericytes to basement membrane. c. d. 6-month-old diabetic capillary displaying electron lucent gapping from basement membrane. Red arrows indicate electron lucent gaps where the endothelium, pericytes and cells surrounding vasculature are separating from BM. P, pericyte, E, endothelium, N, neuron, MG, macroglia.....123

Figure 4-9 Separation of BM from NVU cell components across multiple sections. 6-month-old diabetic capillary 1 from sample 2 (SBF108-5). a. capillary displaying separation of BM from endothelial cell, white box indicates area of separation shown, b, enlarged area of separation of BM from endothelium on section 112, c, section 113, d, section 114. e. capillary displaying separation of BM from pericyte, white box indicates area of separation shown, f, enlarged area of separation of BM from endothelium on section 140, g, section 141, h, section 142. i. capillary displaying separation of BM from cells surrounding vasculature (neurons and macroglia), white box indicates area of separation shown, j, enlarged area of separation of BM from endothelium on section 125, k, section 126, l, section 127.....124

Figure 4-10 Comparative analysis of basement membrane separation in diabetic and non-diabetic capillaries. This graph illustrates the frequency of separation occurrences from the BM to distinct cellular components within the NVU. a. BM to Pericytes: Occurrences of separation between the BM and pericytes in diabetic (orange) and non-diabetic (blue) capillaries. b. BM to endothelium. c. BM to Macroglia and Neurons (combination of cells surrounding vasculature). Data is derived from the analysis of 9 diabetic and 9 non-diabetic capillaries, from a total of 6 mice, 3 diabetic and 3 non-diabetic. Error bars represent standard deviations.....125

- Figure 4-11 Comparison of peg and socket formations in non-diabetic vs diabetic.** a. non-diabetic capillary displaying peg and socket interaction indicated by the red arrow, b. peg and socket interaction in diabetic capillary displaying electron lucent space in the socket surrounding the peg, indicated by red arrows.126
- Figure 4-12 Close-up view illustrating the spatial arrangement around a peg within a diabetic capillary.** The image emphasises the intricate details of the surrounding space, providing a closer examination of the microenvironment.127
- Figure 4-13 Distribution of peg and sockets across 6-month mouse diabetic vs non-diabetic capillaries.** The distribution of peg-and sockets evident across 130 sections examined in 18 capillaries. Note more than one peg-and-socket may appear in the same sections (i.e. at different points of pericyte-endothelial membrane interaction in the same z-plane).128
- Figure 4-14 Peg analysis in non-diabetic and diabetic capillaries.** These panels present a comprehensive analysis of peg count distribution, showcasing a. the quantitative disparity in peg numbers between diabetic and non-diabetic capillaries and b. the percentage of peg coverage within a capillary, calculated by the number of sections within a capillary that contain a peg and comparing this to the total number of sections across the entire capillary. Error bars represent standard deviations.....129
- Figure 4-15 Endothelial tubules in 3D from a mouse diabetic capillary.** a. presence of endothelial tubule on section 1 b. section 2, c. section 3, d. section 4, e. 3D reconstruction of tubule. Red arrows indicate endothelial tubules. Scale bar 2 μ m.130
- Figure 4-16 Endothelial tunnels in non-diabetic vs diabetic capillaries.** a. non-diabetic capillary, b, area of endothelium enlarged showing few numbers of endothelial tubules, c. diabetic capillary, red box indicates area enlarged in d, displaying increased numbers of white electron lucent tubules within endothelium. d. quantitative assessment of endothelial tubules calculated via a morphological count of electron lucent holes within the endothelium of two capillaries from each mouse sample, totalling 6 diabetic and non-diabetic 6-month-old capillaries. Error bars represent standard deviations.....131
- Figure 4-17 Leukocyte contact with endothelial projections** Visualisation of leukocyte interactions with endothelial projections, a. diabetic capillary with presence of leukocyte within lumen, b. enlarged view of leukocyte present on section 100, c. section 106, d. section 116, and e. 118. Red arrows indicate direct contact of leukocytes with endothelial projections. 134

- Figure 4-18 3D reconstruction of endothelium and leukocyte.** 3D visualisation of leukocyte making direct contact with endothelial projections. a-c raw data images of diabetic capillary across serial sections showing leukocyte making direct contact with endothelial projections. d. multiple planes of leukocyte and endothelium direct contacts reconstructed in 3D. Red arrows indicate areas of direct contacts.....134
- Figure 4-19 Quantification of endothelial projections in capillaries with and without leukocytes in diabetic and non-diabetic conditions.** Illustrates the comparison of number of endothelial projections in capillaries with (dark grey) and without (light grey) leukocytes, exploring the distinction between diabetic and non-diabetic capillary environments.....135
- Figure 5-1 Organisation of retinal capillary plexus.** This schematic represents the structure of the human retina, highlighting the three capillary plexuses and the retinal cells in each layer. The superficial capillary plexus, intermediate capillary plexus, and deep capillary plexus form the vascular network, contributing to nutrient and oxygen delivery within the retina. Pericytes and endothelial cells line the capillaries, forming the inner blood-retinal barrier (iBRB), which regulates permeability. The adjacent neuronal layers include ganglion cells, amacrine cells, bipolar cells, horizontal cells, and Müller glia, which provide structural support and maintain retinal function. The lower layers contain rod cells and cone cells, essential for vision, and interact with the retinal pigment epithelium (RPE) at the base of the retina (modified from (Sheng et al., 2024))......143
- Figure 5-2 Ultrastructure of non-diabetic human capillary.** A collection of SBF-SEM micrographs taken from a human retinal capillary to display the morphological changes along the capillary length. a, slice 1 (0.1 μm), b, slice 50 (5 μm), c, slice 100 (10 μm) and d, slice 150 (1.5 μm). Lumen: L, Pericytes: P, Endothelium: E, Macroglia: MG, Neurons: N. Scale bar 5 μm Full dataset can be found: <https://figshare.com/s/3b904ed185d815f690df>.144
- Figure 5-3 Ultrastructure of diabetic human capillary.** A collection of SBF-SEM micrographs taken from a human retinal capillary to display the morphological changes along the capillary length. a, slice 1 (0.1 μm), b, slice 50 (5 μm), c, slice 100 (10 μm) and d, slice 150 (1.5 μm). Lumen: L, Pericytes: P, Endothelium: E, Macroglia: MG, Neurons: N. Scale bar 5 μm . Full dataset can be found: <https://figshare.com/s/2f54a9228dd5cf08f9bc>.145
- Figure 5-4 Lipid-like deposits in non-diabetic capillary 1.** a. shows image of human non-diabetic capillary 1 b. basement membrane (BM) segmented capillary, BM shown in brown. White arrows show where lipid-like deposits are present.146

- Figure 5-5 Lipid-like deposits in diabetic capillary 1.** a. shows image of human diabetic capillary 1 b. basement membrane (BM) segmented capillary, BM shown in brown. White arrows show where lipid-like deposits are present. C. provides a magnified view of the area highlighted in the red box in panel b, offering a closer look at the detailed structure and location of the lipid deposits within the basement membrane.....147
- Figure 5-6 Human pericyte-endothelial interaction via peg-and-socket formations.** Electron micrographs depict the intricate peg-and-socket interactions between pericytes and endothelial cells in the human neurovascular unit. Protrusions from pericytes break through the basement membrane to establish dynamic contact with neighbouring endothelial cells.148
- Figure 5-7 Distribution of peg and sockets across human diabetic vs non-diabetic capillaries.** The distribution of peg-and sockets evident across 130 sections examined in 18 capillaries. Note more than one peg-and-socket may appear in the same sections (i.e. at different points of pericyte-endothelial membrane interaction in the same z-plane).149
- Figure 5-8 Comparative microscopy of peg-and-socket formation structures in non-diabetic capillaries.** a. SBF-SEM image of a capillary cross-section, highlighting the peg-and-socket formation composition. b. Enlarged SBF-SEM image from the area marked in red in panel a, showing a peg-and-socket formation. c. Corresponding area of another capillary shown using TEM. d. High-resolution TEM image from the area marked in red in panel c, displaying cell membranes from peg-and-socket formations. This magnified view clearly shows the intricate details of the peg-and-socket formation, with visible cell membranes, demonstrating the superior resolution of TEM for studying fine cellular interactions.151
- Figure 5-9 TEM analysis of junctions** TEM image illustrating peg-and-socket formation emphasising the structural details of the peg-and-sockets and the absence of clear junctions. Red arrows highlight peg-and-socket formations, while green arrows indicate endothelial-to-endothelial junctions.152
- Figure 5-10 Comparative electron micrographs illustrating basement membrane thickening in diabetic conditions.** (a) shows electron micrograph of a capillary from a non-diabetic human retina. In (b), the BM is segmented in brown to highlight the thickened areas, with the red square indicating the region of interest that is further magnified in (c) for detailed examination. Panels (d), (e), and (f) present a similar layout for a capillary from a diabetic human retina, where the BM thickening segmented in brown in (e), and (f) offers an enlarged view of the highlighted section within the red square. These images compare the morphological

characteristics of BM thickening in capillary vessels between diabetic and non-diabetic samples.154

Figure 5-11 Maximum and mean BM thickening of human diabetic vs non-diabetic. Every 10th section through the depth of the stack, and the thickest sections were analysed consecutively, represented as coloured dots, each colour depicts a separate capillary. Specifically, BM thickness was calculated by analysing every 10th section (e.g., sections 1, 10, 20, 30, up to section 100). After identifying the section with the thickest BM, the thickness for five sections before and five sections after that thickest slice were calculated. These consecutive sections, representing the region around the thickest BM, are shown as coloured dots. Analysis was conducted on three capillaries each state including three diabetic and three non-diabetic human capillaries. Error bars represent standard deviations. .155

Figure 5-12 BM separating from endothelium. a. human diabetic capillary 1, red box indicates area magnified b-e magnified region of capillary displaying electron lucent gapping from basement membrane. White arrows indicate electron lucent gaps where the endothelium is separating from BM, serial sections b. 101, c. 102, d. 103.....157

Figure 5-13 BM separating from pericytes. a. human diabetic capillary 2, red box indicates area magnified b-g magnified region of capillary displaying electron lucent gapping from basement membrane. White arrows indicate electron lucent gaps where the pericytes are separating from BM, serial sections b. 195, c. 196, d. 197, e. 198, f. 199, g. 200.158

Figure 5-14 BM separating from neuroglia. a. human diabetic capillary 2, red box indicates area magnified b-d magnified region of capillary displaying electron lucent gapping from basement membrane. White arrows indicate electron lucent gaps where the cells surrounding the vasculature are separating from BM, serial sections b. 187, c. 188, d. 189. .158

Figure 5-15 Comparative analysis of basement membrane separation in diabetic and non-diabetic capillaries. This graph illustrates the frequency of separation occurrences from the BM to distinct cellular components within the NVU. a. BM to Pericytes: Occurrences of separation between the BM and pericytes in diabetic and non-diabetic capillaries. b. BM to Endothelium. c. BM to Neuroglia (combination of cells surrounding vasculature including neurons and macroglia). Data is derived from the analysis of 3 diabetic and 3 non-diabetic capillaries from 2 human samples. Error bars represent standard deviations.159

Figure 7-1 Key findings of retinal NVU in health and disease. This schematic summarises the key findings from the study on the retinal NVU in both non-diabetic and diabetic conditions discussed in this thesis. Top Panel – Characterising the NVU’s heterocellular composition: The ultrastructural

analysis of the retinal NVU demonstrates the intricate heterocellular arrangement involving endothelial cells, pericytes, and the BM. Advanced imaging reveals the complex interactions between these components, with peg-and-socket formations between pericytes and endothelial cells. The BM intricately weaves around the endothelial cells and pericytes, as highlighted in the color-coded three-dimensional renderings. This analysis also reveals the coverage of macroglial cells, such as astrocytes and Müller cells, which form a supportive network around the vasculature. Middle Panel – Quantitative analysis of key features: This panel highlights the quantitative assessments of key NVU features. Pairwise distance analysis is shown, comparing NVU features from pericytes. Bottom Panel – Exploring diabetes-related changes in the NVU: This panel presents the effects of diabetes on the structural integrity and cellular interactions within the NVU. Comparative analysis between diabetic and non-diabetic samples shows a significant increase in BM-cell separation and altered pericyte-endothelial interactions.....174

Academic Thesis: Declaration of Authorship

I, Mona Albargothy declare that this thesis and the work presented in it are my own and has been generated by me as the result of my own original research.

Three-dimensional Mapping of the Retinal Neurovascular Unit in Diabetic Retinopathy.

I confirm that:

1. This work was done wholly or mainly while in candidature for a research degree at this University;
2. Where any part of this thesis has previously been submitted for a degree or any other qualification at this University or any other institution, this has been clearly stated;
3. Where I have consulted the published work of others, this is always clearly attributed;
4. Where I have quoted from the work of others, the source is always given. With the exception of such quotations, this thesis is entirely my own work;
5. I have acknowledged all main sources of help;
6. Where the thesis is based on work done by myself jointly with others, I have made clear exactly what was done by others and what I have contributed myself;

Signed:



Date: 15th May 2024

Acknowledgements

All praise and gratitude are due to the Almighty Allah, whose boundless grace has guided me to this significant academic milestone. The completion of this thesis stands as a testament to the extraordinary individuals whose guidance, support, and unwavering belief in me have been pivotal.

To my father, Jamal Albargothy, I owe a depth of gratitude beyond what words can convey. His unwavering support, counsel, and profound faith in my potential have been the bedrock of my academic and personal growth. I extend my heartfelt gratitude to my sister, Dr. Nazira Albargothy, for her invaluable guidance, advice, and continuous motivation. The insightful conversations we've had have profoundly shaped my perspective along this journey. I also wish to express my deep gratitude to my mother, my brothers, and my husband, whose firm belief in me has given me the strength to overcome many challenges.

My sincere appreciation is extended to my supervisors, Prof. Michael Taggart, Prof. Tim Curtis, and Dr. David Steel whose support, and expertise has been a guiding light on this journey.

I thank Queen's University Belfast for their support on the diabetic research components of this study. A special thanks goes to Dr. Evan Troendle for his assistance with the quantitative analysis. The collaborative environment and resources provided by the university have greatly enriched my research experience, and I am delighted to have been part of such a vibrant academic community.

I extend my thanks to the Electron Microscopy Unit at Newcastle University. The cutting-edge facilities and exceptional technical support from their staff were indispensable to my research.

To all who have walked this path with me, your support has been immeasurable. Thank you.

Abbreviations

2D	Two-dimensional
3D	Three-dimensional
A	Area
AGE	Advanced Glycation End Product
AIF	Apoptosis-inducing Factor
AJ	Adheren Junction
AMD	Age-related Macular Degeneration
Ang	Angiopoietins
BM	Basement Membrane
BRB	Blood Retinal Barrier
CA	Convex Hull Area
Caco	Cacodylate
CC	Connecting Cilium
cGMP	Cyclic Guanosine Monophosphate
CP	Convex Hull Perimeter
DM	Diabetic Mellitus
DME	Diabetic Macular Edema
DR	Diabetic Retinopathy
E	Endothelium
EC's	Endothelial Cells
ECM	Extracellular Matrix
ELM	External Limiting Membrane

EM	Electron Microscopy
FAB	Fragment Antigen-binding
GA	Glutaraldehyde
GCL	Ganglion Cell Layer
HD	High Density
HG	High Glucose
HSA	Human Serum Albumin
ID	Intermediate Density
iGluRs	Ionotropic Glutamate Receptors
INL	Inner Nuclear Layer
IP	Intraperitoneal
IPL	Inner Plexiform Layer
IRMAs	Intraretinal Microvascular Abnormalities
IS	Inner Segment
IV	Intravenous
K	Potassium
L	Lumen
LD	Low Density
MG	Macrogia
MIB	Microscopy Image Browser
NFL	Nerve Fibre Layer
NO	Nitric Oxide

NPDR	Non-proliferative Diabetic Retinopathy
NVU	Neurovascular Unit
ONL	Outer Nuclear Layer
OS	Outer Segment
OsO₄	Osmium Tetroxide
P	Perimeter
PaCO₂	Partial pressure of carbon dioxide
PBS	Phosphate-buffered saline
PC's	Pericytes
PDR	Proliferative Diabetic Retinopathy
PKC	Protein Kinase C
P2Y₁₂	Purinergic receptor P2Y, G-protein coupled, 12 protein
RGC	Retinal Ganglion Cell
ROP	Retinopathy of Prematurity
RPC	Retinal Progenitor Cell
RPE	Retinal Pigment Epithelium
SBF-SEM	Serial Block Face Scanning Electron Microscopy
SEM	Scanning Electron Microscopy
STZ	Streptozotocin
TBS	Tris-buffered saline
TEM	Transmission Electron Microscopy
TGF β	Transforming Growth Factor β
TJ	Tight Junctions

VEGF	Vascular Endothelial Growth Factor
vEM	Volume Electron Microscopy
VSMCs	Vascular Smooth Muscle Cells
ZO	Zonula Occludens
GFAP	Glial Fibrillary Acidic Protien
FAZ	Foveal Avascular Zone
IOP	Intraocular Pressure
mGluR6	Metabotropic Glutamate Receptor 6
GABA	Gammma-aminobutyric Acid
GFAP	Glial Fibrillary Acidic Proteins
PGE2	Prostaglandin E2
PNS	Peripheral Nervous System
OCT	Optical Coherence Tomography
IL-10	Interleukin-10
IL-3	Interleukin-3
IL-4	Interleukin-4
ICAM-1	Intercellular Adhesion Molecule-1
VCAM-1	Vascular Adhesion Molecule-1
MCP-1	Monocyte Chemotactic Protien-1
MIP-1	Macrophage Inflammatory Protien-1
OCTA	Optical Coherence Tomography Angiography
ICGA	Indocyanine Green Angiography

Chapter 1 Introduction

1.1 The Eye

The eye, is a fluid filled sphere comprised of three layers of tissue. The sclera, the outer most layer is composed of durable white fibrous tissue. At the front of the eye, the outer layer transforms into the cornea, a specialised transparent tissue which allows light to enter the eye (Kolb, 1995). The middle layer comprises three continuous structures: the ciliary body, the iris and the choroid. The ciliary body, encircling the lens, includes a muscular component crucial for adjusting the lens's refractive power, as well as a vascular component (ciliary processes) responsible for producing the eye's front fluid, the aqueous (Bloom *et al.*, 2024). The iris, the coloured part of the eye, visible through the cornea, possesses two sets of muscles with opposing actions, enabling the adjustment of the pupil's size (the central opening) under neural control. The choroid consists of a dense capillary bed serving as the primary blood supply for the retina's photoreceptors. Only the innermost layer, the retina, houses light-sensitive neurons capable of transmitting visual signals to central targets (Blauth *et al.*, 2010).

As light travels towards the retina, it first transverses the cornea, lens and two distinct fluid environments; the anterior chamber and the posterior chamber. Aqueous humour, a transparent, water-like fluid that nourishes both the lens and these tissues, fills the anterior chamber, the area between the lens and the cornea. The posterior chamber, positioned between the lens and the iris, is where the ciliary processes produce aqueous humor (Kels *et al.*, 2015). This fluid subsequently moves to the anterior chamber via the pupil, a process facilitated by a specialised meshwork of cells located at the junction of the iris and cornea. The region between the posterior surface of the lens and the retina is occupied by vitreous humor, a gel-like substance constituting roughly 80% of the eye's total volume (**Figure 1-1**). Apart from preserving the eye's form, the vitreous humour is equipped with phagocytic cells that eliminate blood debris, preventing interference with light transmission (Monteiro *et al.*, 2015).

1.2 Retina

1.2.1 Function of the Retina

The retina is an intricate layer, situated in the posterior segment forming the innermost boundary of the eye and plays a pivotal role in the process of vision. It is a layered structure composed of photoreceptor cells, which include rods and cones for low light and colour vision, respectively, and glial cells that support and protect the neuronal cells. The retina captures incoming photons and converts them into electrical and chemical signals, which are then transmitted along neuronal pathways to the brain, forming functional circuits to facilitate vision (Hoon *et al.*, 2014). This complex process begins with phototransduction, where the capture of light energy by pigment molecules (opsins) in the photoreceptor cells' outer segments. This conversion leverages the wave-particle duality theory of light, where light travels via photons, with the energy of each photon determined by its frequency. Photons with higher frequencies carry more energy, correlating to shorter wavelengths (Palczewski, 2012). Upon absorbing these photons, the pigment molecules undergo conformational changes, transforming the light's wavelength into chemical energy. Following this initial conversion, the visual signals undergo further refinement through signal processing (Mannu, 2014). Bipolar and ganglion cells within the retina play a pivotal role in this stage (**Figure 1-1**). They engage in a complex network of interactions to enhance contrast, adapt to varying light intensities, and fine-tune the visual signal before its transmission to the brain. Bipolar cells act as intermediaries between photoreceptors (rods and cones) and ganglion cells, crucial for processing visual signals (Regus-Leidig & Brandstätter, 2012). They are divided into ON cells, which respond to increases in light, and OFF cells, which respond to decreases, enabling the detailed processing of visual contrasts and brightness. These cells forward the refined signals to ganglion cells, the retina's output neurons, which compile inputs from multiple bipolar cells to encode visual attributes like intensity and movement. The optic nerve, formed from ganglion cell axons, carries this information to the brain (Ireland & Carter, 2024). This intricate signal processing ensures that the visual information relayed to the brain is of the highest clarity and utility for perception. Moreover, the retina's functionality is supported by a unique oxygen supply mechanism. It benefits from a dual blood supply system, which segregates the retina into outer and inner layers. This design is crucial for optimising oxygen delivery to the retina's cells, essential for their health and operational efficiency. The dual supply system ensures that all cells within the retina receive

adequate oxygen to support their high metabolic demands, especially critical during the energy-intensive processes of phototransduction and signal processing (Lange & Bainbridge, 2012).

Retinal dysfunction encompasses a variety of conditions that impair vision, ranging from genetic disorders to age-related degeneration and complications from systemic diseases like diabetes. Age-related macular degeneration (AMD) involves the central portion of the retina, the macula leading to central vision loss (Guymer & Campbell, 2023). Retinitis Pigmentosa, a set of genetic disorders, progressively damages retinal cells, diminishing peripheral and night vision before potentially leading to complete vision loss (O'Neal & Luther, 2024). Diabetic Retinopathy, prevalent in individuals with unmanaged diabetes, arises from damage to the retinal blood vessels (Shukla & Tripathy, 2023). A detailed understanding of the retina's structure underpins the ability to diagnose retinal diseases accurately, develop effective treatments, and implement surgical interventions with greater precision.

1.2.2 Structure of the Retina

The retina is a complex, layered structure with a diverse collection of component cells which work together to form functional circuits to facilitate vision. The vasculature, primarily the central retinal artery and vein, enters the eye through the optic nerve and branches out across the retina. These blood vessels are crucial as they supply blood, oxygen, and nutrients to the retinal layers. Comprising ten layers, the retina is composed of six distinct cell types—photoreceptors (rods and cones), horizontal cells, bipolar cells, amacrine cells, ganglion cells, microglia and macroglia including, Astrocytes and Müller cells—each assigned a specific function in the process of creating and transmitting visual information (**Figure 1-1**). Photoreceptors, the rods and cones, are pivotal in this structure. Rods function primarily under low-light conditions and are highly sensitive to light, making them essential for night vision. Cones, in contrast, operate under higher light levels and are crucial for detecting colour and fine detail. The various neuronal cells collaborate to form functional circuits tailored to detect specific variations and movements of light, contributing to the intricate process of vision. Three layers of nerve cell bodies, interspaced by two plexiform layers of synapses comprise the retina. Photoreceptors are found in the outer nuclear layer (ONL), followed by amacrine, bipolar and horizontal cells in the inner nuclear layer (Schafer et al.) and displaced amacrine cells and ganglion cell bodies in the ganglion cell layer (GCL). Bipolar cells, horizontal cells and amacrine cells

all connect to the ganglion cells in the inner plexiform layer (IPL), ganglion cell axons construct the nerve fibre layer (NFL) (Masland, 2012a).

On a microscopic level, the retinal vasculature can be observed interweaving between the neuronal structures. The microvasculature extends into two capillary beds: in the superficial, intermediate and deep capillary plexuses. The capillaries here provide critical support to the retinal neurons, including photoreceptors, bipolar cells, and ganglion cells. The blood vessels are organised to ensure minimal interference with light reaching the photoreceptors. They are also part of the blood-retinal barrier, which regulates the environment of the retina. In sum, the retinal vasculature is strategically situated to support both the macro and microstructures of the retina, providing essential blood flow while integrating with the neuronal circuitry to maintain optimal visual function.

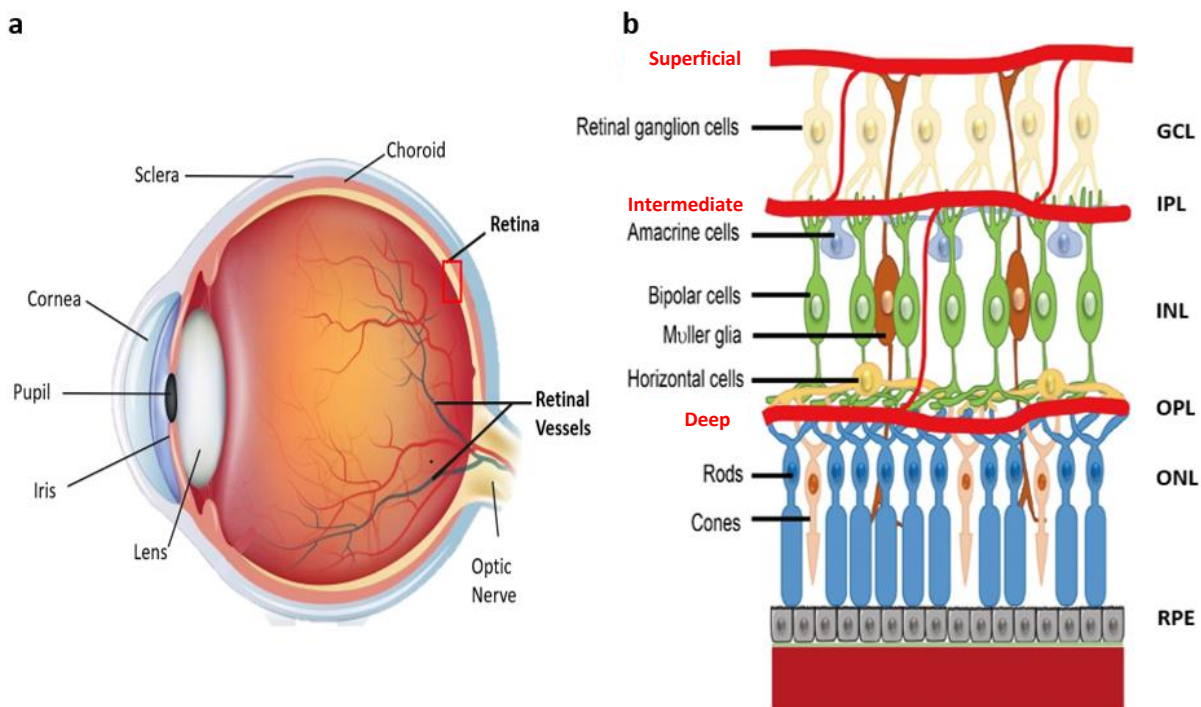


Figure 1-1 Macrostructure and microstructure of the Human Eye. Panel a depicts a sagittal section of the human eye, highlighting its major anatomical features, including the sclera, cornea, pupil, iris, lens, retina, retinal vessels, choroid, and the optic nerve. A red square indicates a magnified area within the retina. Panel b is a magnified view of the retinal structure, detailing the cellular layers and components. It shows the arrangement of retinal cells and their interconnections, from the photoreceptor layer containing rods and cones at the bottom to the ganglion cell layer at the top. The various types of cells such as horizontal cells, bipolar cells, amacrine cells, and Müller

glia are depicted. Blood vessels are also shown servicing the retinal layers. The cellular layers are labelled as follows: ganglion cell layer (GCL), inner plexiform layer (IPL), inner nuclear layer (Schafer et al.), outer plexiform layer (OPL), outer nuclear layer (ONL), and the retinal pigment epithelium (RPE). Modified from (Fu *et al.*, 2020).

1.2.3 Neurons

The retina includes five major types of neurons: photoreceptors, horizontal cells, bipolar cell, amacrine cell and ganglion cells (**Figure 1-1**) (Masland, 2012a). Photoreceptors, which are light-sensing cells and can be further characterised into cone and rod cells, make synaptic connections with bipolar cells and indirectly interact with horizontal cells. Bipolar cells serve as intermediary neurons that relay signals from photoreceptors to ganglion cells, which are the output neurons integrating and transmitting visual information to the brain. Horizontal cells are involved in the modulation of signals between photoreceptors and bipolar cells, contributing to contrast enhancement and spatial processing of visual inputs. Ganglion cell axons send visual signals to the visual cortex through the optic nerve, effectively translating the electrical impulses into a form that the brain can interpret as visual images. The intricate circuitry formed by these neuronal connections is essential for the precise transmission of visual signals, allowing for the encoding of complex visual scenes into a language the brain can understand. Neurons function by transmitting electrical impulses which are converted by photoreceptors to signal the brain to form vision. To support this essential function, glial cells play a crucial role by regulating blood flow and maintaining the optimal environment around neurons. This regulation ensures that neurons receive the necessary nutrients and oxygen to perform efficiently, and it also involves the removal of metabolic waste. Glial cells, therefore, are key to sustaining the health and functionality of the neural circuits involved in vision (Duh *et al.*, 2017).

1.2.3.1 Photoreceptors

Specialised neurons known as rod and cone photoreceptors are integral in the initial stages of vision. Positioned at the posterior of the retina next to the retinal pigment epithelium (RPE), a critical cell layer for photoreceptor survival, these light-sensitive cells have distinct functions. Rod cells, characterised by high sensitivity to light, operate effectively in low-light conditions. Conversely, cone cells function under bright lighting conditions, demonstrating rapid responses to changes in light intensity. Responsible for colour vision and high visual acuity, cone cells are concentrated in the

central or macula region of the retina, with the human retina containing 120 million rod cells and 6 million cone cells (Molday & Moritz, 2015). Unlike humans, mice do not possess a macula. The absence of this specialised region means that mice lack an area where cone cells are densely packed for high acuity color vision, reflecting their nocturnal nature. Instead, their retinal structure is adapted for low light conditions with a higher proportion of rod cells, enabling them to navigate their environment in dim light but without the colour and detail resolution afforded by a macular region (Fletcher *et al.*, 2014).

The structures and functions of photoreceptors, specifically rods and cones, are distinguished by five main components: the outer segment (OS), connecting cilium (CC), inner segment (IS), nuclear region, and synaptic region (Arshavsky & Burns, 2012). The OS plays a critical role in phototransduction, the process by which light is converted into electrical signals, essential for vision. The CC serves as a bridge between the OS and IS, enabling the transport of proteins critical for photoreceptor function. The IS is the site of vital metabolic activities and protein synthesis, hosting a rich concentration of mitochondria and other organelles such as lysosomes, the endoplasmic reticulum, and the Golgi complex. These organelles support the photoreceptor's demanding energy and biosynthetic needs. Additionally, the IS plays a role in the regeneration of the photoreceptor's outer segment, a process crucial for maintaining optimal light sensitivity and visual acuity. The process concludes in the synaptic region, where the neurotransmitter glutamate is released through synaptic vesicles at the ribbon synapse to communicate with bipolar cells and other secondary neurons (Maeda *et al.*, 2003). Glutamate plays a crucial role in the visual system by serving as the primary neurotransmitter for transmitting visual information from photoreceptors to the brain. It modulates the activity of bipolar cells through two main mechanisms: activating OFF bipolar cells via ionotropic glutamate receptors, which signal the absence of light, and inhibiting ON bipolar cells via metabotropic receptors, which become activated in reduced glutamate conditions to signal light detection (Bui *et al.*, 2009).

1.2.3.2 Bipolar cells

Bipolar cells receive visual inputs from photoreceptors and project their axons onto retinal ganglion cells. Bipolar cells are categorised into rod bipolar cells and cone bipolar cells, depending on the source of their inputs. These cells form intricate circuits with photoreceptors, establishing

fundamental elements of vision such as chromatic composition, contrast, polarity, and the temporal profile of incoming visual stimuli (Hoon *et al.*, 2014).

Each cone bipolar cell and rod bipolar cell is further classified based on whether it depolarises (ON-bipolar cells) or hyperpolarises (OFF-bipolar cells) in response to light. This depolarisation and hyperpolarisation response in cone bipolar cells is intricately influenced by glutamate levels. ON cone bipolar cells express metabotropic glutamate receptor 6 (mGluR6) and the ion channel TRPM1, where reduced glutamate availability leads to an increase in TRPM1 activity, causing depolarisation. Conversely, OFF cone bipolar cells express ionotropic glutamate receptors (iGluRs), and a decrease in glutamate causes these cells to hyperpolarise, highlighting a sophisticated mechanism where the reduction in glutamate has opposite effects on these cells. Rod bipolar cells are exclusively ON type while cone bipolar cells are classified as either ON or OFF type. Rods, adapted for scotopic vision, primarily discern the presence or absence of photons on the retina, making ON bipolar cells sufficient for this binary function. In contrast, cone cells contribute to photopic vision, requiring both ON and OFF bipolar cells to qualitatively distinguish incoming photons, facilitating the recognition of fine details, movements, and colours (Euler *et al.*, 2014).

Bipolar cells establish synaptic connections with rods and cones in the IPL of the retina, bridging the inner and outer layers of the retina. The IPL functions as a switchboard, with different bipolar cells stratifying at five layers within the IPL, conveying various forms of primary visual information to specific groups of retinal ganglion cells (RGCs) and amacrine cells. Bipolar cells engage in distinct relationships with RGCs, amacrine, and horizontal cells. Amacrine cells pre-synaptically inhibit bipolar cell terminals in the IPL, while horizontal cells provide GABAergic inhibitory inputs into bipolar cells. Consequently, bipolar cells receive glutamatergic inputs from cones and rods, as well as GABAergic inputs from horizontal cells. Sequentially, bipolar cells offer glutamatergic excitatory input to RGCs and amacrine cells. This parallel information processing model enables highly pre-processed excitatory inputs to form the foundational elements of vision (Euler *et al.*, 2014).

1.2.3.3 Horizontal cells

Horizontal cells play a crucial role in regulating the transmission of information between bipolar cells and photoreceptors, aiding in the adaptation of eyes to both bright and low light conditions. These cells have expansive and diffuse horizontal projections, connecting with neighbouring cells

through gap junctions (Schubert *et al.*, 2010). Three distinct types of horizontal cells exist in the retina, with their cell bodies concentrated mainly in the outer retina within the INL.

Functioning as GABAergic interneurons, horizontal cells provide inhibitory inputs to bipolar cells and offer inhibitory feedback to both rods and cones (McMahon & Dowling, 2023). Horizontal cells establish contacts in the OPL, conveying information about polarity, spectral sensitivity, speed, and structuring the spatial receptive field. By delivering lateral inhibitory GABAergic inputs to the surrounding bipolar cells encircling the ON-type or OFF-type bipolar cells, horizontal cells amplify signals from ON-OFF types. This antagonistic interaction supports contrast enhancement through binary signalling, providing two-point differentiation. Additionally, horizontal cells play a vital role in enveloping bipolar cells, forming contacts by invaginating with dendrites of ON cone bipolar cells and establishing basal contacts with OFF cone bipolar cells, thereby modulating visual signals for enhanced contrast sensitivity and spatial resolution. This interaction is crucial for the precise regulation of excitatory and inhibitory inputs, ensuring accurate signal processing across varying light conditions and contributing to the visual system's ability to adapt and maintain high-resolution perception (Deniz *et al.*, 2011).

The functional significance of regulating ON-OFF signalling in the retina by horizontal cells is profound. This regulation is essential for the high-resolution visual processing required for detailed perception and for adapting to varying light conditions (Barnes *et al.*, 2020). By modulating the activity of bipolar cells, horizontal cells fine-tune the visual signal before it reaches the brain. This modulation ensures that the retina can distinguish between light and dark regions with high precision, enhancing the clarity and contrast of the visual image. The dynamic interaction between horizontal cells, bipolar cells, and photoreceptors facilitates a sophisticated preprocessing of visual information, optimising the detection of edges, motion, and changes in light intensity. This preprocessing is crucial for the early stages of visual perception for complex image processing and interpretation in higher visual centres. Through these mechanisms, horizontal cells contribute to a robust and adaptable visual system, capable of functioning efficiently across a wide range of environmental lighting conditions (Ichinose & Habib, 2022).

1.2.3.4 Amacrine cells

Amacrine cells, serving as intermediate neurons, release the inhibitory neurotransmitters gamma-aminobutyric acid (GABA) or glycine. Amacrine cells exhibit significant heterogeneity and

perform a wide range of roles and responsibilities inside the retina, making them the most versatile cells in the retina (Masland, 2012b). The heterogeneous lineage of retinal ganglion cells contributes to a diverse population of amacrine cells. Researchers have identified 20 distinct ganglion cells accompanied by over 42 different types of amacrine cells (Masland, 2011; Yan et al., 2020). The multitude of amacrine cells enables the formation of specialised operational microcircuits, which enable the retina to identify specific hues and motions of light in particular orientations. The functional microcircuits are categorised based on the type of amacrine cells present, namely wide field, medium field, and narrow field amacrine cells. Wide field amacrine cells have a specific function of facilitating horizontal communication within a single layer of the retina, which aids in the assimilation of horizontal information. Narrow-field amacrine cells exhibit a greater extent of vertical penetration into many layers of the retina. The stratification of amacrine cell output can occur either before or after synaptic transmission, and in combination with gap junctions, enables amacrine cells to exhibit both inhibitory and excitatory effects, despite emitting only inhibitory neurotransmitters. Amacrine cells exert inhibitory control over the terminals of bipolar cells in a pre-synaptic manner, and they also inhibit the dendrites of retinal ganglion cells in a post-synaptic manner (Euler *et al.*, 2014).

1.2.3.5 Retinal Ganglion cells

Retinal ganglion cells (RGCs) serve as the primary output neuron of the retina and constitute a third class of photosensitive photoreceptors (**Figure 1-1**). These cells play a crucial role in transmitting both image-forming and non-image developing information, which is involved in various physiological processes such as regulating the circadian rhythm, modulating melatonin release, and controlling pupil size (Berson, 2007). Approximately 20 different types of RGCs exist, with 1 to 2% being intrinsically photosensitive, akin to cone and rod photoreceptors, due to their selective expression of the G-protein peptide neuromodulator known as melanopsin (Hannibal *et al.*, 2002). RGCs receive both stimulating and suppressing inputs from two categories of intermediate neurons, namely amacrine cells and bipolar cells. RGCs and amacrine cells collaborate to create a functional component consisting of on-off centres, which enables the brain to understand the movement of a small dot at a specific distance (Masland, 2012a). RGCs transmit axonal projections that come together at the optic disc and traverse the lamina cribrosa without myelin sheaths, in order to avoid obstructing incoming light. RGC axons innervate the suprachiasmatic nucleus, olivary pretectal nucleus, intergeniculate leaflet, ventral division of the lateral geniculate nucleus, and preoptic

region, contributing to the coordination of circadian cycles and the pupillary light response (Hattar *et al.*, 2006).

1.2.4 Macrogia

Müller cells and astrocytes are two types of macroglia in the retina. Macroglia processes surround retinal blood vessels, astrocytes form an irregular network around neuronal axons providing support to the blood-retinal barrier (BRB). The BRB consists of two distinct parts: the inner BRB, formed by tight junctions between retinal capillary endothelial cells, and the outer BRB, created by tight junctions between the cells of the RPE. This dual barrier system is crucial for maintaining the retinal environment necessary for optical clarity and neuronal activity. Müller cells extend through multiple retinal layers, playing a key role in the regulation of nutrition metabolism and protection of neurons, while also maintaining the vascular tone through autoregulation and respond to signals such as hypoxia through paracrine signalling (Newman, 2015). Astrocytes contribute to vascular stability and help regulate blood flow, crucially supporting the integrity and functionality of the inner BRB. Astrocytes play a pivotal role in the metabolism and mechanical support of the neurons and serve as an essential component in the internal BRB (Meng *et al.*, 2021).

1.2.4.1 Müller cells

Traversing the full thickness of the retina, radial glial cells—known as Müller cells—are strategically positioned within the OLM (**Figure 1-1**). These cells contribute to the external limiting membrane (Wolf *et al.*) by establishing adherens junctions with the outer processes of the photoreceptors establishing a critical structural and functional bridge across the retinal layers. The ILM of the retina is a distinct extracellular matrix structure, primarily comprising the inner processes ('end feet') of Müller cells which abut it, along with other components of the basement membrane. While the body of Müller cells resides within the INL of the retina, their terminal extensions reach both the outer and inner limiting membranes, thus permeating the entire retinal structure.(Reichenbach & Bringmann, 2013). In the normal state, Müller cells, like other glial cells in the central nervous system, have a crucial role in providing support and nourishment to retinal neurons (Reichenbach & Bringmann, 2013). Müller cells express glutamate transporter and glutamine synthetase to counteract glutamate-induced excitatory toxicity. They also express glutathione to alleviate oxidative stress in the retina (García & Vecino, 2003). Additionally, Müller cells express neurotrophic

receptors and release neurotrophic factors, including brain-derived neurotrophic factor, glial cell line-derived neurotrophic factor, ciliary neurotrophic factor, leukaemia inhibitory factor, nerve growth factor, and basic fibroblast growth factor, to nourish and protect retinal neurons (Reichenbach & Bringmann, 2013). Despite their protective effects, Müller cells can also act as a significant source of cytokines and inflammatory factors in response to retinal injury, further influencing the microenvironment of retinopathy and promoting neuronal death in the retina (Eastlake *et al.*, 2016). This dual-faceted role highlights the complexity of Müller cell responses, which can shift from neuroprotective to pro-inflammatory based on the severity and type of injury, potentially overwhelming their protective mechanisms, especially when they themselves are damaged or under severe stress. During inflammation, Müller cells express major compatibility complex II antigens and participate in retinal immune responses (García & Vecino, 2003). Moreover, in the presence of retinal inflammation, the morphologies of Müller cells and their processes undergo significant alterations, accompanied by reactive gliosis, including the upregulation of glial fibrillary acidic proteins (GFAP) (Zhang *et al.*, 2022). These alterations, marked by reactive gliosis and the upregulation of GFAP proteins, indicate a critical stress response within the retina. This response, while signalling an attempt at protection and repair, can ultimately impair retinal function. It underscores the importance of understanding Müller cell dynamics as they offer crucial insights into potential therapeutic targets for mitigating inflammation and preserving vision in the face of retinal diseases. The regeneration of Müller cells has been associated with Notch-3 and N-cadherin expression (García & Vecino, 2003; Reichenbach & Bringmann, 2013). Dysfunction of Müller cells is linked to various retinal diseases, including macular telangiectasia and diabetic retinopathy (DR). In DR, Müller cell dysfunction disrupts their critical roles in maintaining blood-retinal barrier integrity, neurovascular regulation, inflammation control, neuroprotection, glutamate metabolism and oxidative stress management significantly contributing to the disease's progression and the deterioration of visual function (Powner *et al.*, 2010; Rungger-Brändle *et al.*, 2000).

1.2.4.2 Astrocytes

Astrocytes, named for their characteristic stellate shape, are primarily confined to the innermost layers of the retina, almost entirely restricted to the retinal NFL, establishing close associations with neurons and major blood vessels. Their shape is characterised by a fibrous network of radiating processes and a flattened cell body. As intermediate filaments clog their processes, they exhibit a

strong GFAP antibody stain (Schnitzer, 1988). These retinal astrocytes are not believed to originate from the retinal embryonic epithelium; instead, it is generally accepted that they migrate from the optic nerve, likely entering the retina alongside blood vessels (Stone & Dreher, 1987).

Astrocytes are widely acknowledged as critical for the development and functioning of the retina's vascular system. During retinal development, they form a template necessary for angiogenesis and vessel patterning, influencing factors such as blood flow and the formation of the blood-retinal barrier (BRB) (**Figure 1-1**) (Klaassen *et al.*, 2013). By releasing neurotrophic factors, providing antioxidative support, removing ions and neurotransmitters from the extra neural space, and, similarly to their actions in the brain, facilitating the creation and destruction of synapses, astrocytes and Müller cells both aid in the survival of retinal cells. While Müller cells are primarily thought to mediate neurovascular (NV) coupling in the retina, astrocytes participate in the broader regulation of the retinal environment but are not directly involved in NV coupling. Instead, astrocytes potentially impact other mechanisms, such as the activation of microglial cells and the modulation of the retinal immune response. Both types of macroglial cells play important roles in the regulation of vasodilation and vasoconstriction. While Müller cells directly mediate NV coupling by responding to neuronal activity, releasing signals such as potassium ions (K⁺), which lead to vasodilation by relaxing pericytes and smooth muscle cells around the retinal vessels, astrocytes have an indirect role. Astrocytes release vasoactive substances, including nitric oxide (NO) and ATP, which influence blood vessel diameter by acting on endothelial cells and pericytes (Metea & Newman, 2006). Though their involvement in blood flow regulation is indirect, astrocytes significantly contribute to the broader control of vascular tone within the retinal microenvironment (Bringmann & Wiedemann, 2012; Coorey *et al.*, 2012). This distinction between astrocytes and Müller cells underscores the need for further investigation into the direct contributions of astrocytes to blood flow control within the retinal context. Their proximity to pericytes and endothelial cells, coupled with their ability to release vasoactive agents, suggests they may play a crucial role in modulating vascular tone and maintaining the integrity of the retinal environment. Additionally, understanding the frequency and implications of both types of macroglial cell proximities to basement membranes (BM) and pericytes may offer insights into the interpretation of the roles of these cellular mechanisms, such as neurotrophic support, antioxidative protection, synaptic regulation, immune modulation, and vascular regulation, in retinal health and disease.

1.2.5 Microglia

Microglial cells are the resident macrophages of the central nervous system, including the retina, and are the primary and first line of active immunological defence (Guo *et al.*, 2022). They enter the retina at the same time as the mesenchymal progenitors of the developing retinal blood vessels (Chan-Ling, 1994), and can be found in each layer of the human retina. Microglial originate from two sources; one is assumed to reach the retina during the early stages of development from the mesenchyme of the optic nerve and remain dormant in the retinal layers throughout the majority of the retina's lifespan, while the others appear to be blood-borne cells that may originate from vascular pericytes (Boycott & Hopkins, 1981). Both origins underscore their capacity for both inflammatory and anti-inflammatory actions within the retina. Within the retina, microglial cell bodies typically reside in the plexiform layers, while their processes extend throughout the retina and are in close association with retinal vasculature, ensuring an intimate connection with the vascular components essential for maintaining retinal health and functionality (Mills *et al.*, 2021).

The various morphologies of microglia are intimately associated with their functional characteristics and activation status (Wolf *et al.*, 2017). Despite microglia residing in a quiescent state, they remain perpetually vigilant, ready to respond to or mitigate any deviations from homeostasis that could compromise neuronal function and tissue integrity (van Rossum & Hanisch, 2004). Microglia have a ramified shape with tiny, spherical somas and many long, thin processes when they are in a physiological (resting) state. Leveraging their characteristic morphology, microglia dynamically extend and retract their processes, enabling them to meticulously scan and monitor their surrounding environment, while their cell bodies (somas) remain predominantly stationary. This vigilant surveillance mechanism ensures a comprehensive oversight of their immediate vicinity, facilitating an immediate response to maintain neural integrity and homeostasis (Askew *et al.*, 2017).

Microglial cells actively contribute to the preservation of the retina's structure and functionality. Microglia cells are mostly restricted to the IPL and GCL during retinal development, where they phagocytose the cellular corpses of RGCs that are overproduced at an early stage of development (Bodeutsch & Thanos, 2000). Furthermore, microglia are implicated in pruning of weak RGC presynaptic terminals during the early postnatal phases, when there is a significant synaptic remodelling (Schafer *et al.*, 2012). This process involves a Complement C3 activated pathway, which

helps microglia identify and prune these weaker connections, aiding in synaptic pruning and remodelling during retinal development, which is crucial for eliminating unsuitable neural connections and supporting the retina's and visual cortex's normal growth (Karlstetter *et al.*, 2015). Significantly, the removal of expensive neural connections judged unsuitable for normal functioning and the microglial-dependent death of RGCs are essential for the normal postnatal growth of the retina and cortical visual regions (Schafer *et al.*, 2012). Additionally, akin to Müller cells, prolonged tissue stress, such as from diabetes, can cause microglia to become overly reactive, leading to the production of pro-inflammatory factors and sustained inflammation, impacting the retina's health. This reactivity leads to notable changes in microglial morphology, where resting microglia with small bodies and long, thin processes transition to an activated state characterised by larger bodies and shorter, thicker processes (Kinuthia *et al.*, 2020).

Given the complex interactions among various cell types in the retina, including neurons, glial cells, and photoreceptors, and their pivotal roles in visual processing, it is crucial to broaden the scope of future research and explore different depths of the retina to gain a more comprehensive understanding of its multifaceted functions.

1.2.1 Blood supply within retina

The retina displays one of the highest oxygen consumption rate among most tissues in the human body, necessitating a continuous and substantial supply of oxygenated haemoglobin for sustenance (Noell, 1965). To meet this demand, the anatomy of the retina circulation is intricately designed, consisting of a distinctive dual blood supply system, which divides it into outer and inner layers to optimise the delivery of oxygen (Figure 1-2). The retinal vasculature derives from the central retinal artery, a branch of the ophthalmic artery (Netter, 2014). The retinal vasculature primarily nourishes the inner layers of the retina. The ophthalmic artery is pivotal, branching into the central retinal artery and posterior ciliary arteries, each supplying the retina from different perspectives. The central retinal artery, the foremost branch of the ophthalmic artery, enters the eye through the optic disc then branches out over and through the inner retina across the retinal surface. This crucial artery ensures the delivery of oxygenated blood to the inner layers of the retina, including the ganglion cell layer, inner nuclear layer, and the inner plexiform layer, thereby playing a pivotal role in the visual processing capabilities of the eye. It divides into four major arterial branches in humans, each supplying one quadrant of the retina, ensuring a uniform distribution of nutrients and oxygen

across the entire retinal surface. Parallel to this, the posterior ciliary artery divides into short and long branches, penetrating the sclera to deliver blood flow to the choroid, which provides oxygen and nutrients to the outer retina. This system, known as the choroidal circulation, is instrumental in providing oxygen and nutrients to the outer retina, including the photoreceptor layer and the retinal pigment epithelium (RPE). The choroidal circulation features an extensive vascular network to support the high metabolic demands of these cells. Moreover, neurovascular coupling, alongside pressure autoregulation, ensures that blood flow within the retina is finely tuned to its metabolic activity (Garhöfer et al., 2020). Neurovascular coupling refers to the mechanism by which neuronal activity increases local blood flow, a process crucial in the retina where high visual activity demands rapid adjustments in blood supply. Pressure autoregulation maintains consistent blood flow despite changes in systemic blood pressure, protecting the delicate retinal tissues from damage caused by fluctuations in perfusion pressure. In the foveal region of the retina, the vascular organisation presents a distinct feature known as the foveal avascular zone (FAZ). The FAZ is a specialised area in the center of the macula, which is devoid of retinal blood vessels, a feature that reduces light scattering and improves the resolution of visual information reaching the photoreceptors (Jeremic et al., 2024). This absence of vasculature allows for high visual acuity, which is essential for tasks such as reading and fine visual discrimination. Surrounding the FAZ, the retinal circulation, including the superficial and deep capillary plexuses, supplies the adjacent retinal areas with oxygen and nutrients, maintaining overall retinal function. However, disruptions in the structure or size of the FAZ are closely linked to various retinal diseases. In DR, for instance, microvascular damage leads to FAZ enlargement, contributing to visual deficits. Similar alterations in FAZ size and shape have been documented in retinal vein occlusion and AMD, where progressive vascular changes and ischemia compromise central vision (Riazi-Esfahani et al., 2024). This relationship between the FAZ and retinal disease highlights its crucial role in preserving retinal health and visual function.

It's important to note that the retinal circulation comprises different vascular plexuses: the superficial, intermediate, and deep capillary plexuses (**Figure 1-2**), spanning from the inner nerve fibre layer to the outer plexiform layer, and occasionally reaching the outer nuclear layer (**Figure 1-1**). The choroid's extensive vascular network supports the high metabolic demands of these cells, critical for phototransduction and visual acuity. Moreover, neurovascular coupling, alongside pressure and metabolic autoregulation, and endothelial control, are pivotal mechanisms ensuring the retina's blood flow is finely tuned to its metabolic activity.

Moving forward in this thesis, the focus will be on the retinal vasculature, as it plays a crucial role in sustaining the retina's metabolic demands and maintaining its function. Remarkably, blood flow to the retina remains fairly constant despite changes in intraocular pressure, systemic blood pressure, and lacks dependence on sympathetic autoregulation (Campochiaro, 2015). Local factors, including nitric oxide, prostaglandins, endothelin, and arterial carbon dioxide tension, regulate retinal blood flow. NO is pivotal for its vasodilatory effects, synthesised by endothelial cells and promoting the production of cyclic guanosine monophosphate (cGMP) in vascular smooth muscle cells. This process facilitates smooth muscle relaxation, leading to vasodilation and an increase in blood flow, crucial for adapting to changes in the retina's oxygen demands. Prostaglandins, a diverse group of lipid compounds, exert their regulatory effects through both vasodilation and vasoconstriction, depending on their specific subtype, such as prostaglandin E2 (PGE2), which generally promotes vasodilation to enhance blood flow according to the metabolic needs of the retina. Contrastingly, endothelin, a potent vasoconstrictor peptide, induces vasoconstriction upon binding to its receptors on vascular smooth muscle cells, a mechanism that plays a critical role in finely tuning retinal blood flow, especially to prevent overperfusion. The arterial carbon dioxide tension (PaCO_2) significantly affects vasomotion, the rhythmic contraction and relaxation of blood vessel walls, as well; increased CO_2 levels lead to vasodilation, while decreased levels cause vasoconstriction, mediated by direct effects on vascular smooth muscle and changes in extracellular pH. This is mediated by direct effects on vascular smooth muscle and changes in extracellular pH in the retinal environment. Thus, the pH changes influencing vasomotion in the retina are primarily extracellular, although the overall cellular activities and responses in the retinal vascular smooth muscle can involve both intra- and extracellular processes. This CO_2 -dependent regulation ensures the retina's blood flow is closely matched to its metabolic activity, maintaining oxygen and nutrient supply under varying conditions (Barabas et al., 2020; Klug et al., 2023). These local factors collectively modulate the tone of retinal arterioles and capillary blood flow, dynamically adjusting to meet the metabolic demands of the retina and maintain homeostasis. Their regulation is essential in the retina, where precise blood flow control is necessary due to the tissue's high metabolic activity and sensitivity to ischemic and hypoxic damage. Resembling the brain, retinal blood flow responds by increasing with elevated carbon dioxide levels and decreasing with lower carbon dioxide levels (Koss, 1999). Capillaries are distributed throughout the retina, spanning from the inner nerve fibre layer to the outer plexiform layer, occasionally reaching the outer nuclear layer (**Figure 1-1**) (Lavia *et al.*, 2020). Interestingly, the

inner layers of the retina exhibit heightened sensitivity to hypoxic challenges, while the outer retina demonstrates greater resilience to hypoxic stress (Hartnett, 2005).

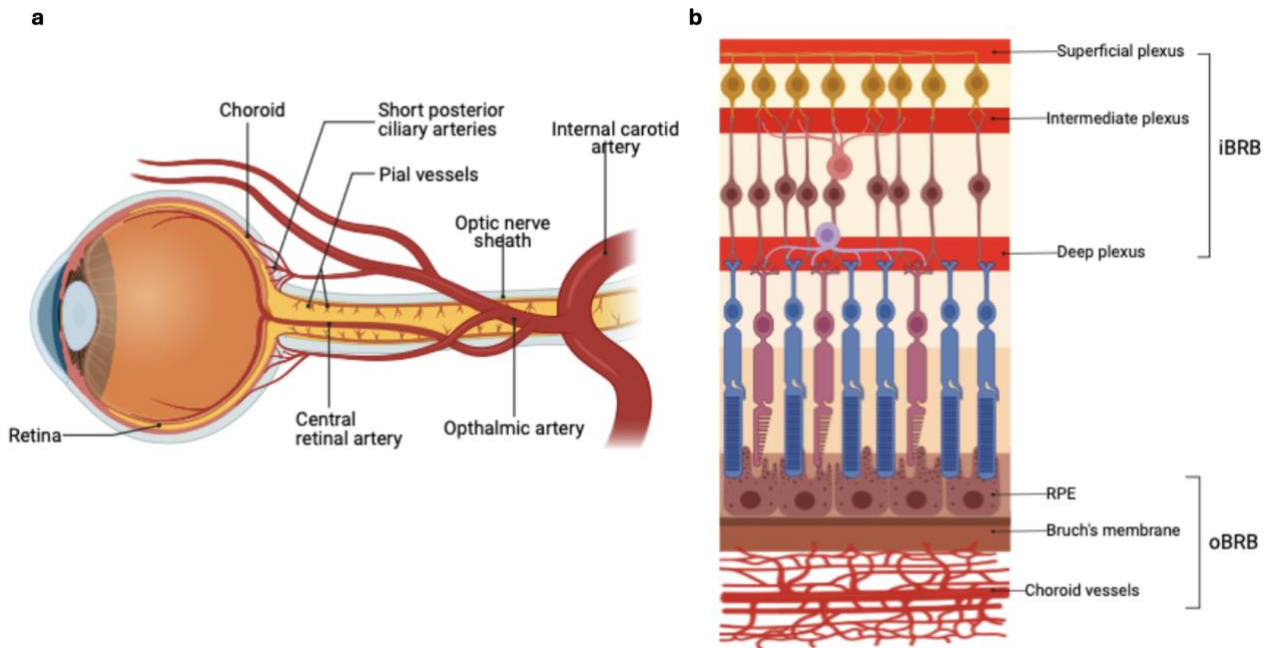


Figure 1-2 Vascular organisation of the retina. (a) Diagram illustrating the blood supply to the eye. The central retinal artery and its branches, along with the short posterior ciliary arteries, supply blood to the retina. These vessels originate from the ophthalmic artery, which branches off the internal carotid artery. The optic nerve sheath and pial vessels are also shown as part of the eye's vascular structure. (b) Cross-sectional schematic of the retina showing the internal blood-retinal barrier (iBRB) and outer blood-retinal barrier (oBRB). The iBRB is formed by the superficial, intermediate, and deep vascular plexuses, which nourish the inner retinal layers. The oBRB is formed by the retinal pigment epithelium (RPE) and Bruch's membrane, which separate the outer retina from the choroid vessels.

1.3 Retinal Metabolic Demand

The retina is one of the highest energy-consuming tissues in the human body, surpassing even the brain in metabolic rate. The retinal metabolic demands are primarily driven by photoreceptors, particularly rods and cones, which require substantial amounts of energy to maintain phototransduction and ion gradients. These photoreceptors, along with other retinal neurons, depend on a tightly coupled vascular network to meet their nutrient and oxygen needs. The metabolic demands of the retina are met through multiple fuel sources, including glucose and lipids.

While glucose is traditionally considered the primary energy source for the retina, studies have shown that photoreceptors also rely on fatty acid β -oxidation to produce ATP. This process accounts for the significant portion of energy not derived from glucose metabolism (Cohen and Noell, 1960; Joyal et al., 2016). The retina's ability to oxidise both glucose and lipids enables it to meet its high energy demands and maintain proper function.

Photoreceptors generate a variety of metabolites as byproducts of their metabolic processes. These include lactate, produced mainly by aerobic glycolysis, and ROS, a consequence of oxidative phosphorylation in the mitochondria. Additionally, CO_2 is produced through oxidative metabolism. Lactate is particularly abundant in the retina and is produced by photoreceptors as part of the Warburg effect, where glycolysis occurs even in the presence of oxygen (Ng et al., 2015). This high rate of lactate production provides fuel for neighbouring cells, including Müller glia and the RPE, which can further metabolise lactate or shuttle it into the bloodstream for removal.

The retina has evolved efficient systems to handle the removal of metabolites and to prevent accumulation of toxic byproducts. Müller cells play a crucial role in this process by buffering extracellular K^+ ions, removing excess neurotransmitters like glutamate, and regulating pH to maintain homeostasis in the retinal microenvironment. These cells are also responsible for lactate uptake, which is transported from the extracellular space and metabolised or removed via the retinal vasculature. The RPE contributes significantly to the removal of ROS, a by-product of the high oxygen consumption in photoreceptors. The RPE neutralises these ROS using antioxidants such as glutathione, protecting the retina from oxidative damage that could otherwise lead to degeneration. The RPE also plays a key role in the continuous renewal of photoreceptor outer segments, ensuring the removal of damaged segments and the regeneration of new ones, thus preventing the accumulation of oxidative damage.

CO_2 produced by oxidative phosphorylation is removed via diffusion into the choroidal circulation, where it is transported out of the retina and exhaled through the lungs. This rapid removal of CO_2 is critical for preventing acidosis and maintaining the retina's metabolic efficiency. Oxygen is essential for oxidative phosphorylation, the primary process by which ATP is produced in the retina. The outer retina, composed predominantly of photoreceptors, consumes more than 60% of the oxygen supplied to the retina (Du et al., 2016). Oxygen levels are highest near the choroid and decrease significantly as oxygen diffuses towards the photoreceptor mitochondria, reflecting the high oxygen

consumption in these cells (Linsenmeier and Zhang, 2017). In addition to glucose metabolism, fatty acids serve as a crucial energy source for photoreceptors through β -oxidation, particularly during periods of nutrient deprivation or increased metabolic demand (Joyal et al., 2016). The oxidation of fatty acids within photoreceptors and the RPE helps meet the high ATP requirements of these cells, supplementing glucose metabolism and providing the energy necessary to sustain phototransduction and outer segment regeneration.

1.4 The Retinal Neurovascular Unit

The neurovascular unit (NVU) is complex, interdependent physical and functional unit important for maintaining the function of the retina and the integrity of the blood retinal barrier (BRB). The components which make up the NVU are endothelial cells, pericytes, basement membrane (BM), glia (astrocytes and Müller cells) and neurons (ganglion cells, bipolar cells and amacrine cells) and microglia (**Figure 1-3**) (Liu *et al.*, 2021). All of these components combine to regulate blood flow, respond to the metabolic demands of the retina by maintaining a supply of oxygen and nutrients, while also removing waste and recycling metabolites (Hawkins *et al.*, 2005).

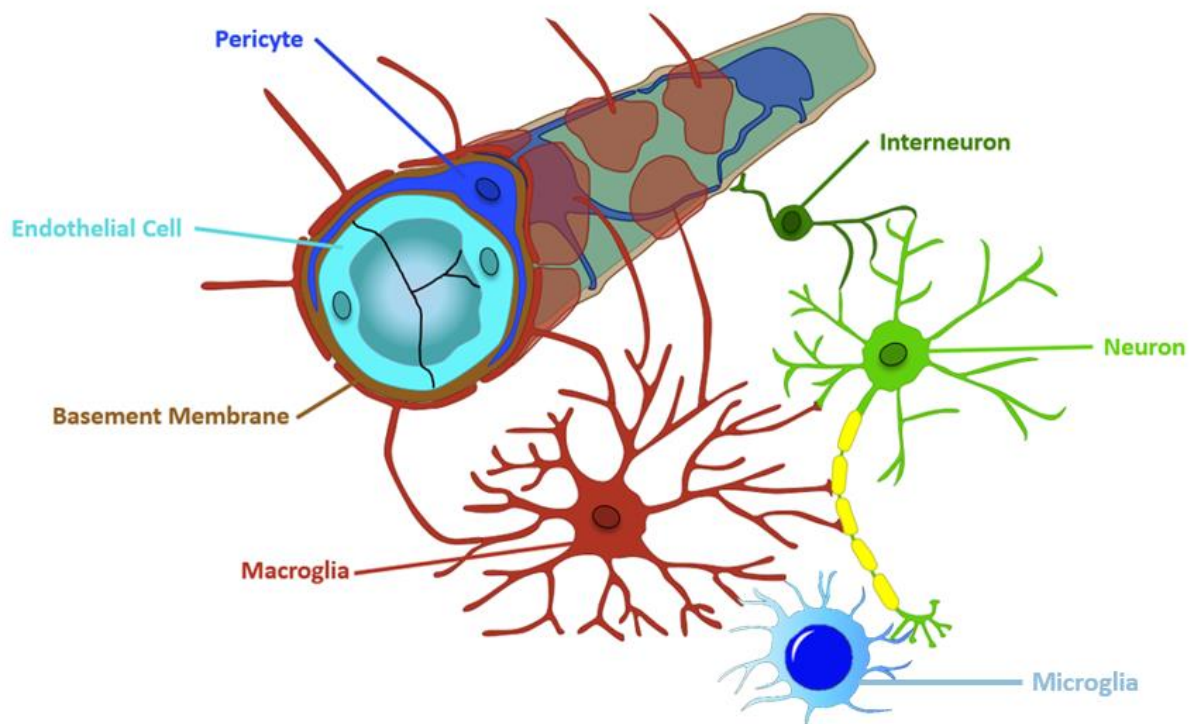


Figure 1-3 The retinal neurovascular unit. The structure of the NVU is formed by pericytes, endothelial cells, basement membrane, astrocytes, Müller cells and neurons. Each of the components are intimately linked to each other and work together to regulation of cerebral blood flow.

1.4.1 Vasculature

The BM, pericytes and endothelial cells make up the structure of the capillary vasculature of the retinal NVU. The BM is composed of extracellular matrix proteins such as collagen type IV, laminin, nidogen and perlecan, and encompasses pericytes and endothelial cells to contribute to the integrity of the blood-retinal barrier (BRB) (Savige *et al.*, 2010). Vascular endothelial cells form a monolayer which covers the inner surface of the vascular lumen. The endothelium forms the inner BRB, a semi-selective barrier which regulates the flux of fluid and macromolecules between the blood and retina through intercellular tight junctions. The structure and function of the retinal capillary vasculature relies on interactions between endothelial cells and pericytes. Pericytes regulate the expression of tight junction proteins in endothelial cells, modulate endothelial cell function through various mechanisms including the regulation of blood-retina barrier permeability, control of angiogenesis, modulation of inflammatory response, regulation of blood flow through their contractile capabilities, and influence over endothelial cell survival and differentiation.

Additionally, they provide structural support by covering retinal capillaries, contributing to the stability and composition of the BM and extracellular matrix, which supports the structural integrity of blood vessels and influences endothelial cell behaviour (Bergers & Song, 2005).

1.4.1.1 BM function

Electron microscopy experiments first revealed the BM, a thin, sheet-like structure, to be a dense meshwork next to cellular monolayers (Younes *et al.*, 1965). Further investigation demonstrated that the BM is a specialised extracellular matrix (ECM) supporting a variety of tissues, such as fat cells, muscle cells, endothelium, and peripheral nerve axons (Jayadev & Sherwood, 2017). The BM (**Figure 1-3**) plays a pivotal role in vascular cell attachment and survival, significantly through integrin/FAK signaling, which is essential for cell adhesion, migration, proliferation, and survival, thereby underpinning the structural and functional integrity of tissues. The fundamental function of the BM is to serve as a foundation for cell attachment and serve as a physical barrier separating various cell types and tissues, therefore preserving cell form and size (Timpl *et al.*, 1979). The process of constructing the supramolecular architecture comprises the assembly of collagen IV, laminin, fibronectin, nidogen, and other elements (Welling & Grantham, 1972). The BM is crucial in regulating the passage of molecules to ensure a balanced environment throughout the inner and outer layers of the retinal blood vessels. The BM functions as a foundation for cell adhesion and prevents the extravasation of growth factors, hormones, and polysaccharides from the bloodstream into the connective tissue. The tight connections between the endothelial cells in the paracellular portion of the capillary endothelial basement membrane control the permeability. Collagen IV and laminin have been shown to contribute to the proper formation of tight junctions (Jayadev & Sherwood, 2017), this suggests that the BM plays a role in preserving the selective permeability of retinal capillaries. Furthermore, the BM influences capillary retinal blood flow by modulating the contractility and relaxation of pericytes, crucial for the dynamic regulation of blood flow (Trost *et al.*, 2016).

1.4.1.2 Endothelial cell

Retinal endothelial cells line the branching microvasculature which supplies the neural retina (Figure 1-3). Endothelial cells structure include many mitochondria and ribosomes, flattened cytoplasm (with the exception of the nucleus bulging), and pinocytotic vesicles (Rhodin, 1968). The absence of fenestrations and the existence of specialised intercellular junctions known as "zonula occludens,"

or tight junctions (TJs), which establish persistent and very tight unions with neighbouring cells, are characteristics that set endothelial cells of the retinal and brain circulation apart (Hogan, 1971). These TJs are comprised of a complex network of proteins, including claudins, occludin, and zonula occludens proteins (ZO-1, ZO-2, and ZO-3), which are integral to maintaining the selective permeability barrier of the BRB. Additionally, the presence of adherens junctions (AJs), primarily through the action of VE-cadherin and associated catenins (α , β , and γ -catenin), along with nectins and afadin, further reinforces cell-cell adhesion and the mechanical integrity of the retinal endothelial barrier. These specialised junctional complexes are crucial for regulating the passage of molecules, ensuring the retinal environment's stability, and maintaining visual function, thus distinguishing the retinal endothelial cells in their unique role in vascular biology. These traits play a major role in the blood-retinal barrier, which regulates circulating solutes from entering the retina in healthy individuals (Cunha-Vaz, 1979). In addition to preserving the structural integrity of the capillary vasculature and safeguarding the retina against potential pathogens, the endothelial layer plays a pivotal role in delivering oxygen and essential nutrients to the metabolically demanding retina. This dynamic layer ensures the meticulous regulation of blood flow and the selective transport of molecules, effectively supporting the retina's high metabolic needs and maintaining its health and functionality. The endothelium also aids the structure and formation of the BRB, which shields the retina from pro-inflammatory leukocytes, circulating molecular toxins and microorganisms (Bharadwaj *et al.*, 2013).

1.4.1.3 Pericytes

Pericytes are specific mural cells embedded within the BM, and are found at the abluminal surface of capillary blood vessels (Figure 1-3) (Díaz-Flores *et al.*, 2009). Pericytes' cytoplasmic processes can span several endothelial cells, with a ratio of pericytes to endothelial cells in the retina being 1:1, indicating their extensive involvement and distribution within the vascular structure they exhibit distinct marker profiles and have diverse morphologies depending upon the vascular bed and the stage of their growth and differentiation (Shepro & Morel, 1993) They exhibit markers such as PDGFR- β , NG2, α -SMA, desmin, RGS5, CD13, and CD146, reflecting their multifunctional roles in vascular health and disease (Dore-Duffy & Cleary, 2011; von Tell *et al.*, 2006).

Pericytes are involved in vessel formation, remodelling, and stabilisation and play a crucial role in angiogenesis (Gerhardt & Betsholtz, 2003). Various signalling pathways and factors have been

identified as significant contributors to the intercellular communication between endothelial cells and pericytes. Transforming growth factor β (TGF β), gap junctions, angiopoietins, platelet-derived growth factor B (PDGF-B), sphingosine-1-phosphate, and Notch are among the signalling pathways and factors that are crucial for the intercellular communication between endothelial cells and pericytes (Winkler *et al.*, 2011).

Pericytes are also thought to be involved in the control of microvascular blood flow since they exhibit contractile proteins (Bandopadhyay *et al.*, 2001) and are found on post-capillary venules, and capillaries abluminal of endothelial cells, where vSMCs are absent. The evidence for pericytes' role in controlling microvascular blood flow, and by implication capillary diameter, is supported by their ability to contract and relax due to these contractile proteins. This allows them to adjust the caliber of capillaries, thus regulating blood flow through the microvasculature. Pericyte relaxation accounts for 80% of the changes in retinal blood flow during neurovascular coupling responses, showcasing the central role these cells play in vascular dynamics (Peppiatt *et al.*, 2006). Specifically, pericytes express contractile proteins such as alpha smooth muscle actin (α -SMA), highlighting their capability for such physiological responses. Positioned on the abluminal surface of capillaries, they directly influence the capillary lumen size through their contraction and relaxation, modulating blood flow according to tissue needs. This mechanism is crucial for tissue perfusion and oxygen delivery, ensuring efficient nutrient distribution and waste removal across various tissues. In situ studies using isolated rat retina (Peppiatt *et al.*, 2006) provided evidence of pericyte contractility in response to vasoactive molecules/neurotransmitters, as did studies utilising isolated retinal vessels (Kawamura *et al.*, 2003; Wu *et al.*, 2003). When pericytes undergo relaxation, the pericyte processes that are spiralling across the longitudinal axis of the retinal microvessels become less tight, which enables a rise in the openness of the vessels. Conversely, the contraction of pericytes leads to a decrease in the diameter of retinal capillaries. Pericytes, characterised as mural cells due to their location within the vessel wall and distinct from smooth muscle cells by their unique functions and markers, together with endothelial cells, contribute to the synthesis of BM components. Pericytes have also been proven to be an essential constituent of the inner BRB, in which pericytes form and maintain together with endothelial, neuronal and glial cells the BRB to guarantee barrier function and tissue homeostasis.

1.4.2 Comparison of Retinal NVU to Other Tissues

NVU is not exclusive to the retina; similar structural and functional units exist in other tissues, particularly in the brain. The NVU in the brain shares many key components with the retinal NVU, including endothelial cells, pericytes, glial cells (astrocytes in the brain and Müller cells in the retina), and neurons. Both NVUs are responsible for maintaining blood-brain and blood-retinal barriers, respectively, ensuring the selective permeability that regulates the entry of ions, nutrients, and waste products while protecting neural tissue from harmful substances (Iadecola, 2017).

However, some differences exist between the NVU in the central nervous system (CNS) and peripheral nervous systems (PNS). In the brain, astrocytes are the predominant glial cells, playing a critical role in neurovascular coupling by responding to neuronal signals and regulating blood flow to meet the metabolic demands of active brain regions. In the retina, Müller cells serve a similar role but are more intimately involved in maintaining retinal homeostasis, contributing to nutrient distribution, ion balance, and the recycling of neurotransmitters like glutamate (Bringmann & Wiedemann, 2012). Müller cells span the entire thickness of the retina, providing structural support and linking neurons and blood vessels more directly than astrocytes do in the brain (Reichenbach & Bringmann, 2013).

Another significant area of comparison is the difference in NVU structure and function between the central and peripheral retina. The central retina, particularly the macula in humans, is highly specialised for detailed vision and color perception, supported by a dense capillary network to meet its high metabolic demands. The NVU in this region is tightly regulated to ensure a constant supply of oxygen and nutrients while preventing leakage through the BRB. In contrast, the peripheral retina, responsible for peripheral vision and detecting motion, has a sparser capillary network (Lavia et al., 2020). This difference reflects the varying metabolic demands and functional priorities of these regions. In terms of function, the central retinal NVU is more susceptible to ischemic injury due to its high demand for oxygen and nutrients, making it a focal point for diseases like DR and AMD. The peripheral retina, with its lower metabolic demand and less dense vasculature, is less prone to early ischemic damage, although it still plays a role in later stages of such diseases (Kooragayala et al., 2015).

The PNS, unlike the CNS, does not have a blood-nerve barrier equivalent to the blood-brain or blood-retinal barriers. In peripheral tissues, the blood vessels are less tightly regulated, and there is more

permeability to various circulating molecules. This key difference highlights the vulnerability of the CNS and retina to damage from systemic factors, such as inflammation and metabolic stress, as seen in diseases like DR (Simard et al., 2014). In the PNS, peripheral nerves are more resistant to ischemia but lack the precise regulation of blood flow seen in the CNS NVUs, making the retina and brain more susceptible to neurovascular dysregulation (Hawkins & Davis, 2005).

1.5 Diabetic Retinopathy

Diabetic retinopathy (DR) is a microvascular condition brought on by the prolonged impact of diabetes mellitus, occurring in both Type 1 and Type 2 diabetes. Type 1 diabetes is characterised by the inability to produce insulin due to autoimmune destruction of the insulin-producing beta cells in the pancreas. In contrast, Type 2 diabetes involves insulin resistance and relative insulin deficiency, typically developing due to genetic and lifestyle factors. DR can cause retinal damage that could potentially result in blindness and vision threatening complications. The prevention of diabetic retinopathy-related blindness is mostly dependent on early identification and prompt intervention. Prevention of diabetic retinopathy-related blindness is primarily achieved through regular screening and monitoring for early detection of the disease. This involves comprehensive eye examinations, including dilated fundus examinations and imaging techniques like optical coherence tomography (OCT) and fundus photography, to identify signs of retinal damage before they progress to severe stages. Early identification enables timely intervention, which can include laser therapy, intravitreal injections of corticosteroids or anti-VEGF agents, and vitrectomy surgery in advanced cases. Moreover, controlling systemic factors such as blood glucose levels, blood pressure, and lipid levels is crucial in slowing the progression of DR and reducing the risk of vision loss (Dodson, 2007).

DR is divided into two stages: non-proliferative diabetic retinopathy (NPDR) and proliferative diabetic retinopathy (PDR). The early stage is NPDR, where there is increased vascular permeability and capillary occlusions and it presents capillary degeneration, neuronal infarcts, microaneurysms and haemorrhages (Heng *et al.*, 2013). Additionally, at this stage, diabetic macular edema (DME) can occur, characterised by the accumulation of fluid in the macula due to leaking blood vessels. This leads to swelling and thickening of the macula, significantly impairing central vision. A more advanced stage, PDR is characterised by neovascularisation (**Figure 1-4**). Neovascularisation is driven by angiogenesis, which involves the formation of new blood vessels from pre-existing ones.

This process is stimulated by the upregulation of proangiogenic cytokines, including vascular endothelial growth factor (VEGF). VEGF production is triggered by retinal ischemia, which results from capillary non-perfusion (Wang *et al.*, 2018). Hyperglycemia is considered to play an important role in the pathogenesis of the retinal microvascular damage seen in diabetes. In some cases, individuals exhibit microvascular changes in the absence of any overt neuroretinal dysfunction, highlighting the variability in disease manifestation and the complexity of its relationship with hyperglycemia (A. R. Santos *et al.*, 2017). This is evidenced by the findings of landmark clinical trials such as the Diabetes Control and Complications Trial (DCCT) and the United Kingdom Prospective Diabetes Study (UKPDS). These studies have shown that intensive glycaemic control significantly reduces the risk of developing diabetic retinopathy and can slow the progression of the disease in individuals with diabetes, thereby directly linking hyperglycaemia with microvascular complications in the retina (Kohner, 2008; Lachin *et al.*, 2015). Multiple metabolic pathways have been implicated in hyperglycaemia-induced vascular damage including the polyol pathway, advanced glycation end products (AGEs) accumulation, the protein kinase C (PKC) pathway and the hexosamine pathway (Brownlee, 2005). In DR, the BM becomes rigid under high glucose (HG) conditions. This rigidity may affect the flexibility of the blood vessels, thus impairing the pericytes' capacity to control blood flow in the retina (Khalilgharibi & Mao, 2021). The BM plays a crucial role in maintaining the balance of the retina, and any changes in its structure and function caused by HG or diabetes can significantly contribute to the retinal dysfunction observed in DR. Pericytes also play a key role in the immune response by producing cytokines as a response to pathological stimuli. Exhibiting both pro-inflammatory and anti-inflammatory roles depending on the context and nature of the pathological stimuli. This dual role involves the secretion of various cytokines and chemokines that can either attract immune cells to promote inflammation or suppress immune responses to aid in the resolution of inflammation, highlighting their crucial balancing act in maintaining tissue health and their potential as therapeutic targets in inflammatory and vascular diseases (Ribatti *et al.*, 2011). In the context of DR, several anti-inflammatory cytokines play a protective role. These include interleukin-10 (IL-10), which is well known for its ability to suppress pro-inflammatory cytokine production, as well as transforming growth factor-beta (TGF- β), which helps regulate immune responses and inhibits excessive inflammation. Additionally, interleukin-4 (IL-4) and interleukin-13 (IL-13) are involved in promoting anti-inflammatory macrophage phenotypes, which may help mitigate inflammation in DR (Tang *et al.*, 2023). These cytokines work together to counterbalance

the effects of pro-inflammatory mediators, reducing chronic inflammation and potentially limiting the progression of retinal damage in DR.

DR is a complex neurovascular disorder that affects the vascular structures but also the retinal neural tissue. In some individuals the deterioration of the neural retina precedes microvascular abnormalities in DR, leading to microvascular changes (Nian *et al.*, 2021). Diabetes, a long-term illness, significantly escalates the risk of altered retinal function through its progression to DR. This association underscores the importance of continuous management and monitoring of diabetes to prevent or delay the onset of DR, thereby protecting retinal health.

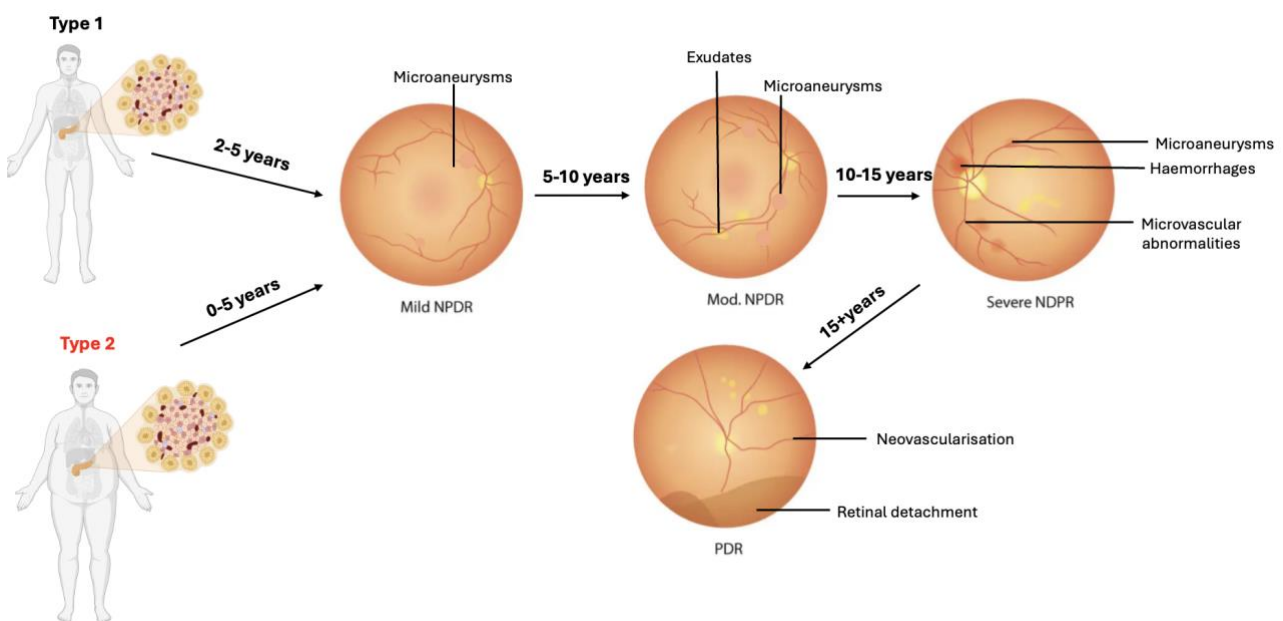


Figure 1-4 Progression of Diabetic Retinopathy (DR) in Type 1 and Type 2 Diabetes Patients. This schematic illustrates the typical progression of DR in patients with Type 1 and Type 2 diabetes. The timeline outlines the development of NPDR through its mild, moderate, and severe stages, progressing towards PDR. For Type 1 diabetes, mild NPDR generally develops 2-5 years after diagnosis, progressing to moderate NPDR within 5-10 years, and severe NPDR in 10-15 years. PDR, characterised by neovascularisation and potential retinal detachment, can develop 15+ years after diagnosis. In Type 2 diabetes, mild NPDR can often be present at diagnosis or appear within 0-5 years. Progression to moderate NPDR follows within 5-10 years, and severe NPDR typically develops within 10-15 years, with PDR occurring after 15+ years if untreated or poorly controlled. Key pathological features of each stage are highlighted: microaneurysms, retinal

hemorrhages, and microvascular abnormalities in NPDR stages, progressing to neovascularisation and retinal detachment in PDR.

1.5.1 Epidemiology

Diabetic retinopathy is a significant neurovascular complication linked to diabetes, emerging as a primary cause of blindness among adults in the working-age demographic. Epidemiological findings reveal a global diabetes mellitus burden of 387 million, projected to rise to 592 million by 2035 (Forouhi & Wareham, 2014). Globally, DR affects 93 million individuals. The prevalence of DR is reported to affect 30-40% of people with DM. (Wilkinson-Berka & Miller, 2008). Among patients with Type 1 diabetes, DR is present in 32.58% of cases, while in Type 2, 23.04% of patients are diagnosed with DR. The incidence and prevalence of DR differ significantly between Type 1 and Type 2 diabetes, DR is commonly identified at the time of diagnosis in Type 2 diabetes, often due to long-standing undetected high blood sugar levels. Conversely, DR is uncommon in Type 1 diabetes at diagnosis, typically manifesting at least five years after the onset and usually post-puberty, with screenings commonly initiated around the age of 12 (Matuszewski et al., 2020).

1.5.1 Animal models for Diabetes

Various animal models have been established to examine the causes and development of DR, as well as to develop and evaluate treatments for the condition. Animal models of DR are created by surgical procedures, laser or chemical-induced damage, administration of medications, or manipulation of nutrition. Generated models of diabetes, and complications associated with DR, encompass several methods such as surgical excision of the pancreas, delivery of the drugs alloxan and streptozotocin, consumption of high-galactose diets, and infliction of eye injury using laser or chemical means (Grossman *et al.*, 2010). The injection of streptozotocin is the most prevalent technique of induction due to its rapid start of illness (Rakieten *et al.*, 1963). Mice and rats are the primary animal models used to induce DR, however dogs, cats, pigs, rabbits, monkeys, and zebrafish are also utilised.

DR in mouse, rat, and zebrafish can also be caused by many genetic factors. The models encompass impulsive, strain-specific, and genetically engineered mutations. Hyperglycaemia, which is one of the fundamental hallmarks of diabetes, is observed in multiple inbred mouse strains such as nonobese diabetic (Noda et al.) and db/db (Leprdb). Genetic mice models of DR are conveniently

manageable, possess thoroughly characterised genetic origins, and may be deliberately altered to produce knockout or transgenic models. There are genetic models available for both type 1 and type 2 diabetes. In the case of type 2 diabetes, the models can be categorised as either obese or nonobese (Weir *et al.*, 2009).

The STZ mouse model, on the other hand, remains one of the most widely used models in DR research due to its efficiency in mimicking type 1 diabetes through selective destruction of pancreatic β cells. This model is characterised by the administration of streptozotocin, which induces a hyperglycaemic state by damaging β cells, resulting in insulin deficiency and diabetic-like symptoms (Chao *et al.*, 2018). STZ can be delivered either in high doses for a single rapid induction or in low doses over a period to induce a slower, immune-mediated β -cell destruction (Furman, 2021). This flexibility allows researchers to model the onset and progression of DR across different stages. The STZ model closely aligns with human diabetes in terms of the early onset of hyperglycaemia and the progression of complications such as DR (Yin *et al.*, 2006).

Streptozotocin (STZ), a glucosamine-nitrosourea chemical obtained from *Streptomyces achromogenes*, is utilised as a chemotherapeutic agent in the treatment of pancreatic β cell cancer, however, it also induces diabetes. Pancreatic β cells are harmed by STZ, which causes hyperglycemia and hypoinsulinemia (Lenzen, 2008). Depending on the dosage, there are two ways that STZ can cause diabetes. The chemical's preferential accumulation in β cells upon entrance through the GLUT2 glucose transporter receptor is linked to its preference for β cells; STZ binds to this receptor due to its structural resemblance to glucose. When administered, in high dosage, usually singly, STZ targets β cells by an alkylating characteristic similar to that of lethal nitrosourea chemicals (Dufrane *et al.*, 2006). STZ causes an immunological and inflammatory response at low dosages, usually after repeated exposures. This reaction is caused by the production of autoantigens associated to glutamic acid decarboxylase. In this scenario, inflammatory infiltrates, including lymphocytes in the pancreatic islets, are linked to the death of β cells and the development of the hyperglycaemic state (Paik *et al.*, 1980). Among the well-known negative side effects of STZ include nephrotoxicity and hepatotoxicity (Greenberg, 2009).

The advantages of the STZ mouse model include the rapid onset of diabetes and the ability to manipulate disease progression through dosage adjustments, making it ideal for examining the early vascular changes seen in DR. It is particularly useful for short-term studies investigating β -cell

destruction, insulin dependence, and the effects of hyperglycaemia on the retinal neurovascular unit. However, one limitation is that this model primarily reflects type 1 diabetes, while most human DR cases are related to type 2 diabetes, where metabolic, genetic, and environmental factors play a larger role (Berbudi et al., 2020). Additionally, STZ-induced models may not fully capture the gradual onset and multifactorial nature of DR observed in humans.

Other models, such as high-fat diet-induced models for type 2 diabetes or genetically modified mice (e.g., *ob/ob* or *db/db*), can mimic metabolic changes associated with human diabetes more closely. However, these models often require extended periods to develop hyperglycaemia and DR-related complications, making them less suitable for short-term experimental studies. Furthermore, genetic models do not fully replicate the complex interplay between lifestyle factors and genetic predispositions seen in human diabetes (Fletcher et al., 2014).

STZ-induced DM in mice typically administered via intraperitoneal injections to ensure efficient absorption and distribution of STZ in the body. The injections are administered over a series of consecutive days to replicate repeated exposures, inducing a robust immunological and inflammatory response akin to human DM pathogenesis. Following STZ administration, a latency period ensues before the onset of diabetes becomes evident. This latency period varies, ranging from a few days to weeks post-administration. The exact duration before the onset of DM symptoms, such as hyperglycaemia, polydipsia (increased thirst), and polyuria (increased urination), may be influenced by factors including the dosage regimen, the strain of mice employed, and individual susceptibility to STZ-induced β -cell cytotoxicity. The STZ model offers several advantages over other diabetic models, such as its rapid induction of diabetes and the ability to control the onset and severity of the disease through dosage adjustments. This model closely mimics type 1 diabetes by specifically targeting pancreatic β -cells, making it valuable for studying β -cell destruction and subsequent insulin-dependent diabetes mechanisms. However, its disadvantages include a lack of genetic similarity to most human diabetes, which is often not solely related to β -cell destruction but also involves complex genetic and lifestyle factors. Despite these limitations, the STZ mouse model remains relevant as it maps onto the diabetic timeline in humans by replicating early hyperglycaemia and its immediate effects on the retinal vasculature, allowing for the study of early-stage DR. Furthermore, its rapid onset and flexibility in disease induction provide an efficient platform for testing therapeutic interventions aimed at halting or reversing retinal damage associated with diabetes.

1.5.2 Pathophysiology

1.5.2.1 Chronic hyperglycaemia and retinal microvasculopathy

Persistent high blood sugar, known as chronic hyperglycemia, alongside blood pressure and hyperlipidaemia, is identified as the primary pathogenic factors in DR (Nathan *et al.*, 1993). Multiple metabolic pathways have been implicated in hyperglycaemia-induced vascular damage including the advanced glycation end products (AGEs) accumulation, the protein kinase C (PKC) pathway and the hexosamine pathway and the polyol pathway, which is one of the alternative glucose metabolism mechanisms that become active in response to hyperglycaemia (Brownlee, 2005). Within the polyol pathway, the aldose reductase enzyme converts glucose into sorbitol. As sorbitol is impermeable, it accumulates in all retinal cells, causing osmotic damage to the cells. Furthermore, more oxidative damage is caused when NADPH (reduced nicotinamide adenine dinucleotide phosphate) is used during the reduction process. AGEs are caused by oxidative stress, not only activate protein kinase C but also modify the vascular BM. This modification affects the attachment and function of cells within the BM, contributing further to endothelial dysfunction (Au & Ma, 2022).

These alternate routes cause capillary endothelial dysfunction, growth factors, and cytokine activation, which ultimately results in increased vascular permeability and microvascular occlusion. Intraretinal microvascular abnormalities (IRMAs), specific pathological features seen in the human diabetic retina but not in diabetic rodent retinas, are pre-neovascular changes characterised by the abnormal growth and branching of existing retinal vessels attempting to compensate for reduced blood flow and oxygen supply. Along with neovascularisation, IRMAs are results of retinal ischaemia, which is brought on by microvascular blockage (Kador *et al.*, 2016).

In response to hyperglycaemia, the initial reactions of the retinal blood vessels involve the dilation of vessels and alterations in blood flow. In diabetic patients, these adjustments are regarded as a form of metabolic autoregulation aimed at enhancing retinal metabolism (Bek, 2017). Emerging evidence highlights the loss of retinal blood flow autoregulation, particularly through the dysfunction of TRPV2 channels in retinal vascular smooth muscle cells (VSMCs). This loss, characterised by an impaired myogenic response and TRPV2 channel downregulation, points to autoregulatory failure rather than purely metabolic adjustments as the underlying issue in the progression of DR (O'Hare *et al.*, 2022).

A distinctive feature of the early stages of DR is the loss of pericytes, with evidence of pericyte apoptosis induced by high glucose observed in vivo and in vitro studies (Romeo *et al.*, 2002). As pericytes play a crucial role in providing structural support for capillaries, their depletion results in localised protrusion of capillary walls. This phenomenon is linked to the formation of microaneurysms, representing the initial clinical manifestation of DR (Ejaz *et al.*, 2008). Beyond pericyte loss, the apoptosis of endothelial cells and the thickening of the basement membrane are also evident in the progression of DR, collectively contributing to the impairment of the blood-retinal barrier (BRB) (Beltramo & Porta, 2013).

A significant reduction in pericytes and endothelial cells leads to the obstruction of capillaries and ischemia. The activation of hypoxia-inducible factor 1 (HIF-1) in retinal ischemia/hypoxia results in the overexpression of VEGF (Huang *et al.*, 2015). There is also evidence suggesting that the elevation of phospholipase A2 (PLA2) in diabetic conditions contributes to the upregulation of VEGF (Lupo *et al.*, 2013). VEGF, a crucial factor in the progression of PDR and DME, is thought to heighten vascular permeability by inducing the phosphorylation of tight junction proteins such as occludin and zonula occludens-1 (ZO-1) (Antonetti *et al.*, 1999). This phosphorylation triggers the internalisation and subsequent degradation of these TJ proteins, disrupting the endothelial barrier and enhancing vascular leakage. Furthermore, acting as an angiogenic factor, VEGF stimulates the proliferation of endothelial cells through the activation of mitogen-activated protein (MAP) (Rousseau *et al.*, 1997). Vitreous VEGF concentrations are significantly elevated in patients with DR, with levels reaching an average of 5744.06 pg/mL in those with PDR. In non-diabetic controls, VEGF levels are much lower, averaging around 817.94 pg/mL. In mouse models of DR, VEGF levels in the retina typically range from 300 to 500 pg/mL, reflecting similar trends of VEGF elevation in response to retinal ischemia and hypoxia. These elevated VEGF levels play a key role in mediating vascular permeability and neovascularisation in DR (Aiello *et al.*, 1994; Li *et al.*, 2010).

By interacting with endothelial receptor tyrosine kinase Tie2, other angiogenic factors, such as angiopoietins (Ang-1, Ang-2) are also implicated in the control of vascular permeability (Patel *et al.*, 2005). Ang-2, acting as an antagonist of Tie2, has been demonstrated to enhance vascular leakage in the retinas of diabetic rats (Rangasamy *et al.*, 2011).

1.5.2.2 Angiogenesis

Abnormal blood vessels in the eye present risks to normal vision. Angiogenesis is a process that involves the growth of new blood vessels. It plays a crucial role in both normal vascular development and abnormal formation of blood vessels. During angiogenesis, endothelial cells multiply and create new arteries in response to signals that guide their growth. These signals can either promote or inhibit angiogenesis (Potente et al. 2011). Angiogenesis that is not properly regulated causes a disruption in the distribution of oxygen and nutrients, leading to an imbalance in the metabolic requirements and availability and causing disturbances in the operation of the neural retina. Pathological angiogenesis is linked to various disorders, such as malignancies, cardiovascular diseases, dementia, and proliferative retinopathies (Folkman 1995). Pathological retinal neovascularisation is distinguished by the presence of vessels that are both leaky and tuft-like. These vessels are often accompanied by haemorrhage and retinal traction. Specifically, the fibrovascular proliferation associated with these new, fragile vessels can contract, pulling on the retinal surface. This mechanical traction can eventually lead to tractional retinal detachment, wherein the retina is physically pulled away from its underlying tissue, disrupting vision and posing a severe threat to sight (Al-Latayfeh et al. 2012). Ocular angiogenesis, which is the formation of new blood vessels in the eye, can occur in several eye conditions including retinopathy of prematurity (Ana Rita Santos et al.), DR, neovascular age-related macular degeneration (AMD), neovascular glaucoma, and corneal neovascularisation (Al-Latayfeh et al. 2012).

1.5.2.3 Retinal neurodegeneration

The initiation of retinal neurodegeneration emerges as an early occurrence in the development of DR, affecting ganglion cells, amacrine cells, and bipolar cells through various mechanisms including oxidative stress, inflammation, and advanced glycation end products accumulation (Barber et al., 1998; Ren et al., 2022). In retinal neurons of diabetic animals and humans, there is an upregulation of pro-apoptotic molecules such as cleaved caspase-3, Bax, and Fas (Kowluru & Koppolu, 2002). Retinal degeneration in DR has been implicated to mitochondrial malfunction as evidenced by a significant increase in the expression of pro-apoptotic mitochondrial proteins like cytochrome c and apoptosis-inducing factor (AIF) in the donor eyes of diabetic subjects (El-Asrar *et al.*, 2004). Recent findings reveal mitochondria remodelling towards hyperfusion during retinal neurodegeneration in human and murine diabetes. This hyperfusion is identified as a key contributor to the impaired

mitochondrial turnover and cellular stress observed in DR (Anderson *et al.*, 2024). The exploration of oxidative stress in diabetes-induced retinal degeneration has also been extensive, with diabetic mouse retinas showing a significant increase in the generation of reactive oxygen species (ROS). Effective suppression of ROS generation has been demonstrated to inhibit visual impairment and caspase-3-mediated retinal neuronal apoptosis (Sasaki *et al.*, 2010).

Retinal degeneration may represent a distinct process from the classic vascular pathology observed in DR (Au & Ma, 2022). While DR is primarily characterised by microvascular changes such as capillary dropout, microaneurysms, and neovascularisation, retinal degeneration focuses on the neuronal component of the retina (Au & Ma, 2022). In this regard, neurodegeneration in the retina occurs earlier and involves direct damage to retinal neurons, independent of the microvascular alterations seen in DR. This distinction is supported by studies showing retinal ganglion cell loss and retinal thinning even before observable vascular changes in diabetic mouse models and humans (Aiello, 2014). The neuronal damage in retinal degeneration may occur due to oxidative stress, mitochondrial dysfunction, and inflammation, without necessarily involving the vascular complications typically associated with DR (Au & Ma, 2022).

Mounting evidence suggests that retinal neurodegeneration may represent an independent pathophysiology of DR. In a diabetes mouse model, the loss of ganglion cells and a reduction in retinal thickness were observed before the onset of microvascular changes (Sohn *et al.*, 2016). Diabetic patients also exhibited inner retinal thinning in the absence of DR or with minimal DR (microaneurysms) (van Dijk *et al.*, 2009).

1.5.2.4 Glial changes in DR

The dysfunction of glial cells, including Müller cells, astrocytes, and microglia, is fundamental to the pathogenesis and progression of DR. Within the retinal environment, these cells play indispensable roles in maintaining neural homeostasis; however, diabetes instigates profound alterations in their functioning, leading to a series of events that amplify retinal dysfunction (Shen *et al.*, 2010). One of the critical disruptions observed is in the regulation of glutamate and potassium (K⁺) transport by Müller cells (Uckermann *et al.*, 2006). The diabetic condition hampers their ability to effectively manage extracellular glutamate levels, leading to neuronal excitotoxicity, where an overabundance of glutamate results in neuronal injury and death. This occurs because excessive glutamate activates glutamate receptors on neurons excessively, causing an influx of calcium ions into the cells. The

heightened calcium levels in turn trigger a cascade of intracellular processes that lead to oxidative stress, mitochondrial dysfunction, and eventually, cell apoptosis or necrosis.

Astrocytes and microglia, too, contribute uniquely to DR's pathology. Astrocytes, vital for the integrity of the blood-retinal barrier and neuronal support, become reactive in diabetes, undergoing changes which compromise their supportive functions and exacerbate vascular leakage and inflammation (Rübsam *et al.*, 2018). Simultaneously, diabetes triggers a hyperactive state in microglia, encouraging a pro-inflammatory response that further intensifies neuroinflammation, neuronal damage, and vascular issues (Diniz *et al.*, 2019).

It is also thought that retinal glial cell dysfunction contributes to the start and exacerbation of retinal inflammation in DR. Retinal glial cells, such as astrocytes, Müller cells, and microglia, play a role in providing structural support and maintaining homeostasis (Sorrentino *et al.*, 2016). Under hyperglycaemic stress, microglia become activated, leading to an increased secretion in TNF- α , IL-6, MCP-1, and VEGF (Abcouwer, 2017). The production of proinflammatory cytokines by Müller cells and astrocytes is linked to the later involvement of inflammation responses (Sorrentino *et al.*, 2016).

During the development of DR, many mechanisms lead to pathological changes in the retina, including inflammation, oxidative stress, and endoplasmic reticulum stress (Meng *et al.*, 2021). During DR, neurons become damaged, glutamatergic and dopaminergic neurotransmitter signalling is impaired, dendritic fields are altered and there is reduced synaptic protein expression, ultimately leading to neuronal apoptosis. In glial cells, interconversion of glutamate and glutamine become impaired. Astrocytes contacts with synapses is also altered during diabetes (Gardner *et al.*, 2016).

1.5.2.5 Inflammation

Inflammation plays a crucial role in the development of DR. Chronic low-grade inflammation has been consistently observed at various stages of DR in both diabetic animal models and patients (Miyamoto *et al.*, 1999; Yuuki *et al.*, 2001). Leukostasis is identified as a significant process in the early phases of DR, as studies have reported the blockage of retinal microvasculature by monocytes and granulocytes followed by increased adherence of leukocytes in retinal vasculature in diabetic mouse models (Miyamoto *et al.*, 1998). Spatial correlation between heightened leukostasis and damage to the endothelium, along with impairment of the BRB in diabetic rats was also observed

(Schröder *et al.*, 1991). Subsequent studies indicated that leukostasis facilitated endothelial cell loss and the breakdown of the BRB through the Fas (CD95)/Fas-ligand pathway (Joussem *et al.*, 2003).

Leukostasis in diabetes is associated with leukocyte-endothelium adhesion mediated by adhesion molecules. Both diabetic rats and patients exhibit increased leukocyte adhesion, along with heightened expression of leukocyte b2-integrins CD11a, CD11b, and CD18 (Barouch *et al.*, 2000). As well as, elevated levels of endothelial cell adhesion molecules, including intercellular adhesion molecule-1 (ICAM-1), vascular cell adhesion molecule (VCAM)-1, and selectins (E-selectin)(Kasza *et al.*, 2017; Limb *et al.*, 1999).

It has also been demonstrated that chemokines, which control leukocyte recruitment and activation, have a role in the pathophysiology of DR. Elevated levels of chemokines such as monocyte chemoattractant protein-1 (MCP-1), macrophage inflammatory protein-1 α (MIP-1 α), and MIP-1 β have been observed in diabetic patients (Suzuki *et al.*, 2011), conversely, the absence of MCP-1 results in reduced retinal vascular leakage in diabetic mice (Rangasamy *et al.*, 2014).

1.5.3 Treatments

The treatment for DR is diverse, with strategies aimed at preventing further progression of the disease and preserving vision. Central to maximising treatment efficacy is the early detection of DR, achievable through routine eye examinations, and management of systemic factors, including blood glucose and hypertension, via both lifestyle modifications and pharmacotherapy (Tomita *et al.*, 2021).

Advancements in DR treatments include the introduction of anti-VEGF therapies which target the critical role of vascular endothelial growth factor in the disease's pathogenesis. Key agents, such as Ranibizumab (Lucentis), Aflibercept (Eylea), and off-label Bevacizumab (Avastin), work by inhibiting VEGF, thus preventing the formation of abnormal blood vessels and reducing vascular leakage, both key drivers of DR (Wang & Lo, 2018). Delivered through intravitreal injections, these therapies offer not just the stabilisation of DR symptoms but, in some instances, can improve visual acuity, marking a pivotal move towards precision medicine that customises treatment to address specific molecular mechanisms, thereby redefining the therapeutic approach to diabetic eye diseases. A recent significant development in the treatment of DR, particularly in cases involving diabetic DME, is the introduction of Faricimab. Faricimab is a novel bispecific antibody that simultaneously targets both

VEGF-A and Ang-2, an angiopoietin involved in vascular destabilisation under diabetic conditions. By inhibiting these two pathways, Faricimab provides a dual mechanism of action that not only reduces vascular leakage and abnormal blood vessel formation but also stabilises the blood vessels, potentially offering a more comprehensive treatment solution for patients with DR (Ferro Desideri *et al.*, 2023).

Complementing the impact of anti-VEGF therapies, the treatment arsenal for DR also includes laser therapy and corticosteroids, further expanding the options available to combat this condition. Techniques such as focal/grid macular laser therapy and panretinal photocoagulation can reduce vascular leakage and areas of retinal ischemia. Laser treatment is required for 5% to 8% of diabetic retinopathy patients (Moutray *et al.*, 2018), while vitrectomy surgery becomes necessary for up to 5-10% of PDR cases (Gupta & Arevalo, 2013). In contrast, corticosteroids, administered intravitreally, offer a potent means to quell inflammation and edema, especially in instances where anti-VEGF therapies may fall short. Investigating the NVU in DR is crucial as it will offers insights into the broader mechanisms of disease progression, including neurodegeneration and the disruption of BRB integrity, which are pivotal in the development and progression of DR. Understanding the interactions within the NVU can lead to the identification of novel therapeutic targets and strategies, potentially offering more comprehensive treatment options that address both the vascular and neuronal aspects of the disease. However, it's critical to acknowledge that these treatments predominantly target the end stages of DR and are associated with various side-effects. This underscores the need for the development of new early-stage treatments that prevent patients from reaching the sight-threatening stages of the disease, aiming to intervene before irreversible damage occurs.

1.6 Electron Microscopy

Electron microscopy (EM) is a commonly used to study the cellular ultrastructure of various tissues. Transmission electron microscopy (Bharadwaj *et al.*) which is typically used, produces high resolution images which enables clear visualisation of the cells ultrastructure (Frankl *et al.*, 2015). However, TEM produces 2-dimensional (2D) micrographs, and for greater understanding of the function of different cellular components and their heterocellular interactions is important to view them in a three-dimensional (3D) view.

1.6.1 Examination of NVU by TEM

The examination of the retinal NVU through TEM has illuminated the intricate cellular and subcellular changes occurring within the retinal capillaries with the effect of diabetes. Several studies employing TEM to investigate retinal capillaries have emphasised the significant thickening of capillary BMs and the subsequent impact on the surrounding neuroglial milieu, highlighting the complexity of interactions within the NVU. These microstructural alterations, characterised by the accumulation of extracellular matrix components and the progressive loss of pericytes, reflect the broader pathophysiological narrative of DR (Curtis et al., 2009; Fehér et al., 2018; Gardiner et al., 2007). As diabetes evolves, early reductions in retinal perfusion exacerbate vascular and neuroglial stress, leading to a vicious cycle of ischaemic hypoxia and capillary dysfunction. However, none of these studies have explored these changes using serial sections, a methodology pivotal for understanding the 3D architecture of the NVU. Examining the NVU in 3D offers a comprehensive view of the spatial relationships and interactions among the various cellular components, providing insights into the pathophysiological processes.

1.6.2 SBF-SEM

Serial block-face scanning electron microscopy (SBF-SEM), a technique developed by Horstmann *et al.* (2004), allows for the automatic serial thin sectioning and scanning of an embedded tissue or sample in an SEM. The SEM differs from the TEM as it does not generate a shadow of a stained section but instead scans the surface of an object. This allows for the collection of several serially-registered ultrastructural images which together give a 3D view of tissue microanatomy and can have a resolution as small as 3-5 nm (Courson *et al.*, 2021). SBF-SEM is a powerful and versatile technique for generating high-resolution 3D images of biological samples. It is a type of volume electron microscopy (vEM) technique that involves serially imaging thin sections of a sample and then stacking the images together to create a 3D reconstruction (**Figure 1-3**). This technique is particularly well-suited for imaging tissues that are difficult to image with other techniques, such as tissues with complex architectures or tissues that are embedded in thick layers of material.

Resin embedded tissue samples stained with a series of heavy metals are positioned into scanning electron microscope (Riazi-Esfahani et al.) with an ultramicrotome with a diamond knife attached. A flat surface of the specimen is cut with the diamond knife and the knife is retracted. To generate a picture of tissue ultrastructure, the knife is withdrawn, and the surface of the block is scanned in

a raster pattern using an electron beam. The SEM contains a mounted computer-controlled ultramicrotome which cuts ultrathin sections (10–120 nm) of the specimen. A flat surface of the specimen is cut with the diamond knife and the knife is retracted. The SEM stage and ultramicrotome work in conjunction to raise the sample (e.g., 100 nm) after each cut, and the electron beam of the SEM microscope then scans the new exposed block face to create an image of the tissue ultrastructure (Goggin *et al.*, 2020). The result is an aligned stack of digital images which together reconstruct the specimen in 3D.

The application of SBF-SEM to investigate the retinal NVU could unveil intricate details about cellular and subcellular structures, offering insights into complex retinal architectures and pathological alterations not visible in 2D. This technique can reveal novel aspects of heterocellular organisation and interactions and any changes under disease circumstance, providing a deeper understanding of retinal function and disease mechanisms.

Employing SBF-SEM to investigate the retinal NVU not only reveals intricate details on cellular structures but also offers unique advantages over other 3D EM techniques. Unlike traditional 3D EM methods, SBF-SEM enables the comprehensive exploration of multiples samples and provides a holistic view of their architecture. SBF-SEM's capacity for large volume data output and high resolution further facilitates precise segmentation and analysis, surpassing the capabilities of alternative techniques (Laws *et al.*, 2022). Thus, SBF-SEM emerges as the preferred choice for studying the retinal NVU, enabling a deeper understanding of retinal function and disease mechanisms.

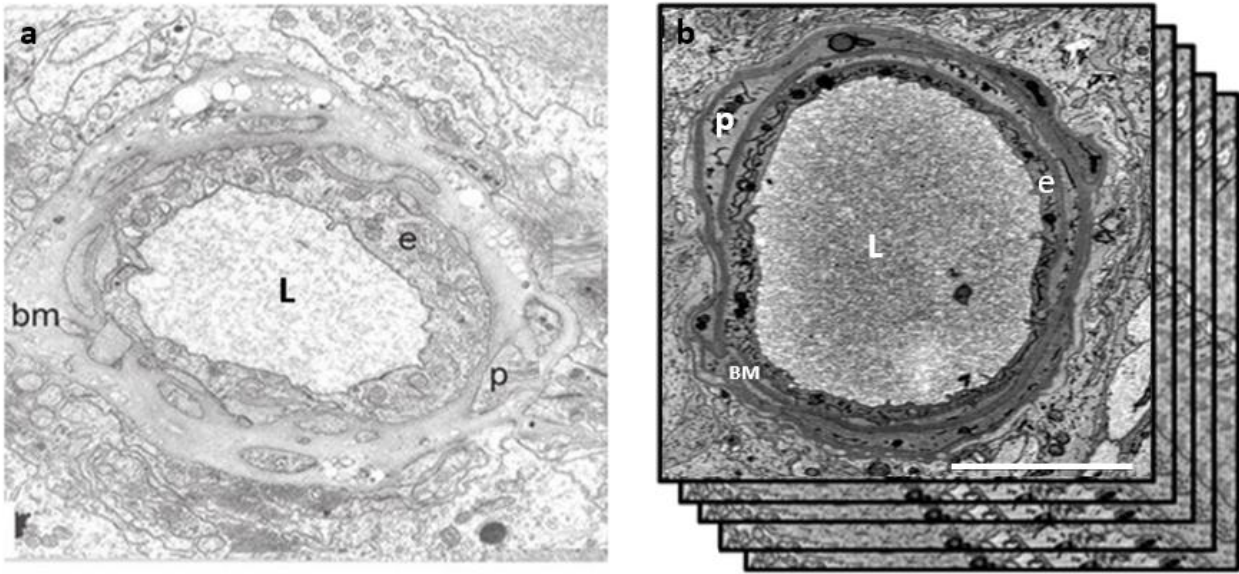


Figure 1-3 TEM vs SBF-SEM a normal retinal capillary. a. TEM of 2D slice of retinal NVU from a human non-diabetic capillary 20,000 X. (Bianchi, Enrica. 2015). b. SBF-SEM serial stack of NVU from a human non-diabetic capillary 1, (for this study, see **Figure 5-2** for fuller description of this dataset). Endothelium (e) basement membrane (bm), lumen (L) and pericytes (p). Scale bar 5 μm .

1.6.3 Other Imaging Modalities for Studying the Retinal NVU

While SBF-SEM offers detailed insights into the ultrastructure of the retinal NVU, other imaging modalities have been employed to study the NVU and associated tissues. Optical coherence tomography (OCT) is a non-invasive imaging technique widely used in both clinical and research settings to visualise the retinal layers in cross-section (Lang, 2007). OCT provides high-resolution images of the retinal structure, allowing for the assessment of retinal thickness, integrity of the retinal layers, and early signs of vascular changes. OCT angiography (OCTA) further enhances this capability by visualising the retinal microvasculature and tracking changes in blood flow (Santos et al., 2024). Although these techniques are highly effective for monitoring *in vivo* changes over time, they lack the cellular and subcellular resolution that SBF-SEM provides.

Confocal microscopy and multiphoton microscopy have also been used for detailed imaging of retinal tissues, particularly for visualising glial cells and capillaries (Nusinovici et al., 2024). However, these techniques are limited by penetration depth and are generally applied to animal models or *ex vivo* samples. While other imaging modalities such as OCT and confocal microscopy offer valuable insights, particularly for non-invasive, *in vivo* imaging, they are limited in their ability to capture the

cellular and subcellular details crucial for understanding the complex architecture of the retinal NVU (Tsai et al., 2024). SBF-SEM, with its ability to generate high-resolution, 3D reconstructions of tissue microanatomy, overcomes these limitations. It allows for the comprehensive examination of the intricate relationships between cells in the NVU, including endothelial cells, pericytes, and glial cells, offering a clearer understanding of their interactions under both normal and pathological conditions. This technique's capacity to provide volumetric data at high resolution makes it particularly well-suited for studying the NVU in conditions such as DR, where changes in cell morphology and BM thickening play a central role in disease progression. As such, SBF-SEM stands out as the optimal technique for gaining deeper insights into the structure and function of the retinal NVU, revealing aspects that cannot be fully captured by other imaging modalities (Laws et al., 2022).

Despite the disruption of the integrity of the retinal NVU being implicated in the pathogenesis of DR, the 3-dimensional ultrastructure of the retinal NVU remains to be fully characterised and quantitative methods for describing its key features have yet to be developed. In the present thesis, we have undertaken the first nanoscale examination of the anatomy of the mouse and human retinal NVU in three spatial dimensions with and without the effect of diabetes using SBF-SEM.

1.7 Hypothesis

The heterocellular communications within the retinal neurovascular units are hypothesised to undergo disruptions during the onset and progression of diabetes, indicating potential structural alterations associated with the disease. We further hypothesised that these changes could be visualised using 3D EM.

1.8 Aims and objectives.

This research project was designed to advance the understanding of the retinal NVU through a detailed investigation of its heterocellular interactions and structural arrangements. Utilising high-resolution imaging techniques, this project aimed to delineate the complex anatomical relationships within the human and rodent retina NVU under normal conditions and with the progression of diabetes. Furthermore, sophisticated analytical methods were employed to quantify essential features, laying a quantitative groundwork to enhance comprehension of the dynamic processes that regulate the NVU. The specific aims were as follows:

1. Characterise the NVU's Heterocellular Composition: To achieve a detailed understanding of the diverse heterocellular features within the retinal NVU.
2. Quantitative Analysis of Key NVU Features: Utilise appropriate analytical methods to quantify key features of interest, providing a quantitative basis for a nuanced comprehension of the dynamic structures and processes governing the retinal NVU.
3. Explore diabetic related changes in the NVU. Investigate how diabetes influences cellular interactions and the NVU's integrity and identify changes that may offer avenues for therapeutic intervention.

Chapter 2 Materials and methods

2.1 Sample Preparation

2.1.1 Fixation and microdissection

Adult C57BL/6 mice (3 and 6 month) were killed by Schedule 1 procedure according to the Animals Scientific Procedures Act (ASPA) 1986. Mice were euthanised via CO₂ asphyxiation and the eyes were enucleated 1-4 mins following death, and fixed in 4% paraformaldehyde (PFA) for 1 hour. The eyes were then washed in phosphate buffered saline (PBS). To extract the retinas for retinal flat mounting, microdissection was carried out. The eyes were placed on a dissection dish and were observed under an Olympus SZX7 microscope. Once the cornea was located, the limbus area was punctured using a 26G needle to allow entry of surgical scissors. Using surgical scissors, cuts were made around the limbus to separate the cornea from the rest of the eye. A few drops of PBS were placed in the eye cap to help soften the retina and lubricate the lining. The back of the eye was held using surgical forceps and the back of the eye was gently rubbed to allow the retina to detach. Once the retina has detached, it was placed into a microcentrifuge tube filled with PBS.

For this study, EM analyses were conducted on a total of ten mice, including seven, 6-month-old mice and three, 3-month-old mice. All mice were prepared at Queen's University Belfast, and fixed retinas for EM. Additionally, one 6-month-old mouse was specifically prepared for CLEM and sent to the Institute of Experimental Medicine in Budapest, Hungary.

Importantly, the animals in this study were not perfusion-fixed, which is typically more complex due to intraocular pressure (IOP) remaining present after death. Successful perfusion fixation requires the input pressure to be high enough to overcome IOP, which is variable, and this is not always controlled—often, only the flow speed is regulated. This variability results in inconsistent percentages of the capillary bed being fixed. However, in the case of mice, perfusion fixation is less critical due to the small size of the eyeball, which allows for sufficiently fast penetration of PFA through the eye tissues.

To further enhance fixation speed, a hole was punched through the cornea with a needle, allowing immediate access of the external PFA to the inside of the eye. This method leads to light fixation of the retina within minutes. In fact, even with very short fixation periods (5-10 minutes), removal of

the anterior half of the eye (cornea, iris, lens) consistently revealed a white-bleached retina in the back of the eye, indicating rapid fixation.

Another downside of perfusion fixation is the removal of blood, which may be undesirable in certain cases. Additionally, it can potentially interfere with the appearance of the endothelial cells' intraluminal side. For this study, the chosen method of fixation allowed the retention of blood for HbA1c measurements and preserved the endothelial structure for EM analysis.

2.1.2 Diabetes-induced mouse samples

Diabetes was induced in C57BL/6J mice (~25 g) by five daily intraperitoneal injections of 50 mg/kg streptozotocin (STZ) in freshly prepared 0.1 M citrate buffer (pH 4.5). STZ is preferentially taken up by pancreatic β -cells via the glucose transporter 2, where it causes DNA alkylation, leading to cell death through the activation of apoptotic pathways. This results in a reduction of insulin production, ultimately disrupting glucose homeostasis. Control animals received citrate buffer alone. One week after injections, glucose level was determined using FreeStyle Lite Blood Glucose Test strips (Abbott, Oxfordshire, UK). All procedures were carried out in strict accordance with the guidelines at Queen's University Belfast and were conformed to Animals Act 1986 under project license (PPL2919).

2.1.2.1 HbA1c measurements

Post-treatment, an initial blood glucose measurement was employed to distinguish between those mice that developed diabetes and those that resisted the induced condition. However, the definitive confirmation of diabetes, as well as the quantification of its severity, was established through glycosylated haemoglobin (HbA1c) measurements at the time of death.

Glycosylated HbA1c serves as a crucial indicator, offering insights not only into the presence of diabetes but also the extent or severity of the condition. Mice with HbA1c levels above a certain threshold (>6.5%) were classified as diabetic, whereas those with lower values were classified as non-diabetic. HbA1c reflects the average blood glucose levels over the preceding 2-3 months, thus providing a reliable metric for long-term glycemic control. **Table 2-1** details the diabetic mouse samples used and their HbA1c levels, with values ranging from non-diabetic levels (e.g., 4.5%) to severely diabetic (>13.1%).

In this study, mice with HbA1c levels: Greater than 6.5% were classified as diabetic, indicating chronic hyperglycemia and insufficient insulin production. Lower than 6.5% were considered non-diabetic, reflecting normal blood glucose regulation.

Table 2-1 Experimental samples and corresponding glycosylated haemoglobin (HbA1c) levels. This table presents data on experimental samples, each identified by a unique number, along with their respective weights in grams, HbA1c ranges in mmol/mol, and the percentage of glycosylated HbA1c. The HbA1c values offer insights into the glycaemic control of each sample, providing valuable information for assessing diabetes severity in the experimental cohort.

Sample Number	Sex	Start Weight (g)	End Weight (g)	Hb1Ac Range (mmol/mol)	Glycosylated Hb1Ac (%)	Diabetic
SBF108-1 (51827)	Male	26	29	26	4.5	No
SBF108-2 (51828)	Male	25.1	25	>120 (outside upper range)	>13.1	Yes
SBF108-3 (51829)	Male	23.7	25.7	85	9.9	Yes
SBF108-4 (52690)	Male	26.2	34	34	5.3	No
SBF108-5 (52691)	Male	25.7	26.7	110	12.3	Yes
SBF108-6 (52692)	Male	22.5	24.9	95	10.8	Yes
SBF108-7 (53177)	Male	27	35.8	26	4.5	No

2.1.3 Diabetic mouse sample preparation

Retinal samples were promptly isolated from four 6-month-old mice within approximately 5 minutes post-mortem. Subsequently, these isolated retinas were directly immersed in a 2% glutaraldehyde (GA) solution with cacodylate (Caco), for EM imaging (detailed outline in Section 2.2).

2.1.4 Human samples

Human eye samples were obtained, following written informed consent (approved by local research ethic committee 17/NE/0361), from patients treated by exenteration for large facial/sinus tumours at the Royal Victoria Infirmary, Newcastle Upon Tyne. Examinations were performed on two human eyes, one from a male subject aged 67 with a 10-year history of diabetes mellitus (DM), characterised as type 2 for the past 6 years and tablet controlled. Minimal background diabetic

retinopathy without maculopathy was documented. The other eye under examination belonged to a 58-year-old male without a history of diabetes. **Table 2-2** details the characteristics of the human retinal samples, including gender, age, diabetes status (DM), and the presence of age-related macular degeneration (AMD). The eyes were isolated from the tissue needed for histology, and the retinas immediately fixed in situ with 2% glutaraldehyde in 0.1 M sodium cacodylate buffer, pH 7.3 for a minimum of 12 h in preparation for electron microscopy.

Table 2-2 Details on human samples. This table provides a comprehensive overview of the human retinal samples, including gender, age, diabetes status (DM), and the presence of age-related macular degeneration (AMD).

Sample number	Gender	Age	DM	AMD
SBf79	male	67	yes	No
SBF90	male	63	no	No

2.2 Electron Microscopy

2.2.1 Serial Block Face Scanning Electron Microscopy

Tissue samples are stained with a series of heavy metals as the images are produced by collecting backscatter electrons which originate from elastic interactions between the beam and the sample. The sample is then embedded in resin and placed in an SEM microscope. The SEM contains a mounted computer-controlled ultramicrotome which cuts ultrathin sections (35–120 nm) of the specimen. A flat surface of the specimen is cut with the diamond knife and the knife is retracted. The SEM stage and ultramicrotome work in conjunction to raise the sample (e.g., 100 nm) after each cut, and the electron beam of the SEM microscope then scans the new exposed block face to create an image of the tissue ultrastructure. The result is a stack of images aligned in the x-, y- and z-axes (**Figure 1-3**). This allows for analysis of changes in tissue structure through a chosen depth of the material under investigation potentially revealing important information not easily established with repeated examination of individual TEM sections.

The samples were imaged using a combined system of a Zeiss Sigma SEM chamber (Zeiss, Cambridge, UK) incorporated with the Gatan 3View software (Gatan, Abingdon, UK). SBF-SEM collects multiple serial-registered ultrastructural images, which allow an unprecedented 3D view of tissue microanatomy. The ultramicrotome cuts 100nm sections of the sample, as this was determined to be the optimal thickness to achieve the highest resolution without introducing damage or artifacts to the sample. This ensures precise and accurate imaging, maintaining the

structural integrity required for detailed analysis. The SEM captures images of the sections blockface with a backscattered electron detector and saved in DM3 format. The Gatan 3View was used to optimise image settings and select the desired location of the sample and ensure the capillary is in the field of view. The image dimensions were set to 3000 x 3000 at a pixel size of 6nm, with a 20 μ s/pixel dwell time. Electron micrographs collected from healthy and diabetic mouse and human retinal capillaries were imaged from the superficial vascular plexus. Capillaries were identified based on their distinctive structural features and location within the sampled tissue, guided by the high-resolution capabilities of the SBF-SEM system. The acquisition parameters were set to capture detailed electron micrographs, with the analysis encompassing 100-300 serial sections per capillary.

2.2.2 Sample preparation for EM

Retinal tissue samples prepared for examination by EM to enable highest spatial resolution viewing of features of interest were micro-dissected into 1 mm sections for adequate fixation and stain penetration and were transferred into EM buffer for at least 12 hours at 40°C for tissue fixation and then washed in sodium cacodylate buffer. The tissue samples then undergo a series of heavy metal staining using osmium tetroxide, uranyl acetate, and lead aspartate. Samples were washed in 3% potassium ferrocyanide and 2% osmium tetroxide in buffer, followed by a wash in thiocarbohydrazide (osmium tetroxide) at room temperature to fix the stain. Samples were then washed in 1% uranyl acetate and left overnight in the refrigerator. Lead aspartate solution was then used to stain the samples. ddH₂O was used to wash the samples between each staining procedure. To dehydrate the samples, increasing concentrations of acetone, from 25% to 100% were used, followed by an infiltration of increasing concentration of resin in acetone, finished with changes of 100% TAAB Epoxy 812 hard resin.

Samples were then embedded in resin and left overnight in the rotator at 600°C for a minimum of 36 hours for polymerisation. Resin embedded samples were then trimmed using a razor blade to form trapezoid block face. Samples were cut to 1 μ m sections using a diamond knife and stained with toluidine blue for an orientation, tissue structure, and staining quality under light microscopy. Samples fit for EM, demonstrating well-preserved tissue integrity, clear structural details, and minimal imaging artifacts. The block was coated with silver and sputter-coated with gold layer to reduce charging caused by the electron beam during imaging.

A sub-set of resin-embedded samples examined by SBF-SEM were also post-processed for viewing by TEM as follows.

2.2.2.1 TEM

Sections containing capillaries, initially observed with SBF-SEM in resin-embedded samples, were sectioned into 70 nm slices onto copper grids then placed into the TEM. A Hitachi HT7800 120 kV TEM attached to an EMSIS CMOS Xarosa camera was used. In a TEM a beam of electrons generated at a cathode is projected through an ultrathin section of a sample. This projection is then captured by a camera and converted into a 2D digital image.

The TEM was used to analyse 34 ultra-thin sections from 5 non-diabetic human samples, totalling 210 capillaries. The magnification range was set between 25,000x and 50,000x, with the electron beam power at 100 kV.

2.2.3 Immunogold EM

Immunostaining and subsequent imaging via confocal microscopy and TEM were performed at the Institute of Experimental Medicine in Budapest, Hungary. Detailed methods employed by the Institute are as follows:

2.2.3.1 Immunostaining

Retinal sections prepared and made flattened by making radial cuts from the periphery towards the center, which helps to spread the tissue out on a substrate without curling or overlapping. These flatmounts were stained with primary antibody, rabbit anti-P2Y12R (1:500) (AnaSpec), and then with secondary antibody, donkey anti-rabbit A647 (1:500) (ThermoFisher). Sections were washed in PB and TBS before and after antibody incubation and mounted using Fluoromount-G or Aqua-Poly/Mount. Nikon Eclipse Ti-E microscope equipped with a laser confocal system, utilising lasers at 405, 488, 561, and 647 nm wavelengths for fluorescence analysis.

2.2.3.2 Pre-embedding Immunoelectron Microscopy:

Retinal flatmount sections were blocked in 1% HSA, followed by incubation with rabbit anti-P2Y12R (1:500) in TBS for 2-3 days. After washing in TBS, sections were incubated with 1.4 nm gold-conjugated goat anti-rabbit Fab-fragment (1:200) (Jackson ImmunoResearch), for 2h hrs at room temperature, extensively washed, and fixed with 2% glutaraldehyde. Silver enhancement and EM-specific preparations, including 0.5% OsO₄ treatment and embedding in Durcupan, were conducted post-immunolabeling.

2.3 Immunofluorescent labelling

2.3.1 Immunohistochemistry of mouse retinal flatmounts

The PBS in the microcentrifuge tubes containing the mouse retinas was discarded and the retinas were washed with 300µl of wash buffer (2% DSA/10% Triton-x) 3 times with 15-minute intervals in between washes. The microcentrifuge tubes containing the retinas were placed on a shaker during each wait period. 300µl of fresh wash buffer was added to block each retina and left for 1 hour at room temperature on a shaker. Primary antibody solutions were made up (GFAP 1:100, NG2 1:100, Isolectin B4 1:100) and 200µl was added to each retina (**Table 2-3**). Retinas were left on the shaker in a cold room overnight. The primary antibody solution was discarded, and the retinas were washed 8 times with 300µl of wash buffer with 30-minute wait in between washes. The microcentrifuge tubes containing the retinas were placed on a shaker each wait period. Secondary antibody solutions were made up (Alexa Fluor 647 Secondary Antibody 1:150, Alexa Fluor 488 Secondary Antibody 1:100, Alexa Fluor 568 Secondary Antibody 1:100) and centrifugal force of 700 g for 10 minutes. 200µl of secondary antibody solution was added to each retina and the samples were left in a cold dark room for 1.5hr. The secondary antibody solution was discarded, and the retinas were washed in the dark 8 times with 30-minute wait in between washes. The retinas were mounted onto labelled slides with vectashield (Vector Labs, San Diego, CA, USA; H-1200) mounting medium was placed on top of each section to prevent fluorophore fading. Coverslips were placed carefully over the retinas with nail varnish to hold them into place.

Table 2-3 Details of antibodies for immunohistochemistry. Details of all primary and secondary antibodies are listed in the table. The type of serum and primary antibody used based on the species in which the primary and secondary antibodies were raised and the protein of interest (target protein). The company and product code for all antibodies are provided.

Antibody	Target Epitope	Working Dilution	Company	Catalogue No.	Host/type
Collagen IV Antibody	Collagen IV	1:100	BIO-RAD	2150-1470	Mouse
NG2 Antibody	Chondroitin Sulfate Proteoglycan 4	1:100	Merck	MAB5384-I- 100UG	Mouse
Isolectin B4 Antibody	Isolectin B4	1:100	Merck	L2140	Biotin Conjugate
Alexa Fluor 488 Secondary Antibody	IgG	1:100	ThermoFisher Scientific	A-21202	Donkey anti-Mouse
Alexa Fluor 568 Secondary Antibody	IgG	1:100	ThermoFisher Scientific	A10042	Donkey anti-Rabbit

Alexa Fluor 647 Secondary Antibody	Streptavidin	1:150	ThermoFisher Scientific	S21374	
P2Y12R Secondary Antibody A647	PYY12 Receptor	1:500	AnaSpec	55043AS	Rabbit
	IgG	1:500	Jackson ImmunoResearch	711-605-152	Donkey anti- Rabbit

2.3.2 STED and Confocal Microscopy

For confocal and STED imaging, slides containing the retinal flatmounts were placed under a Leica TCSSP8 gSTED 3× microscope (Leica Microsystems) equipped with white light lasers. Confocal microscopy, which uses point illumination and a spatial pinhole to eliminate out-of-focus light, provides increased optical resolution and contrast by allowing only light that is in focus to be detected. This technique is well-suited for the high-resolution imaging of thicker specimens, offering clear images of structures within the retina. In contrast, STED microscopy, an advanced form of super-resolution imaging, further enhances resolution by using a depletion laser that selectively quenches fluorescence around the focal spot, effectively shrinking the point of illumination. This results in an ability to achieve higher resolution than is possible with standard confocal microscopy, revealing even finer details within cellular structures. The fluorophore Alexa Fluor 488 was excited at 499 nm and emitted light around 520 nm. Alexa Fluor 568 was excited at 579 nm, with emission observed near 603 nm. Finally, Alexa Fluor 647, excited at 650 nm, had its emission peak close to 665 nm.

2.4 Image processing

2.4.1 Segmentation

Microscopy Image Browser (MIB) (Belevich *et al.*, 2016). Each feature of the NVU was segmented in MIB for visualisation and later 3D rendering of the structures. Due to the complexity of the cellular morphology, a combination of semi-automatic and manual image segmentation was done with the use of tools, filters and interpolation in XY, XZ or YZ planes.

Manual segmentation was done by selecting the brush tool to trace the cell membrane and filled 12 (using F or shift + F for the whole dataset). The selection was added to a material (A or shift + A) depending on the cell type. Colour-coded area lists corresponding to specific features in the images were assigned as follows: the basement membrane (BM) (brown), endothelial cell (aqua), pericyte (blue), astrocyte (purple), macroglia (red shades) and neurons (green shades).

Interpolation was done also using the brush tool to manually trace around the cell membrane, however this was drawn in every 2-5th slice depending on the variability of the cell morphology. Structures with a similar morphology throughout the slices including endothelial cells and neurons had an n value ranging from 2 – 4.

Step-by-step process for manual segmentation:

1. Select the brush tool.
2. Trace the cell membrane.
3. Fill the selection using F or Shift + F for the whole dataset.
4. Add the selection to a material using A or Shift + A based on the cell type.
5. Assign colour codes to the respective areas:
 - a. BM (brown)
 - b. Endothelial cell (aqua)
 - c. Pericyte (blue)
 - d. Astrocyte (purple)
 - e. Macroglia (shades of red)
 - f. Neurons (green)

Interpolation process:

1. Use the brush tool to trace the cell membrane.
2. Draw every nth slice based on morphology variation.
3. For consistent structures (e.g., endothelial cells, neurons), use n values of 2–4.
4. Interpolate by selecting I or Selection > Interpolation to segment the slices with gaps.
5. B/W thresholding was used to automatically segment objects based on the contrast of the dataset:

Step-by-step for B/W thresholding:

1. Select B/W threshold.
2. Adjust the range by moving the sliding panel until the desired selection is segmented.
3. Apply to the entire stack using All.
4. For errors, clean up by holding Ctrl and brushing over them manually.
5. After segmentation is complete, the file was saved in the amira mesh binary format.

After segmentation is complete, the file was saved in the amira mesh binary format, ready to export to Amira (ThermoFisher) for 3D rendering and analysis.

1. Select Model > Save as > .am to save the file.
2. Export to Amira for 3D rendering and analysis.

2.4.2 3D Image Reconstruction

2.4.2.1 AMIRA

Complete segmented objects were then exported from MIB and loaded into an Amira project (ThermoFisher, Loughborough, UK) and rendered in 3D.

Import the data:

1. Locate the model.
2. Select Read into volume memory.

For visualisation:

1. Select Generate surface. Click Apply.
2. Choose Select surf.
3. Enable Surface view for visualisation.

2.4.2.2 ARIVIS

Serial sections of SBF-SEM data were opened as a plane series in a .sis format using the Arivis Vision 4D software (ver. 3.5.1, Arivis AG, Ros-tock, Germany). Once opened the pixel dimensions were set using the information viewer tab as 6nm for X and Y and 100/120nm depending on the dataset.

Steps to set pixel dimensions:

1. Open the Information Viewer tab.
2. Set pixel dimensions: X and Y: 6nm and Z (depending on the dataset): 100nm or 120nm.

The model was then loaded via Objects > Import Objects as labelled images.

The model was then loaded via Objects > Import Objects as labelled images.

1. Navigate to Objects.

2. Select Import Objects.
3. Load the model as labeled images.
4. Each material was assigned an identity by selecting the material > Objects > Add Tag.

Each material was the assigned an identity by selecting the material > Objects > add Tag. 3D reconstruction was completed using show 4D viewer > show objects.

Steps to assign material identity:

1. Select the material.
2. Navigate to Objects.
3. Choose Add Tag to assign the identity.
4. 3D reconstruction was completed using show 4D viewer > show objects.

Steps for 3D reconstruction:

1. Select Show 4D Viewer.
2. Click Show Objects to complete the 3D reconstruction.

2.4.2.2.1 Pipeline Creation

Raw image data files converted to a compatible format (TIFF/SIS) were opened into the ARIVIS Vision 4D software, file > open > locate directory. The segmented model file was then opened on top of the raw data file as a labelled image, objects > import objects from labelled image.

1. Open ARIVIS Vision 4D software.
2. Navigate to file > Open.
3. Locate and open the directory containing the raw image data files.
4. Open the segmented model file as a labelled image:

Objects > Import Objects from labelled image.

Segments are tagged under their allocated material type:

1. Select the material.
2. Navigate to Objects > Show Objects Table.
3. Right-click and select Add Tag to assign the material type.

To create the pipeline to detect endothelial-pericyte intersect using the tagged materials:

1. Go to Analysis > Add New Pipeline.
2. Select Add Operation > Segmentation > Import Document Objects.
3. Add tags:

Endothelium.

Pericyte.

4. Set the output:

Endothelium Imported.

Pericytes Imported.

The segmented materials must be selected for a morphological output:

1. Navigate to Segments > Segment Morphology.
2. Input: Endothelium Imported.
3. Select Modification > Dilate Objects.
4. Set pixels to the desired number.
5. Output: Endothelium Dilated.

The object math calculation for the detection is then selected;

1. Go to Segments > Object Math.
2. Select action: Intersect ($A \cap B$).
3. Objects A: Endothelium Dilated.
4. Objects B: Pericyte Imported.
5. Output: Endothelium – Pericyte Intersect.
6. Press Play to run the calculation.

2.5 MATLAB

2.5.1 Morphological analysis

Several image analysis procedures were implemented in MATLAB (MATLAB ver. R 2021b) to quantify morphological properties of the NVU features of interest. The area (A) of each object was determined by counting the number of pixels comprising it. The perimeter (P) of each object was measured by first using MATLAB 14 to determine boundary pixels, and then estimating the perimeter by analysis of its Freeman chain code (Freeman, 1961). The Freeman chain code is a way of encoding the boundary by tracking the direction between neighbouring pixels and assigning a

numerical value, which allows for the calculation of the perimeter based on these directional changes. Convex hull areas (CA) and perimeters (CP), which enclose the smallest convex area about each object, were calculated equivalently. Radii were measured by determining the central coordinate of the subject area and calculating the 2D Euclidean distance (i.e. $r = \sqrt{\Delta x^2 + \Delta y^2}$) from it to each of the pixels composing the boundary, taking the mean of this distribution. Ratios of these key metrics, which are standard in morphological image analysis were also recorded for interpretation. Convexity (CP:P) denotes the degree that the perimeter of an object deviates from that of its convex hull. Solidity (A:CA) denotes the degree to which an object's area deviates from that of its convex hull. Sphericity denotes the degree to which an object approaches a perfect circle (i.e., Rmin:Rmax from the distribution of boundary-centroid distances used to determine R) (**Figure 2-1**).

2.5.2 Pairwise distance analysis

In plane minimal distances between the boundaries of all pairwise combinations of intercellular and cellular-BM features were used to analyse proximity using MATLAB. For each image slice and feature pair, two minimal distance histograms were generated; one contained the minimal distances from each boundary pixel of the first feature in the pair to the nearest boundary pixel of the second, and the other contained the minimal distances in the opposite direction (i.e. from each boundary pixel in the second feature of the pair to the nearest boundary pixel of the first). The proximity histograms for each feature pair were consolidated into a mean proximity histogram using all data in the image stack. Cumulative distribution functions were calculated for each mean proximity histogram, which assesses the total percentage of boundary pixels that lie within a given distance between each feature pair.

A pictographic summary of the various morphological analyses undertaken in this study is provided in **Figure 2-1**.

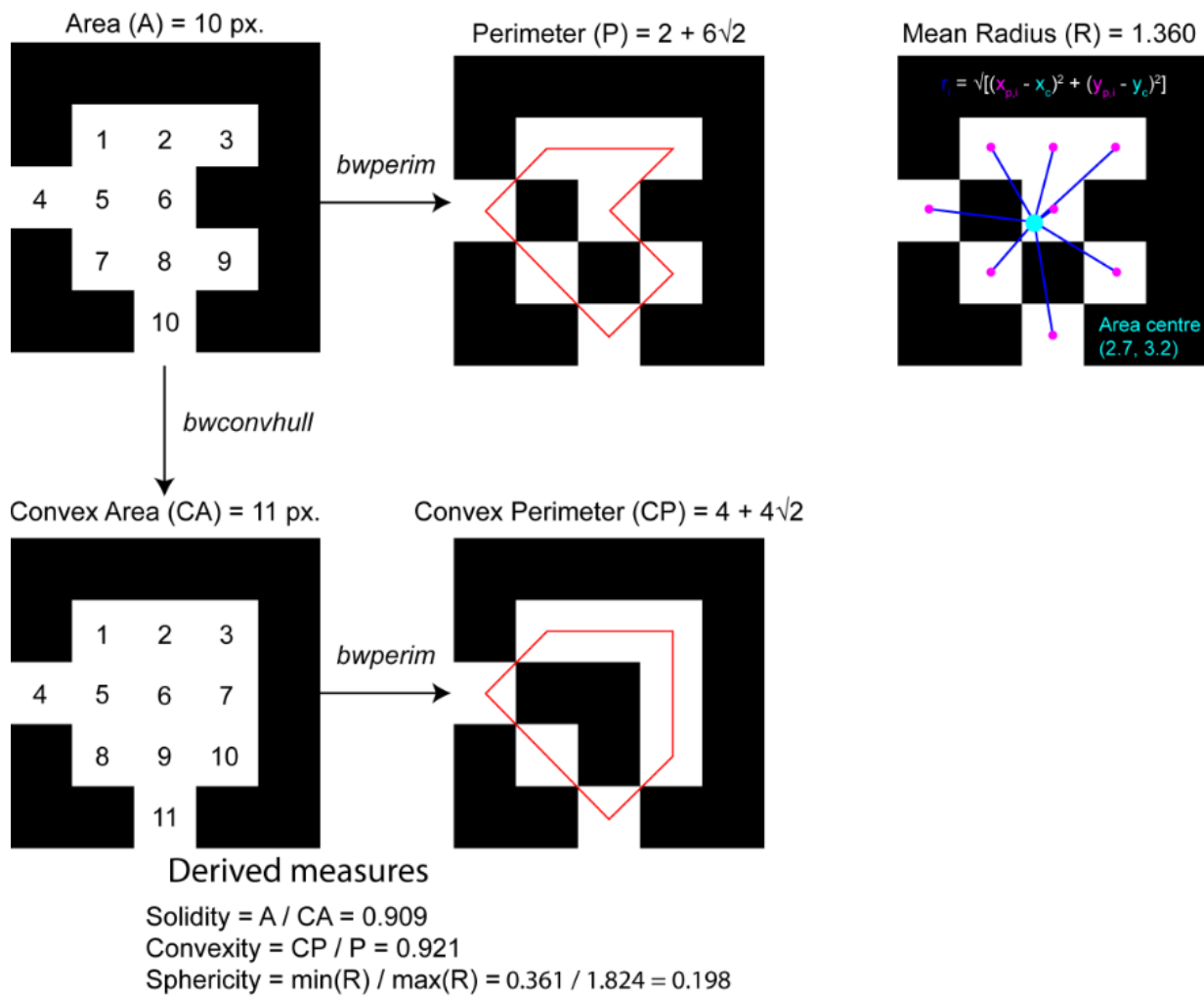


Figure 2-1 Pictographic summary of morphological analysis features. A schematic of intracellular feature morphological assessments to recapitulate from the methods, The area (A) of each object was determined by counting the number of pixels comprising it. The perimeter (P) of each object was measured by first using MATLAB `bwperim` to determine boundary pixels, and then estimating P by analysis of its Freeman chain code. Convex hull areas (CA) and perimeters (CP) (MATLAB `bwconvhull`), which enclose the smallest convex area about each object, were calculated equivalently. Radii were measured by determining the central coordinate of the subject area and calculating the 2D Euclidean distance (i.e. $r = \sqrt{(\Delta x^2 + \Delta y^2)}$) from it to each of the pixels composing the boundary (MATLAB `pdist2`), taking the mean of this distribution. The ratios of these key metrics (A, A:P, and the convex hull equivalents) were calculated for additional interpretation of object shape and compactness. The steps followed for convexity, solidity, and sphericity calculations are further illustrated in the workflow, which shows how each of these measures is applied to provide a comprehensive analysis of object morphology.

2.6 Identification of features of interest

2.6.1 Peg-and-socket formations

Inspection of the data revealed that pericyte-endothelial membrane convolutions of a peg-and-socket-like formation were a common feature of the retinal NVU (detailed in Results and Discussion). A quantitative analysis to calculate the number of such pericyte-endothelial arrangements was performed by manually counting these structures. Each dataset was analysed on a slice-by-slice basis along the pericyte-endothelial borders for the presence of peg-and-sockets. By examining pericyte-endothelial cell boundaries in four retinal capillaries, we determined several compulsory criteria to define peg-and-sockets, which can be either pericyte or endothelial facing. These features must:

- Span across a minimum distance of 200 nm in the z-dimension.
- Contain at least one section where the peg attaches to the cell body
- Transverse the BM.
- Be engulfed by a neighbouring cell.
- Have a minimum transverse extent (width) of 0.07 μm and a minimum longitudinal extent (length) of 0.1 μm .

The criteria for identifying peg-and-socket formations were established to ensure that these structures represent genuine intercellular interactions between pericytes and endothelial cells, rather than incidental morphological convolutions. By setting a minimum distance of 200 nm in the z-dimension and requiring the peg to attach to the cell body and transverse the BM, we aimed to rule out sectioning errors or artefacts that could otherwise resemble these formations. The additional criteria, including minimum transverse and longitudinal extents, were put in place to differentiate peg-and-socket formations from other cell membrane deformations, ensuring that only clear, significant interactions between the two cell types were included in the analysis.

2.6.2 Qualitative assessment of NVU changes

In the qualitative assessment of NVU changes, specific criteria were established to systematically analyse electron micrographs across all analysed capillaries. The criteria for the separation of the basement membrane from both endothelium and pericytes were defined as follows:

2.6.2.1 Separation of basement membrane criterion

The criteria for BM separation from neighbouring cells were carefully designed to distinguish real separations from artefacts caused by sample preparation. Requiring a minimum distance of 200 nm in the z-dimension helps to ensure that the separation is not a result of minor indentations or sectioning errors, which may create the illusion of separation. Additionally, setting a minimum width of 20 nm ensures that the separation is substantial enough to be meaningful in the context of structural analysis, rather than incidental or superficial. The electron lucent appearance and the requirement for continuity further reinforce that the separation observed is a true detachment from the BM, as opposed to a partial or inconsistent gap.

2.6.2.1.1 Basement membrane separation from endothelium

- Electron lucent appearance
- Presence observed between endothelial to basement membrane (BM) space
- Spans across a minimum depth of 200 nm in the z-dimension
- Minimum width of 20nm
- Areas absent of BM because of peg and sockets/pericyte coverage are not considered.
- No break or interruption in the continuity of a separation for a minimum of 200nm

2.6.2.1.2 Basement membrane separation from pericytes

- Electron lucent appearance
- Presence observed between pericyte to BM space.
- Spans across a minimum depth of 200 nm in the z-dimension
- Minimum width of 20nm
- No break or interruption in the continuity of a separation for a minimum of 200nm

Additionally, electron-lucent tubules were identified within the endothelium, traversing its structure. These tubules, appearing as white, electron-lucent holes, varied in size and did not open on either side. The criteria for assessing endothelial tubules were defined as follows:

2.6.2.2 Endothelial tubules criterion

For the endothelial tubules, the criteria were set to differentiate these structures from other features, such as endothelial projections. By requiring that the tubules have a minimum width of 60 nm and a depth of 200 nm in the z-dimension, and ensuring they do not contain any material inside, aimed to avoid mistakenly identifying other structures as tubules. The rounded shape and lack of opening on either side are crucial to prevent confusing these electron-lucent tubules with enveloping endothelial projections or other artefacts. These criteria were intended to ensure a clear and accurate identification of endothelial tubules throughout the study.

- Electron lucent appearance
- Must not form as a result of an endothelial projection
- Contains no matter inside gap on any section where it is present
- Spans across a minimum depth of 200 nm in z-dimension
- Minimum width of 60nm
- Sustains rounded shape throughout 3D depth ensuring no opening on a section from either side of the endothelial membrane.
- Traversing the cytoplasm of the endothelium in either direction

These criteria serve as a robust framework for the consistent and thorough qualitative evaluation of NVU changes observed in the electron micrographs, contributing to the reliability and uniformity of the analysis across all examined capillaries.

2.6.3 Quantitative assessment of NVU changes

2.6.3.1 Basement membrane thickening

A BM specific MATLAB script was tailored for the quantitative analysis of BM thickness across a 3D image stack. After user selection of a TIFF file representing the stack, the script applies binary conversion, distance transform, and skeletonisation to focus on the BM material. Thickness information is extracted and visualised for each image slice, including plots of the skeleton image, distance transform, and thickness result. The script calculates and presents the mean and maximum thicknesses across the specified slice range, offering insights into the spatial variations of BM thickness. The methodology involves parameter configuration, initialisation, a main loop for image

processing, and subsequent thickness analysis. Visualisations include trends in mean thickness and an example thickness distribution. Overall, this script contributes a systematic approach to understanding BM thickness dynamics in a 2D image stack (**Figure 2-2**).

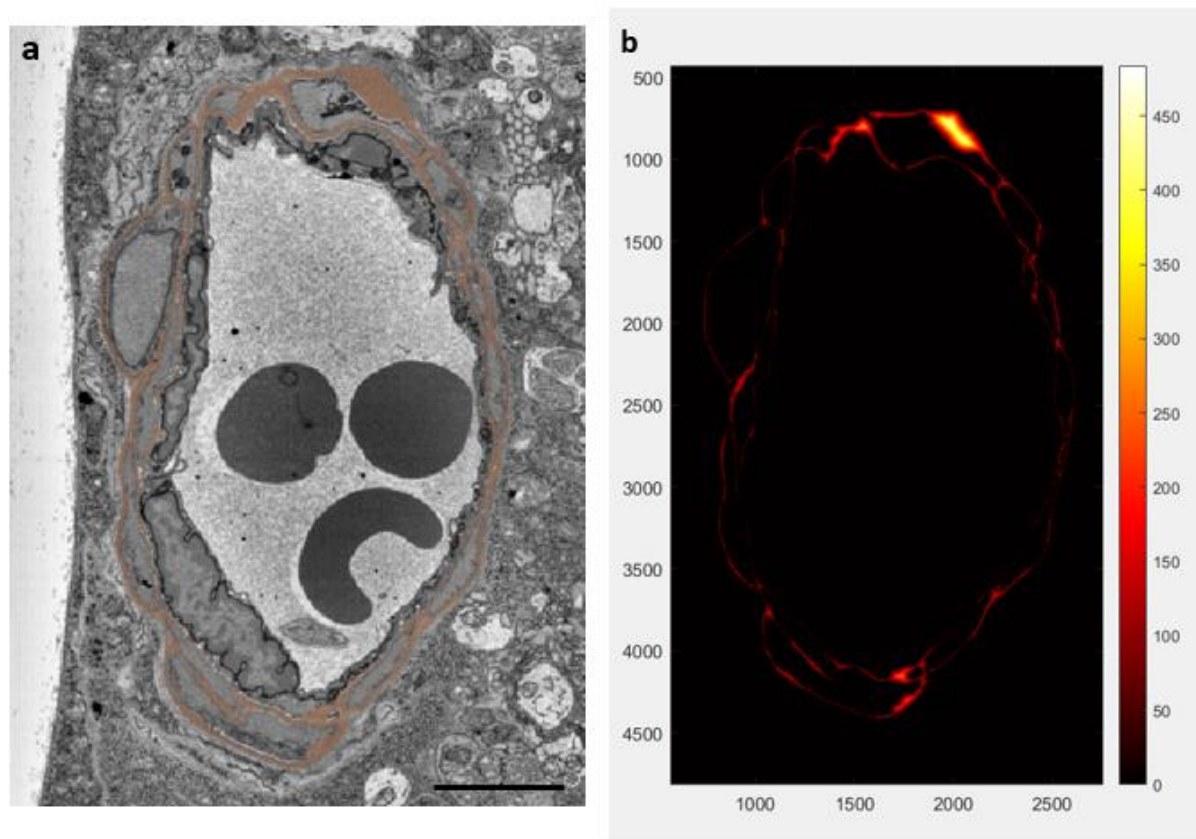


Figure 2-2 Analysis of maximum BM thickness dynamics. A detailed representation of BM thickness variation serves as an illustrative example to elucidate the methodology employed. a. Raw data image highlighting an area of BM thickening (BM segmented in brown). B. Colour graph illustrating the thickness variation across the analysed region. The colour intensity reflects the thickness, with more intense colouring, and cooler tones (yellow-white) indicating thicker basement membrane region. Scale bar 4 μm ..

2.6.3.2 Distances from basement membrane

In-plane minimal distances between the boundaries of all pairwise combinations of intercellular and cellular-BM features were analysed to assess proximity from the basement membrane (BM) to the endothelium, pericytes, and cells surrounding the vasculature. The analysis was performed using MATLAB (MATLAB ver. R2021b). For each image slice and feature pair, two minimal distance histograms were generated. One histogram contained the minimal distances from each boundary pixel of the BM to the nearest boundary pixel of the endothelium, pericytes, or surrounding cells,

and the other contained the minimal distances in the opposite direction. Specifically, distances from each boundary pixel in the second feature of the pair (endothelium, pericytes, or surrounding cells) to the nearest boundary pixel of the BM.

The proximity histograms for each feature pair were consolidated into a mean proximity histogram, utilising all data in the image stack. Cumulative distribution functions were then calculated for each mean proximity histogram. These functions assess the total percentage of boundary pixels that lie within a given distance between the BM and each feature pair, including the endothelium, pericytes, and cells surrounding the vasculature.

To mitigate the potential for multiple measurements for BM distances when assessing BM-endothelium proximity given the intricate and convoluted nature of the BM and its encompassing of pericytes, a manual segmentation of the area where the BM starts and pericytes coexist was performed (**Figure 2-3**). This allowed for a direct comparison of BM-endothelial separation. However, this segmentation step was deemed unnecessary for BM to pericytes, as the BM does not exhibit multiple isolated regions in this context.

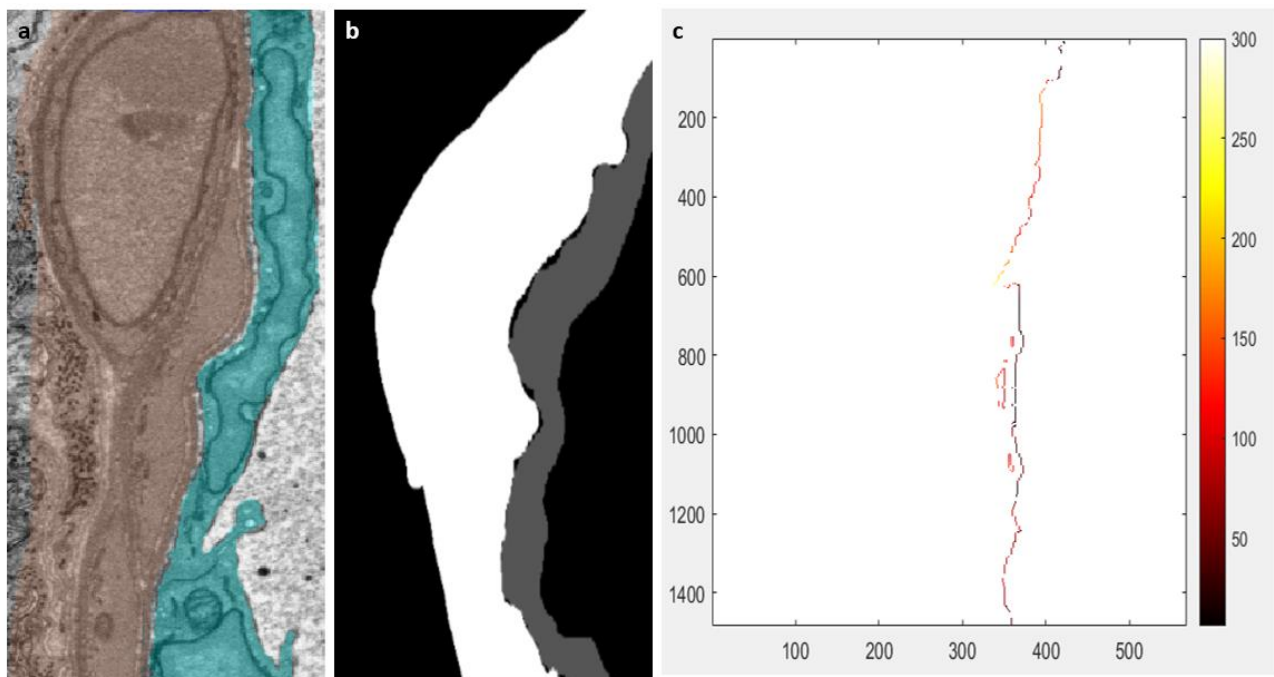


Figure 2-3 Spatial analysis of basement membrane proximity to endothelium and pericytes. This figure presents a comprehensive analysis of the BM in relation to endothelium. a. raw data segmentation highlights the manual delineation of the BM (brown) and endothelium (aqua), capturing the intricacies of their spatial interactions. b. provides a pre-analysis snapshot of the materials, offering a baseline view before undergoing proximity analysis. c. depicts the results

of the analysis with coloured lines, representing points in the materials that are closest (warmer colours) and furthest (cooler colours) from each other.

SBF-SEM work-flow

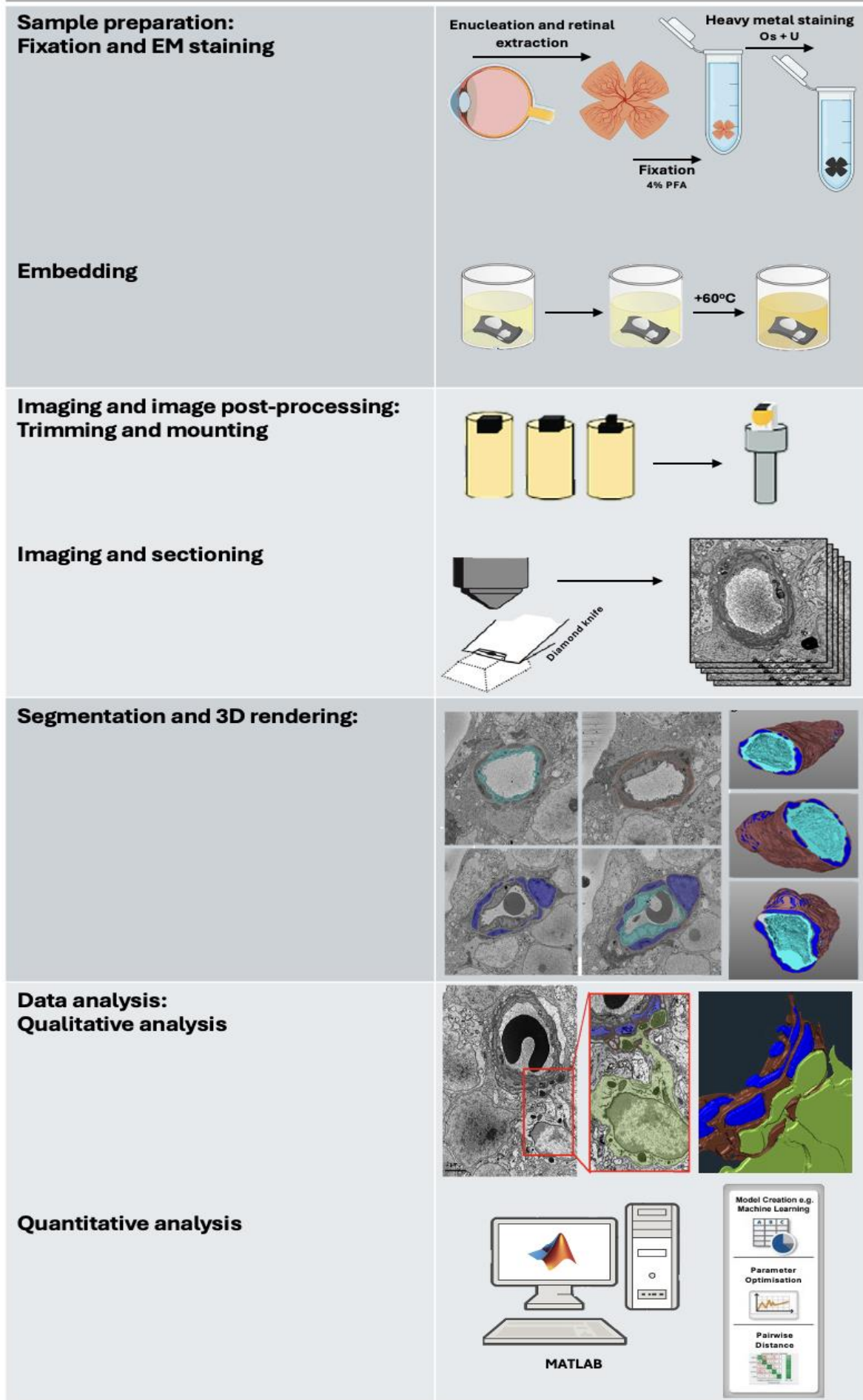


Figure 2-4 SBF-SEM Workflow for Retinal Tissue Imaging and Analysis. The figure illustrates the key steps involved in the SBF-SEM process used for retinal tissue preparation, imaging, and data analysis. Sample preparation - Fixation and EM staining: Retinal tissue is extracted through enucleation, followed by fixation using 4% paraformaldehyde (PFA). The tissue is then subjected to heavy metal staining with osmium tetroxide (Os) and uranyl acetate (U) to enhance contrast for electron microscopy. Embedding: The stained retinal samples are embedded in resin and heated to 60°C to harden. This step ensures that the sample is preserved for imaging and can be sectioned without damage. Imaging and image post-processing - Trimming and mounting: The embedded sample blocks are trimmed and mounted for imaging. Serial sectioning is performed using a diamond knife to create thin sections for electron microscopy. Imaging and sectioning: The tissue block is imaged using SBF-SEM, where each slice is sequentially sectioned and imaged. This generates a stack of high-resolution images. Segmentation and 3D rendering: The image stack undergoes segmentation, where individual structures of interest (e.g., pericytes, BM, endothelium) are identified and delineated. This data is then used to generate 3D reconstructions of the tissue's microarchitecture. Data analysis - Qualitative analysis: The segmented 3D structures are analysed qualitatively, allowing for detailed examination of the heterocellular components. Regions of interest are highlighted, facilitating comparison of different structural features. Quantitative analysis: Quantitative analysis is conducted using computational tools including MATLAB. Parameters such as pairwise distance and sphericity including machine learning techniques, are used to assess structural features and quantify key metrics for further analysis.

2.7 Statistics

Statistical analyses were performed to assess the significance of observed differences in various parameters related to the retinal NVU between different experimental conditions. All statistical analyses were conducted using GraphPad Prism software, and the significance level was set at $p < 0.05$.

2.7.1 T-test (unpaired)

Before applying the unpaired t-test, it was essential to verify that the data met the assumptions required for this parametric test, specifically the assumption of normality. To assess the normality of the data, a Shapiro-Wilk was performed. To evaluate differences between two independent groups, the unpaired t-test was employed. This test is particularly suitable for comparing means of two groups, making it well-suited for the comparative analyses. The unpaired t-test assesses

whether the means of two groups are significantly different from each other, considering the variability within each group.

For each observation, the appropriate datasets were selected, and unpaired t-tests were performed to determine if there were statistically significant differences between groups. This analysis was applied to various aspects of the retinal NVU, including but not limited to morphological features, distances between cellular components, and quantitative measurements derived from the three-dimensional reconstructions.

2.7.2 Standard deviations

Standard deviations were calculated to quantify the amount of variability or dispersion within each dataset. These measures of variability provided insights into the consistency or spread of data points around the mean. The inclusion of standard deviations in the analyses enhanced the robustness of the statistical assessments, allowing for a more comprehensive interpretation of the results.

The application of the unpaired t-test in conjunction with standard deviations ensured that observed differences were not only statistically significant but also considered in the context of the data's variability. This comprehensive statistical approach contributed to the reliability and validity of the findings.

Chapter 3 Mouse Retinal Neurovascular Unit

This chapter delves into the intricate structural characteristics of the NVU within non-diabetic mouse retinal capillaries. Employing the cutting-edge imaging technique, SBF-SEM, the investigation unveils the complex interactions among key NVU components.

3.1 Introduction

The NVU refers to the physical and functional relationship among the capillary blood-vessel endothelial cells, pericytes, macroglia (Müller glia and astrocytes), microglia and neurons (ganglion cells, bipolar cells, horizontal cells and amacrine cells) of the retina (Simó & Hernández, 2014). Collectively, the cells of the NVU play a key role in the maintenance of the inner blood retinal barrier, in mediating cell-to-cell survival via paracrine signalling, and in matching blood flow to the metabolic needs of the retina through a process known as neurovascular coupling (Duh et al., 2017; Metea & Newman, 2007). The latter is particularly important given the absence of autonomic innervation in the retina (Ye *et al.*, 1990). Despite advances in our understanding, several aspects of the NVU's function and dysfunction remain elusive. The mechanisms driving the intricate interplay between the NVU's components and how these relationships are altered under stress or disease conditions are not fully understood. Disruption of the integrity of the retinal NVU has been implicated in the pathogenesis of several retinal diseases, including diabetic retinopathy, glaucoma and retinal neurodegenerative disorders (Ivanova et al., 2019; J. Lechner et al., 2017; Weinreb et al., 2014). Despite this, the three-dimensional ultrastructure of the retinal NVU remains to be fully characterised and quantitative methods for describing its key features have yet to be developed.

The retinal NVU in mice and humans has been previously analysed in two-dimensions at the ultrastructural level using conventional TEM (Fehér et al., 2018; van der Wijk et al., 2018). While this technique has provided valuable information on its structure, a greater understanding of the anatomical arrangements of the different cellular components, and their possible heterocellular interactions, it necessitates analysis in three-dimensions with nanometre spatial resolution, which until now, has not been fully elucidated.

The research in this chapter seeks to provide a comprehensive overview of the NVU within the mouse retina, exploring the complex interactions among its components through SBF-SEM imaging, outlining the ultrastructure of the NVU and its heterocellular relationships in 3D. To achieve this,

the study focuses on 3-month and 6-month timeframes, which map onto early adulthood and middle age in mice, corresponding to approximately 20–30 and 40–50 human years, respectively. These timepoints were selected to examine both healthy aging processes and early disease-related changes.

The 6-month timepoint was chosen as an optimal comparison between health and disease states. While the study of older mice (15–18 months) could provide deeper insights into aging, our preliminary experiments involving STZ-induced diabetes in mice older than 9 months revealed increased frailty and high mortality rates, rendering these timepoints less feasible. Consequently, 6 months was identified as the best compromise, allowing us to balance healthy aging and the onset of disease without the confounding effects of excessive mortality.

3.2 Retinal Ultrastructure

Retinal tissue samples were obtained from 3-month and 6-month-old non-diabetic mice, focusing on the superficial capillary plexus within the GCL. Stacks of 100-300 consecutive micrographs of the capillary ultrastructure were captured across the lengths of the vessel, covering depths from 12 to 36 μm . Predominantly, the analysis was anchored on the samples from the 3-month-old mice, with four capillaries thoroughly examined. The ultrastructure of these capillaries at 3 months is depicted in **Figure 3-2 -Figure 3-4**. Additionally, to enrich our understanding and identify potential age-dependant changes, analyses of capillaries from 6-month-old mice, examining a total of nine capillaries were included. The ultrastructural features from these 6-month-old mice are described in section **3.6**.

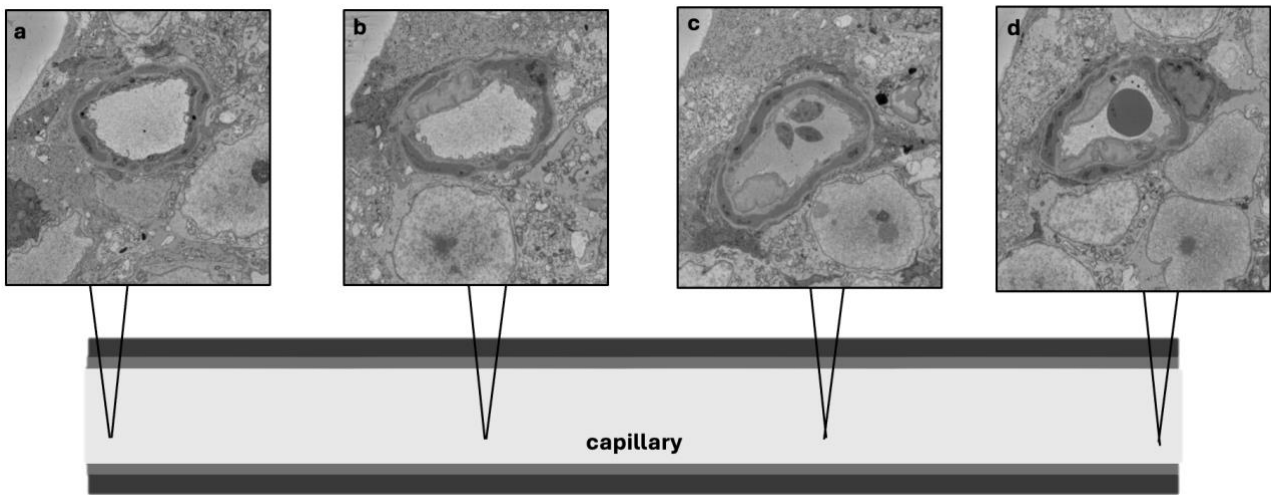


Figure 3-1 SBF-SEM micrographs displaying cross-sections taken at different depths along a mouse retinal capillary. A series of SBF-SEM micrographs illustrating cross-sectional images taken from specific depths along a mouse retinal capillary. The schematic at the bottom highlights the locations from which each section (a–d) was obtained along the capillary’s length. (a): Section 1 ($0.12\ \mu\text{m}$), representing the surface of the capillary. (b): Section 50 ($6\ \mu\text{m}$), taken from deeper within the capillary. (c): Section 100 ($12\ \mu\text{m}$), showing a mid-depth cross-section. (d): Section 120 ($15.6\ \mu\text{m}$), taken from a deeper section towards the base of the capillary.

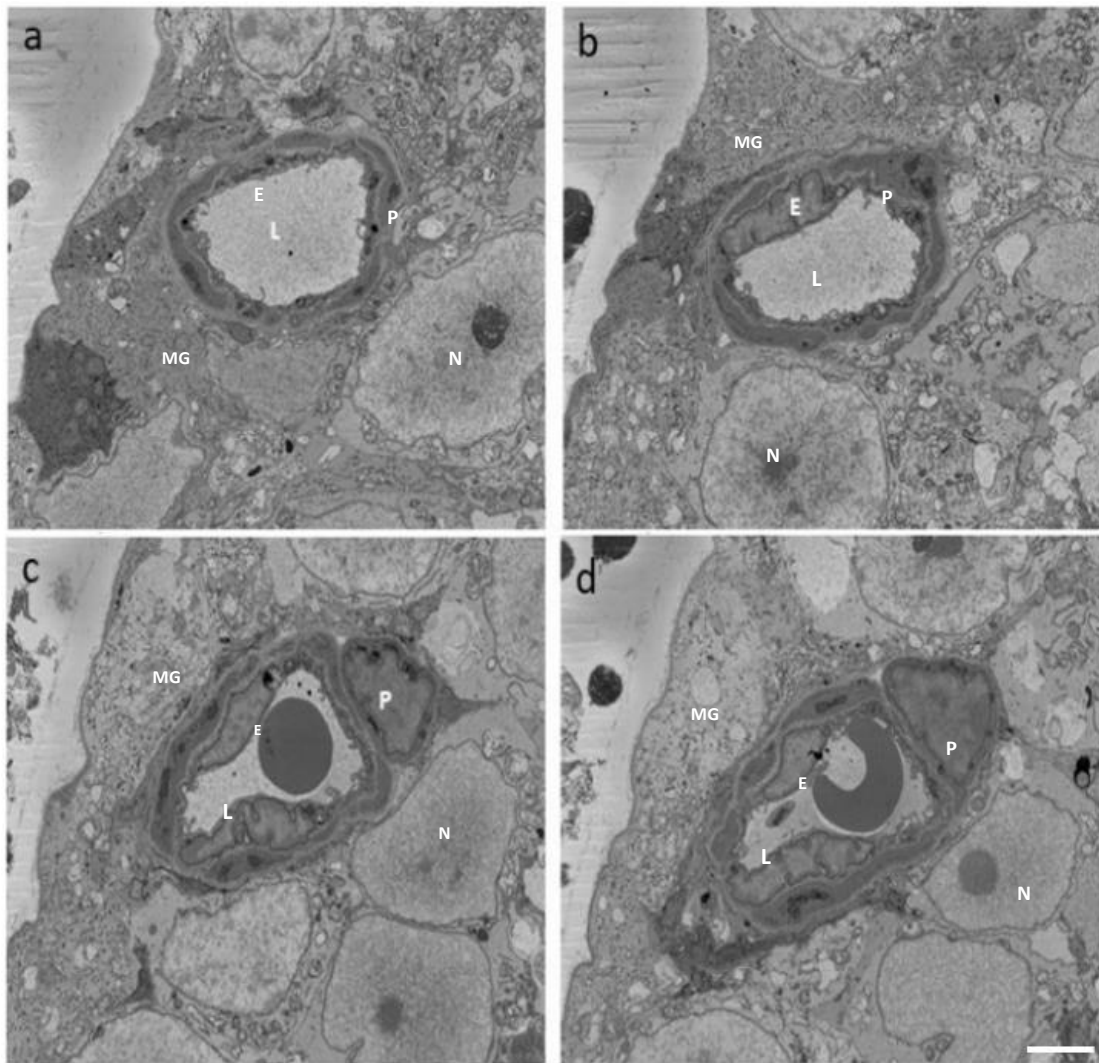


Figure 3-2 Ultrastructure of 3-month old mouse capillary 1. A collection of SBF-SEM micrographs taken from a mouse retinal capillary to display the morphological changes along the capillary length. a, slice 1 (0.12 μm), b, slice 50 (6 μm), c, slice 100 (12 μm) and d, slice 120 (14.4 μm), Lumen: L, Pericytes: P, Endothelium: E, Macroglia: MG, Neurons: N. Scale bar 3 μm . Full dataset can be found here: <https://figshare.com/s/20fbbd90d386a8938a4f>.

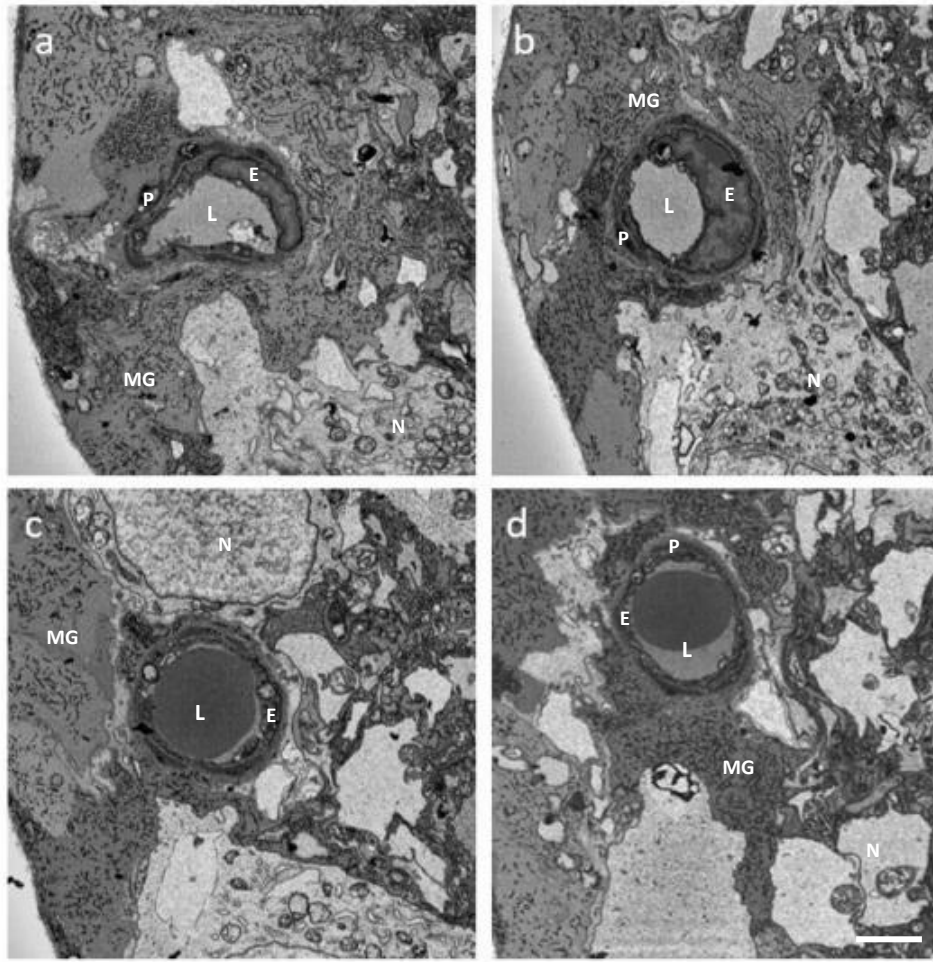


Figure 3--3 Ultrastructure of 3-month old mouse capillary 2. A collection of SBF-SEM micrographs taken from a mouse retinal capillary to display the morphological changes along the capillary length. a, slice 1 (0.10 μm), b, slice 50 (5 μm), c, slice 100 (10 μm) and d, slice 150 (15 μm). Lumen: L, Pericytes: P, Endothelium: E, Macroglia: MG, Neurons: N. Scale bar 2 μm . Full dataset can be found here: <https://figshare.com/s/b8b2f33da20ab5688768>

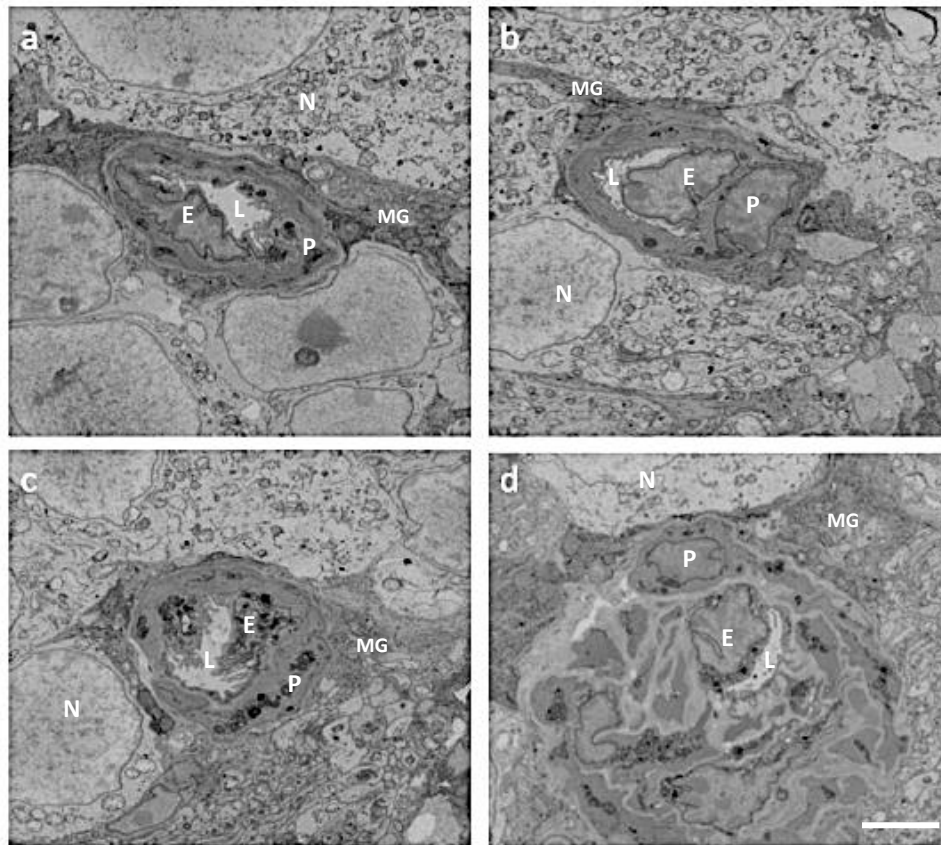


Figure 3-4 Ultrastructure of 3-month old mouse capillary 3. A collection of SBF-SEM micrographs taken from a mouse retinal capillary to display the morphological changes along the capillary length. a, slice 1 (0.12 μm), b, slice 50 (6 μm), c, slice 100 (12 μm) and d, slice 150 (18 μm). Lumen: L, Pericytes: P, Endothelium: E, Macroglia: MG, Neurons: N. Scale bar 2 μm . Full dataset can be found here: <https://figshare.com/s/885aea53a0a501803620>

3.2.1 Ultrastructural Features of the NVU

SBF-SEM images provide an unprecedented level of detail in visualising the mouse retinal NVU at the nanoscale level in three-dimensions. Key to characterising the different cell types, the identification of all cellular components within the NVU is via the detailed observation of their plasma membranes in the images. These plasma membranes appear as thin, electron-dense outlines, enabling the precise differentiation and segmentation of each cell type (**Figure 3-5**). The capillary vasculature, an integral part of the NVU within the retina, consists of three primary components: endothelial cells, pericytes, and the basement membrane. These elements are intricately interwoven with surrounding cellular and neural components, establishing a complex yet essential network for retinal function.

Endothelial cells, the innermost layer of cells forming the capillary walls, are characterised by their flattened, elongated morphology, forming a tight lining along the inner surface of the capillary lumen. Pericytes, located external to the endothelial cells, ensheath the capillaries. Pericytes are closely associated with the endothelial cells, extending multiple cellular processes along the capillaries. The BM surrounds the endothelial cells and pericytes. This thin, electron-dense layer provides structural support and serves as a barrier between the vascular and neural compartments of the retina. Predominantly, the characterisation of the capillary vasculature components; pericytes, BM, and endothelial cells, were based on their specific location within the capillary network. Each feature of the NVU was segmented for easy identification of cell types, visualisation, and 3D reconstruction, with endothelial cells assigned an aqua blue colour, royal blue for pericytes, and brown for the basement membrane (**Figure 3-6, Figure 3-7**).

In addition to these essential vascular components, SBF-SEM images allow the observation of the presence and location of macroglia and neurons within the retinal tissue. Research has shown that macroglia, specifically including astrocytes and Müller cells, are prominent glial cells in the retina. Astrocytes extend their processes towards the retinal vasculature, appearing as fine cell endings, dense, and elongated processes radiating outward from a central cell body and their processes embrace and ensheath capillaries, creating a supportive network around the vessels. The fine branching of these processes is visible, emphasising their close interaction with the vasculature. Müller cells, which traverse the entire thickness of the retina appear as larger, columnar or radial cells, electron-dense in micrographs, with an abundance of microfilaments present within the cell body. SBF-SEM reveals the intricate interactions of astrocytes and Müller cells with the capillaries, highlighting their involvement in the NVU, however, it's important to note that it is difficult to differentiate between astrocytes and Müller glia based on the raw SBF-SEM images alone. This difficulty primarily arises due to the limited depth of capillary capture in data collection, which often does not include the entirety of the astrocyte nucleus. As the astrocyte nucleus is a key feature for accurately identifying these cells, its absence in partial capillary segments complicates definitive identification. To address this issue, macroglia were grouped together under the general category but if an astrocyte nucleus was clearly present and visible in the dataset, then the cell was specifically characterised and segmented as an astrocyte. For the segmentation and 3D reconstruction, macroglia were coded in shades of reds, while astrocyte in purple. Neurons within the retina form the neural tissue that is essential for visual processing. In electron micrographs,

neurons appear as electron-lucent in micrographs due to the lighter staining and relatively less electron-dense composition of their cellular components and were segmented in shades of green.

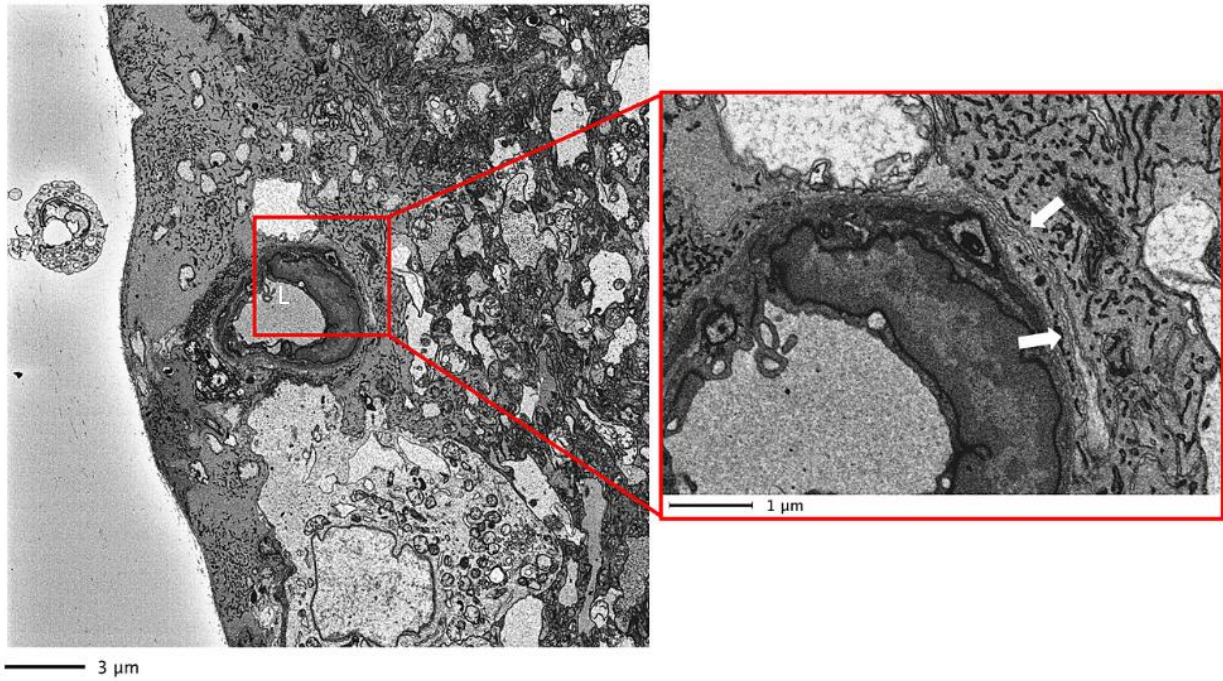


Figure 3-5 Identification of cells from plasma membrane outlines. White arrows indicate plasma membrane outline separating the different cell types.

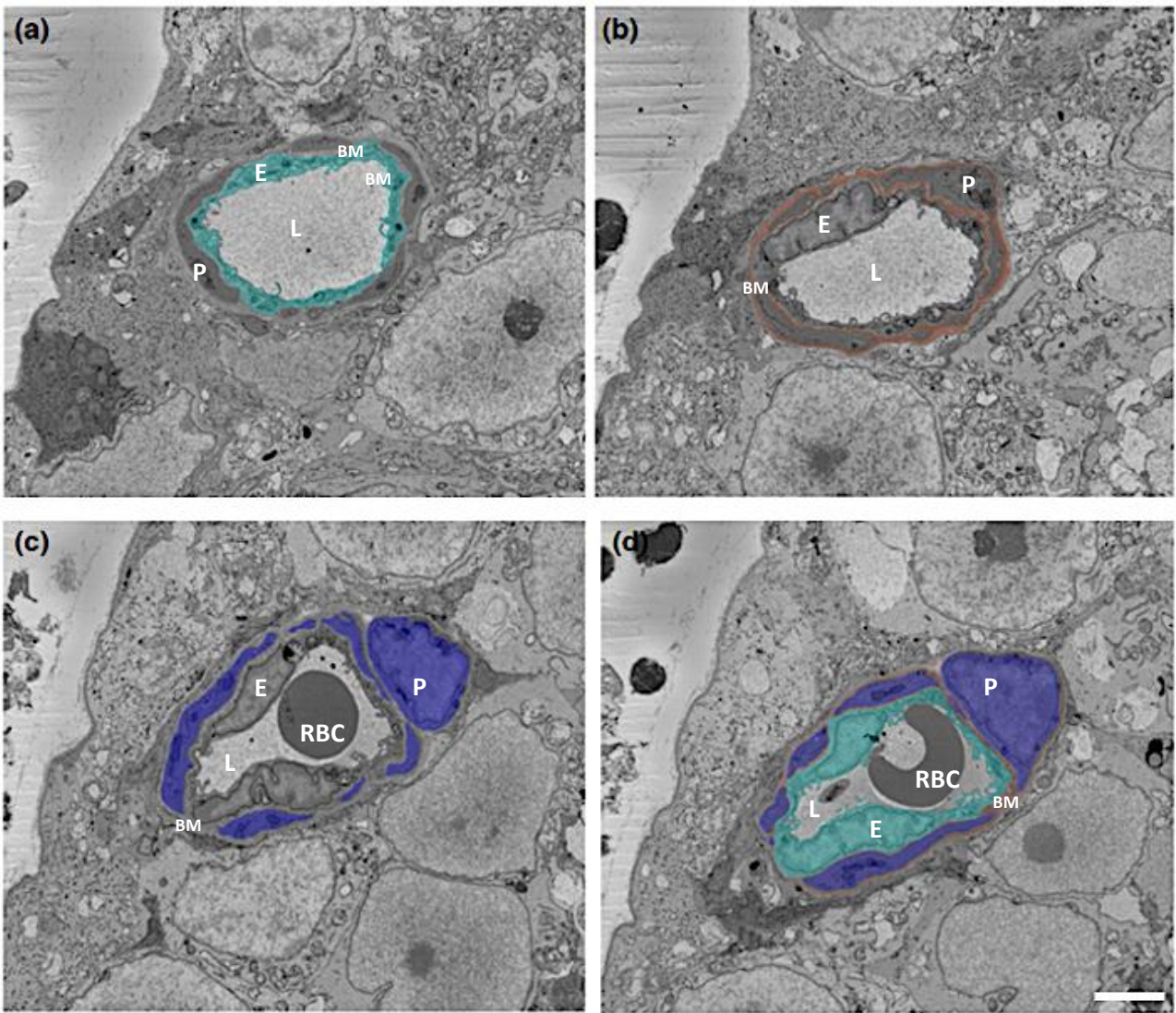


Figure 3-6 Segmented vasculature of 3-month old mouse. The vasculature was identified, and each component was assigned a colour for segmentation through the data stack and subsequent visualisation in 3D reconstructions. a, endothelium, E (aqua), b, basement membrane, BM (brown), c, pericytes, P (blue) d, complete vasculature. RBC, red blood cell. Scale bar 3 μm.

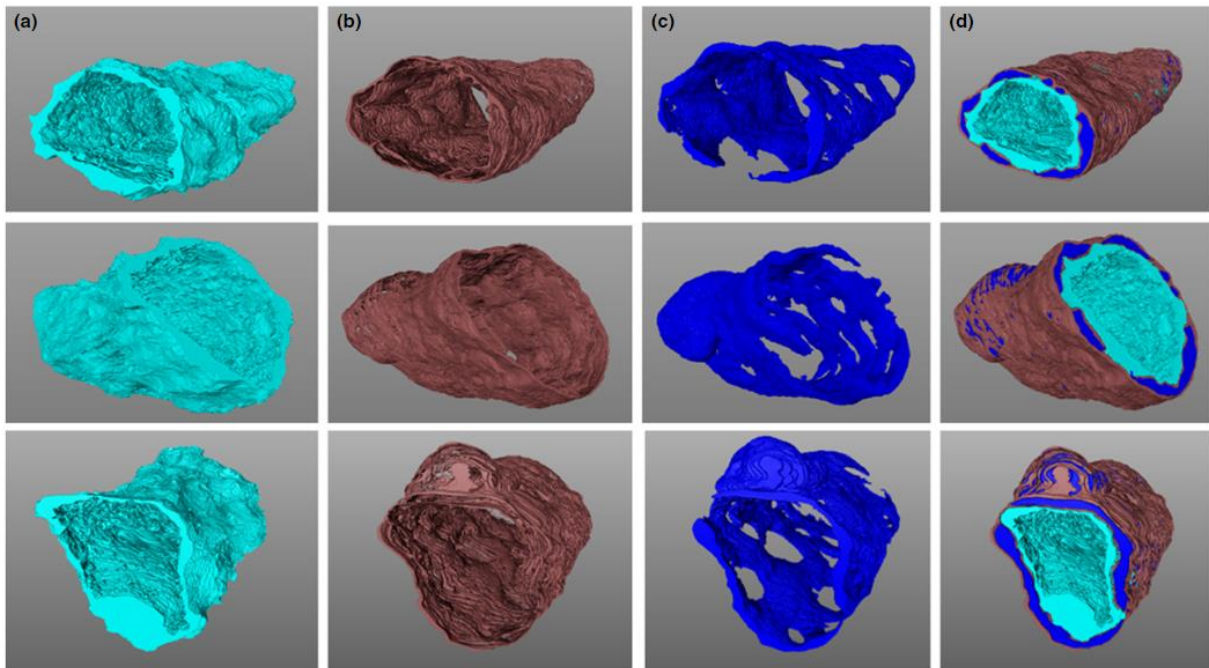


Figure 3-7 3D reconstruction of 3-month-old mouse capillary vasculature. Displayed are features associated with a 3D reconstruction of the vasculature of capillary 1. Column a: endothelium (aqua); column b: basement membrane (brown); column c: pericytes (blue); and column d: combined vasculature.(a)(b)(c)(d). Full 3D animation can be found here: <https://figshare.com/s/43603b11f3fa1bab9886>

3.2.1.1 Endothelial projections

The endothelium has an intricate textured surface which lines the outer surface of the lumen. Adding a layer of complexity to its structural profile, the endothelium surface forms a profusion of finger-like projections, described as endothelial projections. These projections consistently extend into the lumen and are uniformly present on the inner surface of the endothelium. Endothelial projections vary in dimensions, with lengths ranging from approximately 100 nm to widths of 50 nm (**Figure 3-8**). See section 4.2.5 for details on quantification of endothelial projection abundance.

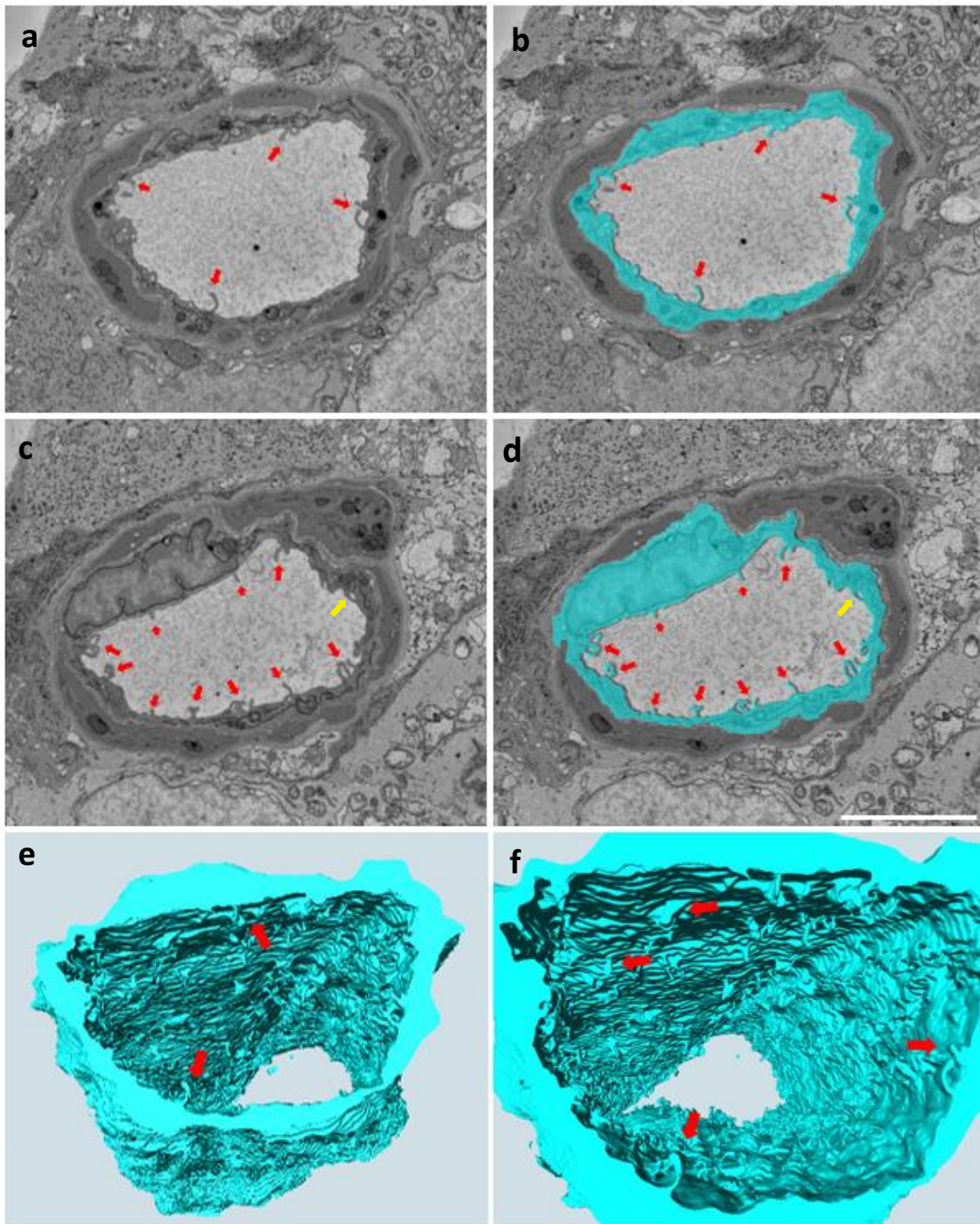


Figure 3-8 3D reconstruction of endothelial projections. Illustration of endothelial projections within a capillary. a. presents the raw data of a section 1 of the dataset, capturing the intricate details of the endothelial structure. b. the segmentation of section 1, highlights the endothelial projections. c. deeper along the capillary to section 50, displays the raw data, providing insights into variations along the capillary length but consist observations of endothelial projections. d. segmentation of section 50. For a holistic perspective, panels e. and f. present 3D

reconstructions of the endothelium, providing a 3D visualisation of the endothelial structure and projections. Red arrows indicate endothelial projections, yellow arrows indicate double stranded projection. Scale bar 4 μm .

3.2.1.2 Endothelial tubules

The endothelium forms the lining of the capillary lumen. SBF-SEM images revealed the presence of electron-lucent tubules within the endothelium (**Figure 3-9**). These tubules, which span across a minimum depth of 200 nm in the z-dimension and have a minimum width of 60 nm, appear as white, electron-lucent holes in the endothelial structure, exhibiting variations in size. They traverse the endothelium, providing a distinctive visual pattern. Intriguingly, these tubules do not open on either side, indicating that they do not form conventional channels within the endothelium. This observation was consistently noted in assessments of endothelium from both 3-month and 6-month-old capillaries, underscoring the structural persistence of these features over time.

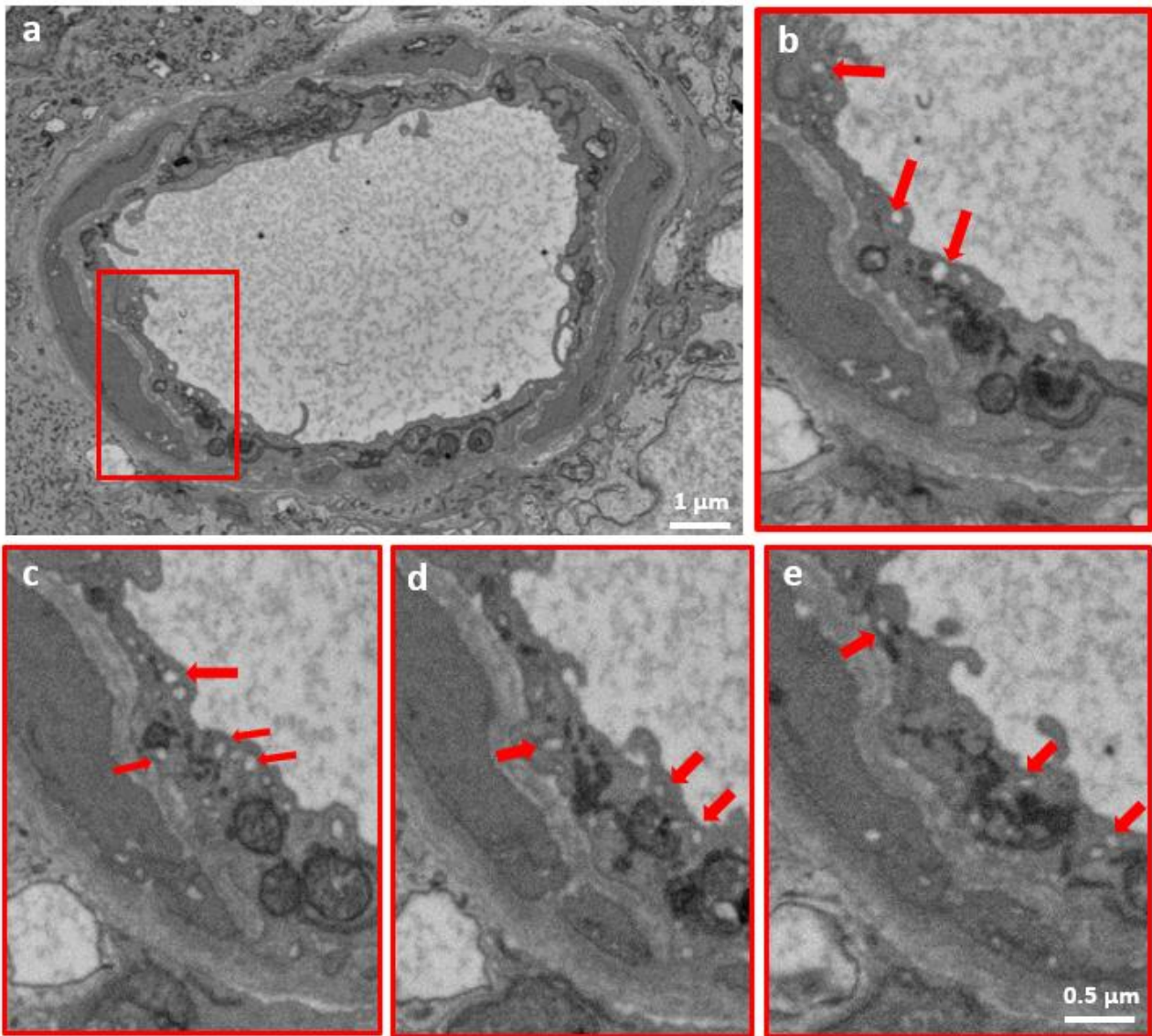


Figure 3-9 Endothelial tubules from non-diabetic mouse capillary. a. Presents an overview of the capillary with a focus area highlighted in red. b – e. provide magnified views of the specified region as consecutive slices 1 -4, showcasing the presence of electron-lucent tubules (indicated by red arrows).

3.3 Pericyte-endothelial interactions

A heterocellular interaction observed along the vessel was the communication between pericytes and endothelial cells. The BM wraps around the abluminal endothelium and pericytes, forming a barrier separating the two cells. However, along the capillary length gaps in the BM were observed allowing pericytes and endothelial cells to come into closer contact, bridging the structural divide imposed by the BM. These interactions were of two types, namely, direct contact points (**Figure 3-10**) and peg-and-socket type contact areas. In direct contact interactions, pericytes and endothelial cells

come into direct physical contact. This occurs when the pericyte and endothelial cell membranes are touching each other in the absence of the BM. In peg-and-socket type interactions, a protrusion from one cell breaks through the BM to contact a neighbouring cell (**Figure 3-11**). This interaction mechanism allows for a more complex form of communication between pericytes and endothelial cells. The pericyte or endothelial cell membrane was observed to protrude towards, and be enveloped by, the neighbouring cell plasmalemma. Pericyte protrusions breaking through the BM to contact endothelial cells were more commonly observed. To precisely identify and quantify these interaction types, a semi-automatic verification pipeline analysis was employed (**Figure 3-12**). This analysis involved the use of specialised software and algorithms to examine the electron micrographs and accurate segmentation to confirm the presence of direct contact points and peg-and-socket contact areas. The semi-automatic approach ensures accuracy and consistency in the identification of these interactions, providing valuable data for further study and analysis. Pericyte-endothelial peg-and-socket formations were noted to occur at several points throughout the data stacks of each capillary analysed. Over the depth of 15 μm in each of the capillaries, peg-and-socket formations appeared many times with each formation spanning across several sections. Their distributions are shown in **Figure 3-13**. This suggests the nature of pericyte–endothelial interactions commonly occur in peg-and-socket-like formations.

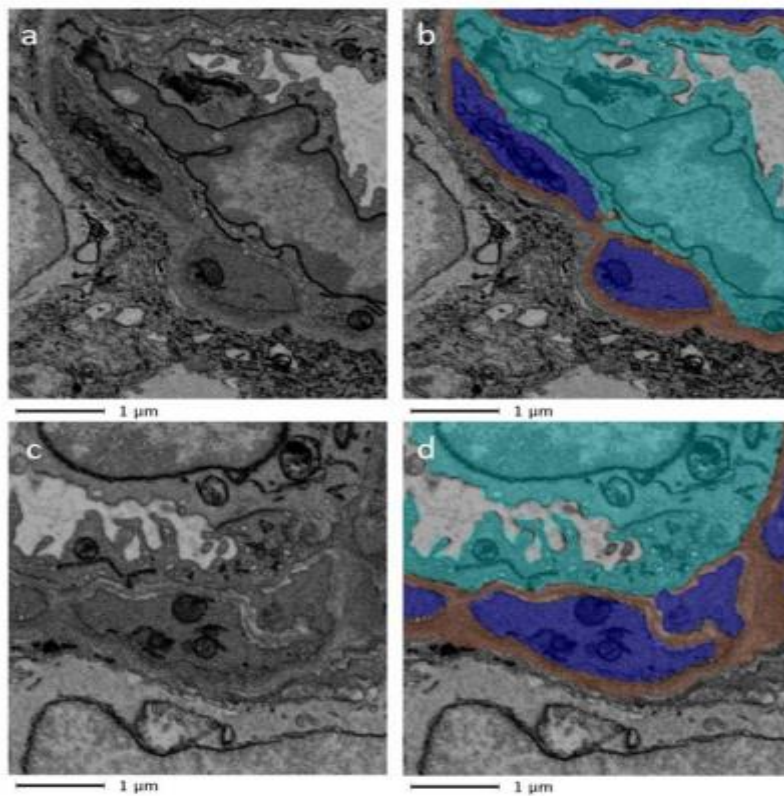


Figure 3-10 Pericyte-endothelial interaction via direct contact. Close contacts of a pericyte (blue) and endothelial cell (aqua) in absence of a bordering BM (brown) are indicated for the raw data (a and c) and segmented data (b and d) of two sections 1.2 μ m apart.

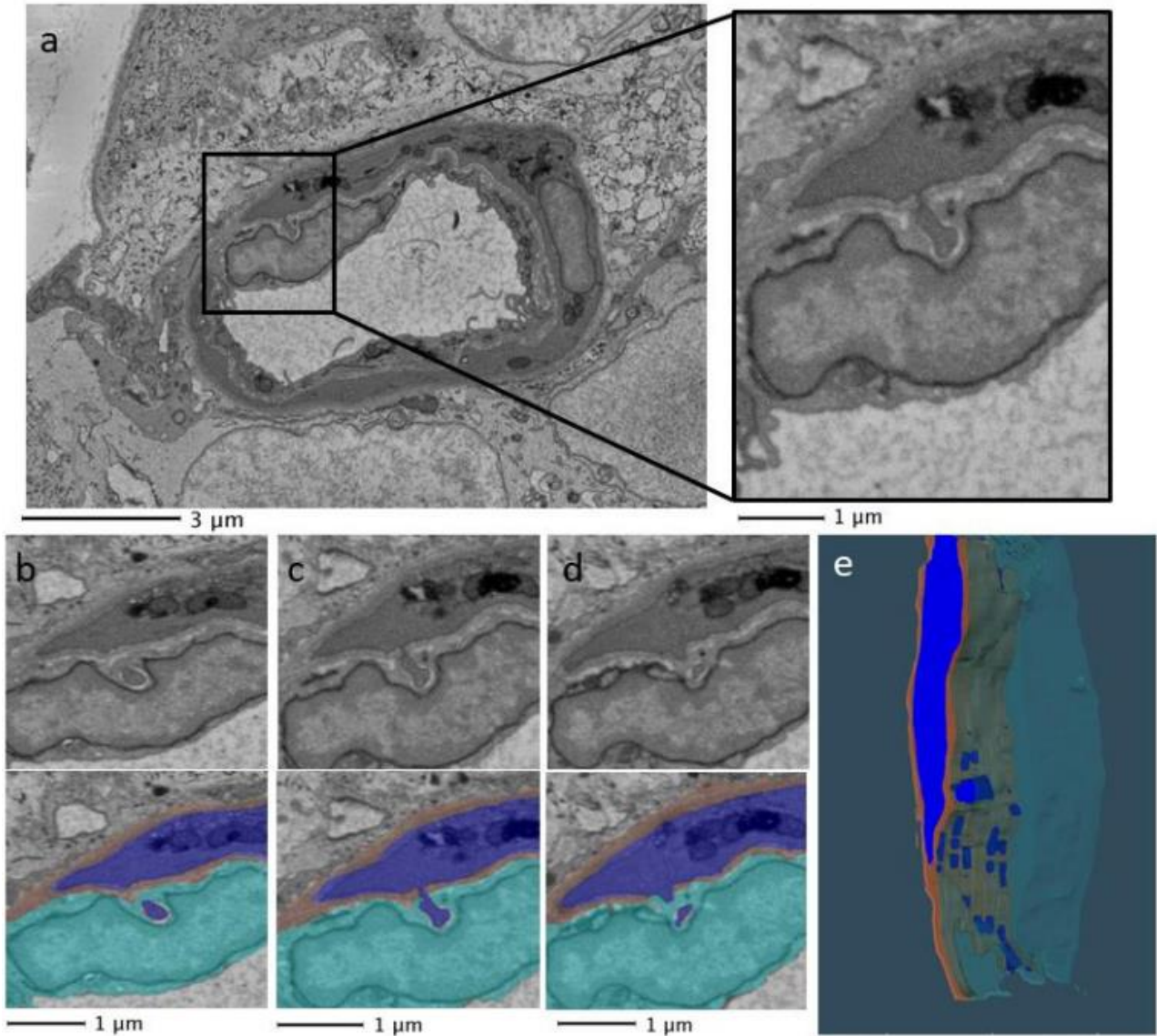


Figure 3-11 Peg-and-socket, pericyte-endothelial formation spanning across multiple sections. a, Peg-and-socket formation identified on a capillary (magnified area evident on right hand side bounded by box). b-d, This peg and socket spanned across three sections (minimum 360 nm). e, displays the 3D nature of peg and sockets. Full 3D animation can be found: <https://figshare.com/s/238d32953dde668ac862>

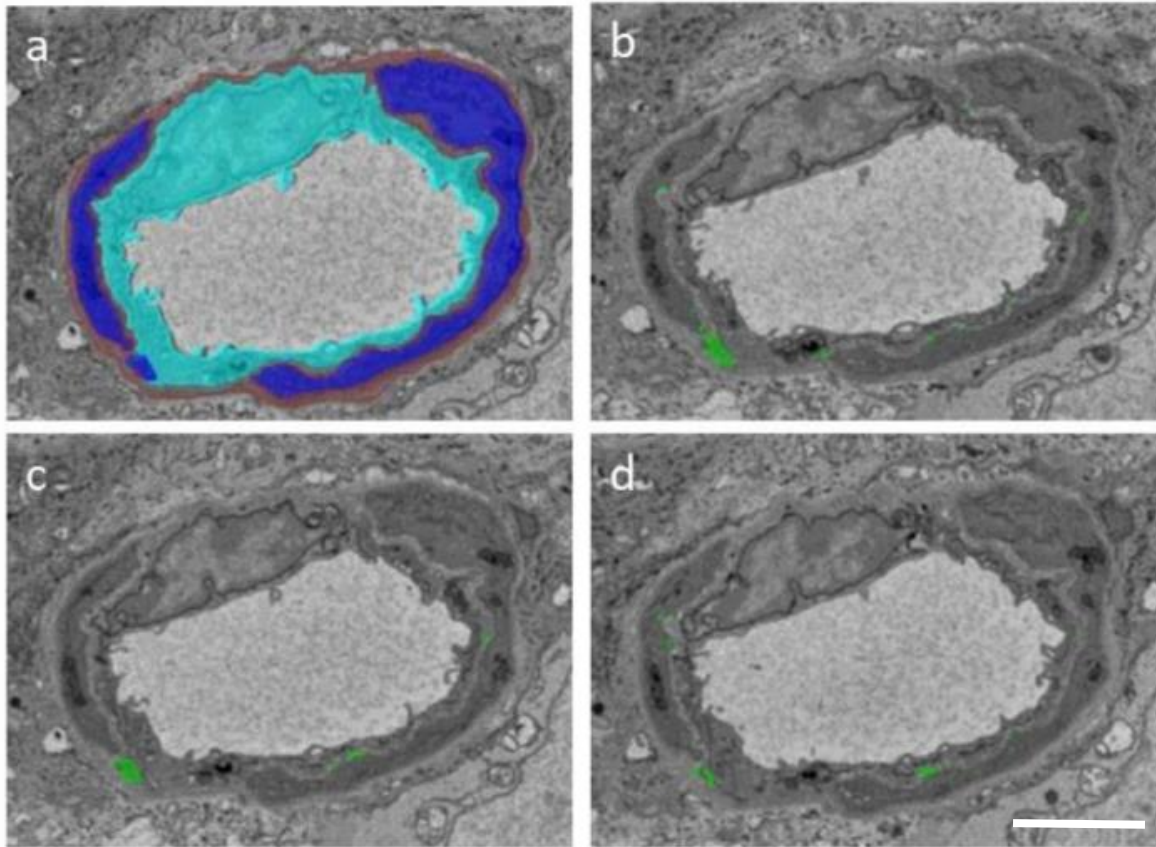


Figure 3-12 Semi-automated detection of pericyte-endothelial interactions. Capillaries were analysed under the Arivis analysis pipeline, which semi-automatically detected endothelial-pericyte closeness via endothelial/pericyte intersect and depicted such occasions in green highlights. Data shown from capillary 1 from which the pipeline assessed all 150 sections. One section (corresponding to section 36) is shown in panels a-d. a) segmented features are endothelium: aqua; basement membrane: brown; pericyte: royal blue. (b)-(d) close contacts are displayed with green elements as quantified in Arivis with user instructed minimal distances of (b) 5 pixels, c) 3 pixels and (d) 1 pixel. Scale bar 3 μm .

Pericyte-endothelial peg-and-socket formations were noted to occur at several points throughout the data stacks of each capillary analysed. Over the depth of 15 μm in each of the 3 month old mouse capillaries and a depth of 13.5 μm for each of the 6 month old mouse capillaries, peg-and-socket formations appeared 2-4 times per micrometer with each formation spanning across several sections (**Figure 3-13**).

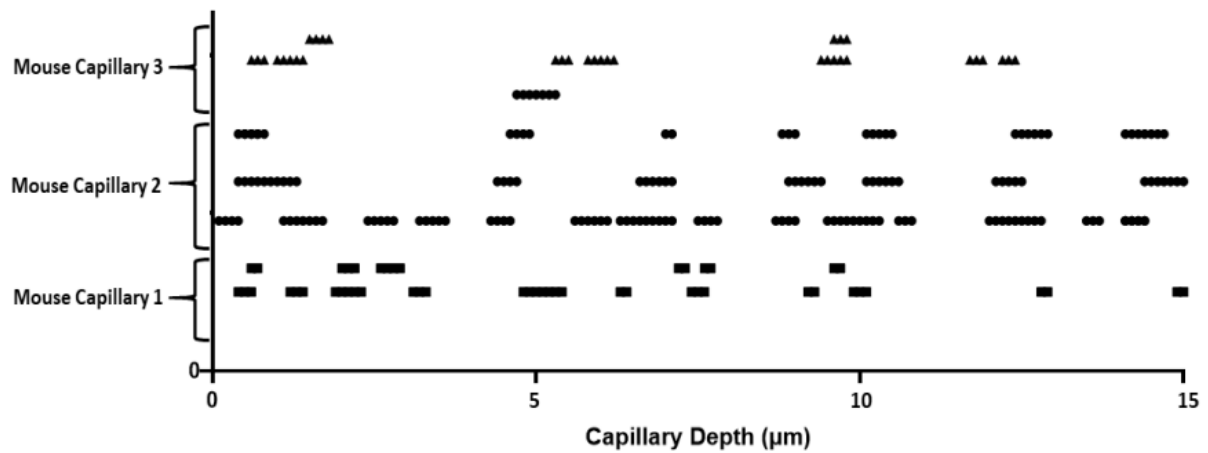


Figure 3-13 Distribution of peg and sockets across 3-month-old mouse capillaries. The distribution of peg- and sockets evident across 150 sections examined in 3 capillaries. Note more than one peg-and-socket may appear in the same sections (i.e. at different points of pericyte-endothelial membrane interaction in the same z-plane).

3.4 Glial cells

3.4.1 Astrocytes and Müller Cells

Glial cells were identified based on their electron dense ultrastructure, radial morphology, and the abundance of microfilaments within their cell body. While some TEM studies suggest astrocytes and Müller glial cells can be differentiated, in SBF-SEM electron micrographs, three distinct categories of electron densities were detected: low, intermediate, and high (**Figure 3-14**). This variation illuminated the fact that relying solely on electron density was insufficient for the accurate classification of macroglia. Consequently, the differentiation of macroglia relied on a comprehensive assessment of their location, morphology, and cellular features. Astrocytes, exhibiting a relatively lower electron density, are exclusively localised in the NFL (Moran *et al.*, 2016). Astrocyte cell bodies are located within the (NFL in close proximity to the capillaries, whereas Müller cell bodies are exclusively situated in the inner nuclear layer INL (Holländer *et al.*, 1991). Given that the imaging was confined to the range between the ILM and the GCL, the presence of a nucleus within any glial cells were conclusively identified as astrocytes. A single astrocyte cell body was identified in the data stack from 3-month old mouse capillary 1 (**Figure 3-15**). This astrocyte closely surrounded the capillary vasculature, exhibiting a star-like morphology (**Figure 3-16**). The astrocyte featured a paler cytoplasm, with darker parallel filaments predominantly located at the proximal segments of its projections surrounding the vasculature. Müller cells too display a cuboidal morphology and

projecting over longer distances, while their cytoplasm exhibited a reticulated pattern with diverse electron densities, there was no indication of the presence of parallel filaments (Figure 3-17).

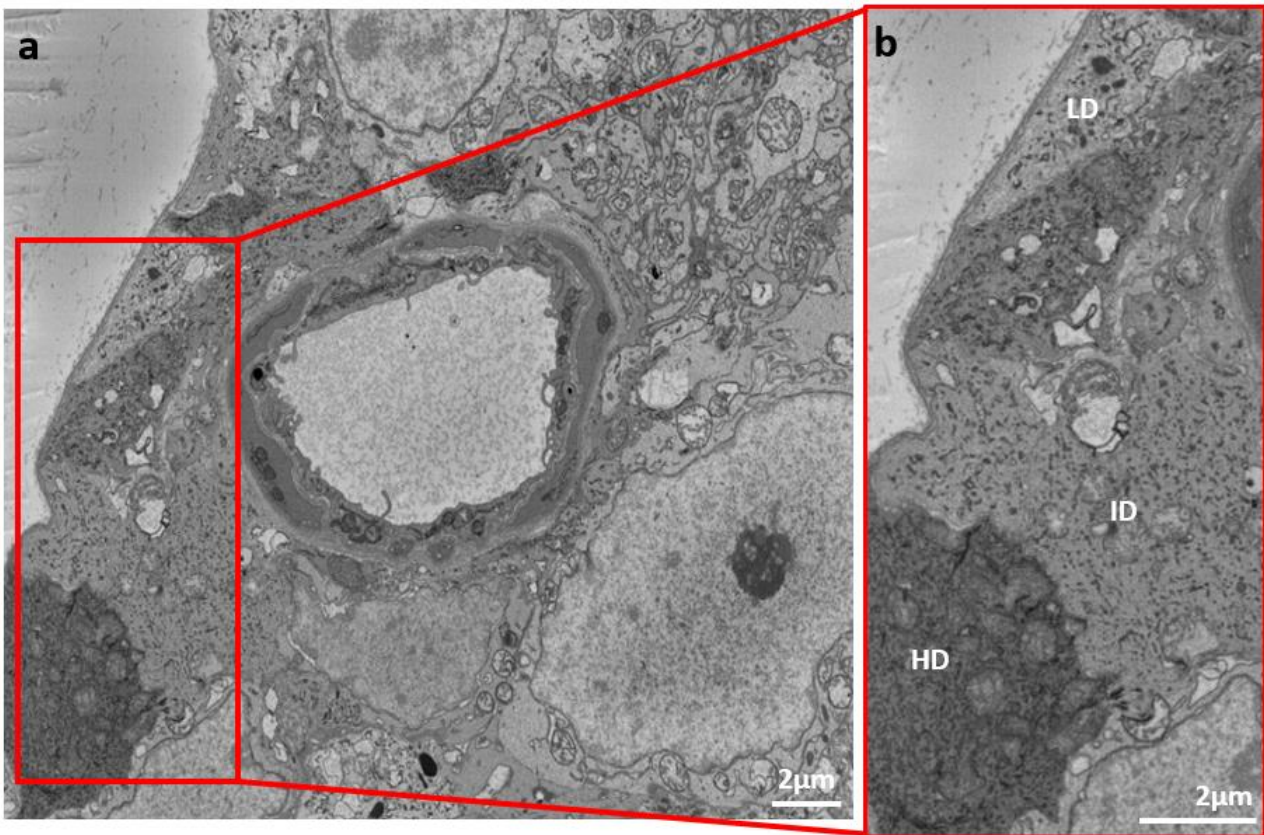


Figure 3-14 SBF-SEM electron micrographs showcasing three distinct electron density categories. Panel a. presents the overall micrograph with a capillary cross-section. Panel b is a magnified view of the highlighted area in panel a, displaying regions of low density (Yildirim et al.), intermediate density (ID), and high density (Timpl et al.).

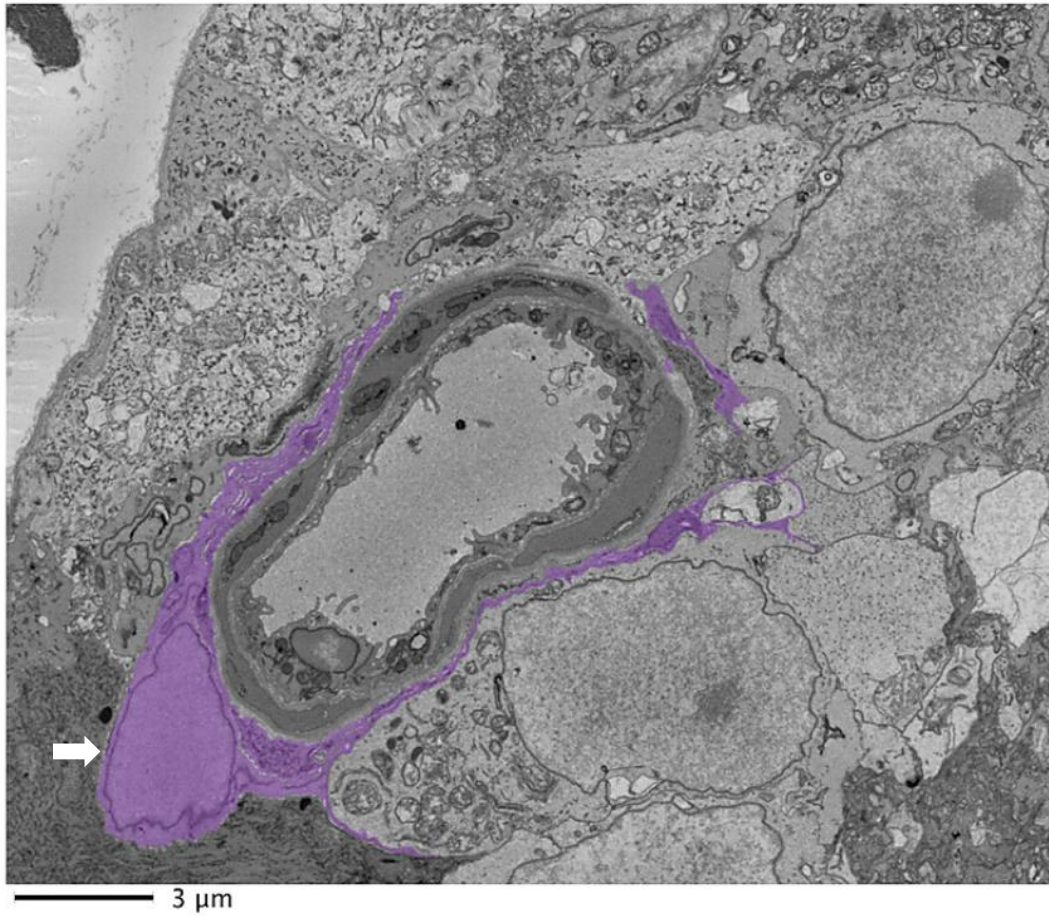


Figure 3-15 Identification of astrocytes via astrocyte nucleus presence within stack of data. Astrocytes indicated in shade of purple. White arrow indicates astrocyte nucleus.

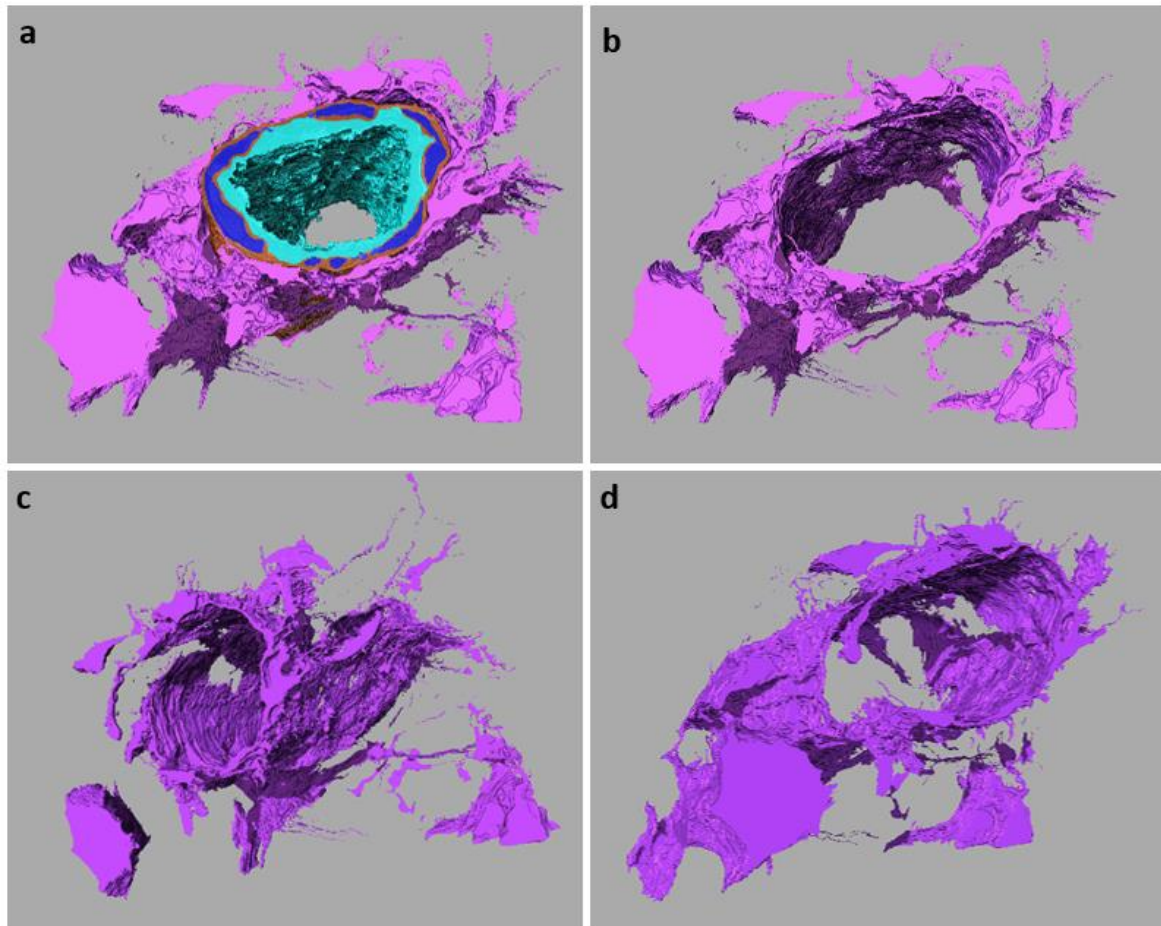


Figure 3-16 3D reconstruction of astrocyte. Panel a shows the astrocytes (purple) enveloping the vasculature, with the basement membrane (brown), pericytes (blue), and endothelium (aqua) clearly distinguished. Panels b, c, and d represent different orientations of the same astrocyte, illustrating the star-like morphology and the extensive connections with the surrounding vasculature.

3.4.2 Glial cell coverage

3D reconstructions of the NVU revealed the intricacy and complexity of the macroglia. Macroglia were found to form an interlocking, ‘patchwork- quilt’ style pattern as they lie over the outer vascular BM (**Figure 3-17**). Macroglia cell processes were observed to extend in directions distant from the capillary and interacting with other cellular components of the retina including neurons (**Figure 3-18**). The interweaving of the macroglia is complex and extensive along the capillary length. Complementing these observations, high-resolution molecular microscopy (STED) has provided additional insights into the spatial relationships between astrocytes and the vasculature, showing a similar pattern of astrocytes closely enveloping the capillary (**Figure 3-18**).

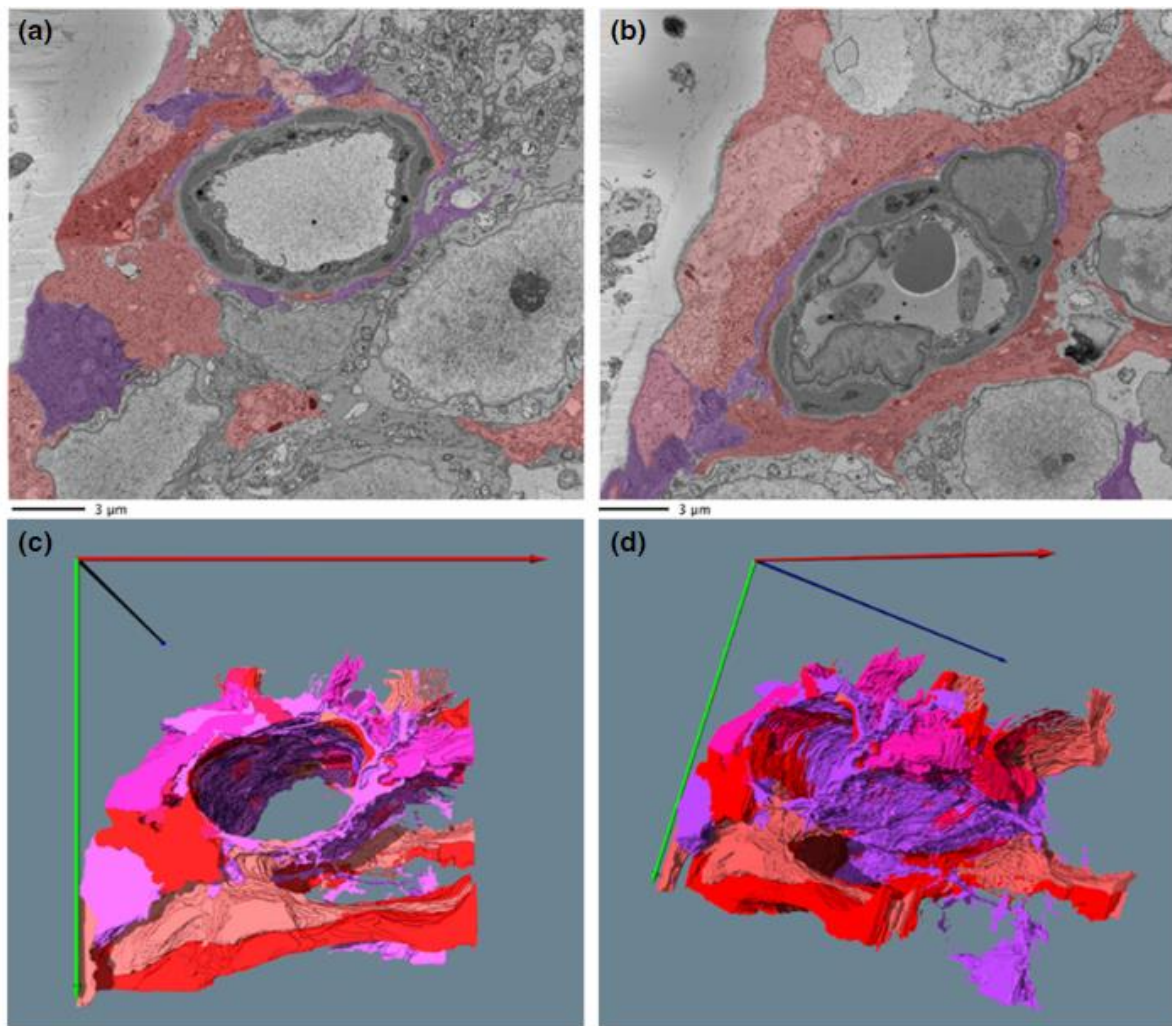


Figure 3-17 Segmented data and 3D reconstruction of macroglia surrounding the vasculature. (a, b) Glial cells in (red and purple shades) can be seen to wrap around the vasculature across different sections along capillary depth. Purple shading depicts a cell identified as an astrocyte. Displayed in a and b are sections 6 μ m apart. 3D reconstruction views (c, d) show the complexity of the wrapping along 18 μ m of vessel. Full 3D animation can be found: <https://figshare.com/s/05be25f5f4da056d5cdf>

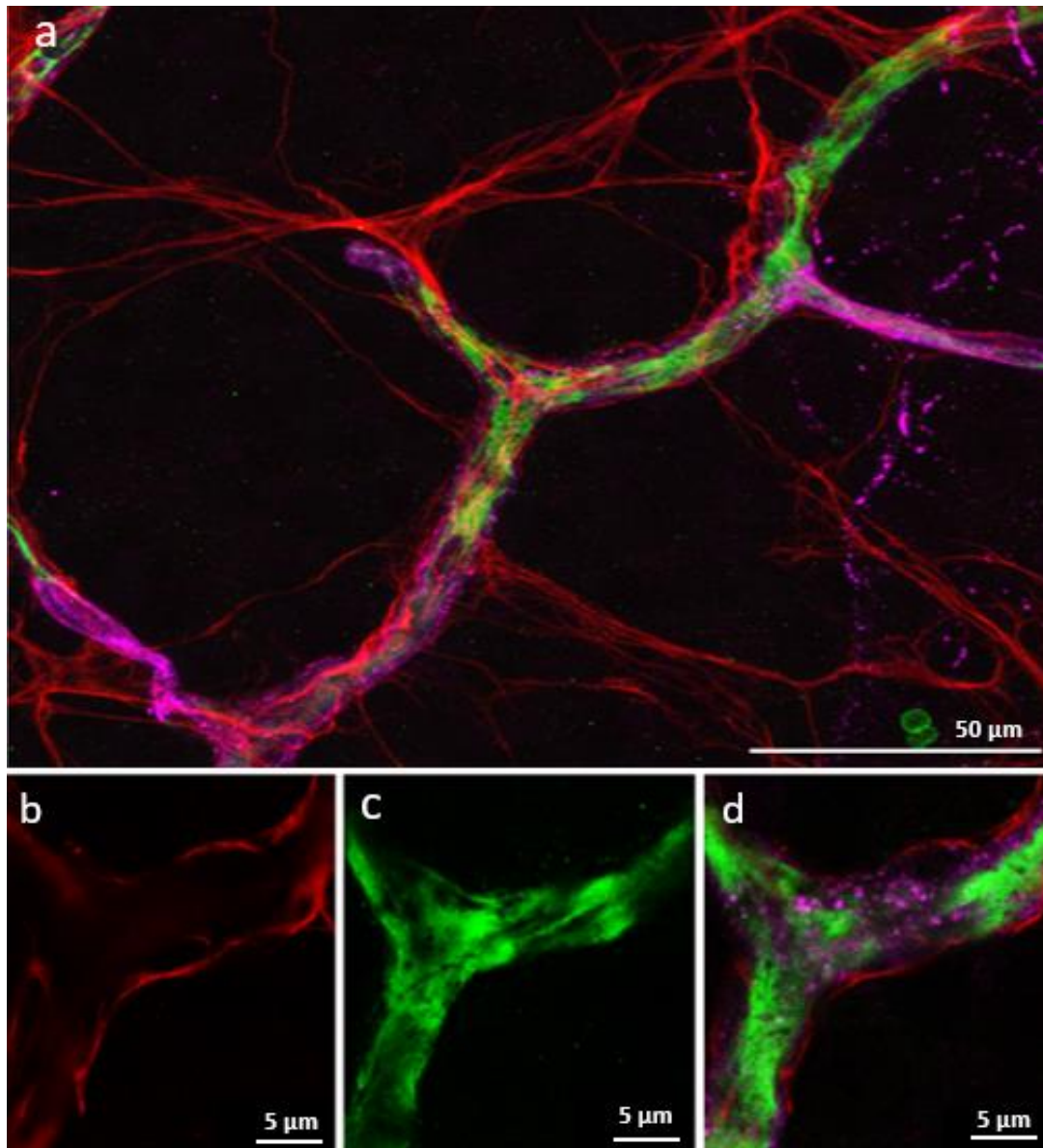


Figure 3-18 Immunostaining of astrocytes surrounding the capillary. Astrocyte stained with GFAP (Reddy et al.) shown to surround the capillary (marked by endothelial cells, stained with Isolectin B4, green and staining pericytes in purple with NG2) and extend its processes in directions distant from capillary. a. Z-stack of entire vessel b.c.d. STED image of astrocytes (Reddy et al.) wrapping around the capillary (b), endothelium (green) forming the capillary wall (d) and combined stains of astrocytes, endothelial cells, and pericytes showing the proximity and interactions of the astrocytic processes with the capillary structure.

3.4.3 Glial closeness to pericytes

Like the BM separating the pericytes from the endothelium, gaps were also present in the BM between the pericytes and macroglia. When such gaps occur at the outer edge of the BM, it allowed macroglia to come into direct contact with the underlying pericytes shown in **Figure 3-19**.

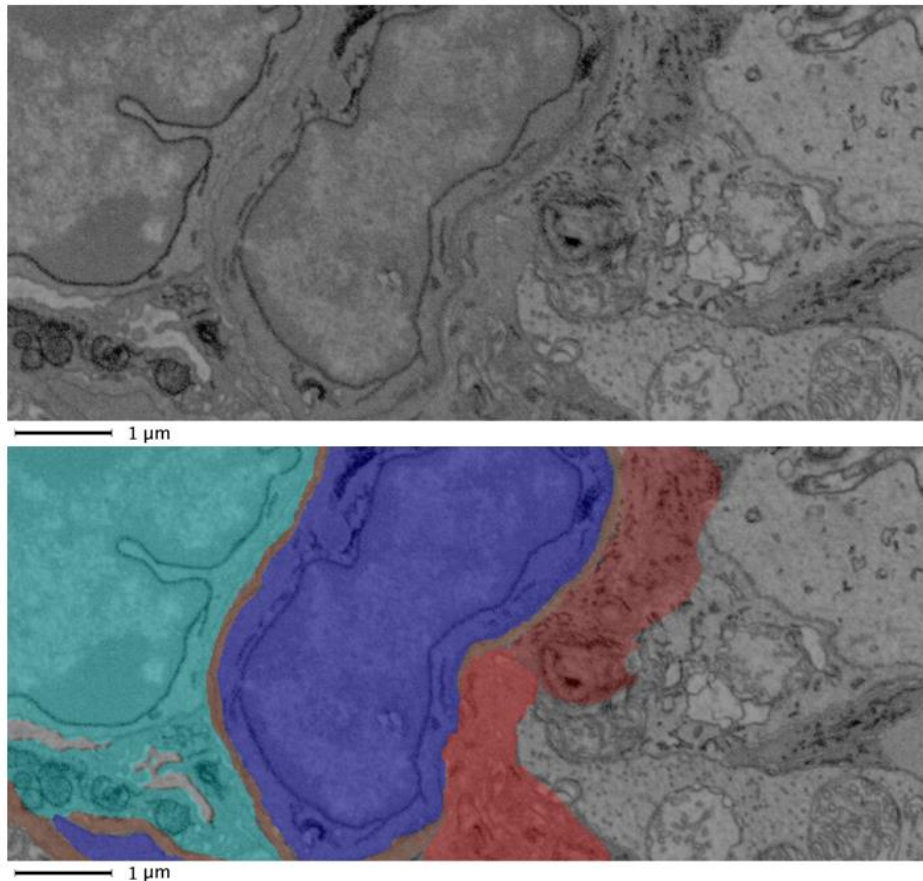


Figure 3-19 Macroglia-pericyte direct contact. Top slide, raw data. Bottom slide, segmented features. Of the two macroglia evident in this image, represented in the bottom panel by red features, one comes within close proximity of the pericytes (blue) by breaking through the BM (brown). Endothelial (auqa) and macroglia (purple and red shades).

3.4.1 Microglia

Retinal microglia exhibit variations in their appearance depending on their location within different retinal layers. The key factor influencing these variations is the functional state of the microglia, as they may appear differently when in their resting state compared to their activated state (Au & Ma, 2022). Microglia in the GCL can exist in different states, primarily categorised as resting or activated, depending on the retinal microenvironment and the presence of injury or inflammation. Resting microglia typically maintain a highly ramified morphology, where their branched processes constantly survey the retinal environment. In contrast, activated microglia, which respond to injury or inflammation, undergo morphological changes, becoming more amoeboid with retracted processes and increased soma size (Goyal *et al.*, 2023). This transition from resting to activated states is critical to understanding their role in neuroinflammation and retinal disease pathology.

To address the challenge of characterising microglia in electron micrographs and their diverse states and functions, a collaborative effort with the Institute of Experimental Medicine, Budapest was established. The initial approach involved performing immunohistochemistry to verify the suitability of the primary antibody, P2Y12R, a marker for microglia. P2Y12R is downregulated when microglia become activated, making it a valuable marker to distinguish between their resting and activated states. Following successful validation, the P2Y12R antibody was conjugated with gold nanoparticles to allow for visualisation in electron microscopy (**Figure 3-20**). This approach not only detected the microglia in a retinal sample process for immunohistochemistry but also enabled the structural intricacies of microglia in electron micrographs to be discerned. TEM micrographs revealed the nanoscale features of microglia, highlighting distinctive characteristics, the nucleus exhibited a high electron density, while the cytoplasm displayed electron lucency (**Figure 3-20** panel c and d). Furthermore, TEM images provided evidence of microglia's proximity to vascular capillaries, reinforcing the idea that cells interact with the retinal vasculature (**Figure 3-20** panel e-j). In the SBF-SEM micrographs, it remained challenging to consistently identify microglia due to limitations in visualising their nuclei. However, the use of P2Y12R immunogold labelling offered a potential solution to identify and differentiate resting microglia in these images. By using this marker, my work aimed to better characterise the resting state of microglia and their functional interactions with other retinal cells, particularly within the NVU.

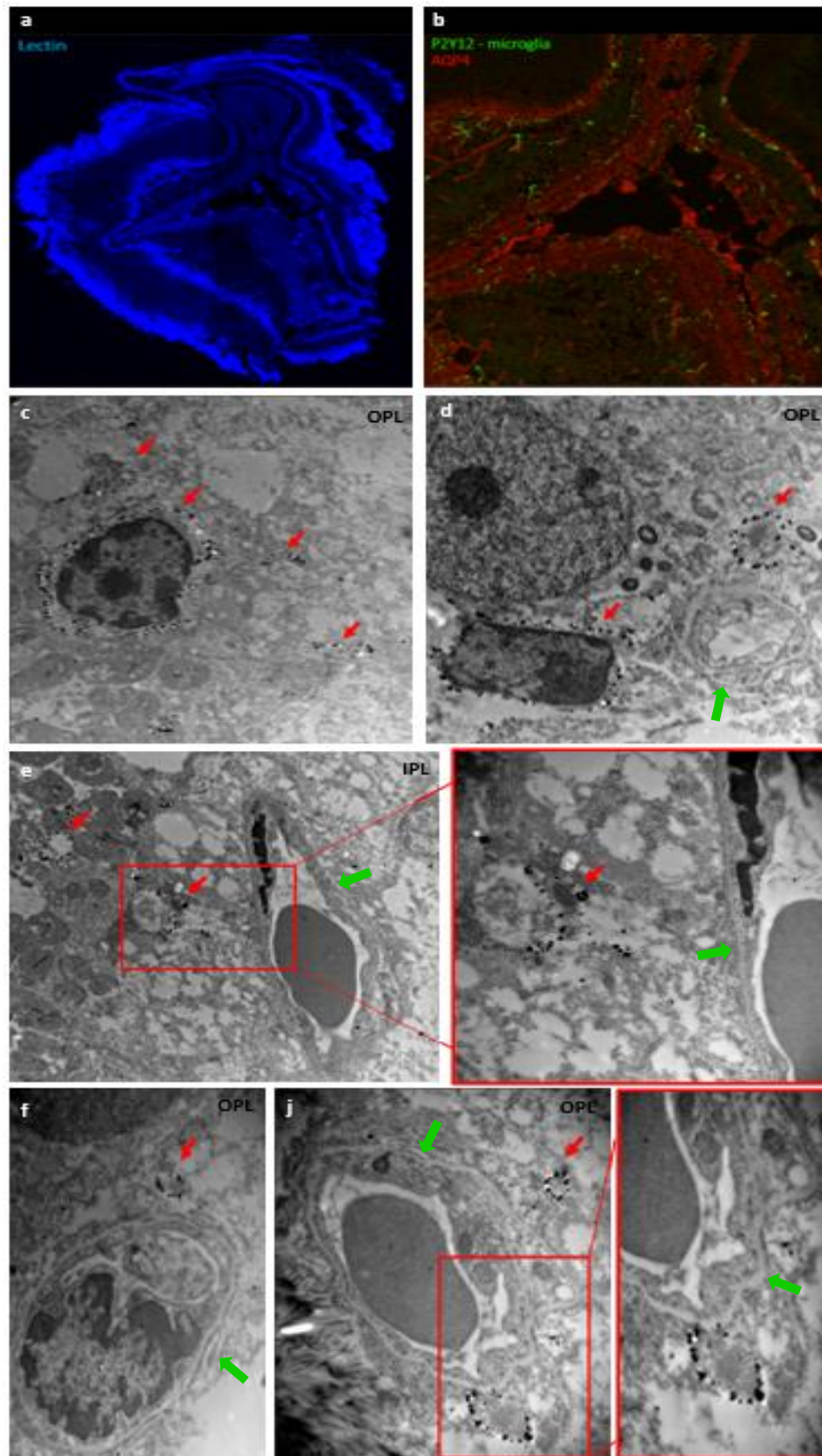


Figure 3-20 CLEM of microglia using P2Y12R in 6-month mouse capillary. a. lectin blue, an endothelial stain, for identification of sample b. P2Y12 stained green for microglia, visualised in the green channel and AQP4 in red, Müller cell stain c. identification of microglia in OPL by indication of gold nanoparticles, shown as black dots, indicated as by red arrow d. example 2 of microglia in IPL e.

identification of microglia near vascular capillaries in IPL f. example of microglia close to vascular capillary in OPL j. example 2 of microglia close to vasculature in OPL. Green arrows indicate capillaries. (Figures from Experimental Institute Budapest).

3.5 Neurons

Neurons, specifically retinal ganglion cells (RGCs) surround retinal capillaries (**Figure 3-21**), however they are separated by glial cells as they predominantly envelop capillaries, therefore they rarely come into close contact with the vasculature. On occasions, regions where glial cells are not surrounding the capillary, neurons come into proximity with the vasculature shown in **Figure 3-22**.

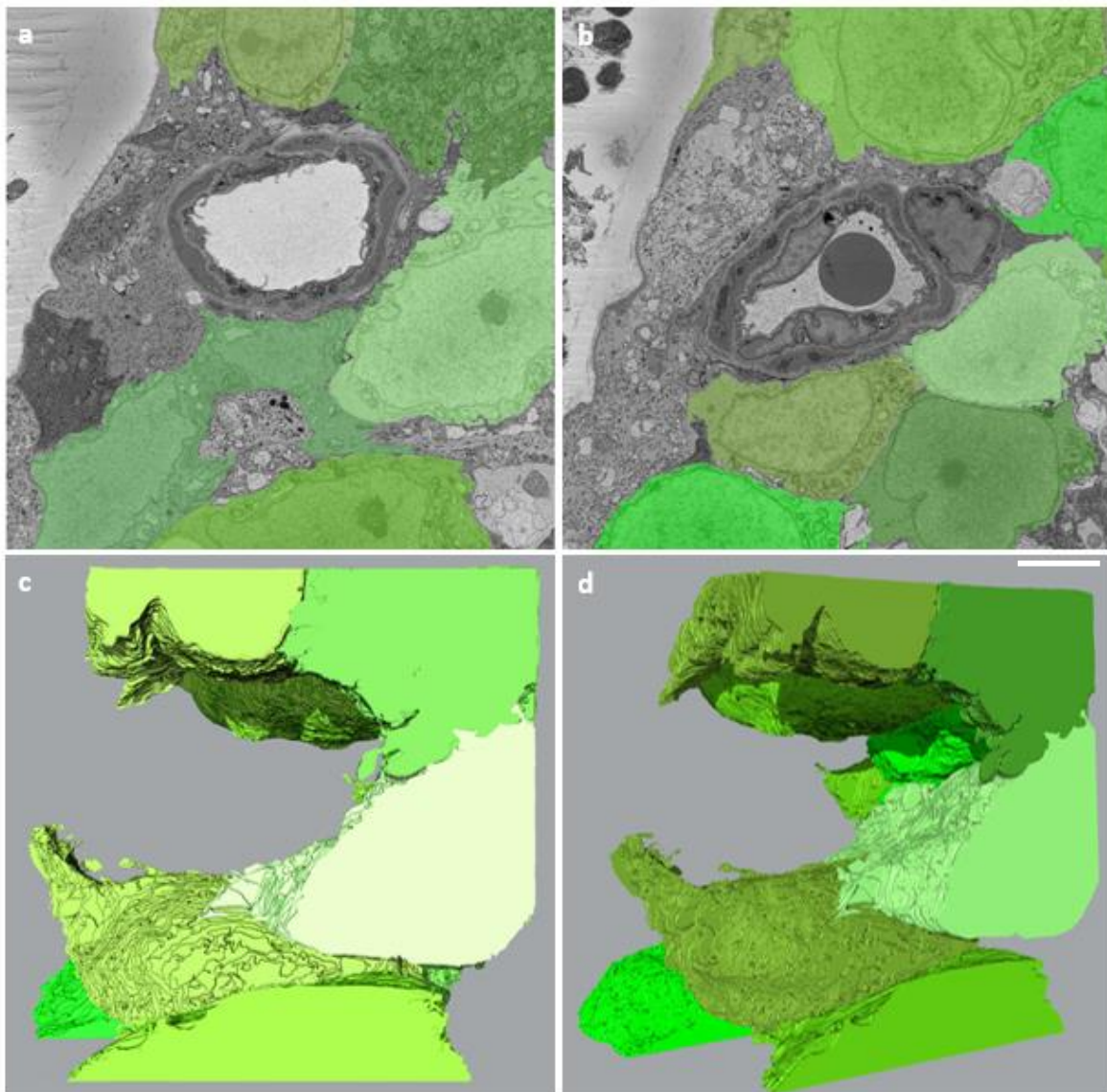


Figure 3-21 Segmented data and 3D reconstruction of neurons surrounding the vasculature. (a, b) neurons in (green shades) can be seen to surround the vasculature across different sections along

capillary depth. Displayed in a and b are sections 12 μ m apart. 3D reconstruction views (c, d) show the complexity of the wrapping along 18 μ m of vessel. Scale bar 3 μ m.

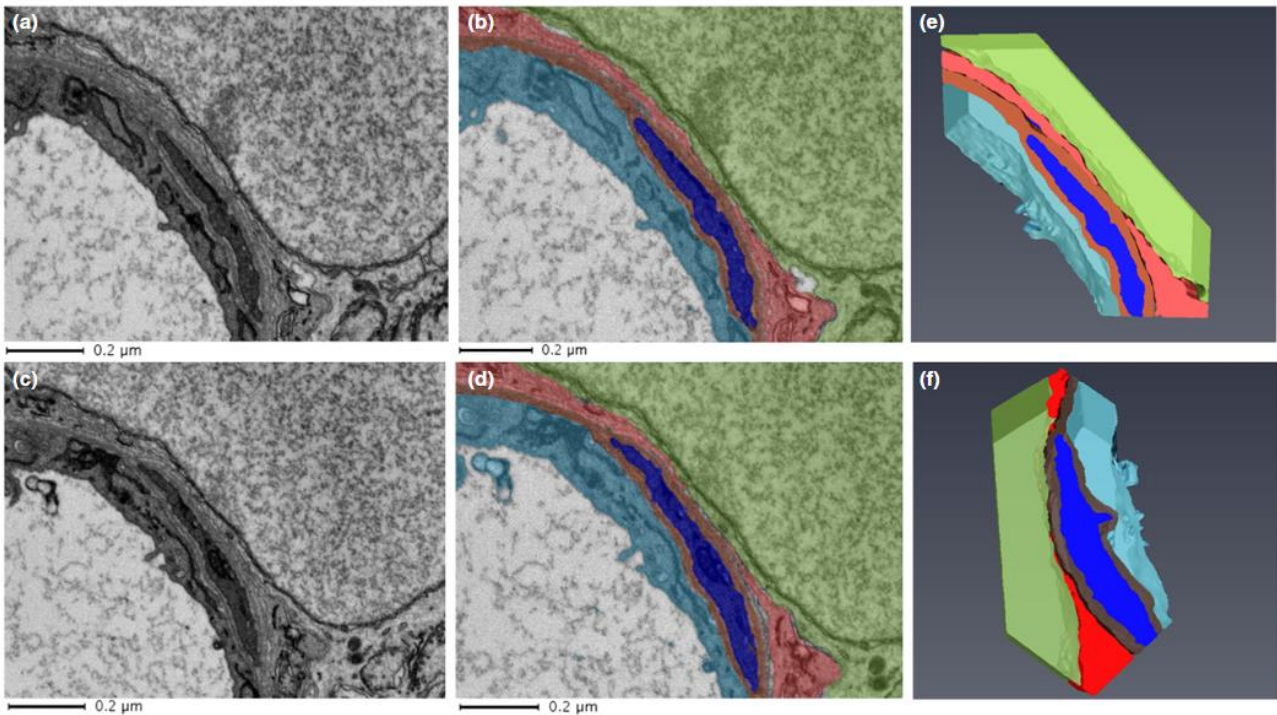


Figure 3-22 Neuron coming into close contact with vasculature. Raw (a and c) and segmented (b and d) data from consecutive sections (120 nm apart) illustrating a neuron in proximity with the vasculature. e and f, 3D arrangements from 6 consecutive sections: neurons: green shades, macroglia: red shades, endothelium: aqua; basement membrane: brown; pericytes: blue. Full 3D animation can be found: <https://figshare.com/s/37a0f2a3d62b1838b413>

3.5.1 Quantitative assessment of NVU components

3.5.1.1 Proximity of NVU components to pericytes

Proximity analysis enabled the determination of the minimal distances between the boundaries of the segmented features of interest, shown in **Figure 3-23**. The stack mean population histogram of the percentage of pericyte boundary pixels to those of the endothelium as a function of distance was assessed. The cumulative distribution function was also assessed from the stack mean population, enabling the total percentage of pericyte boundary pixels that lie within a given distance of the endothelium to be determined. Identical analyses were performed for other intercellular and cellular-BM feature pairs, with a summary table of cumulative distribution function readings at 10nm, 100nm, 250nm, 500nm and 1000nm (**Table 3-1**). As the pixel aspect ratio for our SBF-SEM

images is 6nm x 6nm, distances lying within 10nm are essentially in direct contact, this analysis displays the percentage of boundary pixels in contact for selected intercellular and cellular-BM feature pairs. The cumulative distribution function provides a cumulative measure of how many boundary pixels of one structure (e.g., pericytes) are within a certain proximity to another structure (e.g., endothelium). The CDF allows us to quantify the percentage of pericyte boundary pixels that lie within 10 nm, 100 nm, and so on, of the endothelial boundary. Since distances within 10 nm are considered direct contact, the CDF shows that on average, 10.8% of pericyte boundary pixels were in direct contact with the endothelium, whereas only 0.3% were in contact with the macroglia.

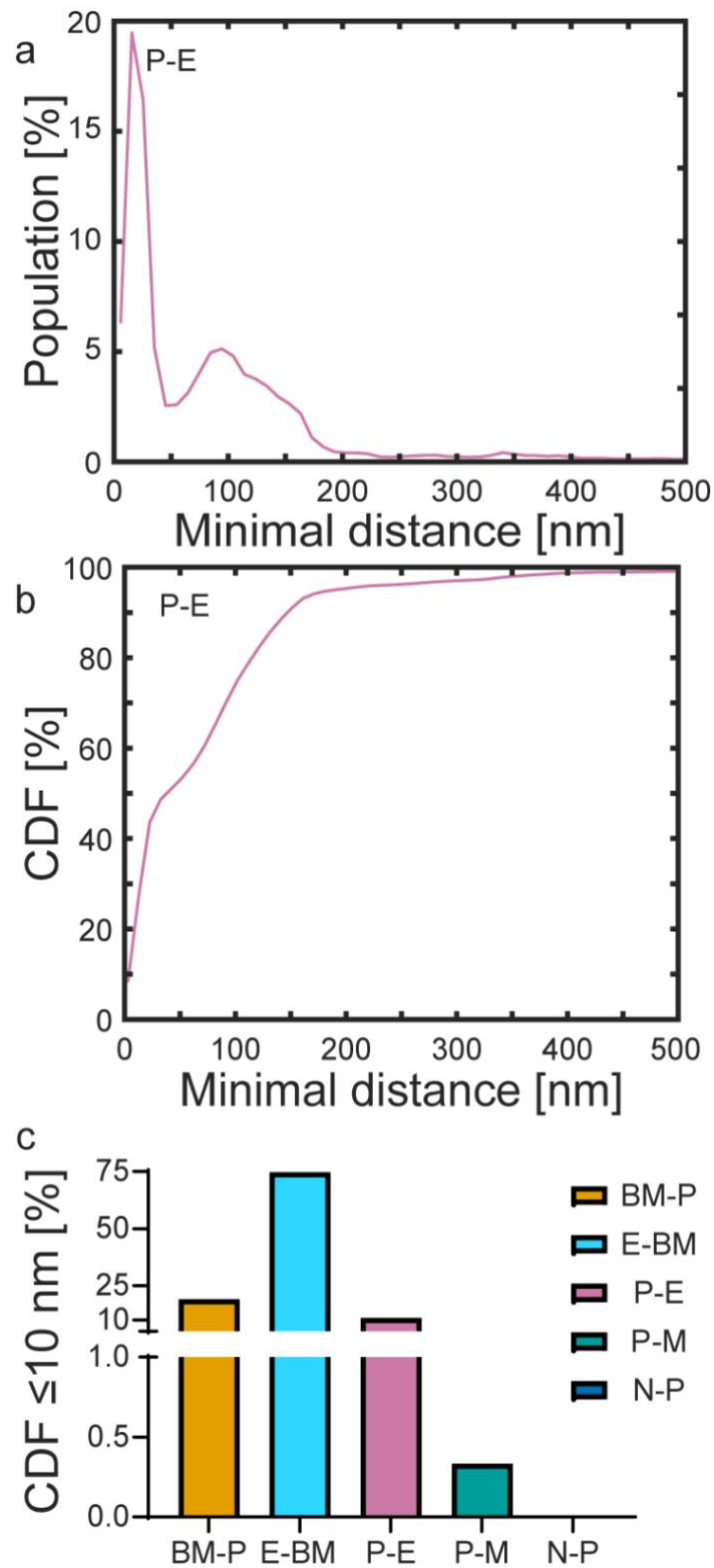


Figure 3-23 Quantitative assessment of intercellular and cellular-BM proximities for 3 month old capillary

1. a, The stack mean population histogram of pericyte to endothelium distances. b, The cumulative distribution function obtained from a. Panel c, 10nm readings of the cumulative distribution functions obtained from selected intercellular and cellular-BM feature pairs to assess the degree of direct contact. CDF, cumulative distribution function; BM, basement membrane; P, pericyte; E, endothelium; M, macroglia; N, neurons.

Table 3-1 Summary of the proximity analyses for the selected NVU feature pairs. Means and standard deviations of the cumulative distribution functions at increasing distances up to 1000nm are provided for the intercellular and cellular-BM pairs. BM, basement membrane; P, pericyte; E, endothelium; M, macroglia; N, neurons.

Feature pair	CDF($\leq 10\text{nm}$)[%]	CDF($\leq 100\text{nm}$)[%]	CDF($\leq 250\text{nm}$)[%]	CDF($\leq 500\text{nm}$)[%]	CDF($\leq 1000\text{nm}$)[%]
BM-P	19.0 \pm 19.1	37.5 \pm 32.6	42.2 \pm 31.9	50.6 \pm 28.4	70.7 \pm 21.0
E-BM	74.7 \pm 34.1	80.9 \pm 32.0	88.2 \pm 25.6	91.6 \pm 20.4	96.2 \pm 11.8
P-E	10.8 \pm 13.5	78.8 \pm 15.0	90.0 \pm 3.3	99.9 \pm 1.0	100.0 \pm 0.0
P-M	0.3 \pm 2.1	8.2 \pm 19.5	20.8 \pm 33.9	32.8 \pm 39.6	59.6 \pm 41.5
N-P	0.0 \pm 0.0	0.2 \pm 1.3	1.5 \pm 5.4	5.2 \pm 12.5	18.3 \pm 26.6

3.5.1.2 Morphological analysis of NVU components

The different morphological properties of the components of the mouse retinal NVU analysed were including convexity, sphericity and solidity were quantified, shown in **Figure 3-24**. Convexity and solidity were lowest for the BM when compared to the cellular components of the mouse retinal NVU. Convexity reflects the regularity and smoothness of the cell boundaries, with lower convexity in the BM indicating its more irregular, intricate structure. This could facilitate cell-matrix interactions and affect the diffusion of molecules across the BM, which is crucial for maintaining the BRB and enabling proper neurovascular coupling. Solidity indicates how compact or filled the structures are. The lower solidity in the BM suggests it is less dense compared to other cellular components, which might impact nutrient and oxygen diffusion across the NVU. In pathological conditions, this lower solidity could be indicative of structural changes. Sphericity measures how close the structures are to being spherical. More spherical shapes can indicate a stable or quiescent state, while deviations from this shape may suggest dynamic processes such as cell migration or proliferation. This is particularly relevant in glial cells like Müller cells, whose shape can change in response to retinal injury or inflammation.

By quantifying these morphological properties, a better understanding of how the NVU's structure supports its biological functions, such as maintaining the BRB, neurovascular coupling, and cell-to-cell interactions. Moreover, deviations from these structural norms may provide early markers for NVU dysfunction, particularly in diseases like DR, where the BM and NVU components undergo significant remodelling.

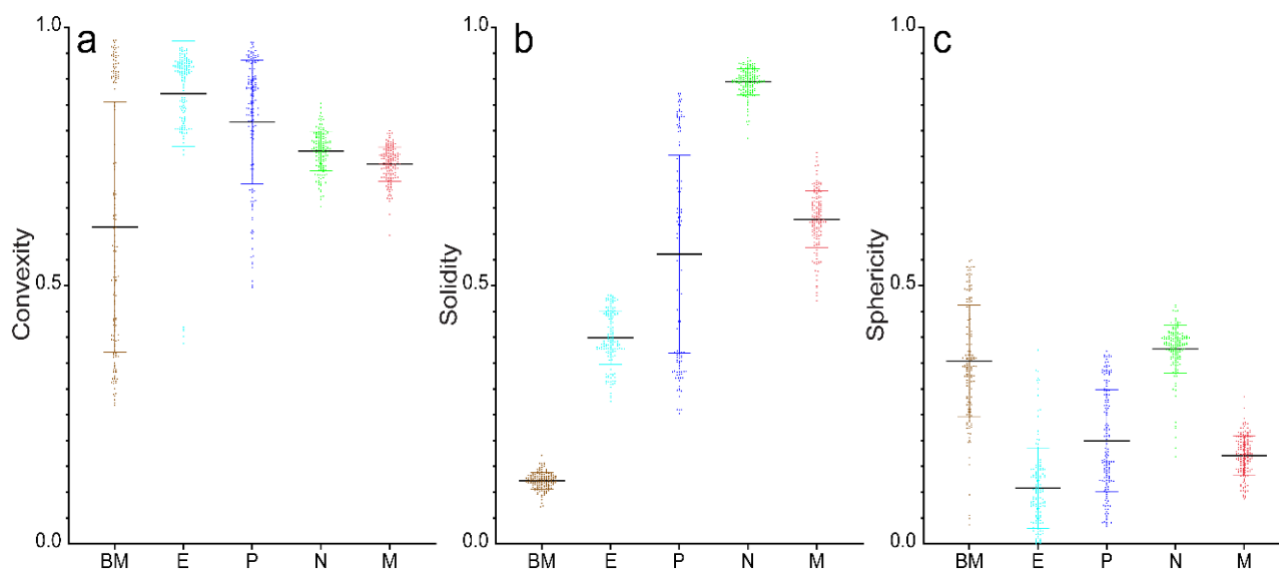


Figure 3-24 Column scatter graphs for convexity, solidity and sphericity of NVU cellular components and the BM for 3 month old mouse capillary 1. All 150 slices were analysed with each dot representing the area weighted mean obtained for all segmented features within each slice. Panels a-c convexities (convex perimeter:perimeter, CP:P), solidities (area:convex area, A:CA) and sphericities (Rmin:Rmax) of NVU component cells and the BM.

3.6 6-month-old mouse ultrastructure

Building upon the detailed exploration of the retina NVU within 3-month-old non-diabetic mice, this section extends our investigation to encompass 6-month-old mice. Utilising SBF-SEM, the retinal capillary ultrastructure and the heterocellular interactions were analysed.

3.6.1 Ultrastructural Consistency

The comparison between the 3-month and 6-month-old mouse models reveals consistency in the retinal NVU's ultrastructure. **Figure 3-25 - Figure 3-27** provide a series of SBF-SEM micrographs showcasing the capillary ultrastructure at 6-months. These images parallel the organisation observed in the 3-month-old specimens, with no discernible differences in the spatial arrangements of endothelial cells; their tubules and projections, pericytes, or the basement membrane. The cellular components maintain their intricate relationships, ensuring the functional integrity of the NVU.

Building on this, figure (**Figure 3-28** and **Figure 3-29**) illustrates 3D visualisation of the 6-month mouse ultrastructure further elucidation of no differences in spatial relationships among the capillary vasculature.

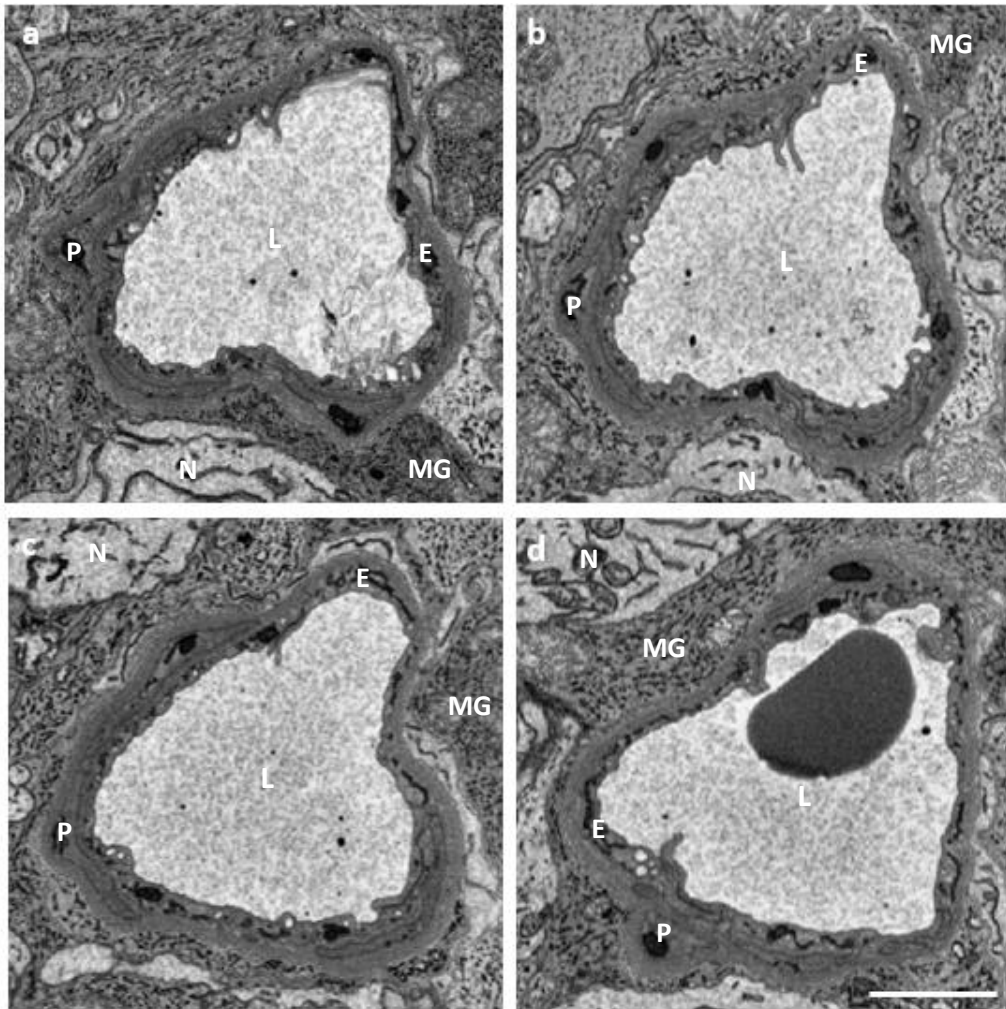


Figure 3-25 Ultrastructure of 6-month-old mouse capillary 1. A collection of SBF-SEM micrographs taken from a mouse retinal capillary to display the morphological changes along the capillary length. a, slice 1 (0.1 μm), b, slice 25 (2.5 μm), c, slice 50 (5 μm) and d, slice 100 (10 μm). Lumen: L, Pericytes: P, Endothelium: E, Macroglia: MG, Neurons: N. Scale bar 2 μm . Full dataset can be found here: <https://figshare.com/s/43917a967b535710cef6>.

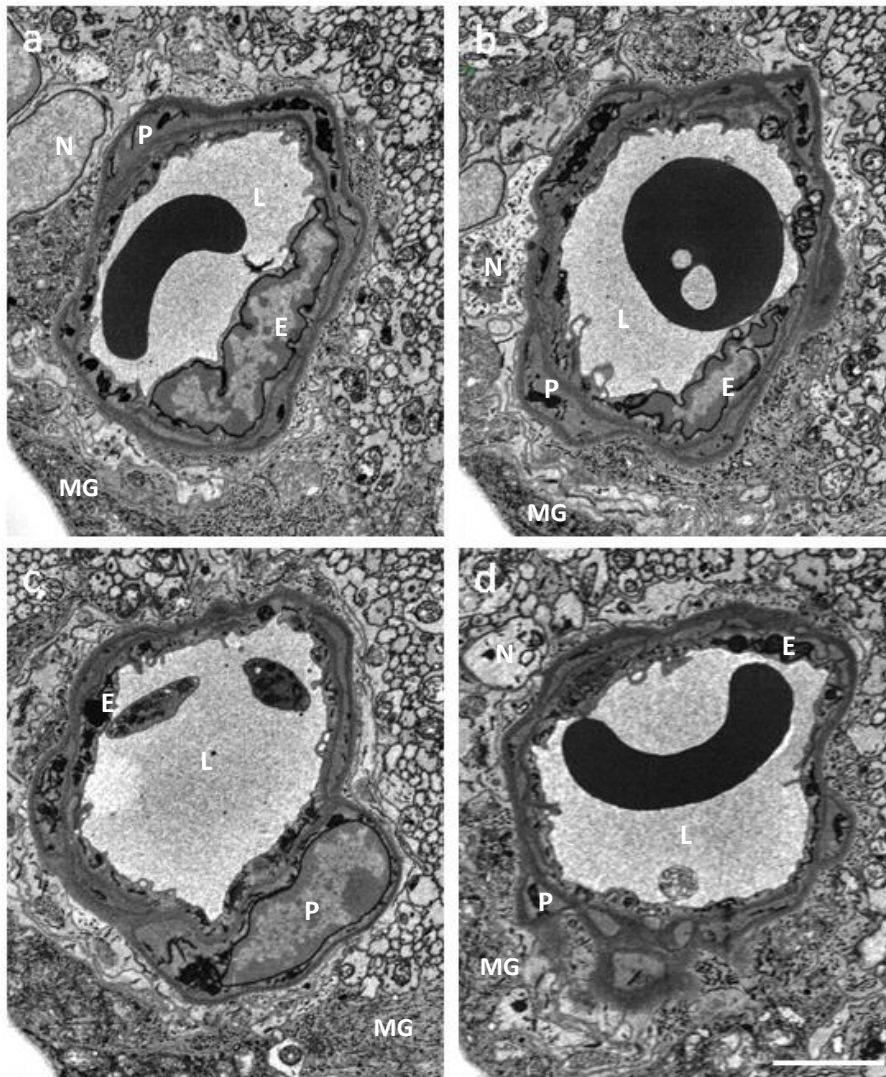


Figure 3-26 Ultrastructure of 6-month-old mouse capillary 2. A collection of SBF-SEM micrographs taken from a mouse retinal capillary to display the morphological changes along the capillary length. a, slice 1 (0.1 μm), b, slice 25 (2.5 μm), c, slice 50 (5 μm) and d, slice 100 (10 μm). Lumen: L, Pericytes: P, Endothelium: E, Macroglia: MG, Neurons: N. Scale bar 3 μm . Full dataset can be found here: <https://figshare.com/s/3dc00501955f6b40b96b>.

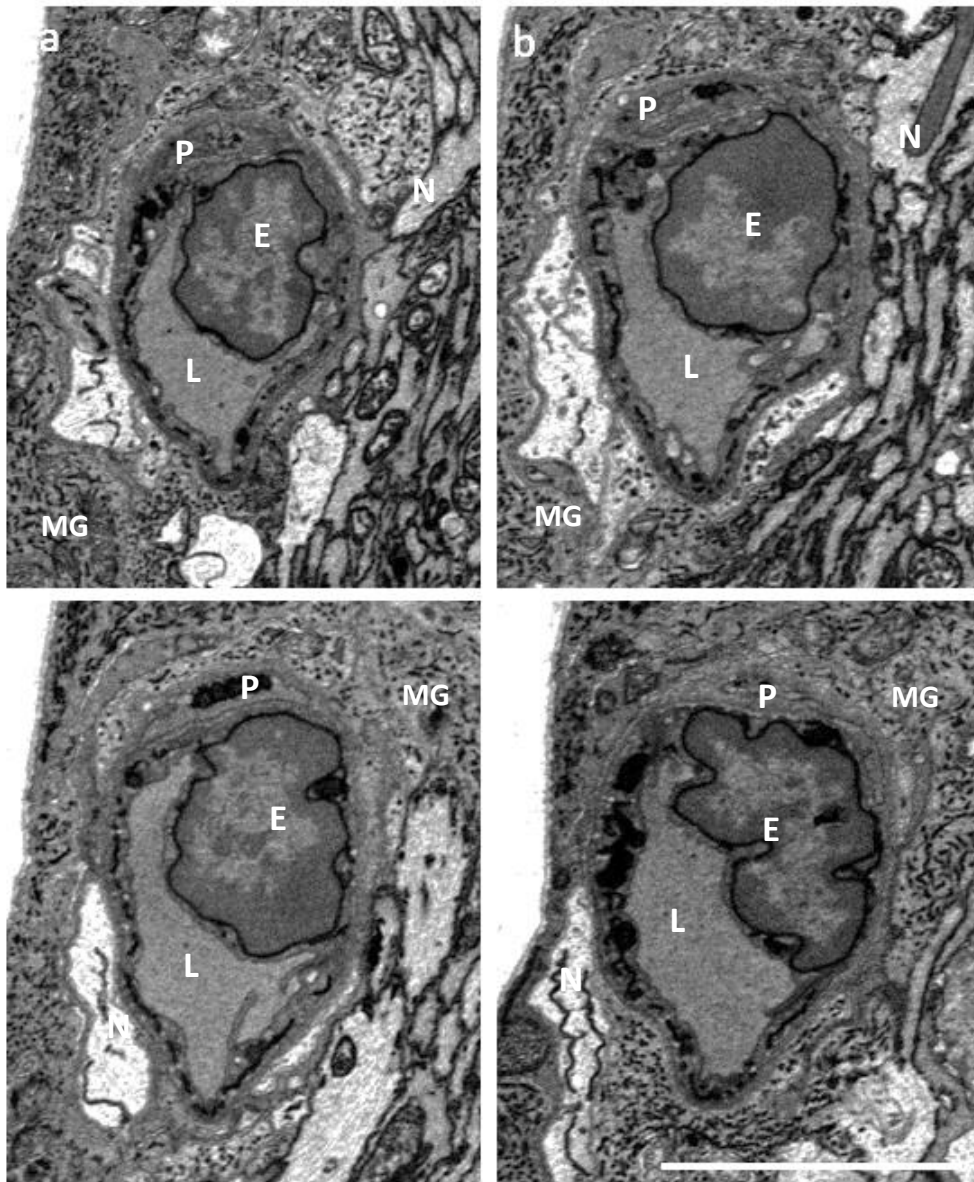


Figure 3-27 Ultrastructure of 6-month-old mouse capillary 3. A collection of SBF-SEM micrographs taken from a mouse retinal capillary to display the morphological changes along the capillary length. a, slice 1 (0.1 μm), b, slice 25 (2.5 μm), c, slice 50 (5 μm) and d, slice 100 (10 μm). Lumen: L, Pericytes: P, Endothelium: E, Macroglia: MG, Neurons: N. Scale bar 3 μm . <https://figshare.com/s/56c634fcab321ac6cf24>

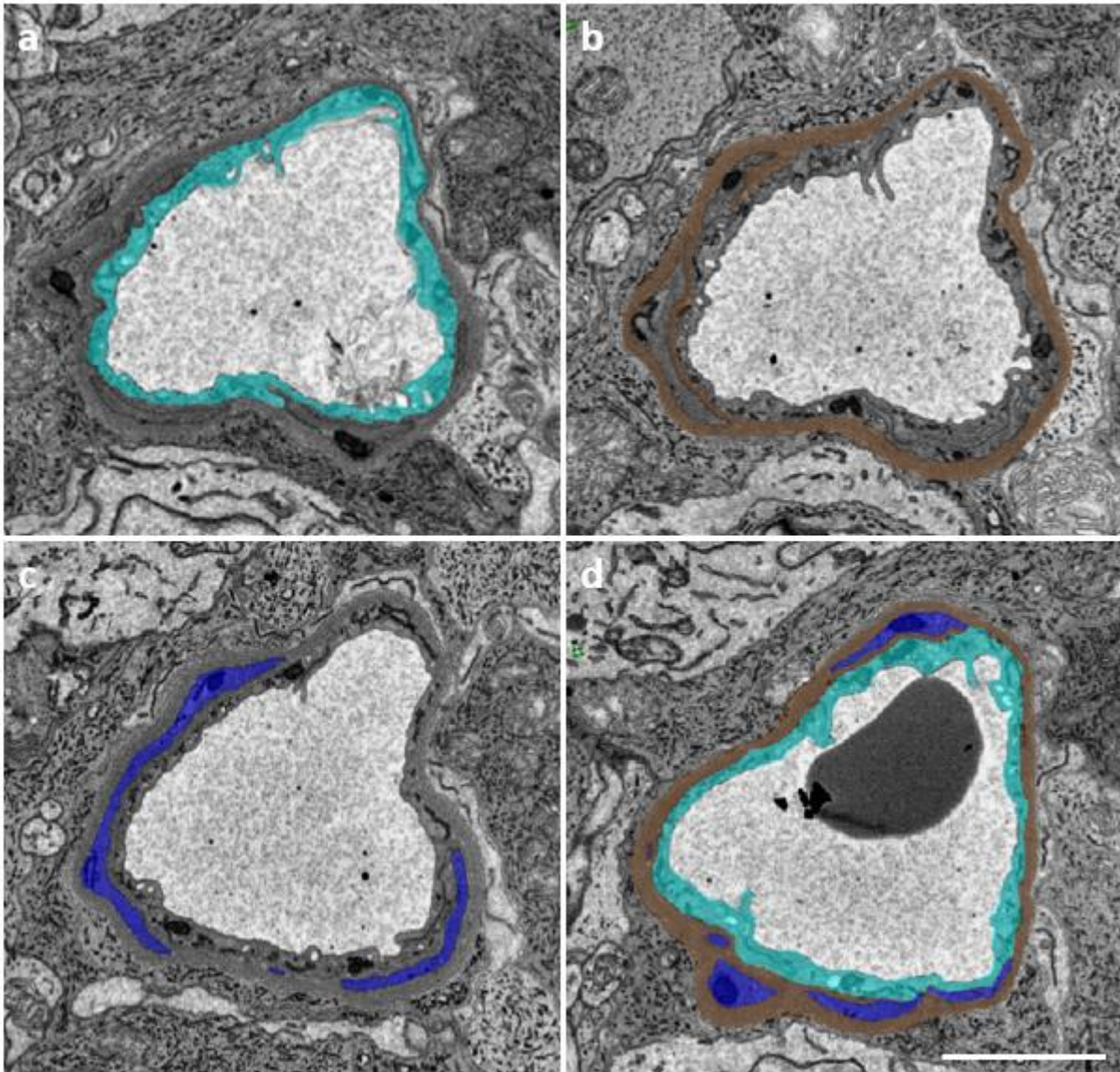


Figure 3-28 Segmented vasculature of 6-month-old mouse. The vasculature was identified, and each component was assigned a colour for segmentation through the data stack and subsequent visualisation in 3D reconstructions. a, endothelium (aqua), b, basement membrane (brown), c, pericytes (blue), d, complete vasculature. Scale bar 2 μm .

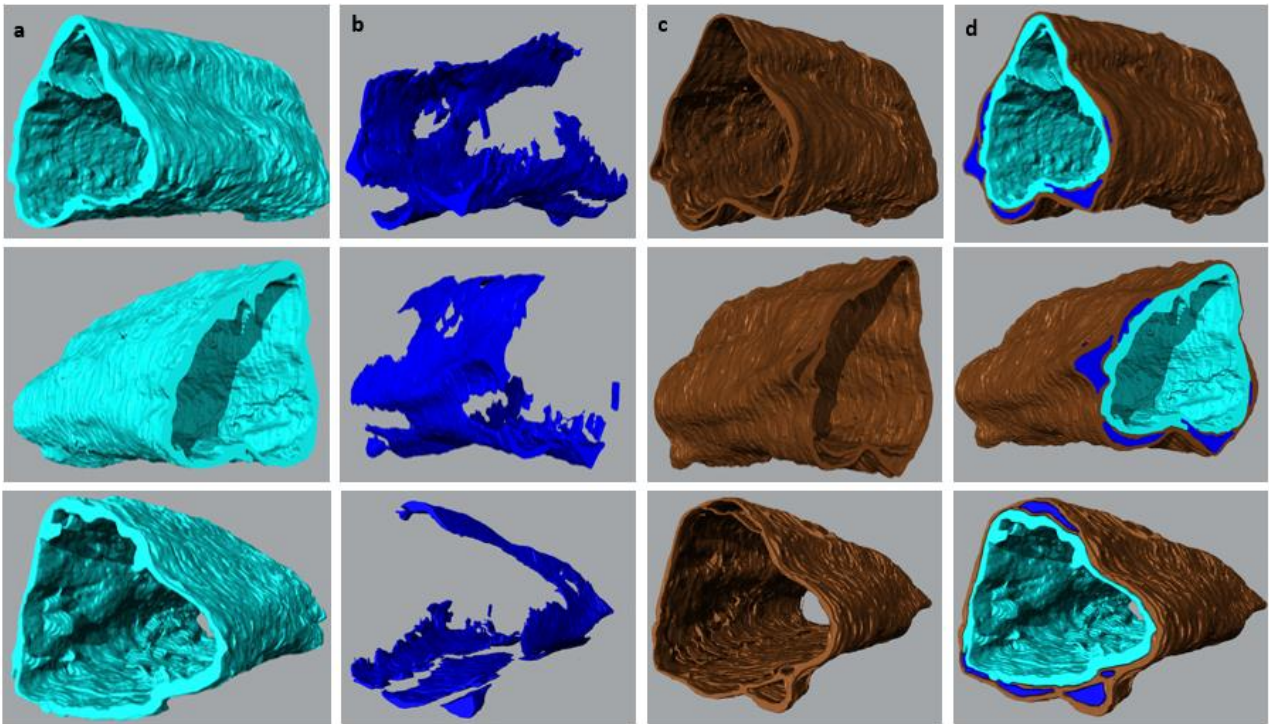


Figure 3-29 3D reconstruction of 6-month-old mouse capillary 1 vasculature. Displayed are features associated with a 3D reconstruction of the vasculature of capillary 1. Column a: endothelium (aqua); column b: basement membrane (brown); column c: pericytes (blue); and column d: combined vasculature.(a)(b)(c)(d)

A hallmark of the NVU's heterocellular interactions is the peg-and-socket formations between endothelial cells and pericytes, serving as critical points of contact for cellular communication. The distribution of peg-and-socket formations within the 6-month-old mouse retinas, as illustrated in **Figure 3-30**, displayed a random distribution pattern that aligns with the observations made in the 3-month-old models, suggesting no age-related changes, as further supported by the data shown in **Figure 3-31**, showing no significant differences in peg numbers or coverage.

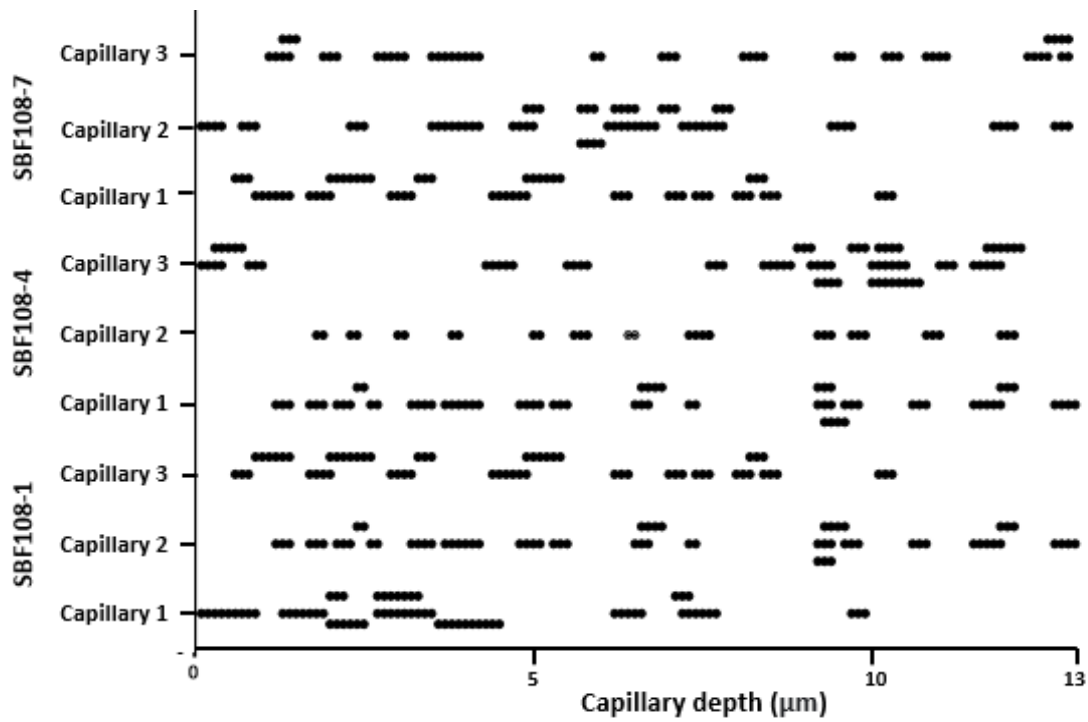


Figure 3-30 Distribution of peg and sockets across 6-month-old mouse capillaries. The distribution of peg- and sockets evident across 130 sections examined in 9 capillaries. Note more than one peg-and-socket may appear in the same sections (i.e. at different points of pericyte-endothelial membrane interaction in the same z-plane).

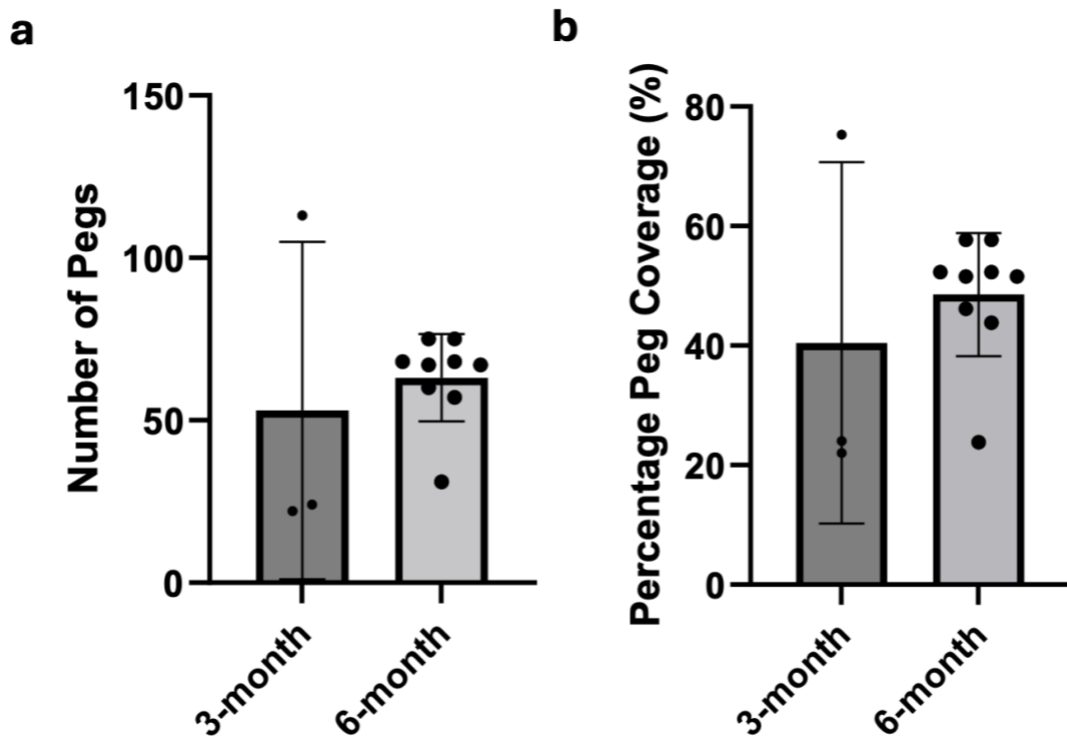


Figure 3-31 Analysis of peg and socket distributions in 3-month and 6-month-old mouse capillaries. a. Number of pegs in capillaries at 3 months and 6 months. b. Percentage of peg coverage per

capillary depth in capillaries at 3 and 6 months. Bars indicate mean coverage, with individual data points as black dots. No significant differences were found between age groups. Error bars represent standard deviations.

3.7 Discussion

Four, 3-month-old, and nine, 6-month-old mouse non-diabetic retinal capillaries were imaged with SBF-SEM for the 3D visualisation and analysis of the NVU. Key ultrastructural features identified in the NVU include pericyte and endothelial interactions through direct contact and peg-and-socket formations, glial cell complex mesh-like wrapping and close contacts with pericytes and neuronal contacts with the vasculature.

Endothelial projections populate a large area of inner surface of the endothelium, underscoring the fundamental importance of these projections in shaping the overall structure and playing a pivotal role in its functionality. SBF-SEM imaging and 3D image reconstruction of endothelial projections, revealed significant morphological diversity, including instances of both single and double endothelial processes projecting into the capillary lumen. Endothelial projections in mesenteric arteries have shown to possess a variety of morphological structures ranging from those penetrating the internal elastic lamina to those in close contact with smooth muscle, suggesting their versatile roles in different tissues (Maarouf *et al.*, 2017). The base of the endothelial projection is identified as a crucial site for internal Ca^{2+} release, potentially activating Ca^{2+} -sensitive targets like nitric oxide synthase and SK/IK channels. This suggests that these projections could be instrumental in enabling endothelial cells to sense blood flow changes, thus contributing to the process of flow-dependent vasodilation. Such a mechanism underscores the functional importance of these projections in mediating vascular responses to varying blood flow, emphasising their role in the regulation of vascular tone and blood supply. While the absence of internal membranous structures within the projection implies that, in the mesentery, their primary function is to serve as an electrical conduit (Isakson *et al.*, 2007). In the retina, the structural design of endothelial projections predominantly supports their role in maintaining a barrier function. This is crucial for preserving the precise microenvironment necessary for optimal visual function. The substantial coverage of endothelial projections and their diverse morphology in the retina could thus reflect adaptations to the unique metabolic and functional demands of the retinal tissue.

Peg-and-socket interactions have been described in both human and mouse retinal and brain capillaries and have also been found in human and murine granulation tissue and cardiac tissue (Díaz-Flores *et al.*, 2011), (Wakui *et al.*, 1990), (Carlson, 1989). SBF-SEM micrographs and 3D reconstructions have revealed that peg-and-socket interactions span across a depth of between 2-9 μm and have an unconstrained distribution along the length of the capillary. The depth of our analysis encompassed a significant span of the capillary depth. For the 3-month-old mouse capillaries, our scrutiny extended to a depth of 15 μm , while for the 6-month-old mouse capillaries, we investigated to a depth of 13 μm . Within these depths, the peg-and-socket formations made a frequent appearance. This high frequency of occurrence underscores the significance of peg-and-socket formations in the retinal capillary architecture. An important feature of peg-and-socket interactions between endothelial cells and pericytes was that pericytes were commonly forming the peg, while endothelial cells acted as the acceptor socket. Physical contact between pericytes and the endothelial cells have been reported to be essential for angiogenesis prevention with inhibition of endothelial cell proliferation (Orlidge & D'Amore, 1987). Although the exact pathway which drives the formation of peg-and-sockets is not yet known, several growth factors including transforming growth factor-beta, angiopoietin 1 and epidermal growth factor have been reported to be present within the pericyte and endothelial cell interdigitation space (Wakui *et al.*, 1993). TEM micrographs have reported gap junctions between peg-and-socket interactions (Kovacs-Oller *et al.*, 2020). These junctions allow for the exchange of ions and molecules in the capillary, which is important for their contribution to the formation of the BRB and its maintenance (Curcio *et al.*, 2010). Pericytes play a crucial role in angiogenesis by modulating the proliferation of endothelial cells (Chiaverina *et al.*, 2019). They also influence the expression of tight junction proteins within these cells, further impacting endothelial cell function. This multifaceted interaction between pericytes and endothelial cells could be a driving force behind the formation of peg-and-socket interactions. More generally, the pericytes and endothelium lying either side of a shared BM, and encircling the capillary lumen along the z-axis, supports a role for integrated regulation of vascular diameter and thereby retinal blood flow and nutrient exchange (Geevarghese & Herman, 2014). Previous research including TEM and light microscopy studies have suggested pericytes and endothelial cells in the retina share a 1:1 ratio (A. Armulik *et al.*, 2005; Choi *et al.*, 2018; Stratman *et al.*, 2010). SBF-SEM has shown us the changes in the vasculature in 3D. Quantifications of our data will allow us to draw firm conclusions of how much pericyte coverage occurs across the depth of a capillary at any given point.

Glial processes surround retinal capillaries and are integral to normal retinal homeostasis (Bringmann & Wiedemann, 2012). They have been reported to play a key role in supporting inner BRB function, retinal vascular development and controlling blood flow via neurons (Liu & Liu, 2019). Previous TEM studies have suggested that the macroglia, especially Müller cells, come into close contact with the outer vascular BM of the retinal pericytes (Stitt *et al.*, 1994). The 3D serial datasets obtained from SBF-SEM illustrated the interweaving of the macroglia into the BM. Like the BM separating the pericytes from the endothelium, gaps were also present in the BM between the pericytes and macroglia. When such gaps occur at the outer edge of the BM, it allowed macroglia to come into direct contact with the underlying pericytes. A close contacts analysis of the NVU components to pericytes showed us that macroglia to pericyte distances commonly occur between 0-2000nm, which supports our visual analysis of their interactions. The closeness of the macroglia to the outer vascular BM and pericytes supports previous studies suggesting that macroglia may directly regulate retinal blood flow through paracrine signalling (Newman, 2015).

Glial cells predominantly envelop capillaries, separating the neurons from the vasculature. Macroglia regulate flux between neurons and circulation as well as supply substrates for aerobic metabolism in neurons (Newman & Reichenbach, 1996). Neurons in the NVU transmit electrical impulses from light signals to the brain for vision (Moran *et al.*, 2016) as well as eliminate metabolic wastes and carbon dioxide. Neurons rely on capillaries for nutrients and oxygen, however, do not make direct contact with the vasculature for their needs. On occasions where macroglia are absent, SBF-SEM micrographs, demonstrated neuronal contact with the vasculature. This supports a previous TEM-based study of retinal capillaries in tree shrews (Ochs *et al.*, 2000). Such interplay between the neurons and the BM of the retinal NVU, even if infrequent, may suggest the possibility of direct neurovascular coupling; this need assumes the diffusional barrier of the BM to be surmountable as, in mice capillaries, no direct contact between neurons and pericytes was observed.

While the utilisation of P2Y₁₂R-conjugated gold nanoparticles has enhanced the visibility of microglia in TEM, the challenges persist in SBF-SEM, particularly regarding the consistent visualisation of microglial nuclei. Addressing these challenges is critical for advancing our understanding of microglial positioning and function within the retinal architecture. Increasing the area and depth of capillary coverage could potentially offer a more comprehensive visualisation of microglial distribution and interactions within the retinal NVU. The adoption of array tomography may also provide a viable solution, as it integrates high-resolution 3D reconstructions with the

capacity to overlay multiple imaging modalities, improving the detection of specific microglial markers. Furthermore, leveraging advanced image analysis software, particularly those employing machine learning algorithms, could streamline the identification process by automating the recognition of microglial features. Such advancements will not only refine our understanding of microglial structural roles but also enhance our insights into their dynamic functions in both healthy and diseased states, which is critical for diseases such as DR where microglial activation is prominently involved. In early stages of DR, microglia migrate towards areas of retinal damage and become activated, shifting from their resting, ramified state into an amoeboid, reactive form. This activation is characterised by the release of pro-inflammatory cytokines such as TNF- α , IL-1 β , and IL-6, contributing to a chronic inflammatory environment that exacerbates retinal damage. Additionally, activated microglia have been shown to disrupt the BRB, further facilitating vascular leakage and capillary degeneration, which are hallmarks of DR (Judith Lechner et al., 2017).

The comparative analysis of retinal NVU ultrastructure's in 3-month and 6-month-old non-diabetic mice reveals a structural and functional consistency within the retinal NVU across these ages. The lack of observable differences in the ultrastructure and the peg-and-socket distributions suggests that the NVU reaches a mature state by 3-months that does not significantly alter with age, at least within the timeframe studied. The heterocellular interactions observed in the non-diabetic murine retina have been confirmed in 13 different capillaries. Therefore, when analysing diabetic samples these interactions will help outline any changes which may occur in diseased states. Vascular alterations are a hallmark in the early development of DR, therefore identifying a change in the number or distribution of peg-and-socket interactions or reduced pericyte coverage could indicate death or loss of pericytes. While traditional imaging techniques have highlighted pericyte loss, SBF-SEM offers a distinct advantage by illuminating early pericyte alterations at a nanoscale level. This includes critical phenomena like potential variations in their engagement with endothelial cells, and shifts in peg-and-socket interactions, enriching our understanding of pericyte dynamics in the progression of DR.

3.8 Conclusion

In conclusion, the detailed investigation of the NVU within the retinal capillaries of non-diabetic mice has revealed intricate and complex interactions among its key components. Utilising advanced imaging technique, SBF-SEM, has provided valuable insights into the structural and functional aspects of the NVU.

The endothelial projections within the capillaries display significant morphological diversity, with both single and double processes projecting into the capillary lumen. These projections are not just structural but reflect the adaptability and plasticity of the NVU in adapting to the metabolic needs of the retina, a crucial feature of neurovascular coupling that can evolve with age. Peg-and-socket interactions, characterised by pericytes forming pegs and endothelial cells acting as acceptor sockets, are identified as essential elements contributing to the formation and maintenance of the BRB. These interactions extend across considerable depths of the capillary network, emphasising their importance in the retinal capillary architecture.

Glial cells, particularly macroglia, play a crucial role in the NVU by forming a complex, mesh-like pattern around the outer vascular BM. The close interactions of macroglia with the BM and pericytes suggest a potential regulatory role in retinal blood flow through paracrine signalling. Neurons, while predominantly enveloping capillaries, occasionally come into close proximity to the vasculature when glial cells are absent. Crucially, the application of CLEM allowed the positive identification of microglia within the NVU. These microglia, stained for P2Y₁₂R, were visualised for their characteristics under EM within the retinal microenvironment.

The key structural insights from this chapter provide a comprehensive baseline for understanding how NVU components interact in the non-diabetic murine retina and how these interactions evolve from early to middle adulthood. Given that 3-month and 6-month mice correlate to approximately 20–50 human years, the findings from this study highlight essential age-related shifts in the NVU's function, providing a foundation for future investigations, particularly in the context of DR. This baseline understanding is critical for exploring how early structural changes in the NVU contribute to the onset of retinal diseases in both mice and humans.

Chapter 4 Diabetic Mouse Neurovascular Unit

This chapter delves into an exploration of the diabetic mouse NVU, unravelling profound structural changes within the retinal microenvironment under the influence of diabetes. Employing nanoscale serial imaging with SBF-SEM, our study investigates the ultrastructure of the diabetic mouse retina, focusing on the BM, pericytes-endothelial interactions, endothelial tubules, and the intriguing presence of leukocytes.

4.1 NVU changes in DR

In DR, profound alterations in the NVU compromise the retina's functionality and structural integrity. The NVU's components, including endothelial cells, pericytes, and various glial cells, interact closely to maintain the BRB, responding dynamically to the metabolic demands of retinal nerve cells. This interaction ensures a tightly regulated environment essential for visual processing. However, a high-glucose environment can disrupt this delicate balance, leading to typical DR manifestations such as vascular leakage, pericyte loss, and neuronal damage (Ji, 2021).

Müller cells exhibit significant stress and gliosis, as indicated by elevated levels of glial fibrillary acidic protein in diabetes experimental models (Yang, 2023). The adverse effects of a high-glucose environment are further manifested by the displacement and decrease of Kir4.1 potassium channels on Müller cell surfaces, alongside an increase in the water channel protein Aqp4 (Li et al., 2021). These alterations are associated with retinal edema, underscoring the vulnerability of retinal cells to their environment. Moreover, the regulation of neurotransmitters is disrupted, evidenced by increased expression of excitatory amino acid transporters EAAT1 and EAAT2 and the heightened uptake of glutamate by glucose-deficient Müller cells. This impaired glutamate regulation can lead to retinal neurodegeneration due to excitotoxicity (Toft-Kehler, 2014), consistent with observed elevations in glutamate levels in DR animal models (Diniz et al., 2019). Müller cells also contribute significantly to vascular pathology in DR by producing substantial amounts of VEGF (Uemura, 2021), which is implicated in early vascular leakage and neovascularisation, hallmarks of advancing DR. Additionally, the BM in the retinal vessel wall, shared by endothelial cells and pericytes, facilitates gap junctional communication and paracrine signalling, crucial for maintaining vascular function. Cytokines such as TNF- α and IL-1 induce retinal endothelial cell dysfunction by promoting oxidative stress and activating pathways like P38 MAPK and nuclear factor- κ B, while growth factors like transforming growth factor- β enhance endothelial cell permeability. Loss of pericytes, a key feature

of DR, along with dysregulated pericyte to endothelial cell communication, significantly contributes to the progression of the disease (Li & Fan, 2023).

The STZ mouse model, utilised to simulate the progression of diabetes, facilitated the exploration of intricate changes within the retinal NVU. By applying SBF-SEM, a method known for its precision in capturing high-resolution, three-dimensional images, this study aimed to provide a deeper understanding of the ultrastructural alterations in diabetic conditions. This technique allows for an in-depth visualisation of the NVU microstructure, including detailed interactions between endothelial cells, pericytes, Müller cells, and the BM. Such detailed ultrastructural analysis is pivotal for examining the microstructural changes within the retina, such as the interactions between pericytes and endothelial cells, the structure of endothelial tubules, and the presence and role of leukocytes. These components were critically evaluated to understand better the underlying changes and their implications in the pathology of DR.

4.2 Results

4.2.1 Ultrastructure

Retinal tissue samples were collected from 6-month-old, diabetic mice, in total, there were three mouse samples, each comprising a set of three capillaries. Stacks of 100-300 consecutive micrographs of the capillary ultrastructure were captured along the length of the vessel, covering depths of 12-36 μm . The ultrastructure of one capillary from each of the diabetic mouse samples is specifically showcased. This detailed analysis of the retinal NVU with the onset or progression of diabetes involved a total of nine capillaries from 6-month-old mice, and the resulting ultrastructural features are presented in **Figure 4-1-4.3**. The comprehensive examination provides valuable insights into the capillary morphology and organisation within the superficial capillary plexus, in the GCL of the diabetic mouse retina. The segmentation and colour assignments were applied as outlined in section 3.2.1 (**Figure 4-4** and **Figure 4-5**). Throughout this analysis, comparisons are consistently made with capillary samples from 6-month-old non-diabetic mice, as detailed in the previous chapter, to underscore the changes and continuities in capillary ultrastructure associated with diabetes.

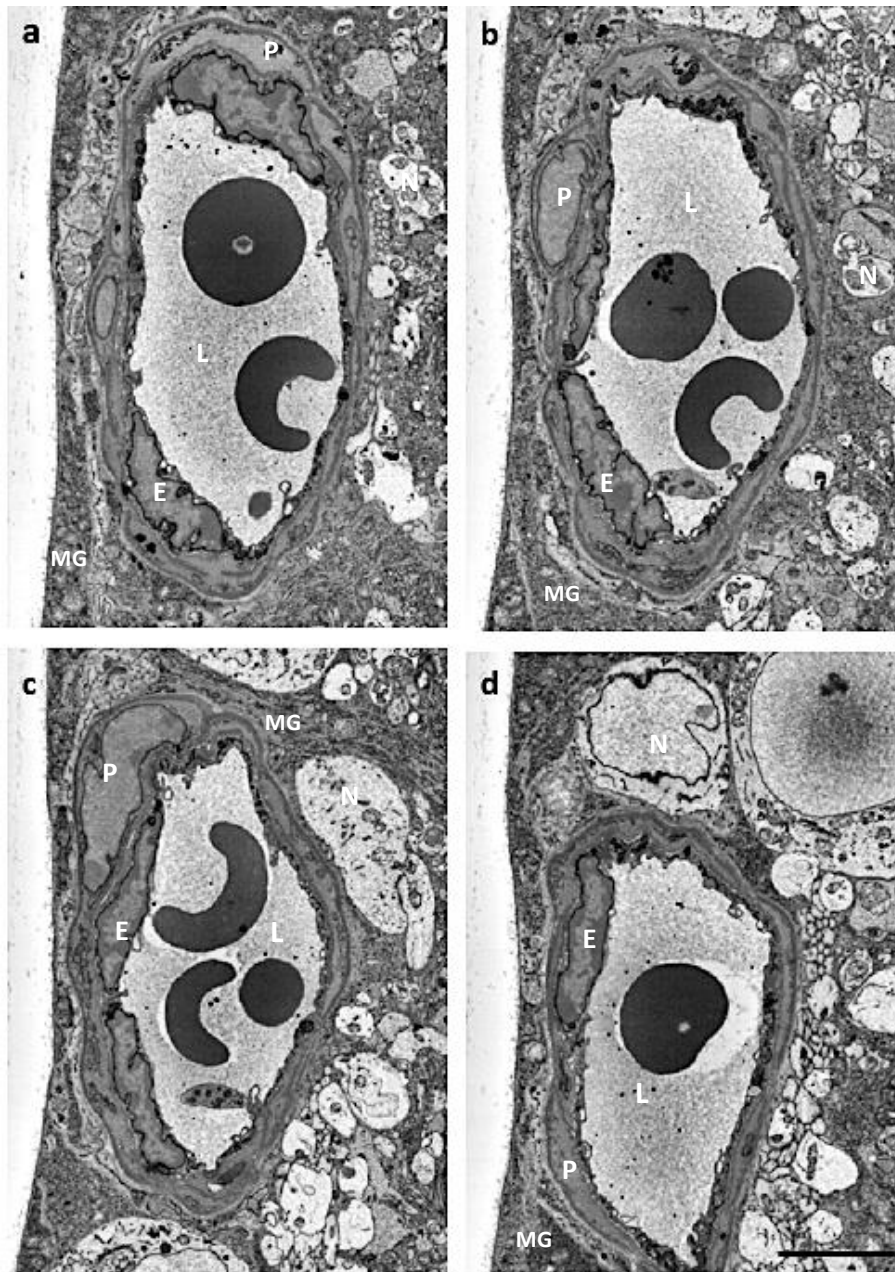


Figure 4-1 Ultrastructure of diabetic 6-month-old mouse capillary, sample 1. A collection of SBF-SEM micrographs taken from a mouse retinal capillary to display the morphological changes along the capillary length. a, slice 1 (0.1 μm), b, slice 25 (2.5 μm), c, slice 50 (5 μm) and d, slice 100 (10 μm). Lumen: L, Pericytes: P, Endothelium: E, Macroglia: MG, Neurons: N. Scale bar 4 μm . Full dataset can be found here: <https://figshare.com/s/f06d367d6da9cc6d1198>.

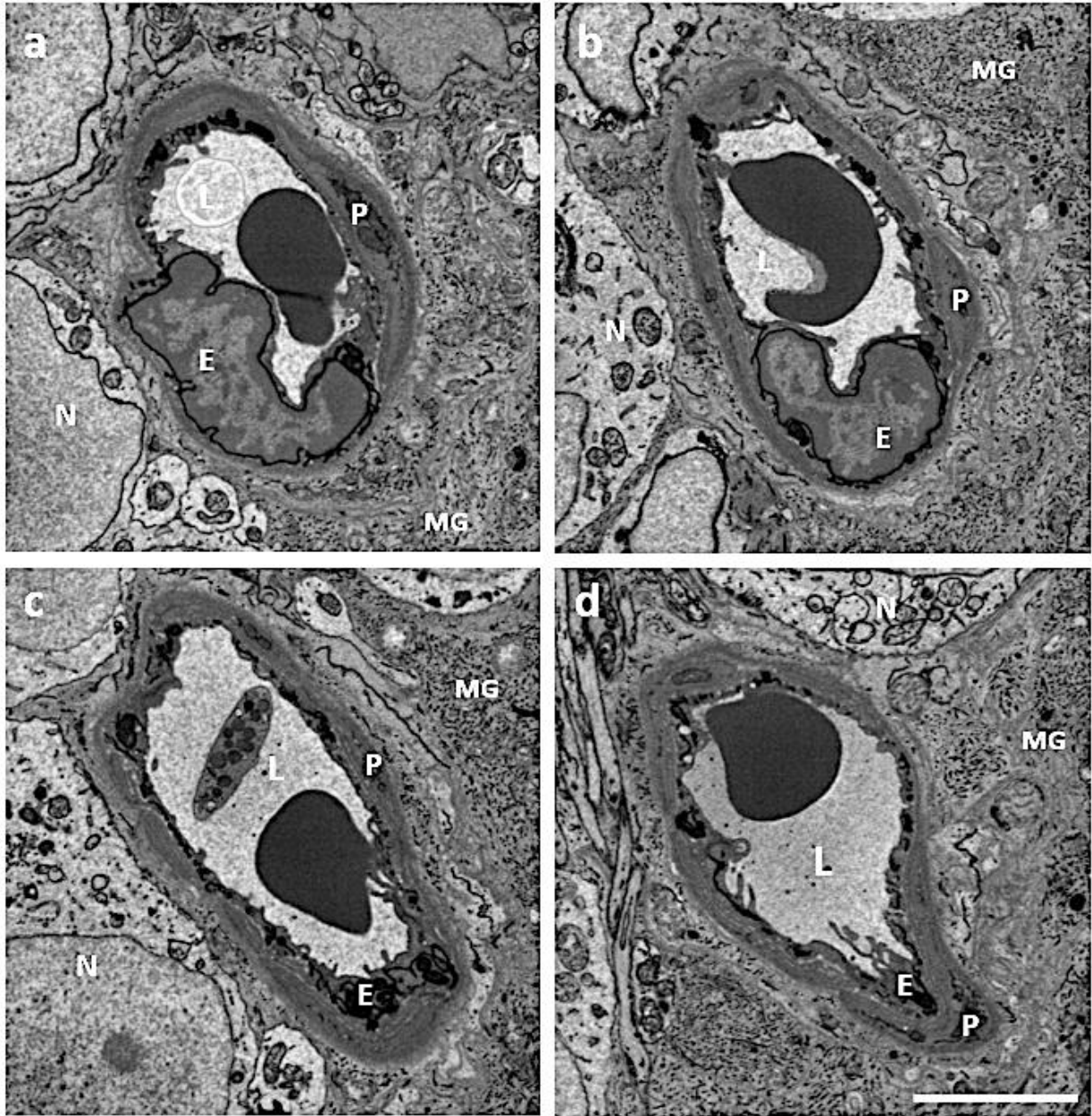


Figure 4-2 Ultrastructure of diabetic 6-month-old mouse capillary, sample 2. A collection of SBF-SEM micrographs taken from a mouse retinal capillary to display the morphological changes along the capillary length. a, slice 100 (10 μm), b, slice 125 (12.5 μm), c, slice 150 (15 μm) and d, slice 200 (20 μm). Lumen: L, Pericytes: P, Endothelium: E, Macroglia: MG, Neurons: N. Scale bar 3 μm . Full dataset can be found here: <https://figshare.com/s/9e650a62724ced4fb585>.

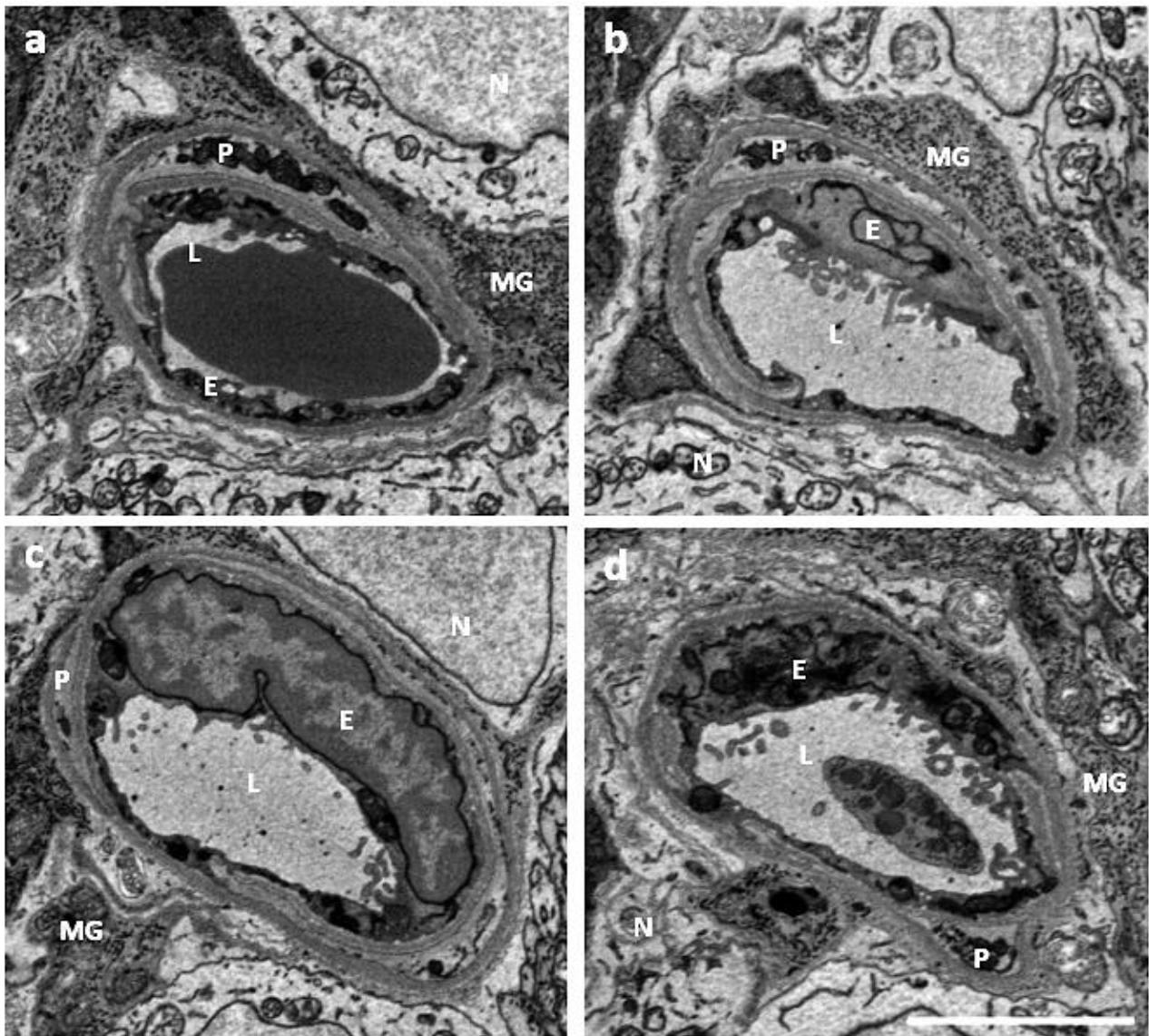


Figure 4-3 Ultrastructure of diabetic 6-month-old mouse capillary, sample 3. A collection of SBF-SEM micrographs taken from a mouse retinal capillary to display the morphological changes along the capillary length. a, slice 100 (10 μm), b, slice 125 (12.5 μm), c, slice 150 (15 μm) and d, slice 200 (20 μm). Lumen: L, Pericytes: P, Endothelium: E, Macroglia: MG, Neurons: N. Scale bar 3 μm . Full dataset can be found: <https://figshare.com/s/43917a967b535710cef6>.

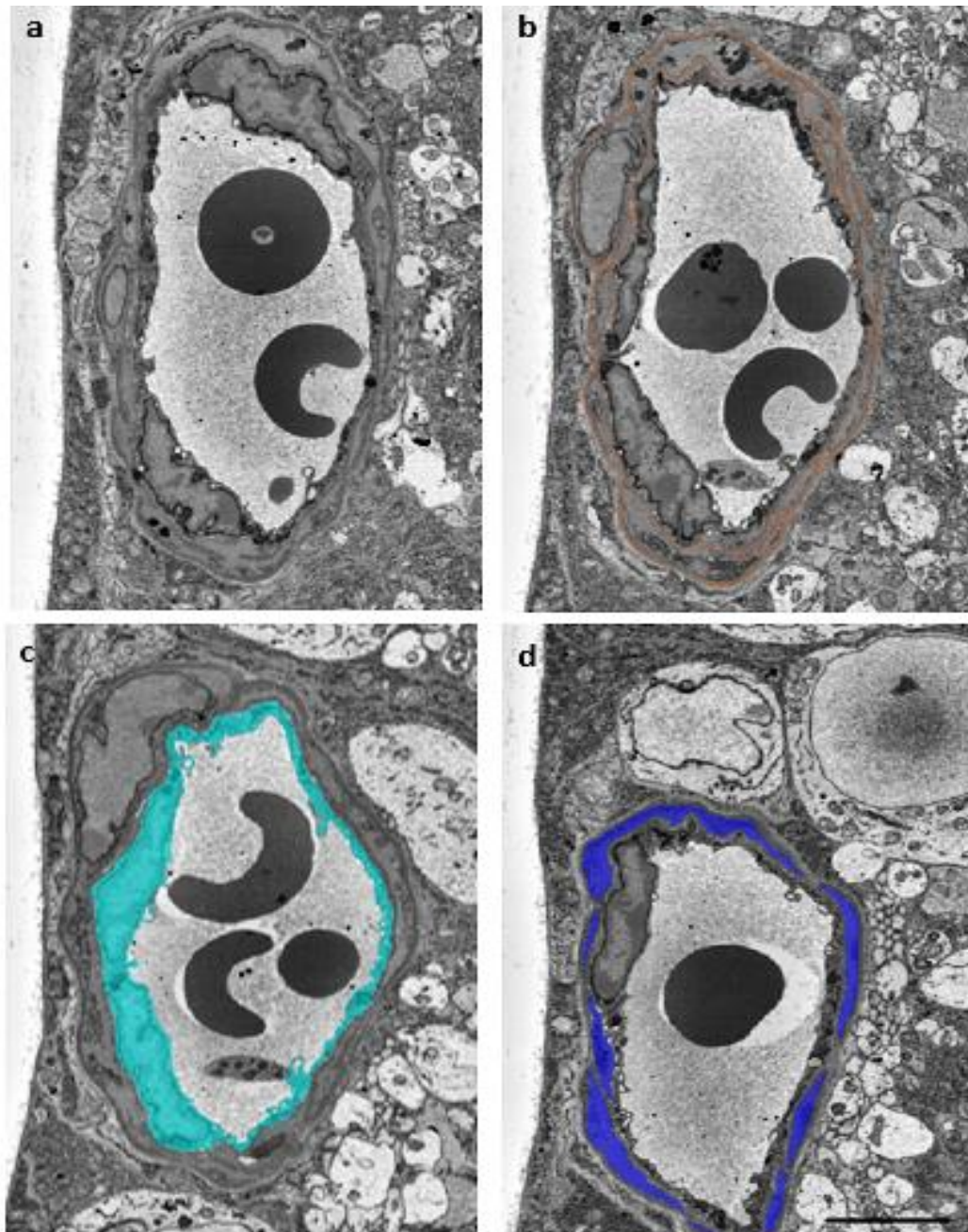


Figure 4-4 Segmented vasculature of diabetic 6 month old mouse capillary 1. A collection of SBF-SEM micrographs taken from a mouse retinal capillary to display the morphological changes of along the capillary length. a, raw image slice 1 (0.1 μm), b, basement membrane (brown), slice 25 (2.5 μm), c, endothelium (aqua), slice 50 (5 μm) and d, pericytes (blue), slice 100 (10 μm). Scale bar 4 μm .

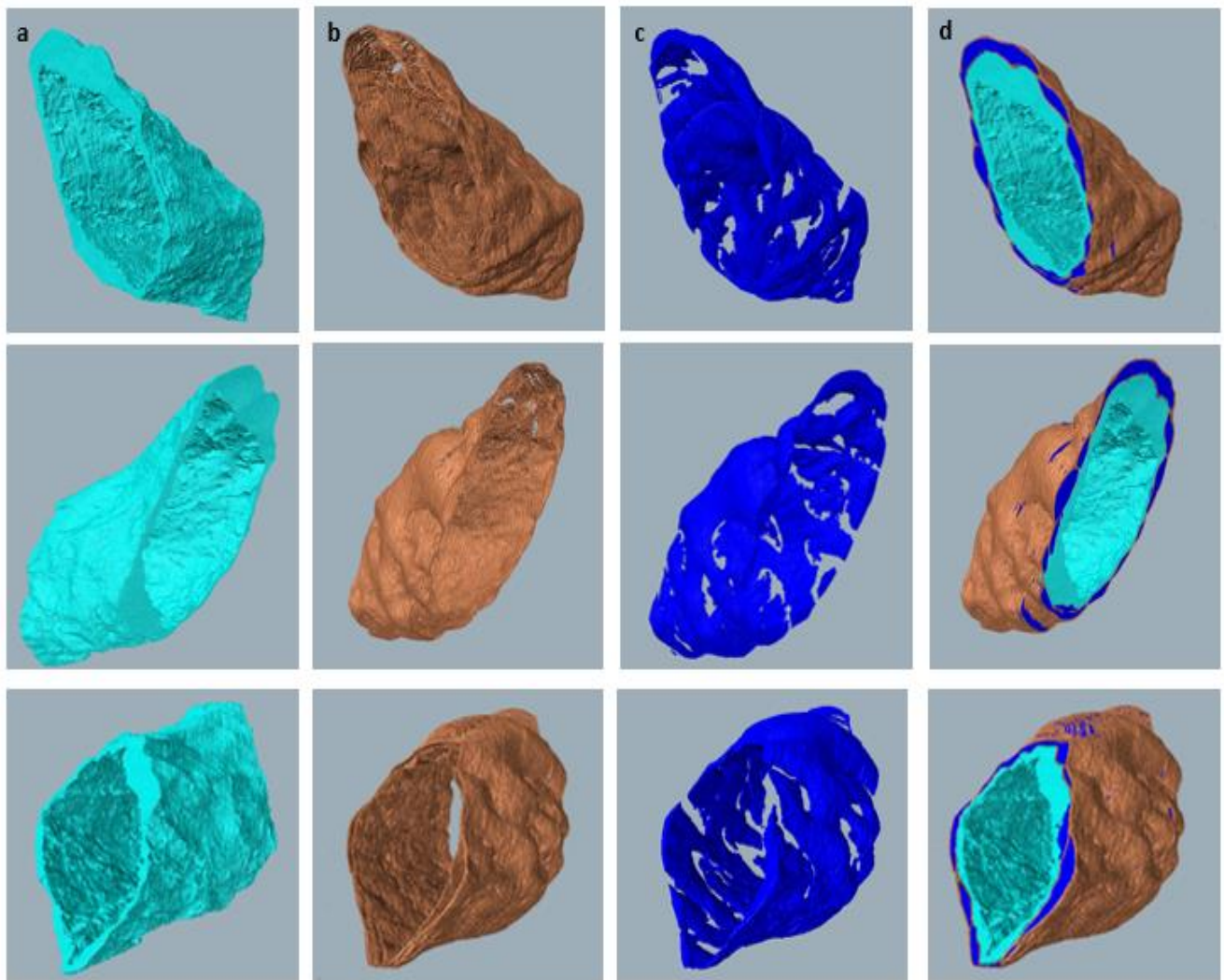


Figure 4-5 3D reconstruction of diabetic 6 month old mouse capillary 1 vasculature. Displayed are features associated with a 3D reconstruction of the vasculature of capillary 2. Column a: endothelium (aqua); column b: basement membrane (brown); column c: pericytes (blue); and column d: combined vasculature.

4.2.1 Basement membrane irregularity and thickening

A comprehensive analysis conducted on 12 diabetic 6-month mouse retinal capillaries, revealed minimal to negligible evidence of basement membrane thickening (**Figure 4-6**). Electron micrographs reveal distinct features within the capillary structure, revealing localised variation in BM thickness. Interestingly, the observed thickening was not uniform, displaying varying levels around the circumference of the capillary. Thorough analysis of BM membrane thickness was performed across multiple sections within each dataset, which provided valuable quantitative insights that complement the qualitative assessment derived from our image data. Analysis of mean thickness revealed that there was no significant BM thickening relative to the stack of data, but maximum

thickness revealed localised thickening in some regions of the capillary. This further confirmed the qualitative assessment of regional BM thickness identified. This pinpointed variations and patterns in BM thickness in 6-month-old non-diabetic and diabetic mouse capillaries, with focus on identifying the maximum thickness observed around the circumference of each capillary (**Figure 4-7**).

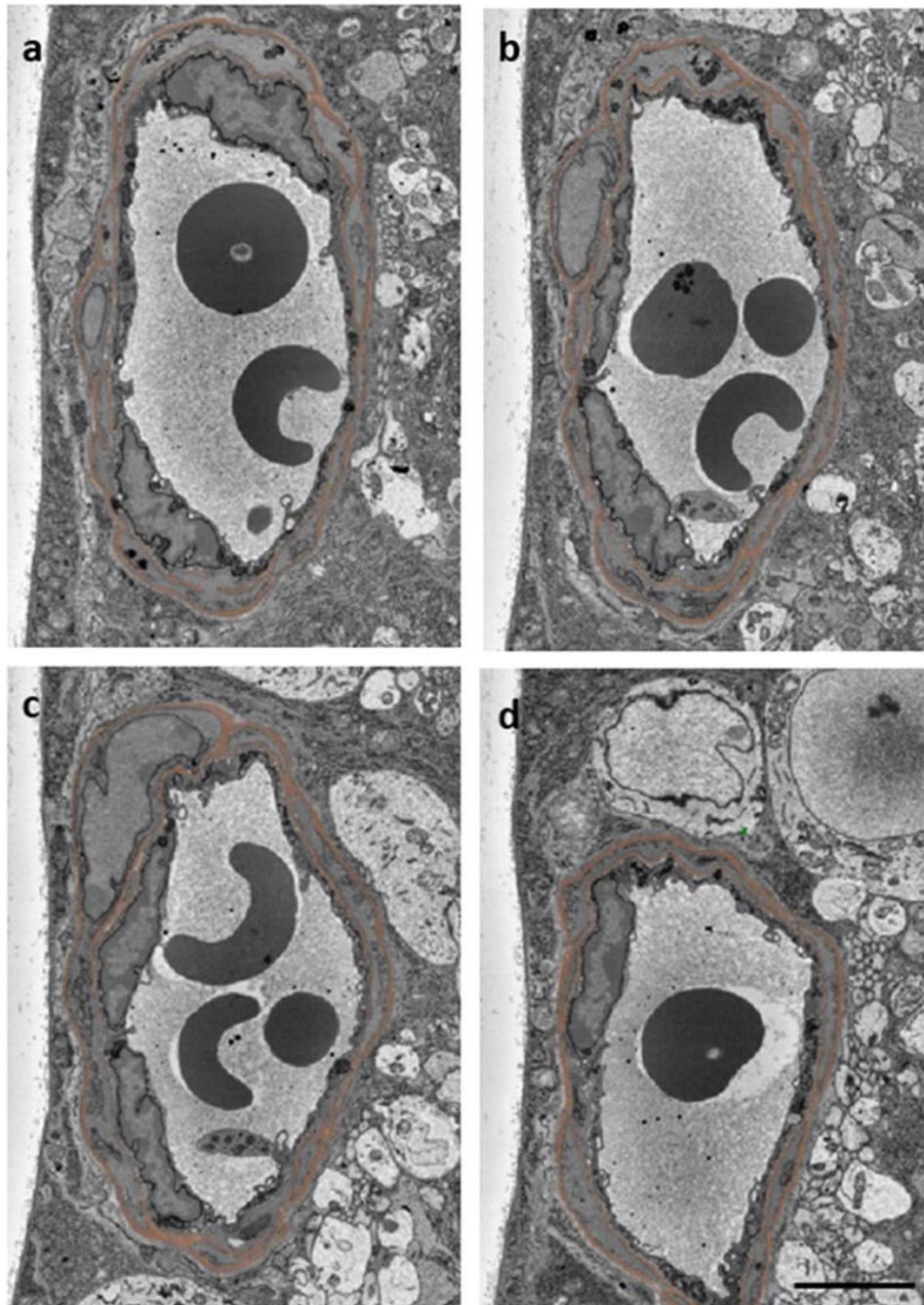


Figure 4-6 Segmented BM showing convoluted nature of diabetic 6 month old mouse capillary 1. A collection of SBF-SEM micrographs taken from a mouse retinal capillary to display the morphological changes of BM (brown) along the capillary length. a, slice 1 (0.1 μm), b, slice 25 (2.5 μm), c, slice 50 (5 μm) and d, slice 100 (10 μm). Scale bar 4 μm .

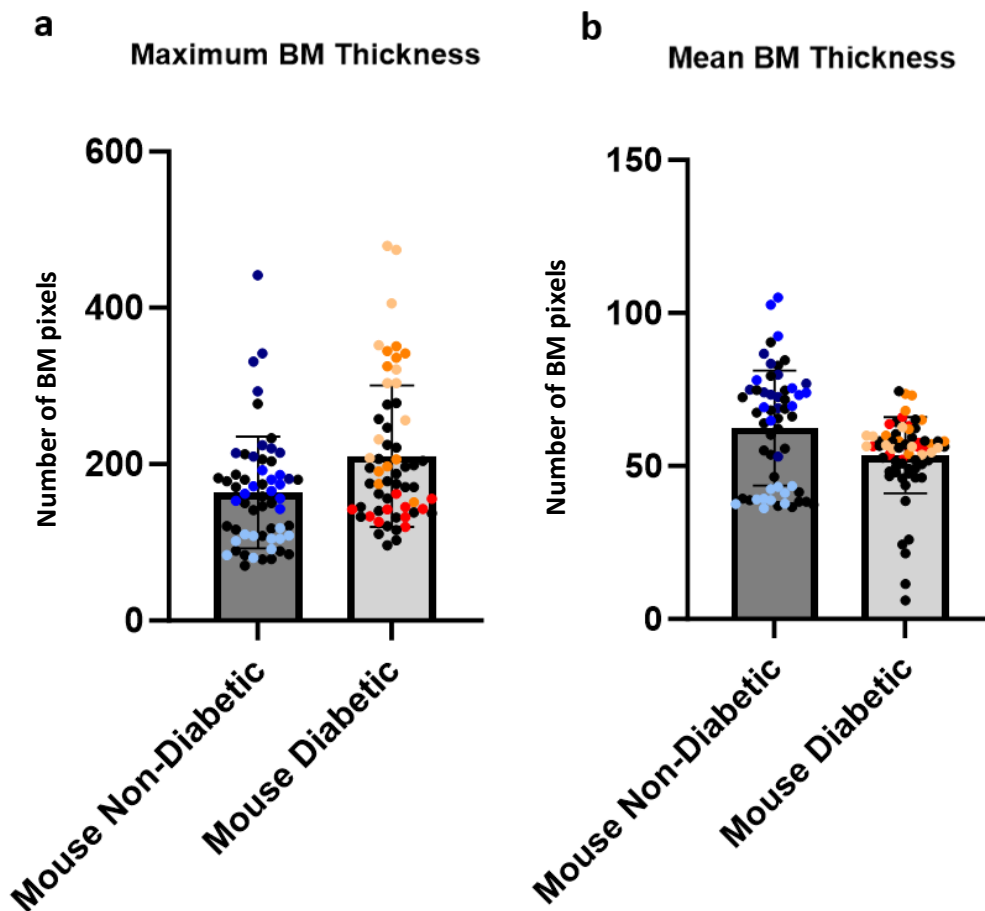


Figure 4-7 Maximum and mean BM thickening of mouse diabetic vs non-diabetic. Every 10th section through the depth of the stack, and the thickest sections were analysed consecutively, represented as coloured dots, each colour depicts a separate capillary. Specifically, BM thickness was calculated by analysing every 10th section (e.g., sections 1, 10, 20, 30, up to section 100). After identifying the section with the thickest BM, the thickness for five sections before and five sections after that thickest slice were calculated. These consecutive sections, representing the region around the thickest BM, are shown as coloured dots. Analysis was conducted on three capillaries each state including three diabetic mice and three non-diabetic mice. Error bars represent standard deviations.

4.2.2 Separation of cells from BM

Cells which make up the retinal NVU have been observed to separate from the BM. Gaps between the endothelium which borders the BM have been observed, similarly in pericytes which are encompassed by the BM. This retraction of cells has also been observed to extend beyond the vasculature and electron lucent gaps were observed between the surrounding glial and neuronal

cells and BM (**Figure 4-8**). Additionally, this separation is evident across multiple sections, as illustrated in **Figure 4-9**. Analysis of 18 capillaries from 3 non-diabetic and 3 diabetic samples, has revealed significant differences in the frequency of BM separation from cells constituting the neurovascular unit (NVU) between diabetic and non-diabetic conditions, as illustrated in **Figure 4-10**. Diabetic capillaries consistently exhibited a greater degree of cell detachment from the BM compared to the non-diabetic capillaries. This finding underscores a alteration in the structural integrity of the retinal NVU under diabetic conditions. **Table 4-1** and **Table 4-2** provide a detailed account of the total occurrences of BM separation observed across all analysed capillaries, along with corresponding information on the specific sections where these occurrences were observed.

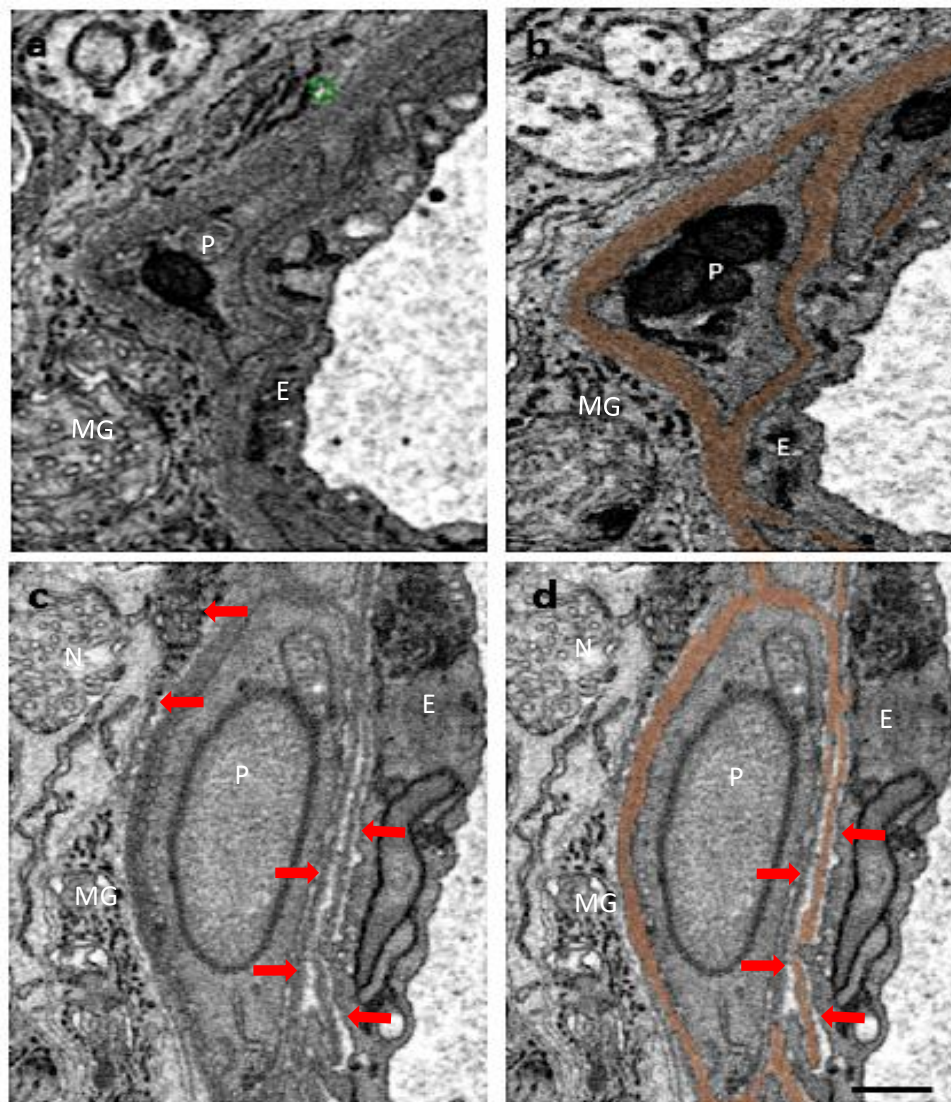


Figure 4-8 BM separating from cells in the NVU. a. and b. 6-month-old non-diabetic capillary 1 displaying the direct contact nature of endothelium and pericytes to basement membrane. c. d. 6-month-old diabetic capillary displaying electron lucent gapping from basement membrane. Red arrows

indicate electron lucent gaps where the endothelium, pericytes and cells surrounding vasculature are separating from BM. P, pericyte, E, endothelium, N, neuron, MG, macroglia.

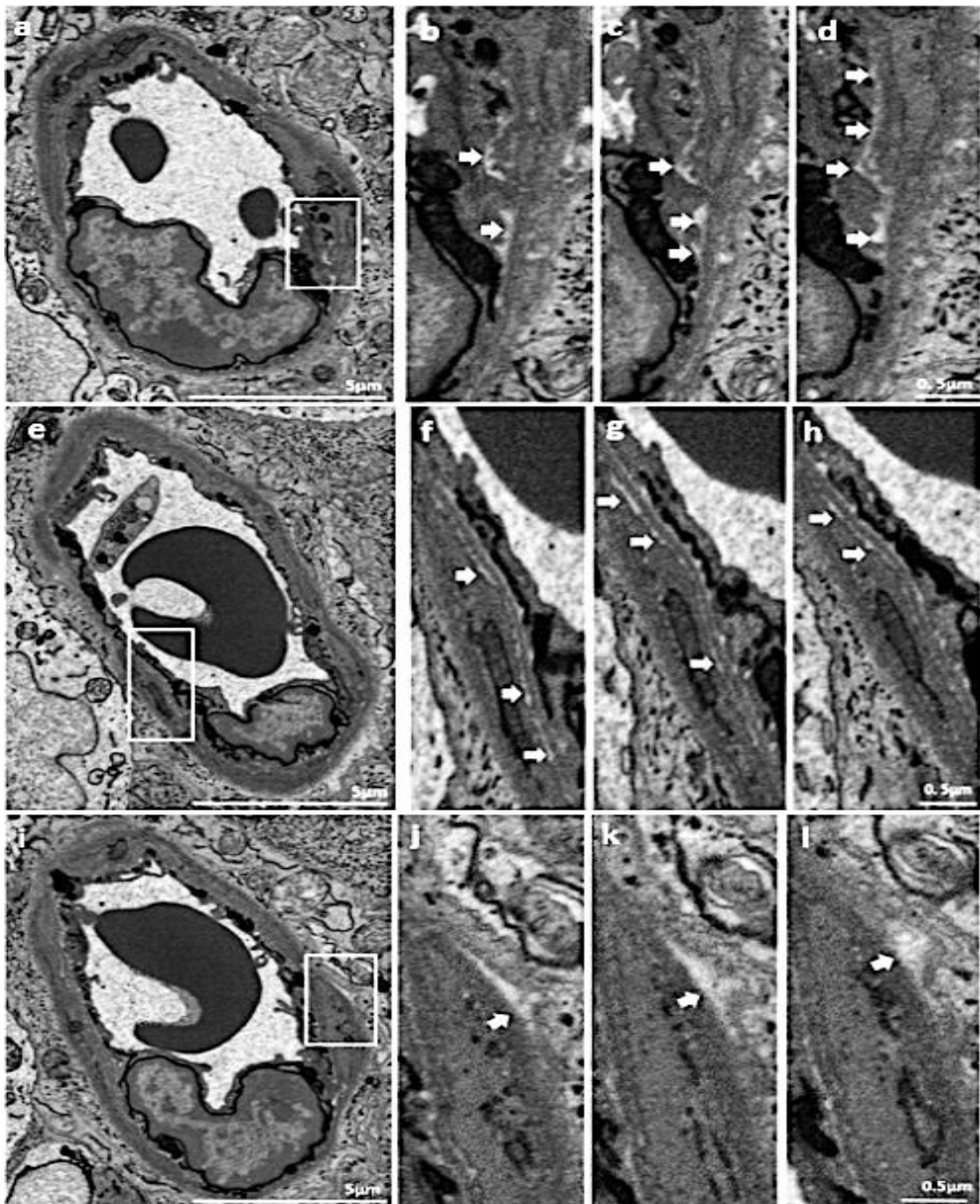


Figure 4-9 Separation of BM from NVU cell components across multiple sections. 6-month-old diabetic capillary 1 from sample 2 (SBF108-5). a. capillary displaying separation of BM from endothelial cell, white box indicates area of separation shown, b, enlarged area of separation of BM from endothelium on section 112, c, section 113, d, section 114. e. capillary displaying separation of BM from pericyte, white box indicates area of separation shown, f, enlarged area of separation of BM from endothelium on section 140, g, section 141, h, section 142. i. capillary displaying separation of BM from cells surrounding vasculature (neurons and macroglia), white box

indicates area of separation shown, j, enlarged area of separation of BM from endothelium on section 125, k, section 126, l, section 127.

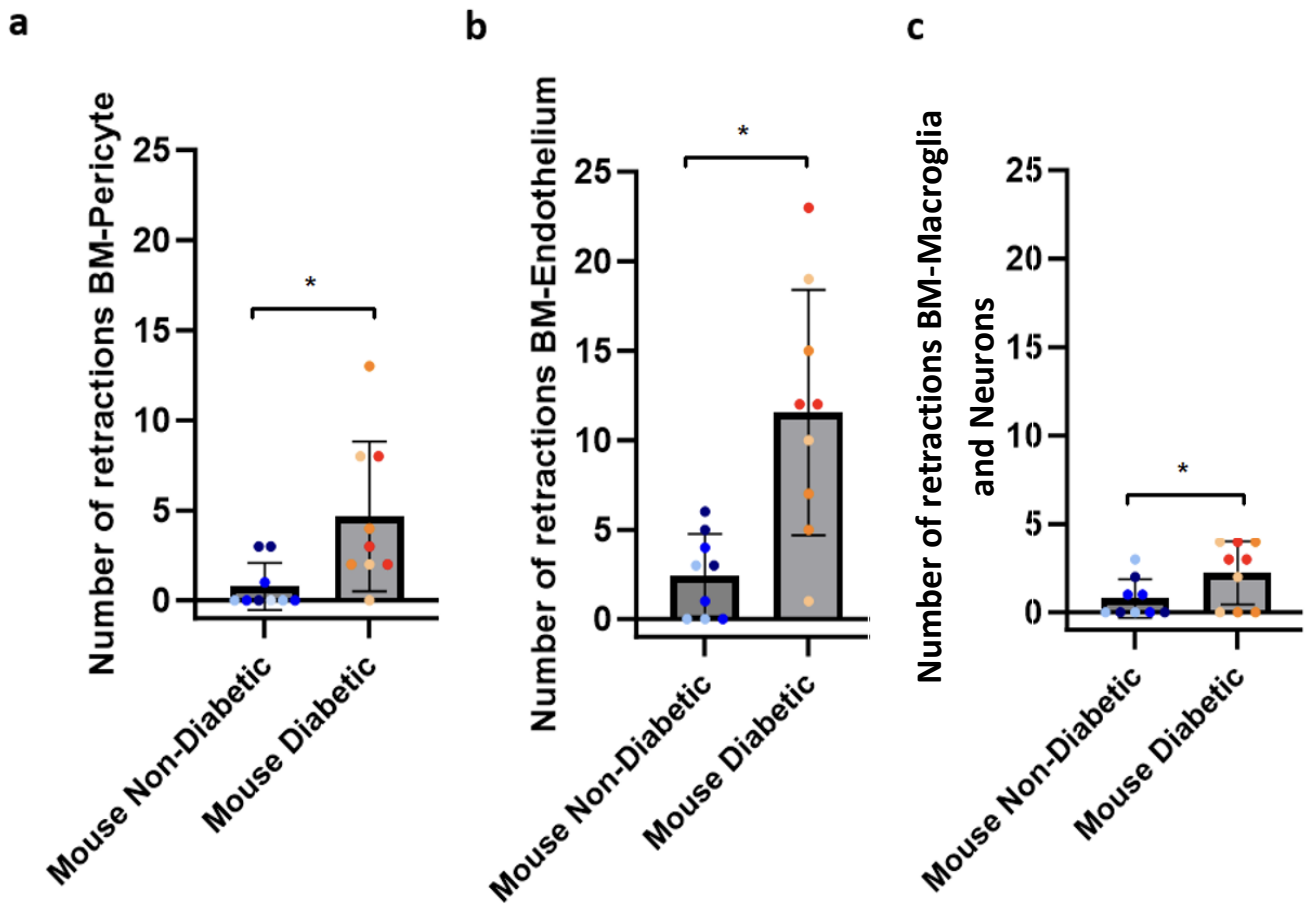


Figure 4-10 Comparative analysis of basement membrane separation in diabetic and non-diabetic capillaries. This graph illustrates the frequency of separation occurrences from the BM to distinct cellular components within the NVU. a. BM to Pericytes: Occurrences of separation between the BM and pericytes in diabetic (orange) and non-diabetic (blue) capillaries. b. BM to endothelium. c. BM to Macrogliia and Neurons (combination of cells surrounding vasculature). Data is derived from the analysis of 9 diabetic and 9 non-diabetic capillaries, from a total of 6 mice, 3 diabetic and 3 non-diabetic. Error bars represent standard deviations.

4.2.3 Pericyte-endothelial interactions

Examination of the retinal NVU has consistently demonstrated frequent interactions between pericytes and endothelial cells, characterised by distinctive peg-and-socket formations. Nanoscale imaging has revealed a distinctive alteration in these heterocellular interactions during diabetes. An increase in electron-lucent socket space surrounding the pegs within peg-and-socket formations was evident under diabetic conditions (**Figure 4-11** and **Figure 4-12**). This observed increase in socket

space hints at a structural modification in the pericyte-endothelial cell interactions within the retinal NVU under diabetic conditions. In non-diabetic capillaries, the presence of peg-and-socket formations is a recurrent observation, indicating their active participation in heterocellular interactions within the NVU. However, an investigation into the distribution of these formations in diabetic samples has brought to light a marked reduction in their frequency under diabetic conditions. The distribution pattern is shown in **Figure 4-13**. This analysis extends to the examination of the peg numbers and percentage of peg coverage across the capillary depth (**Figure 4-14**). This includes detailed calculations of the number of sections along the depth of the capillary which contain a peg. From these calculations, the percentage of peg coverage was derived, calculating the number of sections within a capillary that contain a peg and comparing this to the total number of sections across the entire capillary, offering a comprehensive view of peg distribution across the capillary depth, unveiling a substantial decrease in peg coverage across diabetic capillaries, and a notable reduction in the number of observed pegs compared to the non-diabetic.

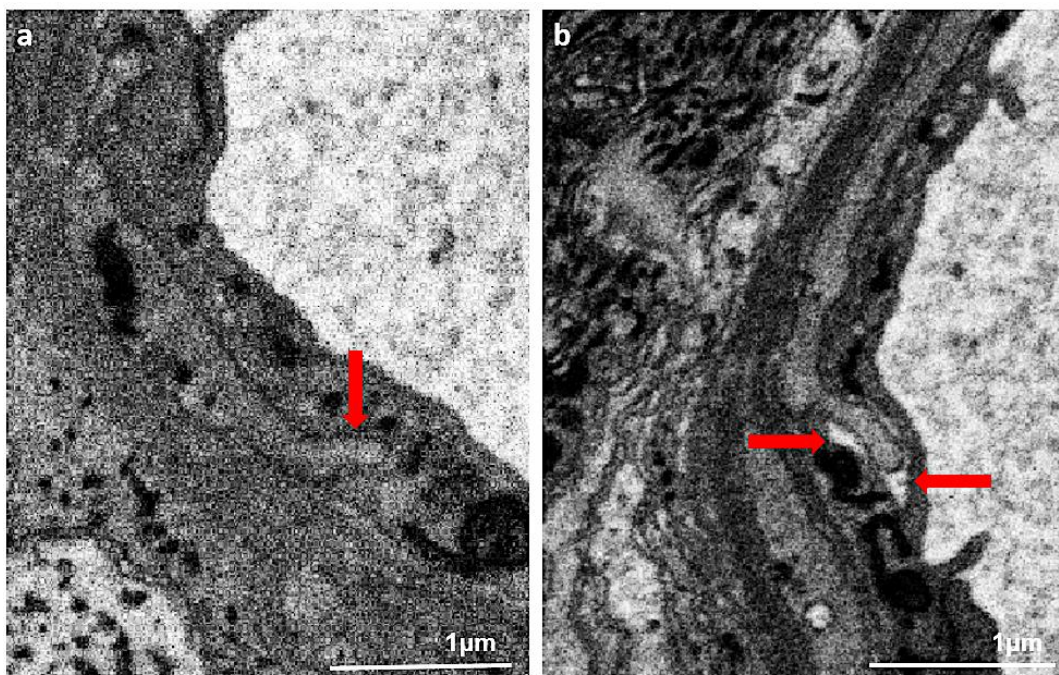


Figure 4-11 Comparison of peg and socket formations in non-diabetic vs diabetic. a. non-diabetic capillary displaying peg and socket interaction indicated by the red arrow, b. peg and socket interaction in diabetic capillary displaying electron lucent space in the socket surrounding the peg, indicated by red arrows.

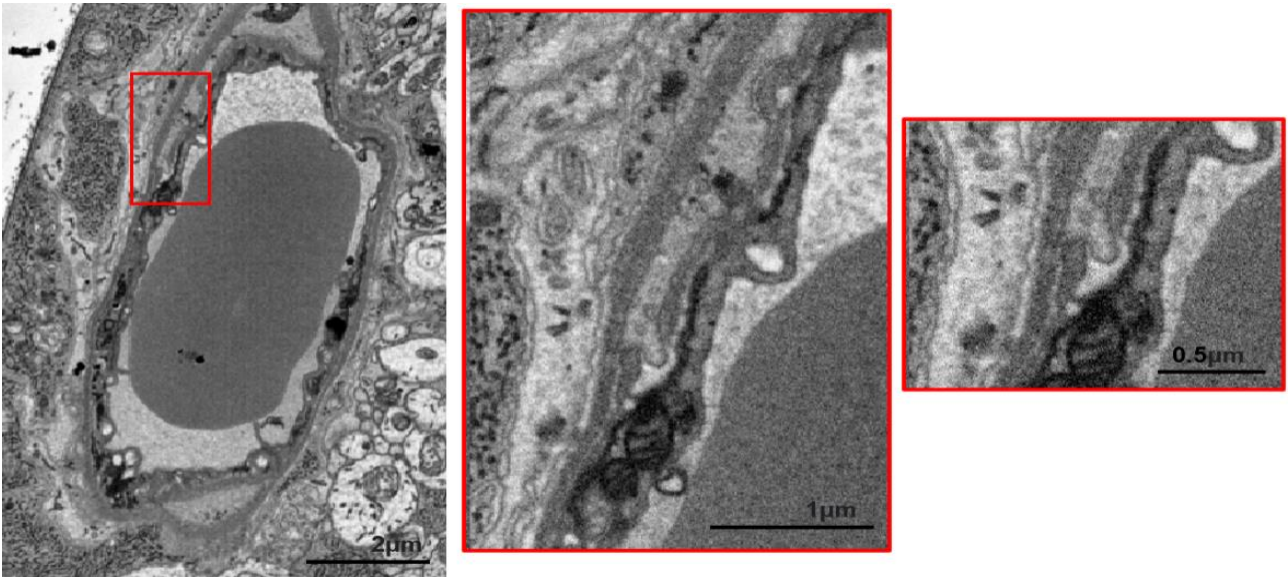


Figure 4-12 Close-up view illustrating the spatial arrangement around a peg within a diabetic capillary. The image emphasises the intricate details of the surrounding space, providing a closer examination of the microenvironment.

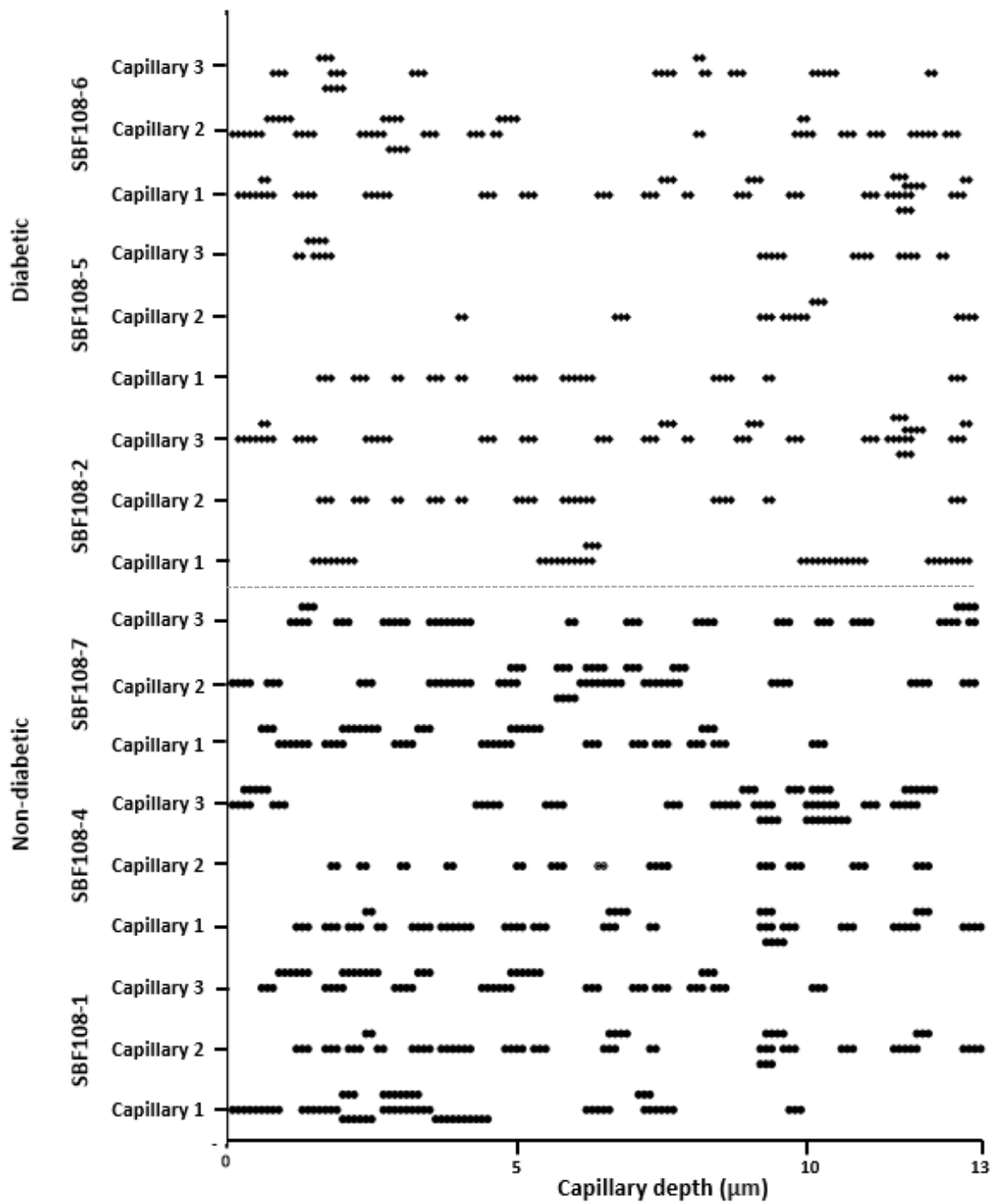


Figure 4-13 Distribution of peg and sockets across 6-month mouse diabetic vs non-diabetic capillaries. The distribution of peg-and sockets evident across 130 sections examined in 18 capillaries. Note more than one peg-and-socket may appear in the same sections (i.e. at different points of pericyte-endothelial membrane interaction in the same z-plane).

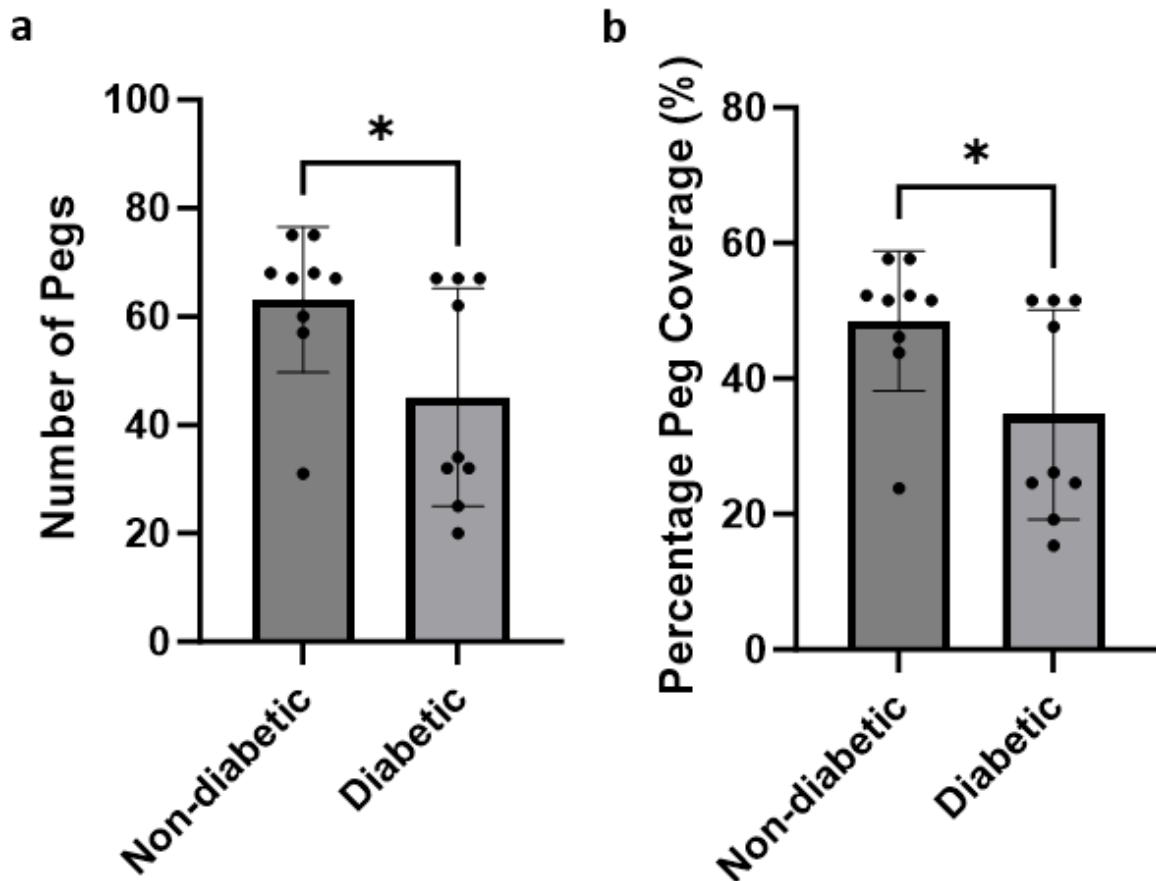


Figure 4-14 Peg analysis in non-diabetic and diabetic capillaries. These panels present a comprehensive analysis of peg count distribution, showcasing a. the quantitative disparity in peg numbers between diabetic and non-diabetic capillaries and b. the percentage of peg coverage within a capillary, calculated by the number of sections within a capillary that contain a peg and comparing this to the total number of sections across the entire capillary. Error bars represent standard deviations.

4.2.4 Endothelial tubules

Presence of electron-lucent tubules, appearing as white, electron-lucent voids with size variations were identified within the endothelial structure (**Figure 4-15**). In diabetic capillaries, there was an increase in the quantity and clustering of these tubules. This increase was quantitatively assessed by counting each tubule within the endothelium, allowing for a precise comparison between diabetic and non-diabetic conditions (**Figure 4-16**). The results indicate a significant rise in the number of these structures in the diabetic endothelium.

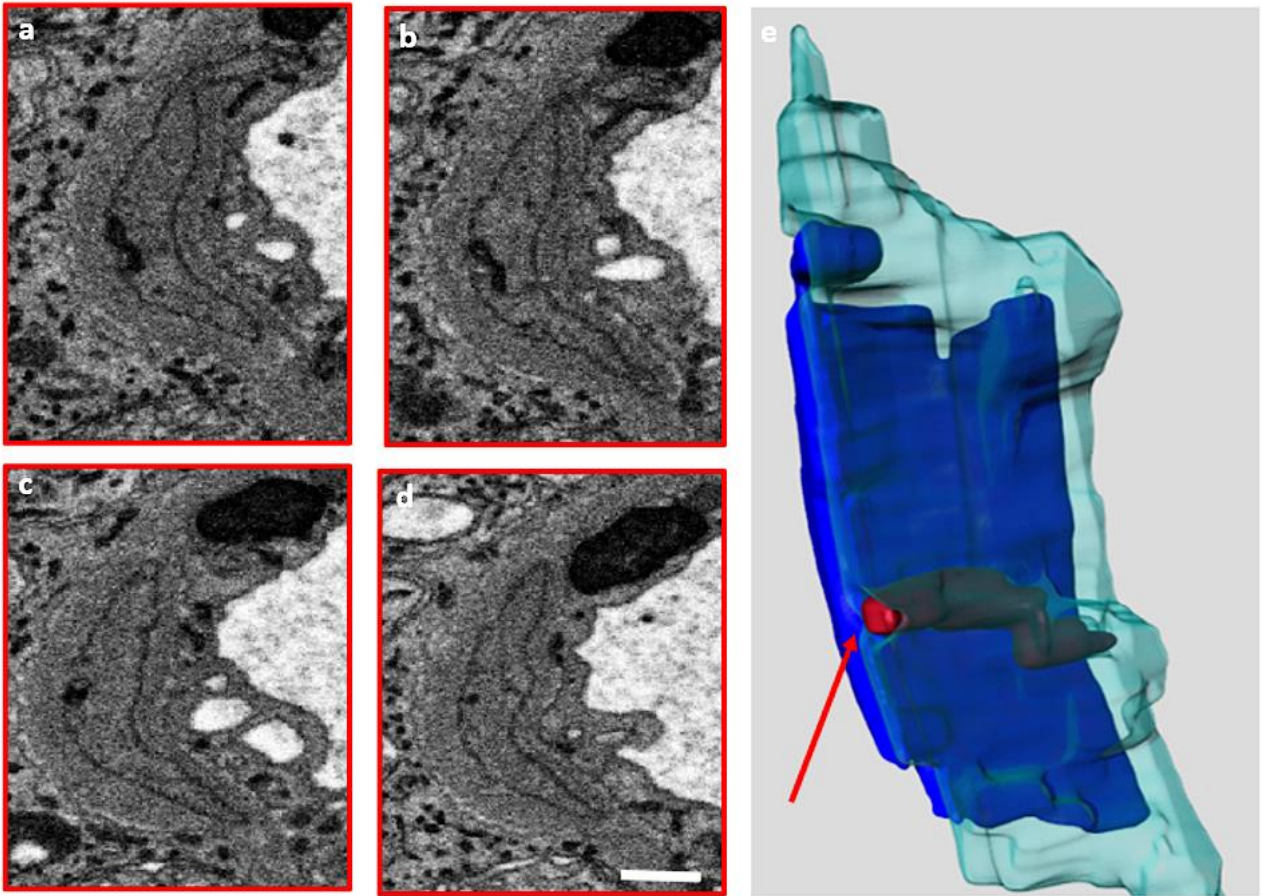


Figure 4-15 Endothelial tubules in 3D from a mouse diabetic capillary. a. presence of endothelial tubule on section 1 b. section 2, c. section 3, d. section 4, e. 3D reconstruction of tubule. Red arrows indicate endothelial tubules. Scale bar 2 μ m.

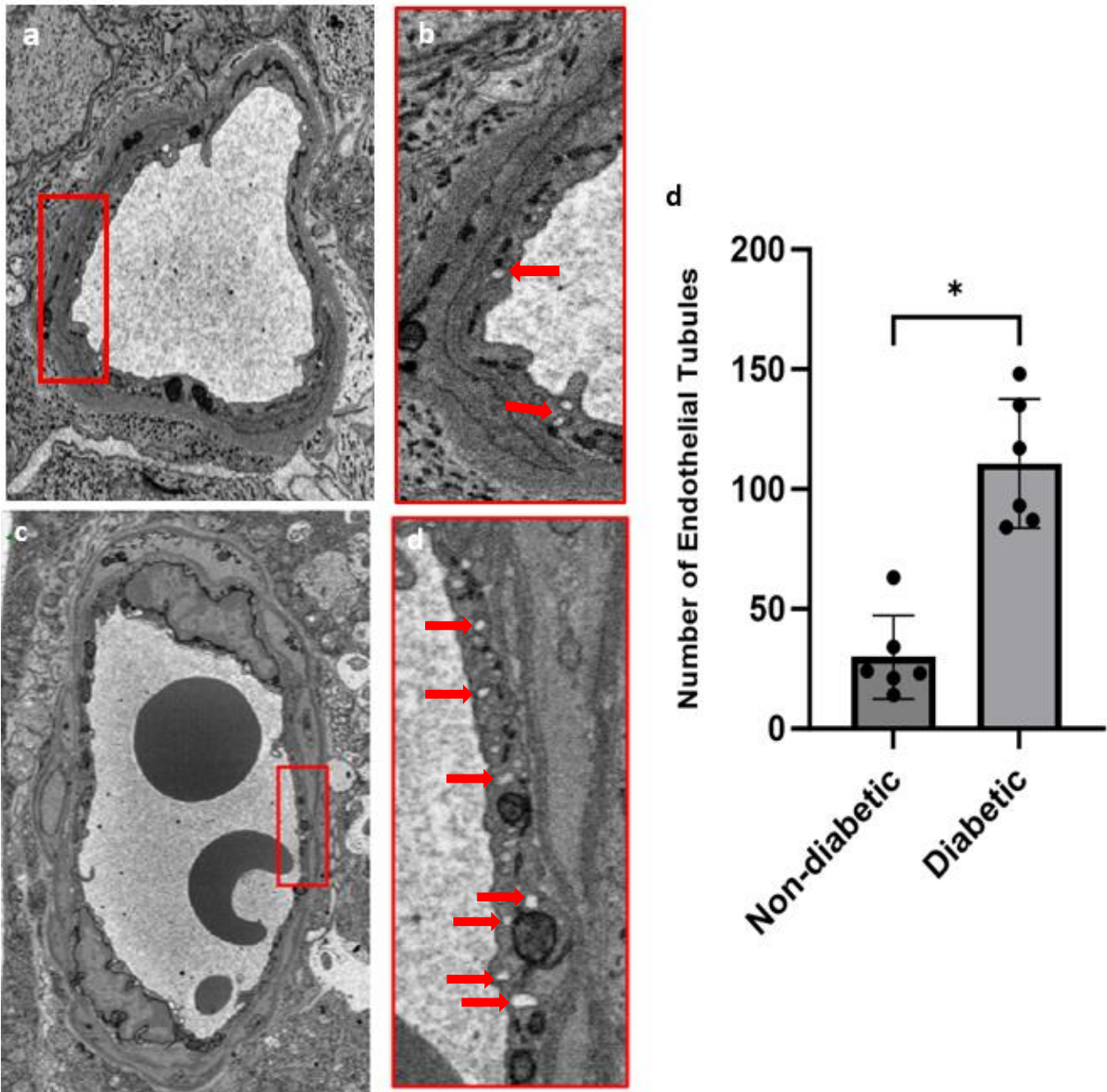


Figure 4-16 Endothelial tunnels in non-diabetic vs diabetic capillaries. a. non-diabetic capillary, b, area of endothelium enlarged showing few numbers of endothelial tubules, c. diabetic capillary, red box indicates area enlarged in d, displaying increased numbers of white electron lucent tubules within endothelium. d. quantitative assessment of endothelial tubules calculated via a morphological count of electron lucent holes within the endothelium of two capillaries from each mouse sample, totalling 6 diabetic and non-diabetic 6-month-old capillaries. Error bars represent standard deviations.

4.2.5 Leukocytes

Leukocytes were identified within the capillary lumen in a subset of our datasets, and a notable observation emerged when comparing diabetic and non-diabetic capillaries (**Table 4-3**). Intriguingly, a higher prevalence of leukocytes was observed in the diabetic capillaries. In SBF-SEM images of retinal capillaries, leukocytes can be distinguished from other vascular and luminal cell types by several key characteristics. Leukocytes typically exhibit a prominent, often lobulated nucleus with condensed chromatin, in contrast to the elongated, flattened nuclei of endothelial cells lining the capillary walls. Additionally, leukocytes often have cytoplasmic granules, particularly in granulocytes like neutrophils, which appear as electron-dense structures. Their cytoplasm is generally less electron-dense compared to endothelial cells or pericytes, and may contain vacuoles or lysosomes, further aiding in their identification. Importantly, leukocytes are round or irregular in shape and are found freely floating within the capillary lumen or occasionally adhering to the capillary wall, but they are not integrated into the vessel structure itself. To ensure accurate quantification and prevent duplicate counts, each leukocyte was meticulously traced through consecutive sections of the stack, allowing us to confidently identify and distinguish individual cells across the dataset.

Upon closer examination, leukocytes were observed making direct contact with endothelial projections, suggesting a potential interaction between leukocytes and the endothelial components within the capillary microenvironment (**Figure 4-17 – 4-18**). This finding suggests a possible association between diabetes and altered leukocyte dynamics within the retinal capillaries, shedding light on the intricate interplay within the retinal neurovascular unit in diabetic conditions. The detailed distribution and interactions of leukocytes within the capillary microenvironment are presented and discussed in the following sections.

A qualitative assessment was undertaken to investigate the presence of endothelial projections in capillaries with leukocytes compared to those without leukocytes, considering both diabetic and non-diabetic capillary contexts. This was done by systematically tracing endothelial projections, through the dataset, encompassing a stack of images that enabled the tracing of each endothelial projection in three dimensions (**Figure 4-19**). Quantifications were performed via a morphological count, where each identified endothelial projection was followed through the stack of data to facilitate a comprehensive 3D assessment.

Table 4-3 Leukocyte count in diabetic and non-diabetic capillaries. The table provides a comprehensive listing of diabetic and non-diabetic samples, indicating the respective counts of leukocytes

observed within each sample. Entries highlighted in green denote samples where leukocytes were identified.

	Capillary number	Leukocytes count
Non-diabetics	SBF108-1 C1	1
	SBF108-1 C2	0
	SBF108-1 C3	0
	SBF108-4 C1	3
	SBF108-4 C2	0
	SBF108-4 C3	0
	SBF108-7 C1	0
	SBF108-7 C2	0
	SBF108-7 C3	0
Diabetics	SBF108-2 C1	6
	SBF108-2 C2	0
	SBF108-2 C3	0
	SBF108-3 C1	1
	SBF108-3 C2	0
	SBF108-3 C3	1
	SBF108-5 C1	4
	SBF108-5 C2	8
	SBF108-5 C3	0
	SBF108-6 C1	2
	SBF108-6 C2	1
	SBF108-6 C3	0

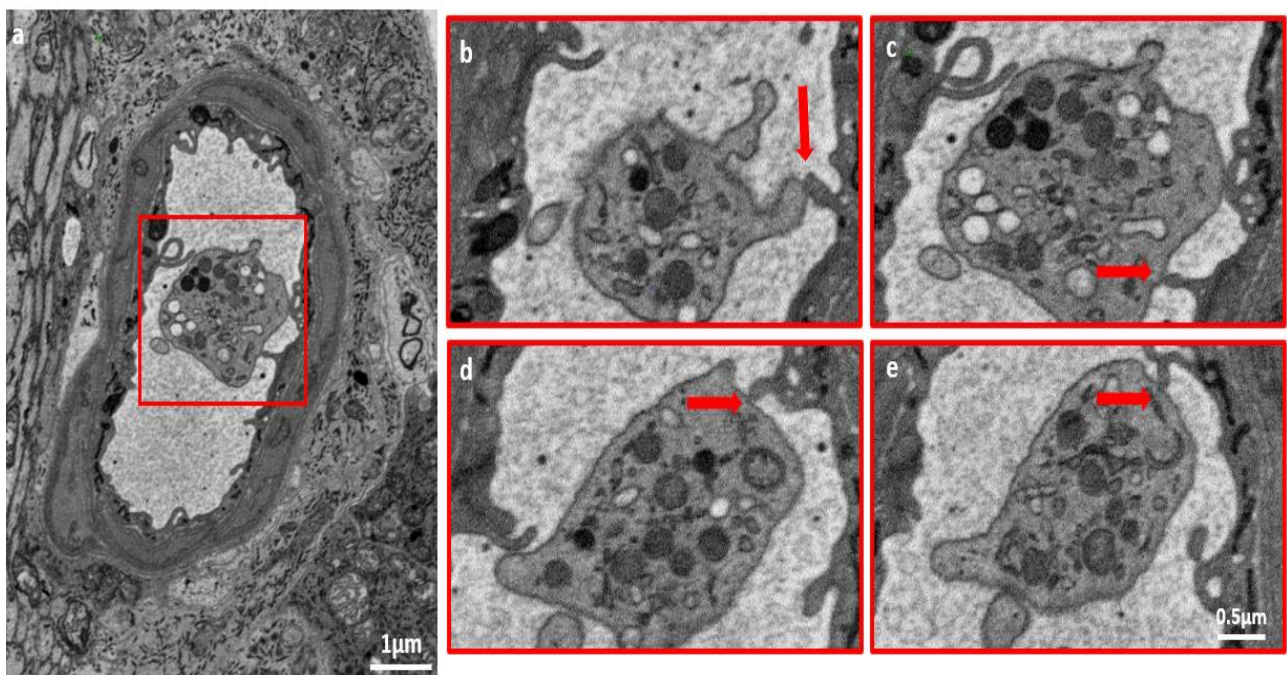


Figure 4-17 Leukocyte contact with endothelial projections Visualisation of leukocyte interactions with endothelial projections, a. diabetic capillary with presence of leukocyte within lumen, b. enlarged view of leukocyte present on section 100, c. section 106, d. section 116, and e. 118. Red arrows indicate direct contact of leukocytes with endothelial projections.

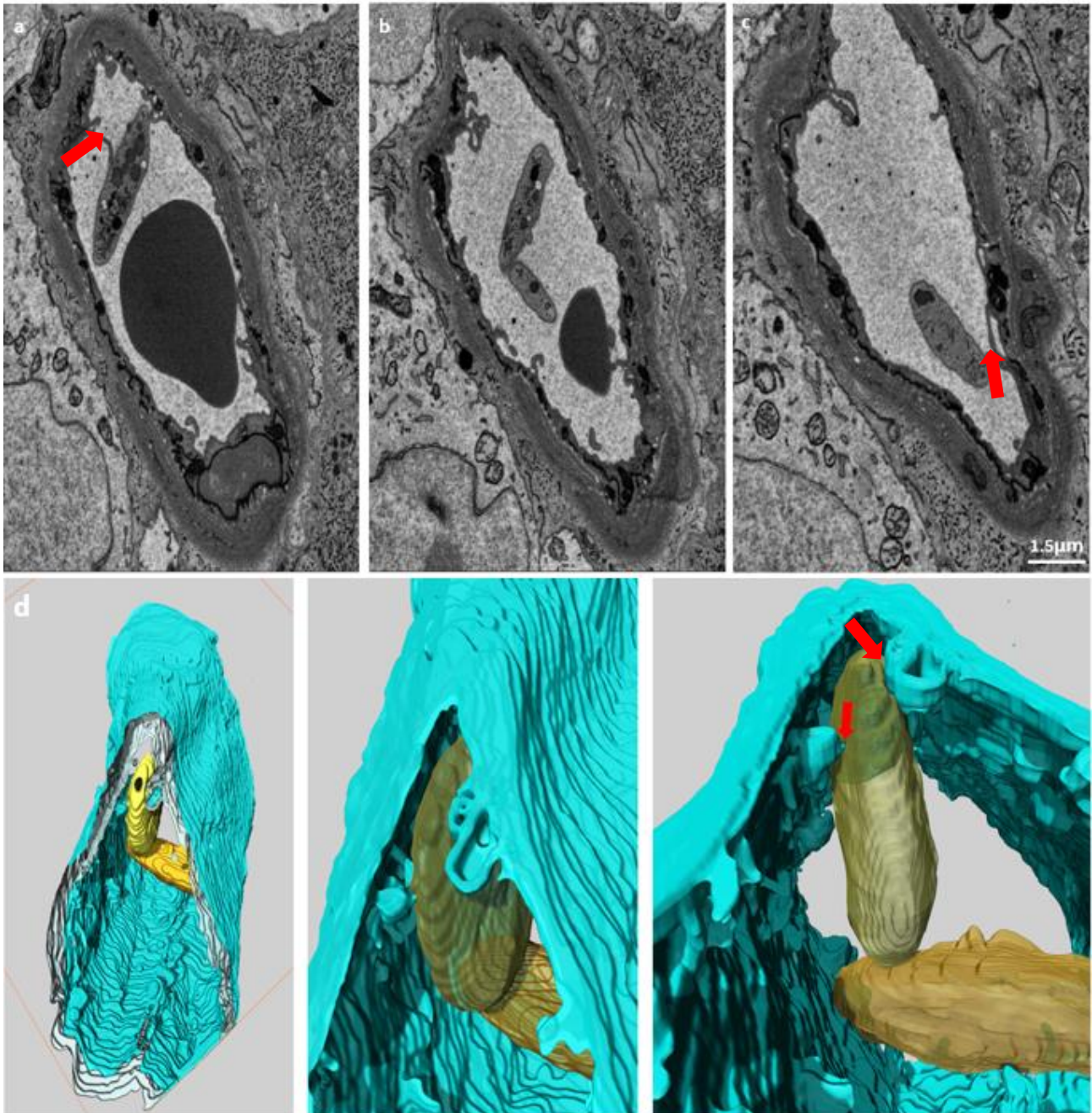


Figure 4-18 3D reconstruction of endothelium and leukocyte. 3D visualisation of leukocyte making direct contact with endothelial projections. a-c raw data images of diabetic capillary across serial sections showing leukocyte making direct contact with endothelial projections. d. multiple

planes of leukocyte and endothelium direct contacts reconstructed in 3D. Red arrows indicate areas of direct contacts

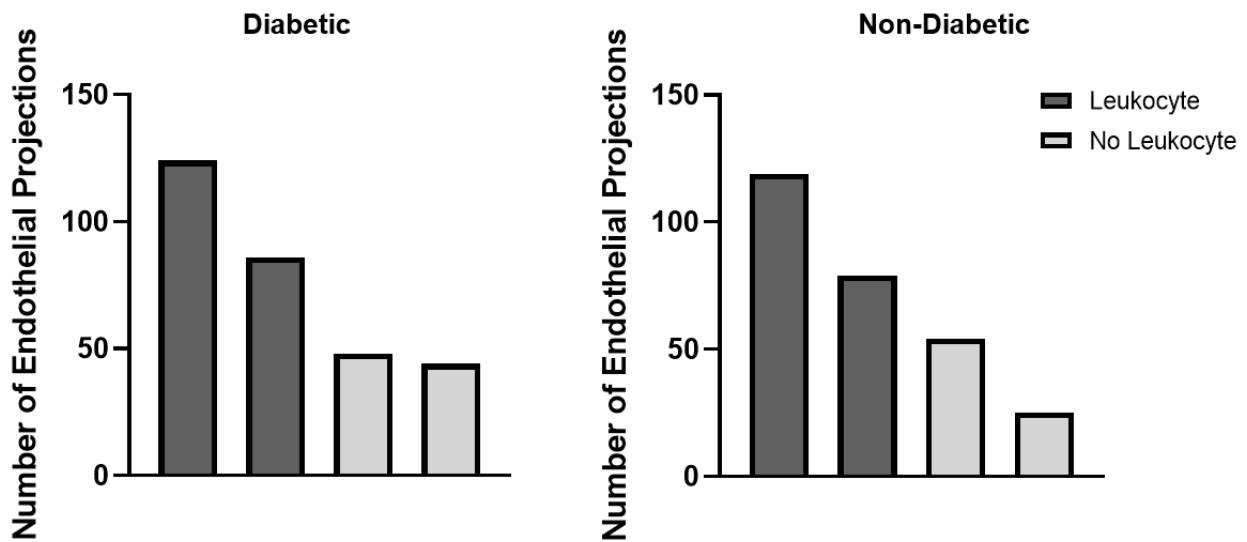


Figure 4-19 Quantification of endothelial projections in capillaries with and without leukocytes in diabetic and non-diabetic conditions. Illustrates the comparison of number of endothelial projections in capillaries with (dark grey) and without (light grey) leukocytes, exploring the distinction between diabetic and non-diabetic capillary environments.

4.3 Discussion

Six-month-old, adult mouse retinal samples, three diabetic and three non-diabetics underwent nanoscale serial imaging with SBF-SEM. All of which revealed morphological evidence of cellular and BM changes in the retinal neurovascular unit with the effect of diabetes.

The BM is a specialised extracellular matrix which provides structural support to the vessel and plays a crucial role in maintaining the integrity of the retinal neurovascular unit. Thickening of the BM is an early histological change in retinal blood vessels in DR. BM thickening occurs due to an increase in the synthesis of vascular BM components like collagen IV and laminin, coupled with reduced degradation by catabolic enzymes, such as matrix metalloproteinases, which normally break down extracellular matrix proteins (Simó *et al.*, 2018). Our electron micrographs have not only displayed the convoluted nature of the BM but revealed occasional featuring of non-uniform areas of BM

thickness within capillaries. This non-uniform distribution of BM thickening suggests localised alterations in the extracellular matrix, potentially indicative of region-specific physiological responses or pathological changes. Similar findings of BM thickening have been documented in human DR studies, where BM alterations were noted to progressively worsen with disease progression (Sayon Roy & Dongjoon Kim, 2021). Further analysis and correlation with other experimental findings will be instrumental in elucidating the significance and implications of this observed heterogeneity in BM thickening within the capillary microenvironment. Interestingly, the lack of widespread BM thickening in our diabetic mouse model contrasts with the findings in previous studies (Sayon Roy & Dongjoon Kim, 2021). This discrepancy raises questions about potential differences in the experimental conditions or the stage of disease progression at the time of analysis. Thickening of the BM has been reported to disrupt cell-to-cell communications, particularly between endothelial cells and pericytes.

An additional interesting observation of the BM was increased extracellular spaced, via the appearance of electron lucent gaps between the BM and neighbouring cells; endothelium, pericytes, neuronal and glial. Serial EM images have revealed detachment of the BM from both sides of the inner and outer BM. The detachment of the endothelium from the BM can influence the reduction of integrin signalling, potentially due to AGE modification of the BM, which reduces the availability of key BM attachment motifs such as RGD, thereby affecting cell survival. Similarly, pericytes, survival signalling could be impair affecting pericyte cell when detaching from BM. These observations indicate structural alterations within the retinal NVU, involving disruptions in the interactions between vascular and neural components. The retraction of cells from the BM suggests potential changes in cell adhesion and signalling processes, highlighting a dynamic and complex remodelling of the NVU microenvironment in the retina. Further investigation into the implications of these structural changes is crucial for understanding the functional consequences and potential contributions to retinal pathologies. The BM also plays a crucial role in regulating the selective permeability of molecules, maintaining a balance between the inner and outer layers of the retinal vasculature. Within the retinal capillaries, the inner layer is comprised of endothelial cells, which rest upon a thin layer of BM. This BM serves as a foundation for cell attachment, preventing the leakage of growth factors, hormones, and polysaccharides from the bloodstream into the connective tissue. Tight junctions formed between endothelial cells in the paracellular region of the capillary endothelial BM actively control permeability. Studies indicate that Collagen IV and laminin contribute to the effective assembly of these tight junctions, suggesting that the BM plays a key role

in maintaining the selective permeability of the retinal capillaries (Jayadev, 2017). The observed separation of the BM in our study may signify an early indicator of diabetic alterations within the NVU, and BM thickening is not required for this cell detachment. This initial BM separation could be considered an early sign of diabetic changes, suggesting vulnerability in the structural integrity of the NVU. and that the subsequent thickening of the BM, is observed in later stages, might function as a compensatory mechanism. This thickening could potentially serve as an adaptive response aimed at addressing the initial BM separation, representing the NVU's attempt to restore structural stability in diabetic-related alterations.

The BM wraps around the abluminal endothelium and pericytes for the most part forming a barrier separating the two cells. However, along the capillary length gaps in the BM were observed allowing pericytes and endothelial cells to come into closer contact via peg-and-socket formations. Peg-and-socket interactions are enriched at pericyte somata and represent as focal points for pericyte-endothelial communication in the expansive capillary network (Ornelas et al., 2021). Research has suggested the existence of adhesion proteins like fibronectin and other dense plaques, particularly situated at the pericyte-endothelial interface (Courtoy & Boyles, 1983). The existence of adhesive proteins, coupled with the numerous pegs along the pericyte edges, implies a robust anchoring of pericytes to the endothelium. This secure connection suggests the ability of pericytes to uphold endothelial coverage and effectively transmit force to the underlying endothelium during contraction or relaxation. In the diabetic samples, the appearance of peg-and-socket junctions exhibit distinctive alterations, characterised by increased extracellular space surrounding the peg, withing the socket space.

Alterations in pericyte biology are acknowledged to be closely linked to biochemical changes in diabetes, contributing to widespread microvascular complications. Recent studies indicate that early disruptions in the interactions between pericytes and endothelial cells might be an initial step affecting communication between these two cell types. These disruptions, marked by altered signalling and protein expression, thereby contribute to the loss of survival signalling (Braunger et al., 2015). The early depletion of pericytes is believed to impair the delivery of pericyte-derived pro-survival signalling to endothelial cells, leading to the formation of acellular capillaries devoid of blood flow and resulting in local ischemia (Hammes et al., 2011). Consequently, pericyte loss and dysfunction emerge as key contributors across the entire spectrum of DR. Pericyte-endothelial communication impairments are seen in other metabolic diseases, like hypertension and metabolic syndrome (Wong & Mitchell, 2007), highlighting the broader impact of metabolic dysregulation on

microvascular health. This further alludes to the impairment of important factors of cell survival mechanisms in the NVU as a result of diabetes.

The observed increase in leukocytes within the capillary lumen of diabetic mice compared to non-diabetic counterparts raises intriguing questions about the potential mechanisms underlying this phenomenon. Diabetes can impact the systemic environment, affecting circulating immune cells. Elevated levels of circulating leukocytes may contribute to their increased presence within the retinal capillaries. Several factors may contribute to the heightened presence of leukocytes in diabetic capillaries. Diabetes is associated with a chronic low-grade inflammatory state. The presence of hyperglycaemia can trigger an inflammatory response, leading to the release of pro-inflammatory cytokines (Berbudi, 2020). This inflammatory milieu may attract and activate leukocytes, contributing to their increased presence within the capillaries. Observations of leukocytes within vessels are critical because they may reflect early stages of inflammation and microvascular damage, key features of DR (Yildirim et al., 2012). Leukocyte adhesion and infiltration are early markers of endothelial dysfunction, and their presence in the retinal vasculature suggests increased inflammatory activity that can exacerbate capillary occlusion, ischemia, and subsequent retinal damage (Rangasamy et al., 2012). In addition, leukostasis (the adhesion of leukocytes to the capillary walls) has been implicated in promoting capillary non-perfusion and increasing the permeability of the BRB. This can lead to further vascular complications, including retinal oedema, a hallmark of DR progression (Noda et al., 2012).

In this study, it was observed that endothelial projections make direct contact with neighbouring leukocytes. Diabetes is known to induce endothelial dysfunction, characterised by impaired endothelial function and altered vascular reactivity. Dysfunction in the endothelial layer can result in increased adhesion of leukocytes to the vessel wall and their subsequent transmigration across the capillary lumen. Endothelial projections could be playing a key role in capturing leukocytes, significantly enhancing the interaction surface area and localising critical adhesion molecules like ICAM-1 and VCAM-1, crucial for leukocyte adhesion. Endothelial cells extend filopodia to establish initial contacts with leukocytes, essential for subsequent firm adhesion and effective transmigration during inflammatory response (Langer, 2009). In the process of angiogenesis, endothelial cells engage with type I collagen, leading to the increased expression of P-selectin and monocyte chemoattractant protein-1 (MCP-1) through ERK1/2-dependent mechanisms. These molecular changes actively participate in bolstering leukocyte attachment (Ruiz-Torres et al., 2006). Simultaneously, vascular smooth muscle cells (VSMCs) play a role in fortifying the endothelial barrier

function. They achieve this by resisting mechanical stress, partly through the synthesis of ECM, and by contributing to the regulation of vascular tone (MacLeod et al., 1994).

The observed increase in the number of endothelial projections in capillaries containing leukocytes, particularly pronounced in diabetic conditions, raises intriguing questions about the interplay between vascular components and immune cells in the diabetic retinal environment. Endothelial projections are known to play crucial roles in vascular physiology, including the regulation of blood flow and barrier functionality (Davignon, 2004). Their increase in the vicinity of leukocytes could suggest a reactive or adaptive vascular response to the inflammatory state typically observed in diabetes. The identified patterns of leukocyte localisation near endothelial projections and their contact with these projections further emphasise the intricate dynamics within the retinal NVU during diabetic conditions. Understanding the mechanisms driving these observations is crucial for unravelling the complexities of DR and may offer potential targets for therapeutic interventions aimed at mitigating the impact of inflammation and immune responses within the retinal microvasculature. Further investigations, both *in vitro* and *in vivo*, are warranted to elucidate the specific molecular and cellular pathways contributing to the observed alterations in leukocyte behaviour in diabetic capillaries.

4.4 Conclusion

In conclusion, this chapter has provided a comprehensive exploration of the diabetic mouse neurovascular unit and has unveiled intricate structural changes within the retinal microenvironment under the influence of diabetes within the murine retina. The ultrastructure of the diabetic mouse retina was investigated and any changes emphasising the morphological changes within the capillaries, BM, pericytes-endothelial interactions, endothelial tubules, and the presence of leukocytes.

Observations in the diabetic murine retina, variations in BM thickness, and the separation of cells from the BM, indicative of structural alterations within the retinal NVU. The altered pericyte-endothelial interactions, with their distinctive peg-and-socket formations, provide insights into the interactions that underlies the structural integrity of the capillary network. The peg-and-socket interactions displayed a decrease in frequency and coverage, revealing structural changes indicative of the diabetics on this cellular interaction. Retinal NVU changes because of diabetes include the presence of electron-lucent tubules within the endothelium, alterations in number of pericytes-

endothelial interactions, and an increased prevalence of leukocytes in diabetic capillaries. The intricate interactions between leukocytes and endothelial projections within the capillary microenvironment were highlighted, suggesting a complex interplay in diabetic conditions.

In summary, the findings presented in this chapter contribute valuable insights into the structural changes within the diabetic mouse NVU, providing a foundation for understanding the pathophysiology of DR.

Chapter 5 The Human Neurovascular Unit in Health and Diabetes

5.1 Introduction

In the preceding chapters, our exploration of the NVU has provided valuable insights into the structural changes associated with DR using murine models. This chapter extends the investigation to the human retinal NVU, aiming to bridge the translational gap and enhance the clinical relevance of our findings. Despite the inherent differences between murine and human physiology, the parallels observed in murine retinas have prompted an examination of whether similar structural alterations manifest in the human NVU during DR.

5.1.1 Differences between human and mouse retina

The human and mouse NVU exhibit several notable distinctions, particularly in the anatomy of the retina and BRB function. The human retina is significantly larger than the mouse retina, with a lower cell density and a more complex blood vessel arrangement. This complexity includes differences in retinal capillary plexuses. Humans have a well-developed three-layered capillary plexus in the retina (Figure 5-1), which supports the higher metabolic demands of more diverse photoreceptor cells, including both rods and cones for vision, enabling colour perception, while mice have also both cones, they solely rely on rods for vision in low-light conditions (Peirson *et al.*, 2018). This difference in capillary complexity might also influence the integrity and functional characteristics of the BRB. The human BRB features more elaborate tight junctions and a greater density of transporter proteins, such as such as glucose transporter-1, aquaporin-4, and multidrug resistance-associated proteins, which contribute to its enhanced integrity and selective permeability (Derevjanik *et al.*, 2002). The BRB is more intact in humans, due to the formation of more robust tight junctions in retinal endothelial cells and the higher expression of transporter proteins. These features make the human BRB less permeable and more efficient at preventing toxins, and pathogens from entering the retina from the bloodstream (Coburn *et al.*, 2016). In contrast, the simpler vascular arrangement and less complex tight junctions in mice may reflect and accommodate their different metabolic and sensory requirements. This comparative simplicity in the mouse BRB makes it more permeable, which might increase the vulnerability of the mouse retina to pathological conditions such as

inflammation or DR. Thus, the reduced barrier function in mice may contribute to a higher susceptibility to retinal diseases under stress or disease conditions (Bennis et al., 2015).

Mouse models offer several advantages for studying the retina. Mice are genetically tractable, allowing for precise manipulation of genes related to retinal function and disease. The availability of transgenic and knockout models helps researchers explore molecular pathways and mechanisms that are challenging to study in humans (Janssen et al., 2013). Additionally, the structural similarities between the mouse retina and the human peripheral retina support the use of mouse models for studying retinal degenerative diseases. Mice have a relatively short lifespan, making it possible to study retinal changes across different stages of life, as well as disease progression over time (Coffey et al., 2007).

However, mouse models also have limitations. A pivotal distinction between the human and mouse retina lies in the absence of maculae in mice (Carter-Dawson & LaVail, 1979). Being a nocturnal species, the mouse retina predominantly comprises rod photoreceptor cells (97%), with cones constituting only 3% of photoreceptors, specifically S-cones (blue light) and M-cones (green light). In contrast, humans possess three types of cones, including S-cones, M-cones, and L-cones (red light) (Roorda & Williams, 1999). The cellular composition further varies, with the mouse retina featuring 3.1% horizontal cells, 41% bipolar cells, 16% Müller cells, and 39% amacrine cells. In primates, these cell populations differ, with 9% horizontal cells, 40% bipolar cells, 22% Müller cells, and 28% amacrine cells (Jeon *et al.*, 1998). The average cone density in the mouse retina mirrors that of the primate retina at 3–4 mm eccentricity. Evolutionarily, cones played a foundational role in retinal organisation, and the structural similarities between the mouse retina and the human peripheral retina underscore the mouse's utility as a model for studying retinal degenerative diseases (Naggert et al., 2022).

The superficial capillary plexus was chosen for this study as it is the most accessible and well-characterised layer in both human and mouse retinas. Additionally, the superficial plexus is located in the ganglion cell layer, which is particularly relevant for diseases like DR, where early vascular changes are prominent in this layer. By focusing on the superficial plexus, comparisons between human and mouse retinas can be made more accurately, aligning with the data collected from mouse models. Given that the GCL and its vasculature are relatively conserved across species, this approach allows for more straightforward translation of findings from mouse models to human retinal pathologies.

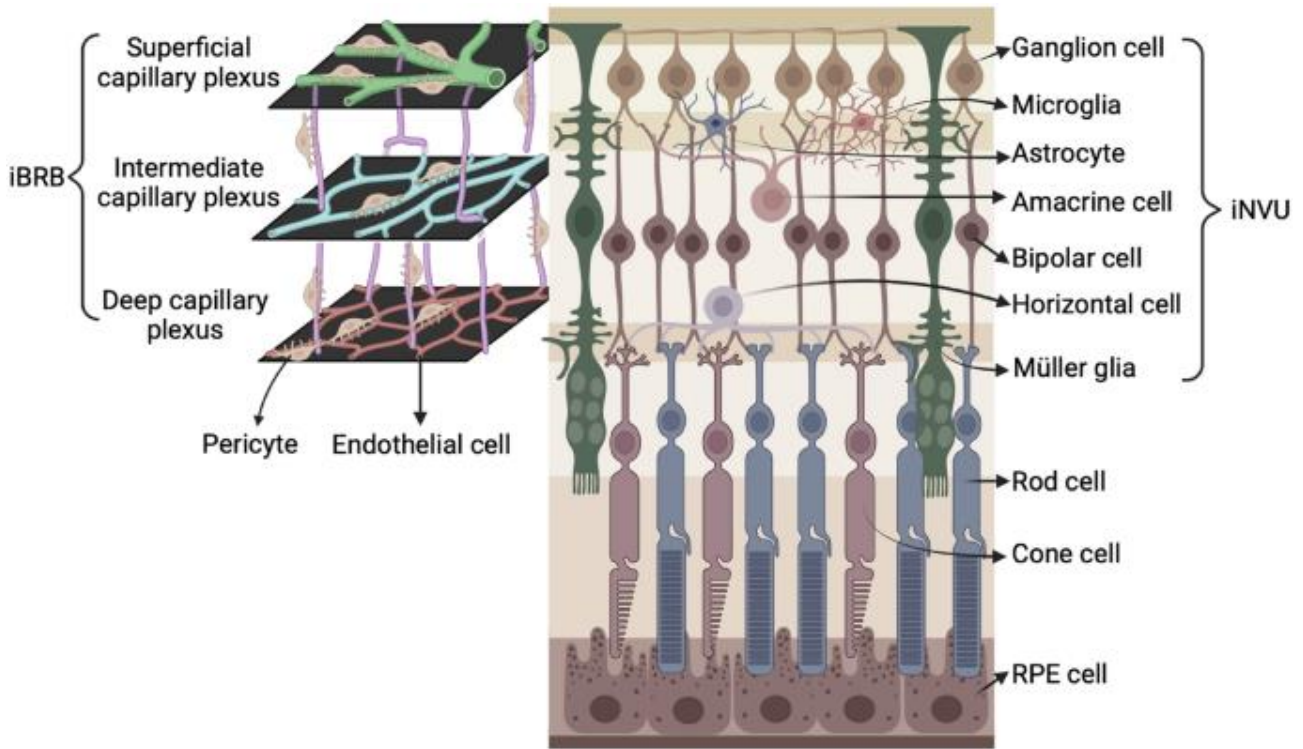


Figure 5-1 Organisation of retinal capillary plexus. This schematic represents the structure of the human retina, highlighting the three capillary plexuses and the retinal cells in each layer. The superficial capillary plexus, intermediate capillary plexus, and deep capillary plexus form the vascular network, contributing to nutrient and oxygen delivery within the retina. Pericytes and endothelial cells line the capillaries, forming the inner blood-retinal barrier (iBRB), which regulates permeability. The adjacent neuronal layers include ganglion cells, amacrine cells, bipolar cells, horizontal cells, and Müller glia, which provide structural support and maintain retinal function. The lower layers contain rod cells and cone cells, essential for vision, and interact with the retinal pigment epithelium (RPE) at the base of the retina (modified from (Sheng et al., 2024)).

5.2 Results

5.2.1 Ultrastructure

Retinal tissue samples were collected from non-diabetic and diabetic human samples, each comprising a set of three capillaries in the superficial plexus. The non-diabetic sample was obtained during an exenteration surgery where the patient had cancer and the globe needed to be removed, while the diabetic sample was a post-mortem specimen. Stacks of 100-300 consecutive micrographs of the capillary ultrastructure were captured along the length of the vessel, covering depths of 12-36 μm . The ultrastructure of one representative capillary from each of the sample is specifically

showcased (Figure 5-2 - Figure 5-3). The comprehensive examination provides valuable insights into the capillary morphology and organisation within the superficial capillary plexus, in the GCL of the retina.

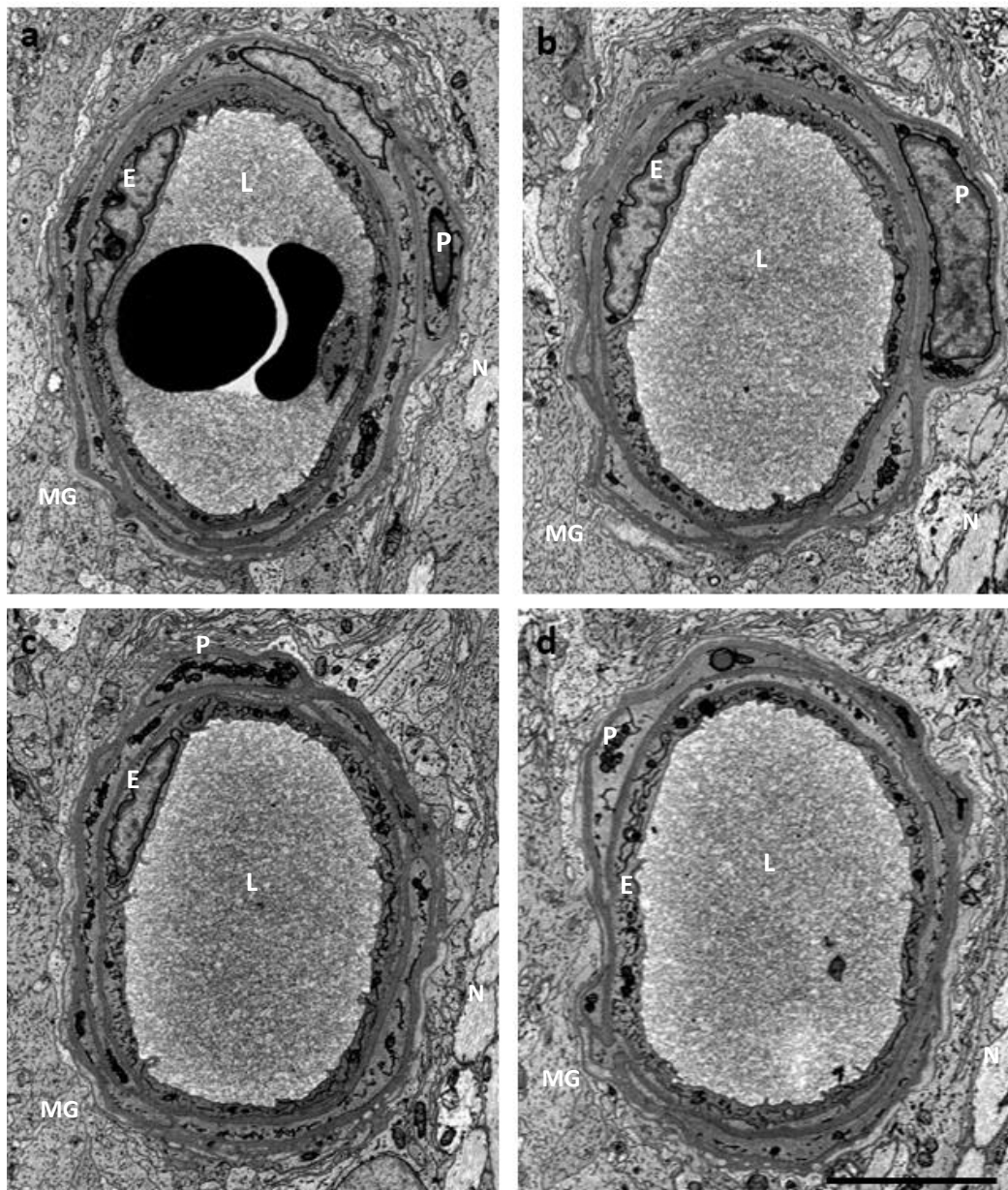


Figure 5-2 Ultrastructure of non-diabetic human capillary. A collection of SBF-SEM micrographs taken from a human retinal capillary to display the morphological changes along the capillary length. a, slice 1 (0.1 μm), b, slice 50 (5 μm), c, slice 100 (10 μm) and d, slice 150 (1.5 μm). Lumen: L, Pericytes: P, Endothelium: E, Macroglia: MG, Neurons: N. Scale bar 5 μm Full dataset can be found: <https://figshare.com/s/3b904ed185d815f690df>.

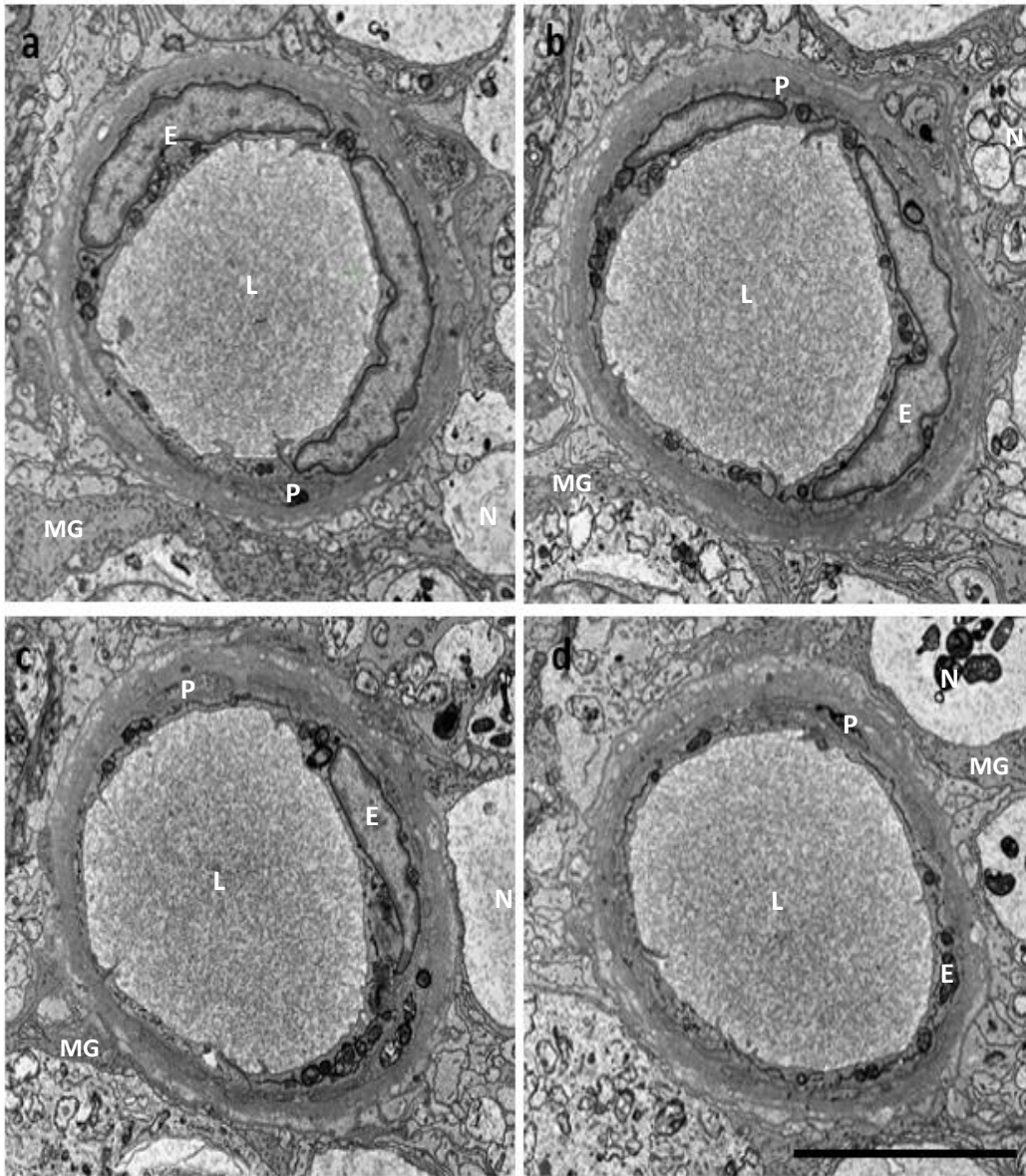


Figure 5-3 Ultrastructure of diabetic human capillary. A collection of SBF-SEM micrographs taken from a human retinal capillary to display the morphological changes along the capillary length. a, slice 1 (0.1 μm), b, slice 50 (5 μm), c, slice 100 (10 μm) and d, slice 150 (1.5 μm). Lumen: L, Pericytes: P, Endothelium: E, Macroglia: MG, Neurons: N. Scale bar 5 μm . Full dataset can be found: <https://figshare.com/s/2f54a9228dd5cf08f9bc>.

5.2.2 Basement membrane

Under electron microscopy, the BM of the human retinal NVU reveals a finely intricate and organised structure. Comprising a complex network of extracellular matrix components, such as include collagen type IV, laminin, fibronectin, nidogen, and heparan sulfate proteoglycans, such as perlecan (Sayon Roy & Dongjoon Kim, 2021), the BM appears as a dense and continuous sheet positioned between the retinal vascular endothelial cells and adjacent pericytes, shown in **Figure**

5-4b in brown. The human BM is a very complex structure with a convoluted nature, interweaving and encompassing cells within its architecture, contrasting from mouse capillaries where the vascular BM structure was less complex.

5.2.2.1 Lipid-like deposits

In the electron micrographs of human retinal capillaries, a distinctive feature was identified within the BM – white structures referred to as lipid droplets. Under electron microscopy, these lipid-like droplets appeared as rounded, white formations, often clustering together in multiple aggregations. Remarkably, these lipid-like droplets exhibited a prominent presence in the outer region of the BM. They were present in both diabetic and non-diabetic capillaries.

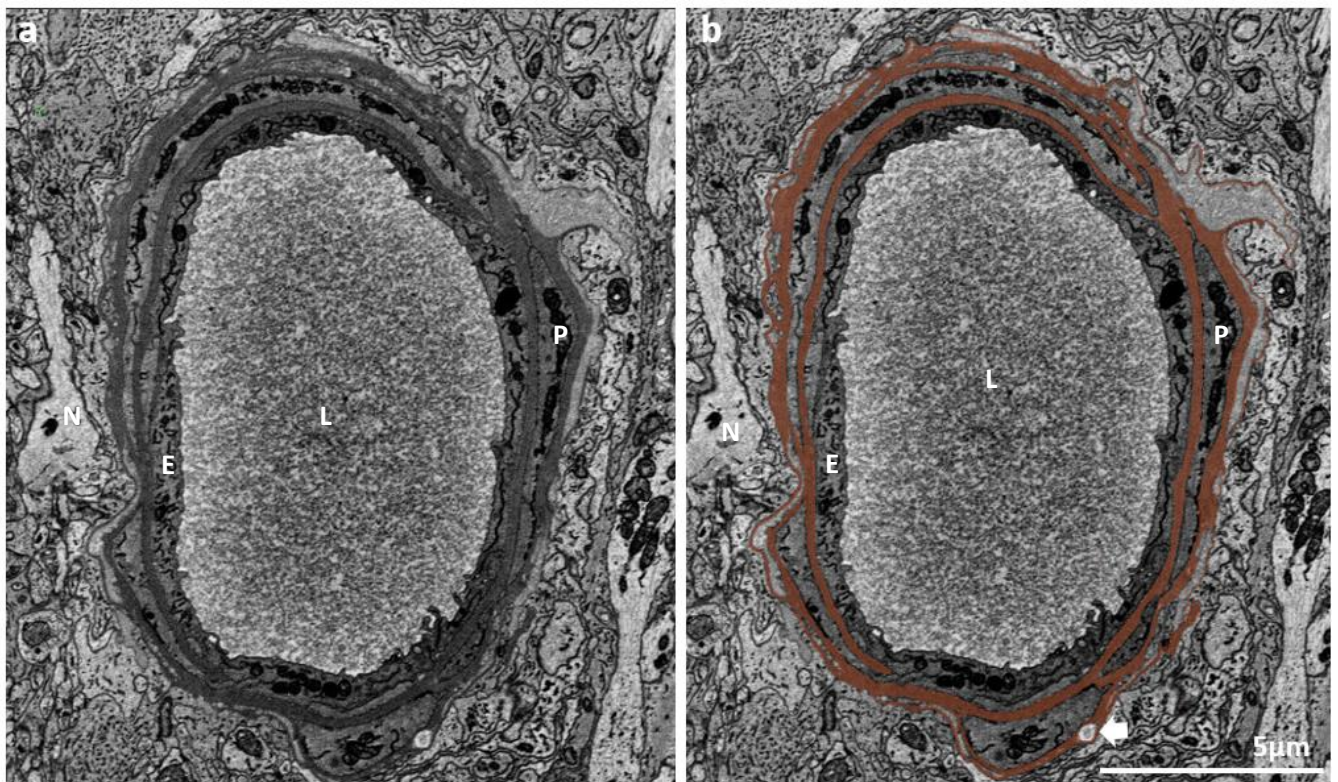


Figure 5-4 Lipid-like deposits in non-diabetic capillary 1. a. shows image of human non-diabetic capillary 1
b. basement membrane (BM) segmented capillary, BM shown in brown. White arrows show where lipid-like deposits are present.

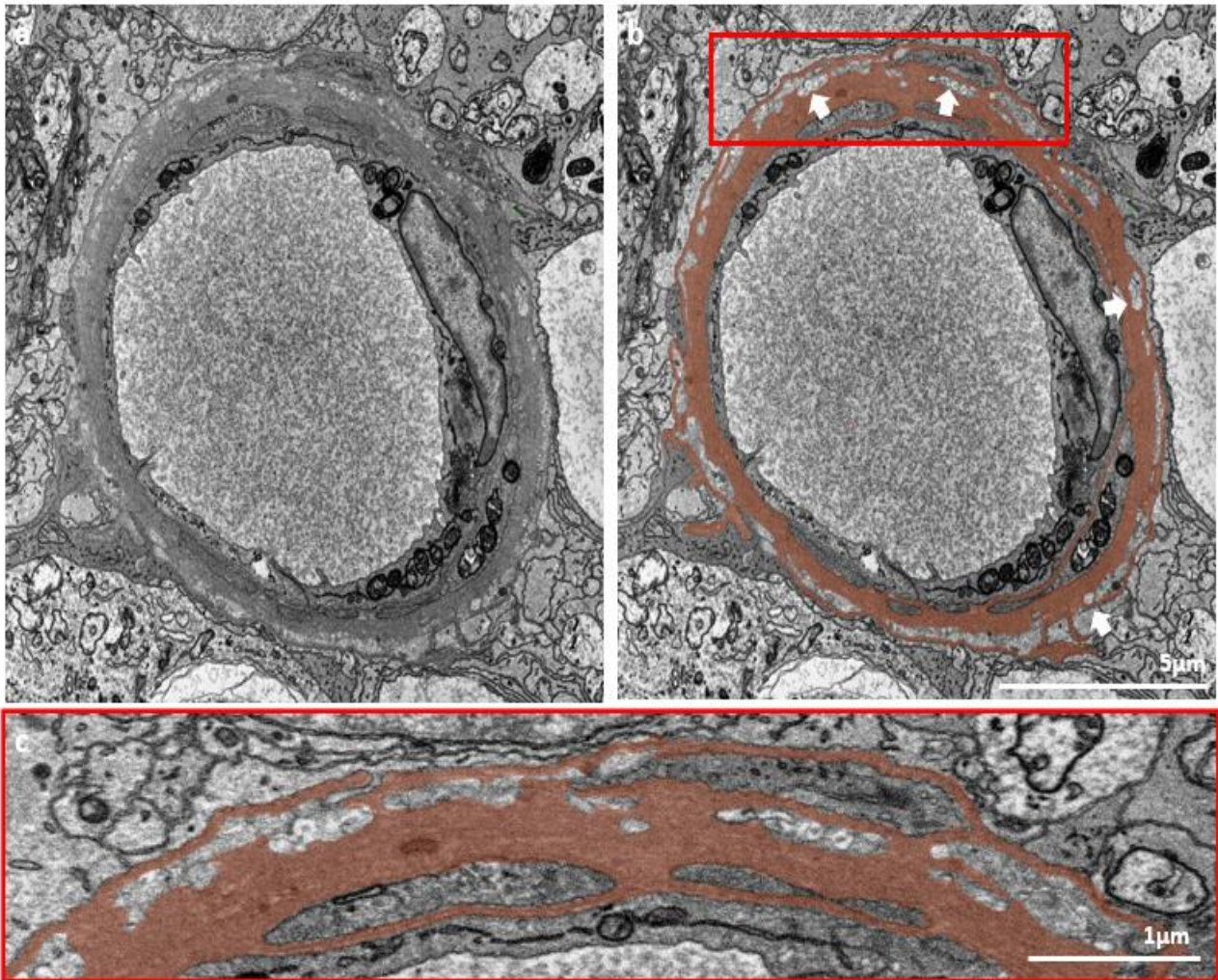


Figure 5-5 Lipid-like deposits in diabetic capillary 1. a. shows image of human diabetic capillary 1 b. basement membrane (BM) segmented capillary, BM shown in brown. White arrows show where lipid-like deposits are present. c. provides a magnified view of the area highlighted in the red box in panel b, offering a closer look at the detailed structure and location of the lipid deposits within the basement membrane.

5.2.3 Pericyte to endothelial interactions

Extending our investigation from Chapter 3, we delve into the heterocellular interactions of the human NVU, particularly focusing on pericyte-endothelial interactions. In parallel to our findings within the murine NVU, our analysis in the human NVU unveils an intricate network of communication between pericytes and endothelial cells along the vessel. The BM, traditionally acting as a barrier, reveals breaks in the structure that allow for closer contact between pericytes and endothelial cells. This intricate interplay mirrors our findings in mice, encompassing direct contact points and peg-and-socket type interactions, as illustrated in **Figure 5-6**, revealing the

distinctive peg-and-socket formations observed in human pericyte-endothelial interactions. Peg-and-socket differences in diabetic samples are discussed in 5.2.3.1.

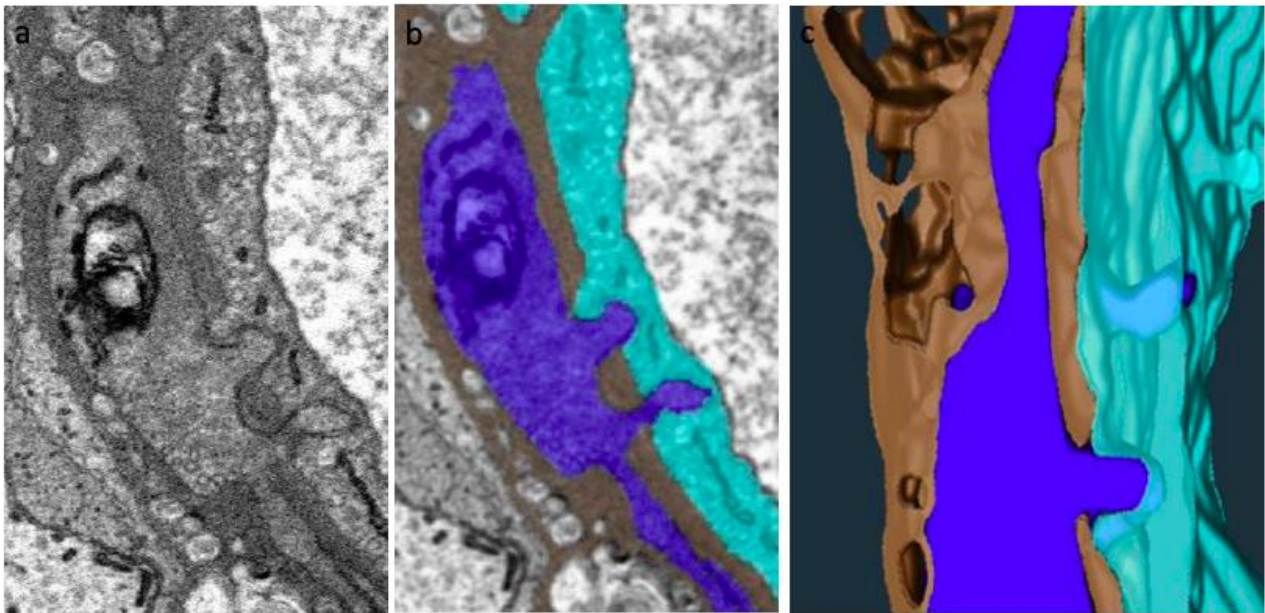


Figure 5-6 Human pericyte-endothelial interaction via peg-and-socket formations. Electron micrographs depict the intricate peg-and-socket interactions between pericytes and endothelial cells in the human neurovascular unit. Protrusions from pericytes break through the basement membrane to establish dynamic contact with neighbouring endothelial cells.

5.2.3.1 Pericyte-endothelial interactions in diabetes

An in-depth exploration into the intricacies of pericyte-endothelial interactions within the retinal NVU extended to the examination of peg-and-socket formations, revealing pertinent insights into their structural alterations in diabetic conditions. The investigation encompassed the analysis of these formations across six human capillaries, three diabetic and three non-diabetics from each sample.

In the non-diabetic capillaries, the presence of peg-and-socket formations was a recurrent observation, signifying their active participation in heterocellular interactions within the NVU. Strikingly, an examination of the distribution patterns in the diabetic capillaries revealed an evident reduction in the frequency of these peg-and-socket formations (**Figure 5-7**). This marked decrease in their distribution was consistently observed across all the diabetic capillaries analysed.

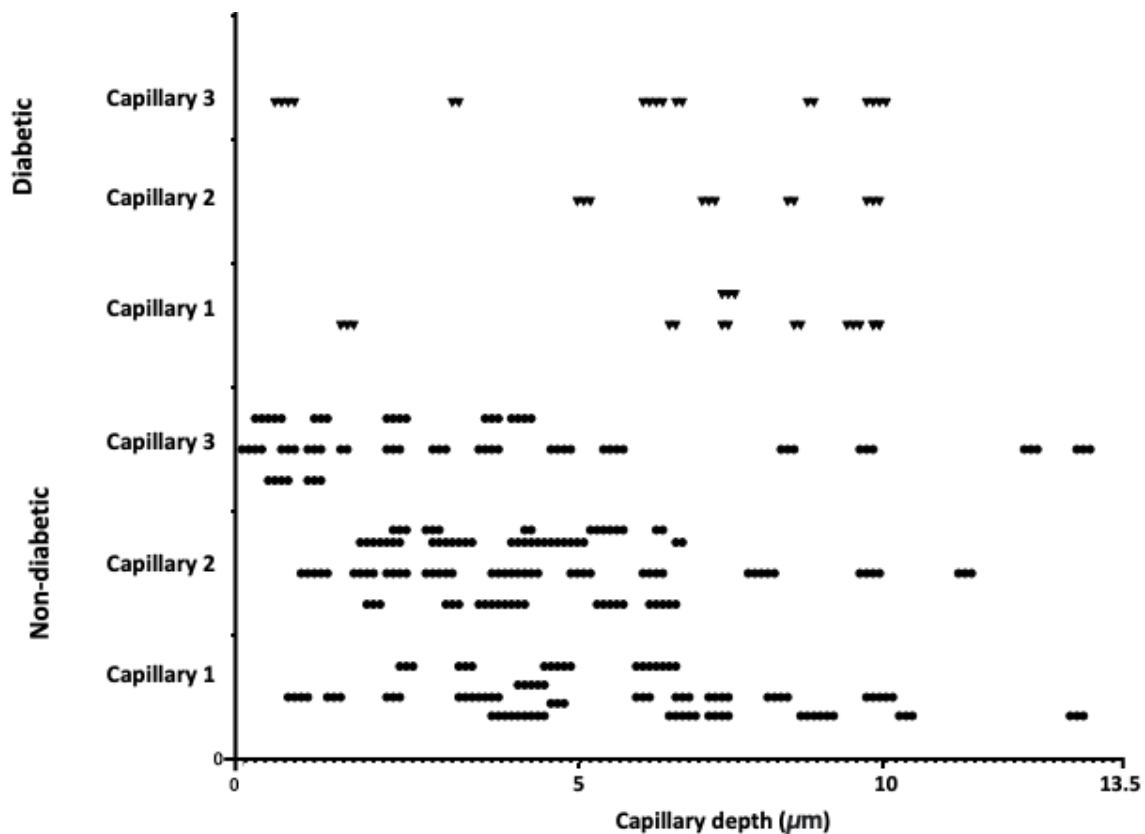


Figure 5-7 Distribution of peg and sockets across human diabetic vs non-diabetic capillaries. The distribution of peg-and sockets evident across 130 sections examined in 18 capillaries. Note more than one peg-and-socket may appear in the same sections (i.e. at different points of pericyte-endothelial membrane interaction in the same z-plane).

5.2.3.2 Pericyte-endothelial complexes

In the investigation of pericyte-endothelial interactions within non-diabetic human samples, TEM was also used to examine for the presence of cellular junctions at the peg and socket level. The choice to utilise TEM at this stage is founded on its superior resolution capabilities, which are essential for a more granular analysis of the junctional complexes critical for vascular stability and function. While SBF-SEM provided valuable structural overviews and initial identifications of peg-and-socket formations, its resolution limitations did not allow for the high degree of detail required to scrutinise the intricate features of the junctional complexes. In contrast, TEM offers the enhanced resolution necessary to capture these complex cellular interactions with greater clarity and precision, thus providing a more definitive examination than was possible with SBF-SEM (**Figure 5-8**). A total of 32 sections from 4 different human samples, which were previously identified to contain peg-and-socket formations based on SBF-SEM data collection, were thoroughly examined via

qualitative assessments for cell-to-cell junctions between pericytes and endothelial cells when forming peg-and-socket formations. These selected datasets were further sections for TEM analysis, focusing on identifying peg and socket formations indicative of pericyte-endothelial junctional complexes.

Across the extensive examination of 89 peg-and-socket formations in the examined sections, no discernible pericyte-endothelial junctions were observed. These findings are summarised in **Table 5-1**, providing a comprehensive overview of the absence of such junctional complexes within the investigated samples. Despite the absence of pericyte-endothelial junctions, our analysis revealed a noteworthy presence of endothelial-to-endothelial junctions (**Figure 5-9a**, green arrows). Additionally, for a detailed view of the pericyte-endothelial formations structure under TEM showing no junctional complex, refer to the magnified image in **Figure 5-9b**.

Table 5-1 Summary of TEM analysis of peg-and-socket junctions results. This table provides a comprehensive summary of TEM analysis results for pericyte-endothelial interactions in non-diabetic human samples. The data includes the number of human samples analysed, total sections examined from each sample, count of observed peg and socket formations, and the number of pericyte-endothelial junctions identified.

Sample No.	Number of sections analysed	Number of peg-and-sockets	Number of peg-and-socket junctions
SBF90	2	5	0
SBF114	12	29	0
SBF126	14	36	0
SBF130	4	19	0

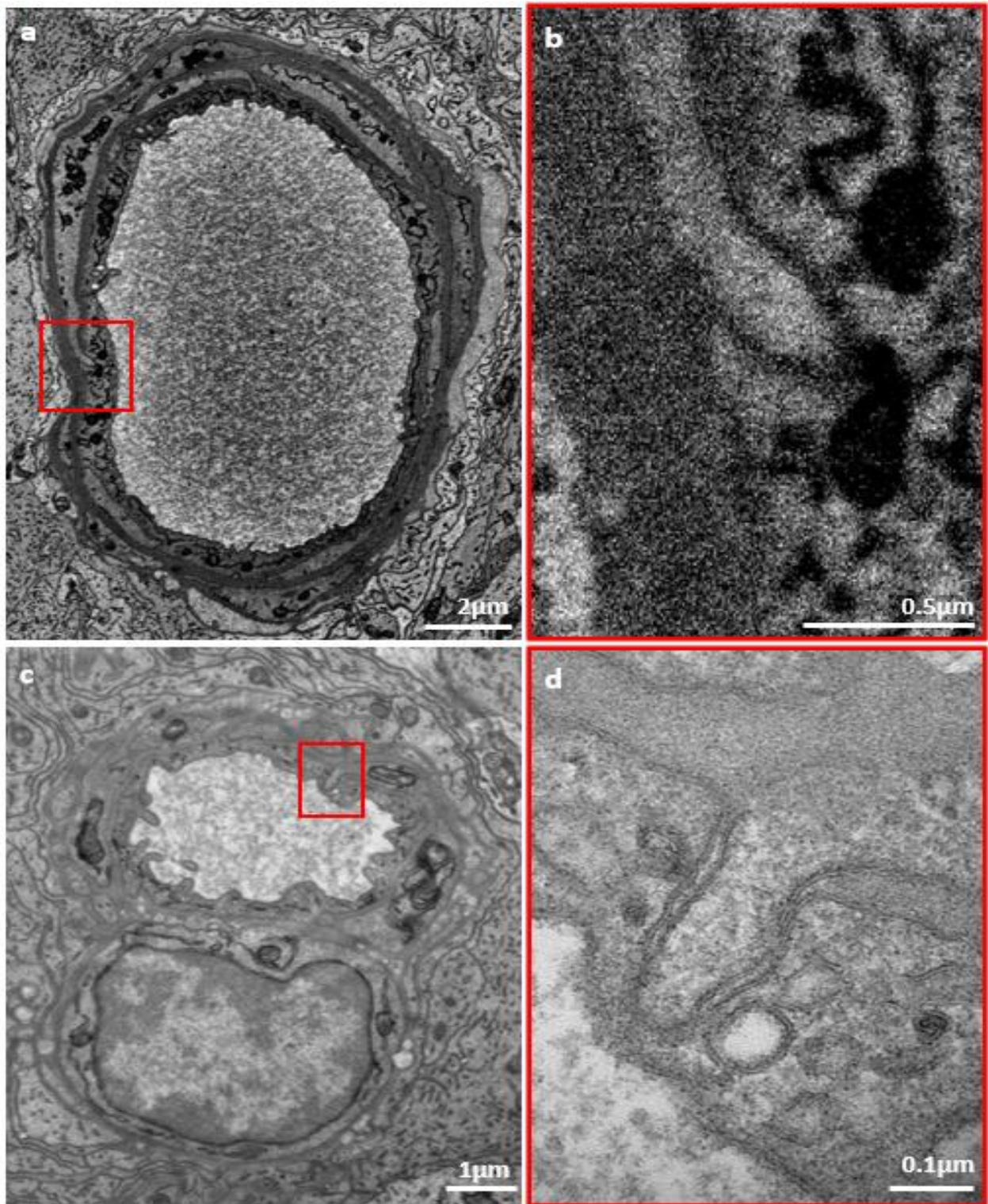


Figure 5-8 Comparative microscopy of peg-and-socket formation structures in non-diabetic capillaries. a. SBF-SEM image of a capillary cross-section, highlighting the peg-and-socket formation composition. b. Enlarged SBF-SEM image from the area marked in red in panel a, showing a peg-and-socket formation. c. Corresponding area of another capillary shown using TEM. d. High-resolution TEM image from the area marked in red in panel c, displaying cell membranes from peg-and-socket formations. This magnified view clearly shows the intricate details of the peg-

and-socket formation, with visible cell membranes, demonstrating the superior resolution of TEM for studying fine cellular interactions.

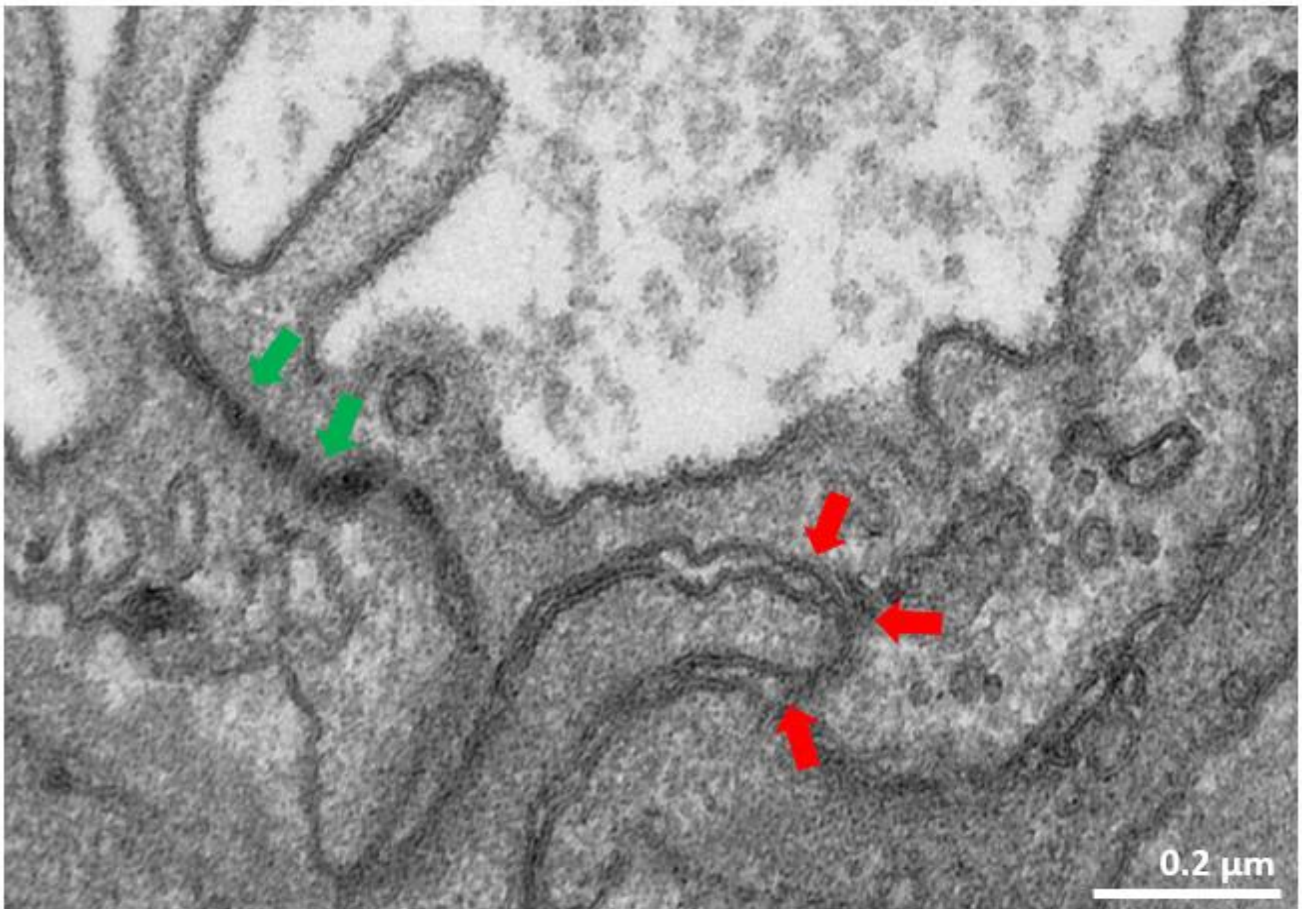


Figure 5-9 TEM analysis of junctions TEM image illustrating peg-and-socket formation emphasizing the structural details of the peg-and-sockets and the absence of clear junctions. Red arrows highlight peg-and-socket formations, while green arrows indicate endothelial-to-endothelial junctions.

5.2.4 Human neurovascular unit with diabetes

Through SBF-SEM, we uncovered structural changes in the murine retinal NVU, such as detachment from the basement membrane, alterations in pericyte-endothelial interactions, and the presence of electron-lucent gaps in diabetic capillaries. These observations serve as the foundation for our exploration into the human retinal NVU under the effect of diabetes, providing valuable insights that prompt further investigation in a clinical context.

5.2.4.1 Basement membrane changes

5.2.4.1.1 Thickening

While the exploration of BM alterations in the diabetic mouse NVU has provided valuable insights, a nuanced examination of human sections initially suggested a pattern of BM thickening around the capillary vessels. Upon qualitative visual assessment, electron micrographs of human retinal capillaries showed what appeared to be a thickening BM around the circumference of capillary structures compared to those observed in murine models (**Figure 5-10**), as compared to the murine capillaries. However, when these observations were subjected to a quantitative analysis, which involved measuring the BM mean and maximum thickness across 20 sections per capillary (including 10 consecutive sections), it yielded unexpected results. These consecutive sections were selected based on their status as the thickest in the stack. The statistical analysis revealed no significant differences between diabetic and non-diabetic capillaries in terms of BM thickening (**Figure 5-11**). The BM may have only appeared thicker in images due to the larger size of human capillaries compared to murine ones.

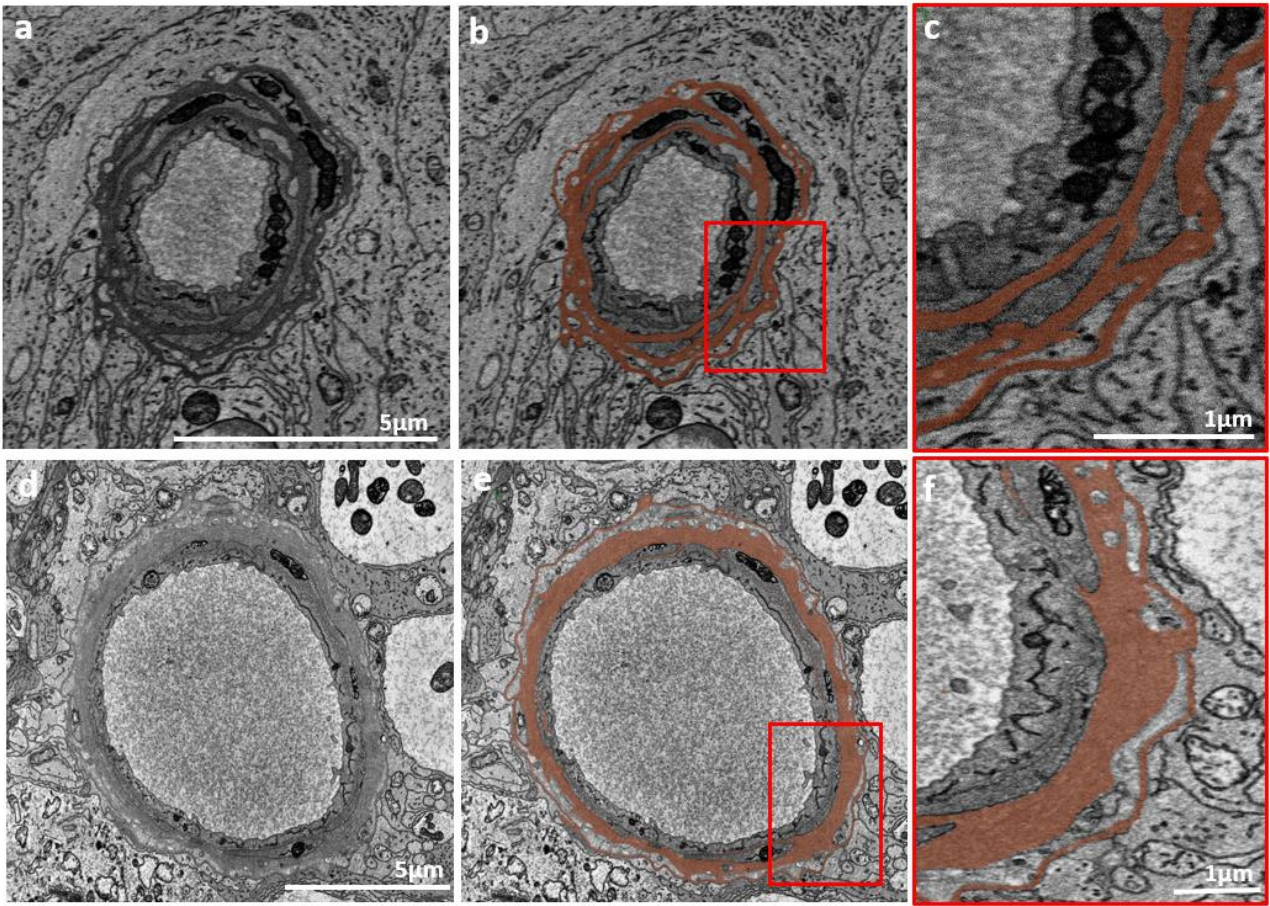


Figure 5-10 Comparative electron micrographs illustrating basement membrane thickening in diabetic conditions. (a) shows electron micrograph of a capillary from a non-diabetic human retina. In (b), the BM is segmented in brown to highlight the thickened areas, with the red square indicating the region of interest that is further magnified in (c) for detailed examination. Panels (d), (e), and (f) present a similar layout for a capillary from a diabetic human retina, where the BM thickening segmented in brown in (e), and (f) offers an enlarged view of the highlighted section within the red square. These images compare the morphological characteristics of BM thickening in capillary vessels between diabetic and non-diabetic samples.

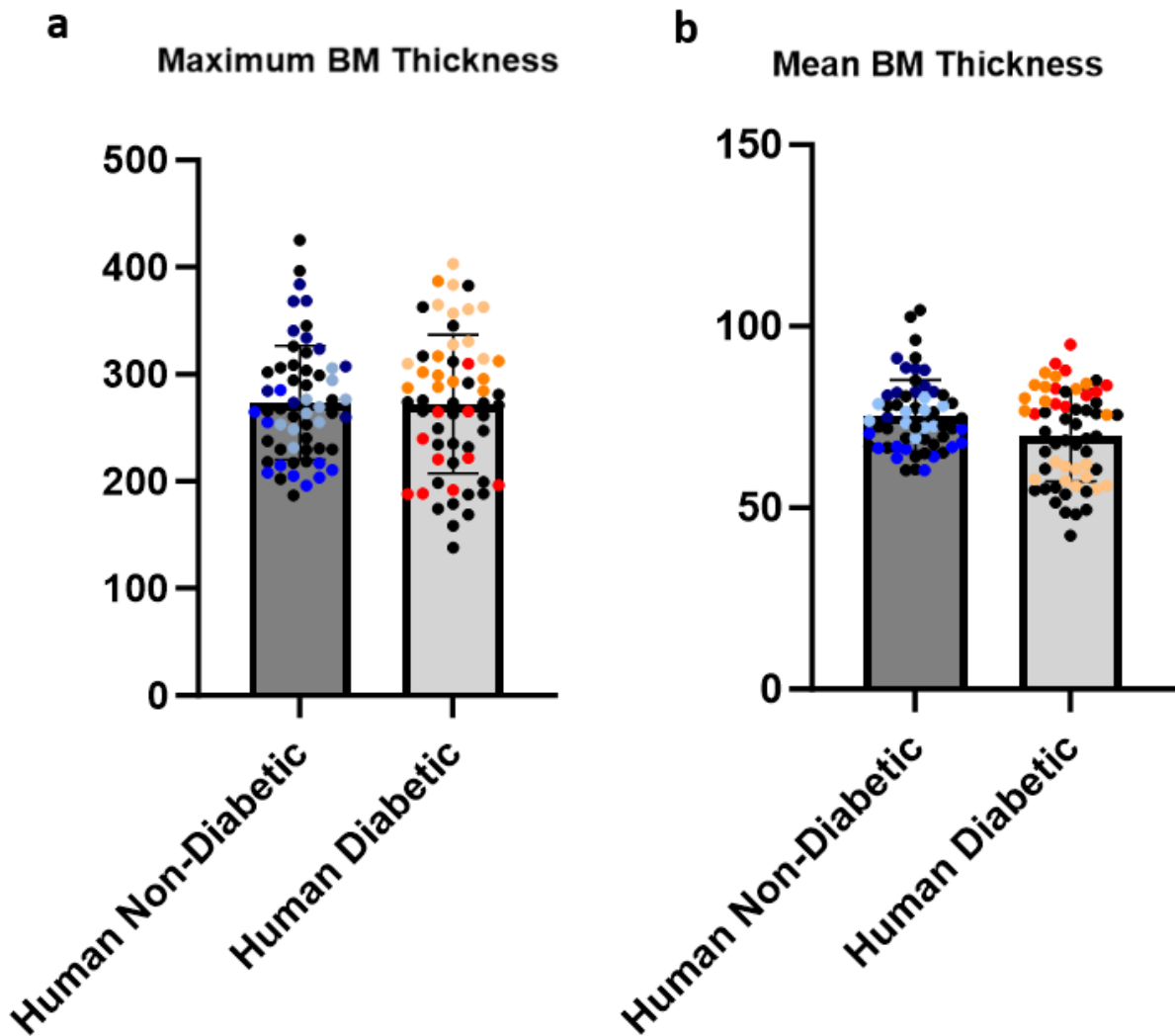


Figure 5-11 Maximum and mean BM thickening of human diabetic vs non-diabetic. Every 10th section through the depth of the stack, and the thickest sections were analysed consecutively, represented as coloured dots, each colour depicts a separate capillary. Specifically, BM thickness was calculated by analysing every 10th section (e.g., sections 1, 10, 20, 30, up to section 100). After identifying the section with the thickest BM, the thickness for five sections before and five sections after that thickest slice were calculated. These consecutive sections, representing the region around the thickest BM, are shown as coloured dots. Analysis was conducted on three capillaries each state including three diabetic and three non-diabetic human capillaries. Error bars represent standard deviations.

5.2.4.1.2 Separation from basement membrane

Electron micrographs reveal compelling evidence of BM separation from various components of the NVU in human diabetic capillaries, mirroring observations identified in the mouse models. Gaps between the endothelium (**Figure 5-12**), which forms the immediate border of the BM, are

conspicuous in the human diabetic capillaries. Similarly, pericytes (**Figure 5-13**), encompassed by the BM, exhibit discernible electron-lucent gaps, indicating a detachment from the BM structure. This retraction of cells extends beyond the vasculature (**Figure 5-14**), with electron-lucent gaps observed between surrounding glial and neuronal cells and the BM. The dynamic and pervasive nature of BM separation within the retinal microenvironment is shown in **Figure 5-12 -Figure 5-14**.

Quantitative analysis conducted on 3 non-diabetic and 3 diabetic human capillaries uncovers significant differences in the frequency of BM separation from NVU cells between diabetic and non-diabetic conditions (**Figure 5-15**). This analysis involved a detailed morphological count of electron lucent spacing between each cell-to-cell interface. Each identified electron lucent gap, indicative of cell separation was then followed through the depth of the capillary to facilitate a comprehensive 3D assessment. Diabetic capillaries consistently exhibit a heightened degree of cell detachment from the BM, while no gapping was observed in the non-diabetic capillaries. This finding underscores a notable alteration in the structural integrity of the retinal NVU under diabetic conditions in the human retina.

In the three non-diabetic human capillaries examined, no separations in the BM were identified. In contrast, **Table 5-2** offer a detailed account of the total occurrences of BM separation observed across all three analysed human diabetic capillaries. The tables provide corresponding information on the specific sections where these occurrences were observed, offering a comprehensive overview of the spatial distribution of BM separation within the human diabetic retinal microvasculature.

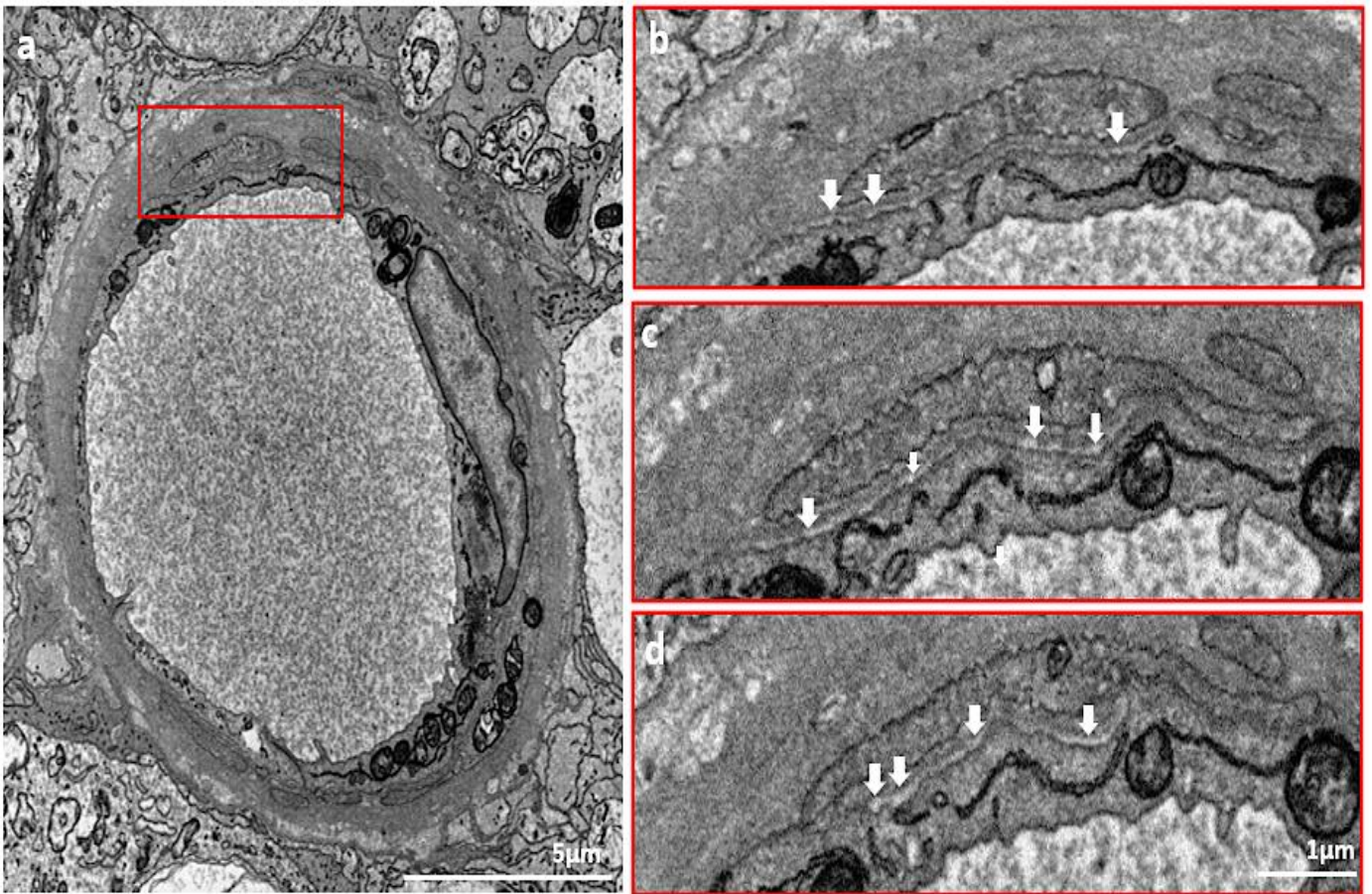


Figure 5-12 BM separating from endothelium. a. human diabetic capillary 1, red box indicates area magnified b-e magnified region of capillary displaying electron lucent gapping from basement membrane. White arrows indicate electron lucent gaps where the endothelium is separating from BM, serial sections b. 101, c. 102, d. 103.

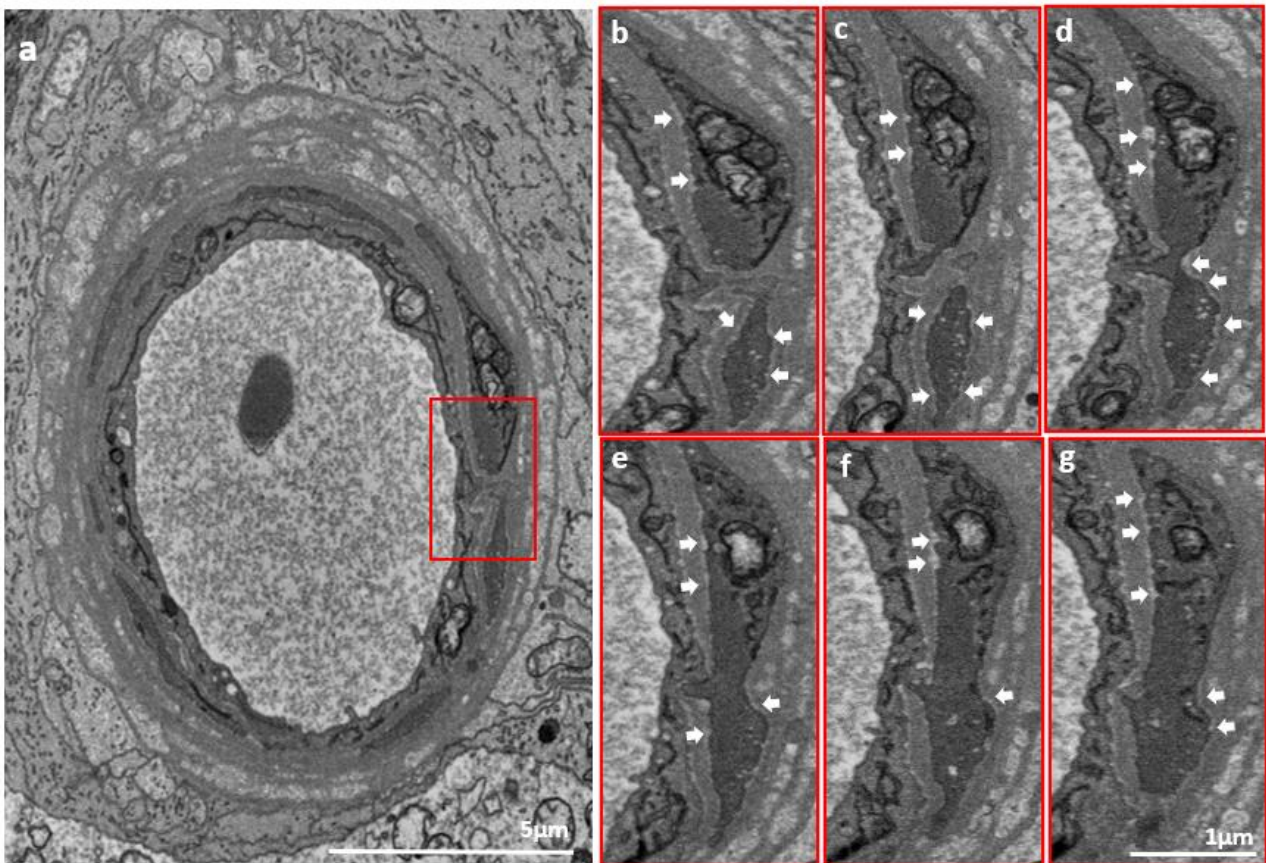


Figure 5-13 BM separating from pericytes. a. human diabetic capillary 2, red box indicates area magnified b-g magnified region of capillary displaying electron lucent gapping from basement membrane. White arrows indicate electron lucent gaps where the pericytes are separating from BM, serial sections b. 195, c. 196, d. 197, e. 198, f. 199, g. 200.

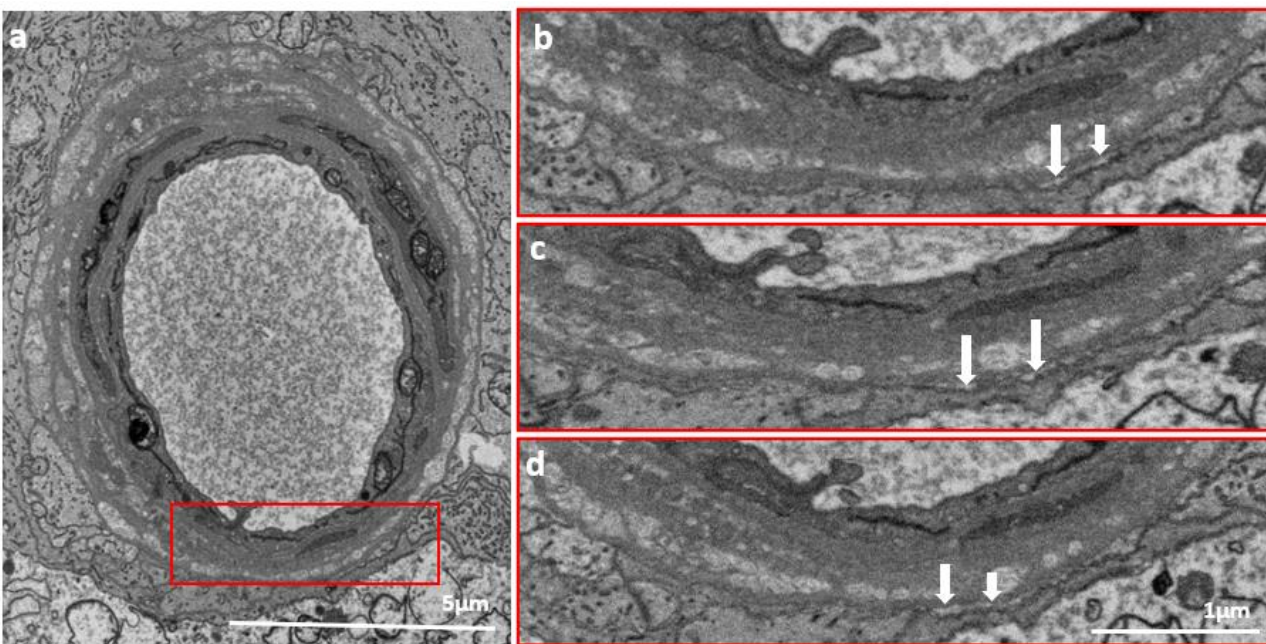


Figure 5-14 BM separating from neuroglia. a. human diabetic capillary 2, red box indicates area magnified b-d magnified region of capillary displaying electron lucent gapping from basement membrane.

White arrows indicate electron lucent gaps where the cells surrounding the vasculature are separating from BM, serial sections b. 187, c. 188, d. 189.

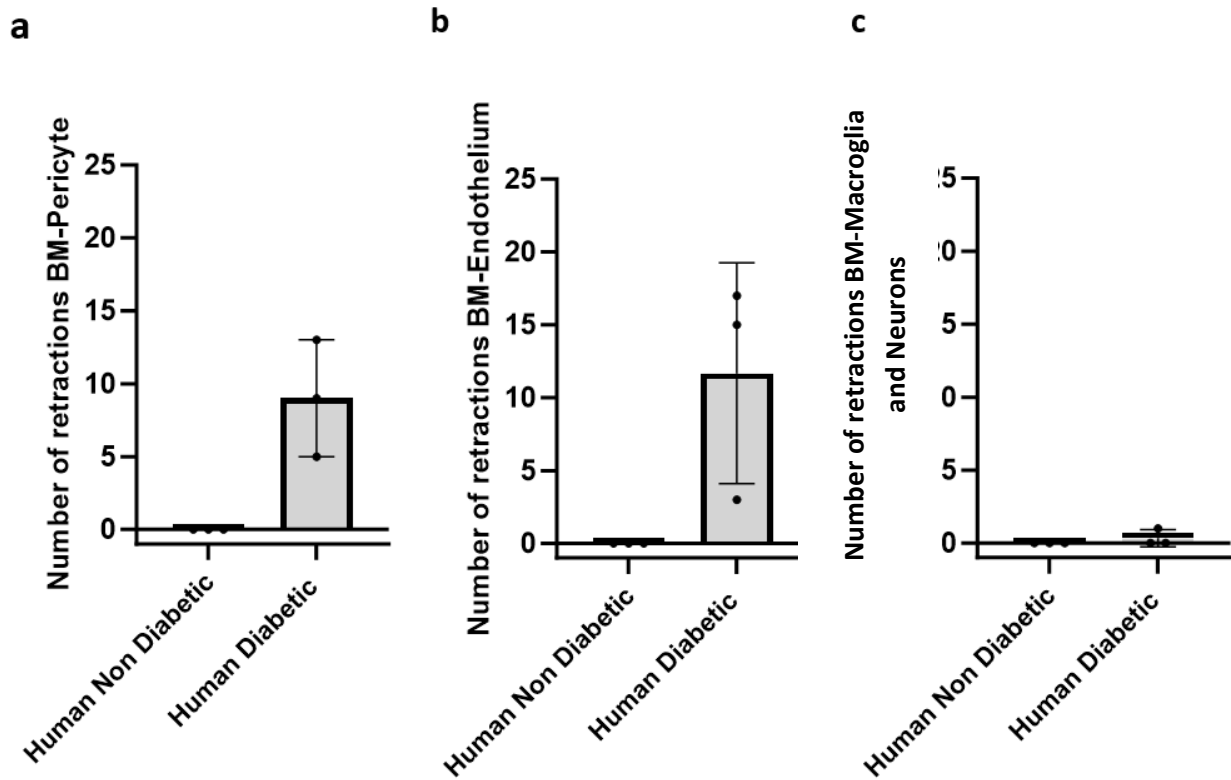


Figure 5-15 Comparative analysis of basement membrane separation in diabetic and non-diabetic capillaries. This graph illustrates the frequency of separation occurrences from the BM to distinct cellular components within the NVU. a. BM to Pericytes: Occurrences of separation between the BM and pericytes in diabetic and non-diabetic capillaries. b. BM to Endothelium. c. BM to Neuroglia (combination of cells surrounding vasculature including neurons and macroglia). Data is derived from the analysis of 3 diabetic and 3 non-diabetic capillaries from 2 human samples. Error bars represent standard deviations.

Table 5-2 Total occurrences of BM separation in diabetic human capillaries. This table summarises the counts of basement membrane (BM) separation occurrences in three different diabetic human capillaries. The occurrences are categorised into BM-Endothelium, BM-Pericyte, and BM-Neuroglia, providing insights into the distribution of BM separation types across the examined capillaries.

Human Diabetic Capillary 1	Human Diabetic Capillary 2	Human Diabetic Capillary 3
----------------------------	----------------------------	----------------------------

BM-Endo	BM-Peri	BM-Macrogliia and Neurons	BM-Endo	BM-Peri	BM-Macrogliia and Neurons	BM-Endo	BM-Peri	BM-Macrogliia and Neurons
100-103	104-106	-	101-104	104-108	187-189	61-63	53-56	-
100-105	121-123		107-115	121-125		76-78	60-64	
105-108	128-132		109-111	122-123		95-96	92-99	
107-117	134-138		111-113	140-144			96-100	
107-141	148-156		111-117	146-148			97-100	
111-114	153-155		118-122	156-159				
120-126	159-165		121-125	161-163				
128-132	160-163		123-127	186-191				
137-156	165-172		130-132	195-200				
163-177	184-194		130-133					
175-184	188-189		131-142					
182-191	190-200		137-147					
190-194	196-200		143-145					
191-193			159-163					
194-200			186-189					
			191-196					
			193-197					

5.3 Discussion

In this chapter, exploration of the retinal NVU from murine models extended to the human retina, aiming to enhance the clinical relevance of our findings in the context of DR. Three human non-diabetic and three diabetic capillaries underwent nanoscale serial imaging with SBF-SEM. Through ultrastructural analysis, we show distinctive features of the human NVU, providing a foundation for comprehensive discussions regarding the structural changes associated with DR.

In comparing the human and mouse retinas, several differences emerge, spanning anatomical, physiological, and functional dimensions. The size and scale of retinal structures vary significantly between species, with the human eye being substantially larger than that of the mouse (Bennis et al., 2015). Vascular density in the human retina is generally lower compared to the highly vascularised mouse retina. Anatomical distinctions extend to the arrangement and tortuosity of

capillary beds (Fletcher et al., 2014). Physiologically, mice exhibit a higher metabolic rate and a shorter lifespan, influencing the nutritional and oxygen demands on the retina. Functional dissimilarities include variances in visual acuity and colour vision, with humans possessing superior capabilities. Furthermore, disease susceptibility, regenerative capacity, and genetic and molecular differences contribute to distinctions in the retinal NVU between these species. Recognising these dissimilarities is pivotal for contextualizing findings from murine models and understanding the translational relevance of research to human retinal health and disease in the clinical setting. Despite this, the diabetes related structural changes and characteristics of the retinal NVU identified through serial electron micrographs in humans remain consistent with that of the murine retinal NVU.

Investigation of human retinal capillary ultrastructure revealed pericyte and endothelial interactions via peg-and-socket formations which have been described in both human and mouse retinal and brain capillaries and have also been found in human and murine granulation tissue and cardiac tissue (Carlson, 1989; Díaz-Flores et al., 2011; Wakui et al., 1990). SBF-SEM micrographs and 3D reconstructions have revealed that peg-and-socket formations span across a depth of between 2-9 μm , in the human retinal capillaries and have an unconstrained distribution along the length of the capillary. Compared with the mouse NVU, no discernible differences between humans and mice concerning the structure and formation of peg-and-sockets were observed. The absence of discernible differences across species underscores the remarkable cross-species consistency in these intricate pericyte and endothelial interactions. This parallelism not only validates the utility of murine models in investigating the NVU but also emphasises the broader significance of these interactions in diverse vascular systems. The robustness of peg-and-socket formations in both humans and mice accentuates their pivotal role, making them valuable focal points in advancing our understanding of vascular physiology and pathophysiology on a comprehensive scale.

Investigating the diabetic retinal capillaries electron micrographs revealed a disruption of peg-and-socket formations within the diabetic microenvironment, implying structural modifications in pericyte-endothelial cell interactions. Quantitative analysis of peg-and-socket distribution, elucidates the substantial decrease in peg coverage across diabetic capillaries, accompanied by a notable reduction in the number of observed pegs compared to their non-diabetic counterparts. These findings underscore the impact of diabetes on the intricate pericyte-endothelial interactions, unveiling a disrupted landscape of peg-and-socket junctions within the human diabetic retinal microvasculature. Interestingly, the differences observed in human capillaries appear to be more

pronounced than those seen in mouse capillaries, possibly due to the longer duration of diabetes in humans compared to the relatively shorter experimental timelines used in mice. The repercussions of these alterations in terms of vascular stability, permeability, and overall neurovascular unit functionality warrant further investigation to unravel the underlying mechanisms and potential therapeutic interventions.

Pericyte and endothelial interactions have long been referred to as peg-and-socket junctions, indicating a close and intricate connection facilitated through these specific junctions. This terminology suggests a structural interplay where pericytes and endothelial cells establish communication via numerous interacting proteins, enabling the entry of specific molecules into neural tissues while restricting the entry of harmful material such as anaphylatoxins, bacteria and viruses (Hudson & Campbell, 2021). A thorough examination using TEM was conducted across multiple human retinal capillaries, focusing on the intricate peg-and-socket formations within the NVU. This analysis revealed the absence of discernible junctions between pericytes and endothelial cells. This intriguing finding prompts a critical discussion point, indicating that the traditional peg-and-socket structures, while present, do not manifest as the canonical junctions seen in other vascular contexts. This notable absence raises pivotal questions about the communication dynamics between pericytes and endothelial cells within the retinal NVU. The need to explore alternative modes of communication becomes evident, emphasising the complex and nuanced nature of pericyte-endothelial interactions in the retinal microenvironment.

Electron microscopy revealed a highly convoluted nature of the BM, adding a layer of intricacy to its structural organisation. Significantly, this convoluted BM not only forms a protective border along the endothelium but also intricately encompasses pericytes within its complex architecture. Moreover, in human retinal capillaries the encapsulation of lipid deposits within this convoluted BM was observed. The identification of lipid-like deposits within human retinal capillaries emerges as a distinctive feature, setting them apart from the retinal capillaries of mice. This observation implies a unique characteristic specific to human retinal capillaries. TEM have previously described a similar phenomenon as cavitation or vacuolisation within the BM, in adult human capillaries, coining the term 'Swiss-cheese vacuolization' to depict the structural appearance (Hogan, 1971). While this feature was primarily associated with human retinal capillaries, it's worth noting that they also observed this feature in monkey retinal capillaries (Anderson & Hoyt, 1969). Research indicates that the presence of lipid deposits tends to escalate with age, suggesting it as a normal attribute of the ageing retina (Bianchi et al., 2016; Powner et al., 2011). Furthermore, previous studies have

documented the existence of these lipid deposits in samples from diabetic individuals, both with and without diagnosed diabetic retinopathy (Fehér *et al.*, 2018). These deposits may resemble the soft drusen material seen in AMD, which is a hallmark of lipid-related pathologies in the retina. Recent studies on AMD, such as the accumulation of lipoprotein-related lipids in Bruch's membrane (BrM), have shown that these deposits can contribute to the formation of soft drusen and basal linear deposits (BLinD), precursors of advanced AMD (Fehér *et al.*, 2018; Ruberti *et al.*, 2003).

Qualitative assessments of human capillary ultrastructure revealed no discernible differences in lipid deposit accumulation between the diabetic and non-diabetic capillaries, which may be attributable to the close ages of the human subjects, 63 and 67. However, further investigation involving a wider range of ages and more diverse samples is essential to confirm these findings. While the precise nature of the vacuolisation observed in the BM remains ambiguous, there is a logical inclination to consider them as lipid deposits. This supposition is supported by the resemblance of this feature to cholesterol deposits previously reported in Bruch's membrane, which serves as a separation between the retina and the outer choroid layer (Ruberti *et al.*, 2003). The similarity in structural characteristics between the observed vacuolisation and known lipid deposits in a related anatomical context lends credence to the hypothesis that these vacuolisations might indeed be lipid deposits within the BM. Lipid accumulation within the BM of diabetic retinal capillaries mirrors these age-related changes observed in AMD. Lipid staining techniques, such as those used to detect esterified cholesterol and neutral lipids in BrM, could be applied to donor eye studies to confirm the identity of these vacuolations (Chen *et al.*, 2022). Phosphatidylethanolamine lipid markers, which are known to play a role in retinal cell signalling and membrane dynamics, may provide additional specificity in identifying lipid deposits. These markers have already proven valuable in correlating lipid accumulations with AMD progression and could offer similar insights in the context of diabetic retinal disease (Bianchi *et al.*, 2016). This association prompts further exploration into the potential implications and role of these lipid deposits in the context of retinal physiology and pathologies. The characteristic appearance of these structures in electron micrographs led the proposal that they are lipid deposits; however, further investigations are necessary to conclusively identify these as lipid droplets. Future studies could benefit from using correlative light microscopy with specific lipid markers, which would provide a more definitive characterisation of these structures. Phosphatidylethanolamine lipids markers could be targeted as they play roles in cell signalling and membrane dynamics within the retina are found exclusively in the inner retina (Zemski Berry, 2014). Triacylglycerols are lipids highly localised in the accessory

tissue, these are important as energy storage molecules but may also have implications in the pathophysiology of retinal diseases when aberrantly accumulated. Indocyanine green angiography (ICGA) has revealed hypofluorescent spots, such as age-related scattered hypofluorescent spots (ASHS-LIA), which correlate with lipid deposits in the BrM of AMD patients. These hypofluorescent areas indicate regions where lipoprotein-derived lipids prevent the passage of dye, suggesting a buildup of lipid material (Bianchi et al., 2016). Similar approaches could be employed to visualise and quantify lipid deposition in the BM, potentially identifying early markers of disease progression. Furthermore, these imaging techniques could be combined with histopathological analyses to validate the presence of lipid deposits in diabetic retinas, as seen in AMD studies (Chen et al., 2022). Such correlative studies would not only confirm the presence of lipid deposits but also help delineate their role and significance in the retinal physiology and pathology.

The thickening of the BM is a recognised early histological change in retinal blood vessels associated with DR. In the human retinal capillaries examined, this phenomenon manifests as a notable and consistent feature, suggesting a potentially more pronounced impact of diabetes on BM structure in the human retina compared to the mouse model. A relevant consideration in our study involves the potential impact of age-related changes on BM thickness in human samples, which may have contributed to differences compared to the mouse model. The human specimens used in our analysis were obtained from aged individuals, and it is well-established that aging can lead to BM thickening in various tissues (Nagata *et al.*, 1986). However, the absence of BM thickening in the diabetic samples might not be primarily due to age and is likely that the duration of diabetes was relatively short, or the condition was well-controlled in these individuals, potentially delaying the expected microvascular changes. This observation indicates that other pathological features may precede BM thickening in human DR, challenging the notion that it is the first ultrastructural change in diabetic retinal vessels. The challenge of acquiring human samples, particularly those from healthy and younger individuals, adds an additional layer of complexity. Given the inherent difficulty in obtaining a pool of young and healthy human samples, the study may be influenced by age-related variations, complicating the distinction between changes induced by aging and those specific to diabetes. Despite this limitation, our findings shed light on the intricate interplay between age-related and diabetic-associated BM modifications, underscoring the necessity for further research to disentangle these complex factors in the context of the human retinal NVU.

5.4 Conclusion

In conclusion, Chapter 5 of the exploration into the human NVU in health and diabetes provides a comprehensive analysis of the human retinal NVU, extending our understanding from murine models to bridge the translational gap. Despite the inherent anatomical, physiological, and functional differences between human and mouse retinas, our findings reveal remarkable parallels in structural alterations associated with diabetes, emphasising the clinical relevance of murine models. The thorough collection of human retinal samples, adherence to ethical guidelines, and the application of advanced techniques such as TEM and SBF-SEM allowed for a detailed examination of the ultrastructure of the human NVU. The investigation encompassed aspects such as pericyte-endothelial interactions, BM characteristics, and the impact of diabetes on these components. This combination of advanced imaging technologies has allowed us to observe ultrastructural changes at a level that provides new insights into the microvascular impacts of diabetes, particularly the dynamic remodeling of the BM, a feature similarly noted in other chronic conditions such as AMD (Fehér et al., 2018; Powner et al., 2011).

The analysis of human retinal capillaries unveiled intricate details of the BM, including the presence of lipid deposits within its convoluted architecture. The examination of pericyte-endothelial interactions through TEM revealed the absence of discernible junctions, prompting a critical discussion about alternative modes of communication in the NVU. The investigation of peg-and-socket formations, indicated a reduction in frequency in diabetic capillaries, highlighting the structural modifications induced by diabetes. This parallels other vascular systems affected by diabetes, where peg-and-socket formations are similarly disrupted (Bianchi et al., 2016). Furthermore, the presence of electron-lucent gaps and detachment of cells from the BM in diabetic conditions underscored the dynamic nature of BM separation within the retinal microenvironment.

Chapter 6 General Discussion

This thesis unravelled the heterocellular interactions within the NVU in both the human and murine retina, with a particular focus on the impact of diabetes. The investigation revealed striking cross-species consistency in structural alterations, establishing the translational relevance of murine models for studying retinal pathologies. This thesis not only shed light on the convoluted nature of the BM, and its encompassing of pericytes and endothelium within the vasculature but also revealed a wider intricate network extending beyond the vasculature. This network involved macroglia cells and neurons, showcasing the intricate relationships and communication networks that exist both within and outside the vascular structure. Endothelial to pericyte interactions emerged as pivotal components in the intricate landscape of heterocellular interactions within the NVU, through peg-and-socket formations across both human and murine capillaries. Unique features of the human NVU were identified, including the presence of lipid deposits within its architecture, potentially associated with age and pathology. Diabetes-induced alterations, such as localised BM thickening and structural modifications, highlighted the dynamic nature of the NVU under diabetic conditions.

Peg-and-socket formations represent specialised cellular interactions within the NVU, crucial for maintaining the structural integrity and functionality of the vascular system. These formations are characterised by protrusions from pericytes or endothelial cells that extend through the BM, establishing dynamic contacts with neighbouring cells. These intimate connections facilitate intricate communication between pericytes and endothelial cells. Despite the presence of peg-and-socket formations, the absence of discernible pericyte-endothelial junctions prompted a discussion on alternative modes of communication within the retinal microenvironment. The peg-and-socket formations may serve as channels for the exchange of signalling molecules, ions, or other mediators, playing a vital role in the regulation of blood flow, response to hypoxic conditions, and maintenance of the BRB (Goncalves & Antonetti, 2022). Brain pericyte studies have revealed the synergistic roles of endothelial cells and pericytes in angiogenesis, reinforcing the universal importance of interactions across different vascular beds for maintaining vascular stability (Li *et al.*, 2024). Disruptions in endothelial cell to pericyte communications in brain microvasculature pathologies, offer a model for understanding the pathogenesis of DR, where altered signalling pathways, such as VEGF/VEGFR and PDGF-B/PDGFR- β , play a crucial role (Caporali *et al.*, 2017). The potential applicability of antiangiogenic therapies, explored in brain disorders, to retinal diseases suggests novel therapeutic avenues that restore or modulate endothelial to pericyte communication. Despite

our growing understanding, significant gaps remain in our knowledge of the functional significance of peg-and-socket formations in the retina and their role in health and disease. Future research, leveraging advanced imaging techniques and molecular biology approaches, is essential to elucidate the mechanisms of communication between pericytes and endothelial cells. To investigate the communication between pericytes and endothelial cells, identifying which proteins are enriched at the sites of endothelial and pericyte communications and applying co-localisation techniques for these markers could provide insights into the molecular composition and potential signalling pathways involved in these interactions. In the postnatal retina, the ECM protein vitronectin presents a notable pattern of distribution, being significantly enriched in pericytes that are associated with proximal vessels, which boast a fully functional BRB (Wisniewska-Kruk et al., 2012). This is in contrast to the situation in distal vessels, where the BRB is still developing and tends to be leaky (Trevino & Lutz, 2022). This observation highlights the essential role of vitronectin in contributing to the integrity and functionality of the BRB, suggesting that pericytes play a crucial role in the maturation of the retinal vascular system. Proteins that show increased expression in endothelial cells, such as platelet and endothelial cell adhesion molecule 1 (PECAM1) and CD34 molecule, are recognised as key endothelial markers (Goncharov *et al.*, 2020). These markers are extensively utilised in clinical pathology for diagnostic purposes, particularly in the study of angiogenesis. The presence of these proteins is indicative of the endothelial origin of cells and is instrumental in identifying processes such as the formation of new blood vessels (Starke *et al.*, 2011). Their elevated expression levels serve as crucial indicators for evaluating angiogenic activity within various tissues, highlighting their significance in both research and clinical diagnostics. Exploring and using co-localisation methods to study proteins concentrated at the communication points between endothelial cells and pericytes can uncover the molecular landscape and signalling mechanisms that facilitate their interactions (Annika Armulik et al., 2005). Additionally, introducing a stimulant in one cell type over the other, and then observing its presence or effect in both, could reveal the bidirectional nature of their communication. Once these sites are pinpointed, STED microscopy could be employed for its high molecular resolution capabilities to identify the peg-and-socket sites. Such studies could unveil new aspects of retinal vascular biology, offering insights into the development of targeted therapies for retinal diseases. Understanding the intricacies of endothelial cell and pericyte communication at a molecular level could pave the way for innovative therapeutic strategies aimed at preserving or restoring the integrity of the vascular system in retinal and other neurovascular diseases.

The phenomenon of BM thickening is observed across different species, including humans and mice, and plays a significant role in various pathological conditions. BM thickening can be indicative of underlying disease processes, such as those seen in diabetes mellitus, where it is a hallmark feature in the kidneys (diabetic nephropathy), the eyes (DR), and other organs (Marshall, 2016). The thickening of the BM is often associated with the accumulation of ECM components, which can include collagens, laminins, fibronectin, and proteoglycans. The reasons behind BM thickening can vary but often involve a combination of increased production of ECM components by resident cells, decreased degradation of the ECM, or both (S. Roy & D. Kim, 2021). A hallmark of diabetic pathology, ECM turnover plays a central role. During normal aging and disease progression, the ECM undergoes remodelling, which involves both synthesis and degradation of its components, such as collagen, laminin, and fibronectin (Hayden et al., 2005). This turnover is tightly regulated by matrix metalloproteinases and tissue inhibitors of metalloproteinases, which ensure balance in ECM composition (Stetler-Stevenson, 1996). In diabetes, this balance is often disrupted, leading to ECM accumulation, and thickening of the BM (Sayon Roy & Dongjoon Kim, 2021). Adjacent cells, such as pericytes, endothelial cells, astrocytes, and Müller cells, respond to these changes by altering their behaviour and signalling pathways (Simó et al., 2018). Over time, these cells may experience changes in gene expression, oxidative stress, or apoptosis in response to increased BM thickness, ultimately contributing to the dysfunction of the retinal NVU and progression of vascular diseases (Simó et al., 2018).

Comparing BM thickening in humans versus mice, it is important to recognise that while mice are commonly used as models to study human diseases, there are species-specific differences in the composition and response of the BM that may influence the extent and implications of thickening. For instance, genetic and environmental factors, as well as the duration and intensity of disease processes, can differ significantly between humans and mice, leading to variations in the manifestation of BM thickening. The examination of 6-month-old mouse models revealed minimal BM thickening. Where present, such thickening was confined to specific regions of the vasculature, suggesting a localised rather than widespread pathological response within these murine models. Despite no evidence of pronounced BM thickening in either the mouse models or human samples, which would indicate a more advanced or extensive pathology. The absence of BM thickening in both these mouse models and human capillaries suggests that the developmental stage of diabetes-induced pathology in these instances might not be sufficiently advanced to manifest this change. It would be beneficial to examine samples with a longer duration of diabetes or confirmed DR to better

understand the progression of these changes. Additionally, investigating more depths of the capillary could provide further insights into the varied impacts of diabetes on vascular structures at different stages. Given that the mice were only 6-months-old, the pathology associated with BM thickening might not have reached the severity observed in human samples reported in the literature, where the disease has likely progressed over a longer period. This underscores the significance of accounting for the age and stage of disease progression when comparing diabetic pathologies across species, highlighting that the manifestations seen in human diabetes might develop at a later stage in murine models, potentially due to the shorter duration of diabetes at this age. Ideally, to mirror the advanced diabetic pathologies observed in humans more closely, employing older diabetic mouse models would be advantageous. However, inducing diabetes in mice older than 6-months, for example 9-months poses significant challenges as these older mice tend to become frail and succumb quickly to the condition, rendering them impractical for long-term diabetes research.

In the pursuit of advancing our understanding of the retinal NVU and its intricate cellular interactions, particularly in the context of diabetes, adopting CLEM stands out as a powerful methodology. Previously, our use of CLEM to characterise microglia within the NVU has shed light on their presence and closeness to the microvasculature. Extending this approach to other cell types within the NVU, such as astrocytes, Müller cells, and neurons, could provide unparalleled insights into their morphology, interactions, and changes under diabetic stress. This technique allows for the precise localisation of specific cellular components in their native environment, followed by detailed ultrastructural analysis, offering a unique blend of spatial context and molecular detail.

While this thesis predominantly addressed changes within the superficial capillary plexus, recent advancements in imaging technologies, optical coherence tomography angiography (OCTA), have shed light on the vulnerabilities of deeper vascular layers, specifically the deep capillary plexus. OCTA's capability to distinctly visualise different capillary networks within the retina reveals that the deeper capillary plexus often undergoes more significant changes in diabetes than the superficial plexus (Lavia, 2019). This observation is critical as it highlights the deeper capillary plexus susceptibility to diabetic microvascular damage, which could be pivotal in the progression of DR (Agemy, 2015). Changes in the deeper capillary plexus include increased capillary non-perfusion, greater disruption in blood flow, and more pronounced vascular remodelling (Lavia et al., 2020). Despite evidence showing that the deep capillary plexus is more susceptible to diabetic damage, the superficial capillary plexus was chosen for study due to its relative accessibility and the availability

of high-resolution imaging techniques specific to this layer. Furthermore, recent findings suggest that although the deep capillary plexus undergoes more significant vascular remodeling, changes in the superficial plexus often precede those in the deeper layers, serving as an early indicator of retinal pathology in diabetes. This rationale supports the investigation of the superficial layer as a first point of study. However, further exploring different regions of the retina, particularly the deeper layers, and observing the distinctions across various microvascular networks could yield critical insights into the spatial heterogeneity of the capillary microvasculature but also diabetic impact on retinal health. Such an exploration would illuminate how diabetes differentially affects the various components of the retinal vascular and neural network, potentially uncovering region-specific changes within the NVU.

Moreover, investigating the effects of potential therapeutic interventions on the NVU in diabetes is essential. Assessing how various treatments influence the structural and functional integrity of the NVU can identify promising strategies to repair or protect the retinal microenvironment from diabetic damage. This could include evaluating the efficacy of anti-inflammatory agents, angiogenic inhibitors, or neuroprotective drugs in restoring NVU homeostasis and preserving retinal function. Ultimately, combining advanced imaging techniques like SBF-SEM with comprehensive evaluations of treatment effects will contribute significantly to the development of targeted therapies aimed at preserving vision in diabetic patients.

Chapter 7 Conclusion

The experiments in this study confirm the hypothesis that the heterocellular communications within the retinal NVU to undergo disruptions with the effect of diabetes, indicating potential structural and functional alterations associated with the disease.

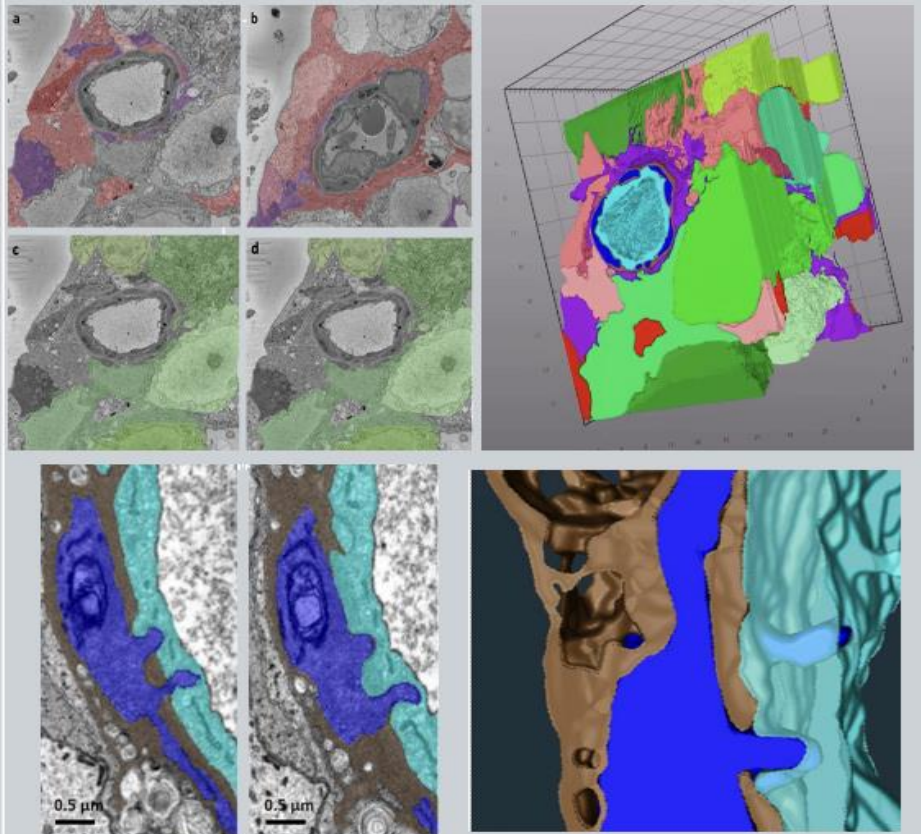
Below is a summary for the results obtained for each of the aims outlined in the introduction.

- 1. Characterising the NVU's Heterocellular Composition:** The ultrastructural analysis conducted on both murine and human samples under non-diabetic conditions successfully achieved the aim of delineating the heterocellular composition of the retinal NVU. Utilising advanced imaging techniques, this study mapped the cellular architecture within the NVU. This exploration unveiled the intricate arrangement of endothelial cells, pericytes, and the BM, highlighting the complex nature of the BM, which was observed to intricately weave around and encapsulate endothelial cells and pericytes within its architecture, and the extensive sheath like coverage from a singular pericyte. This study also revealed the mesh-like coverage provided by macroglia, including astrocytes and Müller cells, which envelop the vasculature, forming a supportive and protective network. Heterocellular communications of pericyte and endothelial interactions via peg-and-socket formations were revealed, further detailing the complex cellular interactions that underpin the functionality of the NVU.
- 2. Quantitative Analysis of Key NVU Features:** This aim was achieved through quantitative assessments which measure key features of the NVU, providing a measure to highlight the different components attributes, including a measure of convexity to underscore the convoluted nature of the BM and the proximity of NVU components to pericytes. Comparative measures between disease states were also made, including the thickness of the BM in diabetic versus non-diabetic conditions. These quantitative findings provided a crucial basis for understanding the heterocellular conditions of the NVU and the extent and impact of structural alterations which may occur under diseased conditions.
- 3. Exploring Diabetes-related Changes in NVU:** Utilising the baseline established under non-diabetic conditions, this aim explored the impact of diabetes on cellular interactions and the integrity of the NVU through comparative analysis between non-diabetic and diabetic samples across murine and human models. Diabetic samples showed enhanced cell-BM separation, and alterations in cellular interactions, indicating significant structural changes

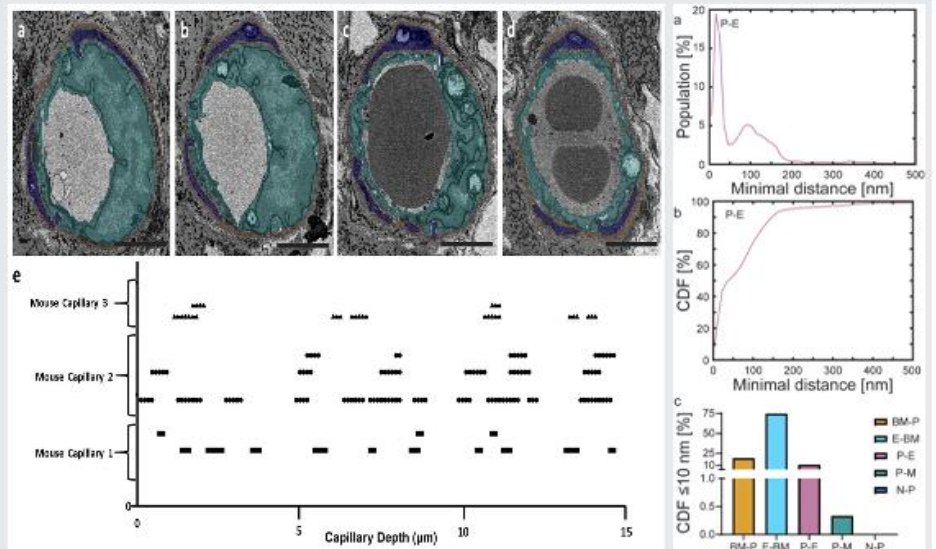
and breakdowns in communication within the NVU. This study identified altered pericyte-endothelial interactions structures and an increased presence of endothelial tubules and leukocytes in diabetic samples, suggesting alterations in vascular permeability and heightened inflammatory responses within the diabetic NVU. These comparative analyses elucidated the profound alterations induced by diabetes, offering insights into the mechanisms underlying DR progression.

Key findings of retinal NVU

Characterising the NVUs heterocellular composition: Identifying the cellular components and providing a deeper look at cell-cell interactions.



Quantitative analysis of key features: Developing unique assessments for NVU features and measuring structural characteristics.



Exploring diabetes-related changes in NVU: Investigating the structural alterations induced by diabetes.

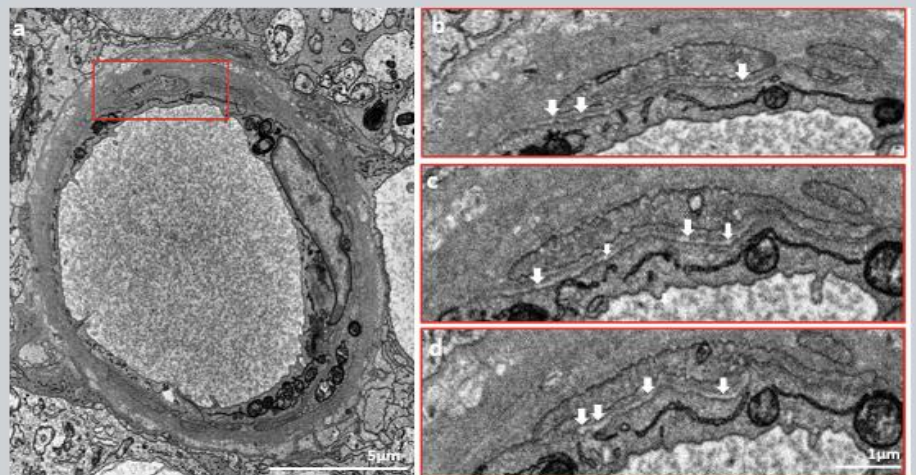


Figure 7-1 Key findings of retinal NVU in health and disease. This schematic summarises the key findings from the study on the retinal NVU in both non-diabetic and diabetic conditions discussed in this thesis. Top Panel – Characterising the NVU’s heterocellular composition: The ultrastructural analysis of the retinal NVU demonstrates the intricate heterocellular arrangement involving endothelial cells, pericytes, and the BM. Advanced imaging reveals the complex interactions between these components, with peg-and-socket formations between pericytes and endothelial cells. The BM intricately weaves around the endothelial cells and pericytes, as highlighted in the color-coded three-dimensional renderings. This analysis also reveals the coverage of macroglial cells, such as astrocytes and Müller cells, which form a supportive network around the vasculature. Middle Panel – Quantitative analysis of key features: This panel highlights the quantitative assessments of key NVU features. Pairwise distance analysis is shown, comparing NVU features from pericytes. Bottom Panel – Exploring diabetes-related changes in the NVU: This panel presents the effects of diabetes on the structural integrity and cellular interactions within the NVU. Comparative analysis between diabetic and non-diabetic samples shows a significant increase in BM-cell separation and altered pericyte-endothelial interactions.

Appendix

Table 4-1 Basement membrane separation occurrences in non-diabetic capillaries. The table provides a comprehensive listing of diabetic samples, indicating respective number of total occurrences of basement membrane (BM) separation in all analysed capillaries and a detailed distribution of these occurrences across specific sections. Endothelium (Endo), Pericytes (Peri), Macroglia and Neurons (Neuroglia).

SBF108-1								
Mouse Non-Diabetic Capillary 1			Mouse Non-diabetic Capillary 2			Mouse Non-diabetic Capillary 3		
BM-Endo	BM-Peri	BM-Neuroglia	BM-Endo	BM-Peri	BM-Neuroglia	BM-Endo	BM-Peri	BM-Neuroglia
23-26		92-100	1--14	22-24		1-8	3--7	1--6
67-79			2--5	23-26		15-20	16-21	
68-70			50-56	57-60		32-36	69-73	
			74-78			51-62		
			19-24			79-84		
						89-96		
SBF108-4								
Mouse Non-Diabetic Capillary 1			Mouse Non-diabetic Capillary 2			Mouse Non-diabetic Capillary 3		
BM-Endo	BM-Peri	BM-Neuroglia	BM-Endo	BM-Peri	BM-Neuroglia	BM-Endo	BM-Peri	BM-Neuroglia
18-22			107-113	153-157	105-107			
			121-128		115-132			
			159-163		140-145			
			167-171					
SBF108-7								
Mouse Non-Diabetic Capillary 1			Mouse Non-diabetic Capillary 2			Mouse Non-diabetic Capillary 3		
BM-Endo	BM-Peri	BM-Neuroglia	BM-Endo	BM-Peri	BM-Neuroglia	BM-Endo	BM-Peri	BM-Neuroglia
						1-3		2-4
						24-28		63-67
						76-83		

Table 4-2 Basement membrane separation occurrences in diabetic capillaries. The table provides a comprehensive listing of diabetic samples, indicating respective number of total occurrences of basement membrane (BM) separation in all analysed capillaries and a detailed distribution of these occurrences across specific sections (i.e 1 indicated section 1, 1-5 indicated the separation was analysed on section 1 through to section 5). Endothelium (Endo), Pericytes (Peri), Macroglia and Neurons (Neuroglia)

SBF108-2								
Mouse Diabetic Capillary 1			Mouse Diabetic Capillary 2			Mouse Diabetic Capillary 3		
BM-Endo	BM-Peri	BM-Neuroglia	BM-Endo	BM-Peri	BM-Neuroglia	BM-Endo	BM-Peri	BM-Neuroglia
1-5	1-14	48-57	1--3	39-42	1--14	3--10	43-47	56-63
1-12	10-19	87-89	3--11	21-23	16-23	14-19	53-56	81-85
1-19	11-16	91-99	12--26		68-74	18-22	68-71	93-100
7-14	24-30	93-96	24-27			25-33		
7-15	44-51		22-30			25-32		
14-33	5-12		33-45			41-45		
15-20	63-69		51-53			54-64		
24-34	69-76		72-79			61-65		
31-47			66-72			74-89		
32-46			82-88			89-97		
32-47			84-88			94-100		
34-44			89-96			93-100		
42-47								
49-59								
51-57								
51-57								
56-65								
68-79								
74-86								
80-100								
82-91								
85-93								
93-100								
SBF108-5								
Mouse Diabetic Capillary 1			Mouse Diabetic Capillary 2			Mouse Diabetic Capillary 3		
BM-Endo	BM-Peri	BM-Neuroglia	BM-Endo	BM-Peri	BM-Neuroglia	BM-Endo	BM-Peri	BM-Neuroglia
100-104	105-111	125-127	100-104	181-186		250-265	268-270	
100-107	105-130	153-156	101-111	126-129		256-264	310-314	
100-122	111-118	191-194	122-138			273-280	312-317	

105-117	114-122	191-200	182-187			287-293	324-329	
106-130	134-141		197-200			305-314		
121-125	140-143					310-322		
125-132	159-161					324-344		
140-169	159-164							
149-165	162-166							
152-157	163-170							
153-162	171-177							
156-161	172-174							
163-176	185-187							
164-169								
167-176								

SBF108-6

Mouse Diabetic Capillary 1			Mouse Diabetic Capillary 2			Mouse Diabetic Capillary 3		
BM-Endo	BM-Peri	BM-Neuroglia	BM-Endo	BM-Peri	BM-Neuroglia	BM-Endo	BM-Peri	BM-Neuroglia
168-176			100-119	119-127	113-115	1-18	4-8	50-52
			104-117	158-161	121-128	1-11	33-35	73-77
			114-119		133-136	21-26	40-43	
			115-120		168-177	42-44	53-57	
			117-125			48-52	60-64	
			120-128			56-62	68-73	
			123-133			61-70	88-91	
			133-135			77-82	96-100	
			135-138			86-90		
			143-149			97-99		
			147-155					
			158-167					
			169-172					
			171-176					
			174-179					
			184-187					
			194-196					
			196-198					
			197-199					

List of References

- Abcouwer, S. F. (2017). Müller Cell-Microglia Cross Talk Drives Neuroinflammation in Diabetic Retinopathy. *Diabetes*, 66(2), 261-263. <https://doi.org/10.2337/dbi16-0047>
- Aiello, L. P. (2014). Diabetic retinopathy and other ocular findings in the diabetes control and complications trial/epidemiology of diabetes interventions and complications study. *Diabetes Care*, 37(1), 17-23. <https://doi.org/10.2337/dc13-2251>
- Aiello, L. P., Avery, R. L., Arrigg, P. G., Keyt, B. A., Jampel, H. D., Shah, S. T., Pasquale, L. R., Thieme, H., Iwamoto, M. A., & Park, J. E. (1994). Vascular endothelial growth factor in ocular fluid of patients with diabetic retinopathy and other retinal disorders. *New England Journal of Medicine*, 331(22), 1480-1487.
- Anderson, A., Alfahad, N., Wimalachandra, D., Bouzinab, K., Rudzinska, P., Wood, H., Fazey, I., Xu, H., Lyons, T. J., Barnes, N. M., Narendran, P., Lord, J. M., Rauz, S., Ganley, I. G., Curtis, T. M., Wallace, G. R., & Hombrebueno, J. R. (2024). Relaxation of mitochondrial hyperfusion in the diabetic retina via N6-furfuryladenine confers neuroprotection regardless of glycaemic status. *Nature Communications*, 15(1), 1124. <https://doi.org/10.1038/s41467-024-45387-9>
- Anderson, D. R., & Hoyt, W. F. (1969). Ultrastructure of Intraorbital Portion of Human and Monkey Optic Nerve. *Archives of Ophthalmology*, 82(4), 506-530. <https://doi.org/10.1001/archophth.1969.00990020508017>
- Antonetti, D. A., Barber, A. J., Hollinger, L. A., Wolpert, E. B., & Gardner, T. W. (1999). Vascular endothelial growth factor induces rapid phosphorylation of tight junction proteins occludin and zonula occluden 1: a potential mechanism for vascular permeability in diabetic retinopathy and tumors. *Journal of Biological Chemistry*, 274(33), 23463-23467.
- Armulik, A., Abramsson, A., & Betsholtz, C. (2005). Endothelial/pericyte interactions. *Circ Res*, 97(6), 512-523. <https://doi.org/10.1161/01.RES.0000182903.16652.d7>
- Armulik, A., Abramsson, A., & Betsholtz, C. (2005). Endothelial/Pericyte Interactions. *Circulation Research*, 97(6), 512-523. <https://doi.org/10.1161/01.RES.0000182903.16652.d7>
- Arshavsky, V. Y., & Burns, M. E. (2012). Photoreceptor signaling: supporting vision across a wide range of light intensities. *J Biol Chem*, 287(3), 1620-1626. <https://doi.org/10.1074/jbc.R111.305243>
- Askew, K., Li, K., Olmos-Alonso, A., Garcia-Moreno, F., Liang, Y., Richardson, P., Tipton, T., Chapman, M. A., Riecken, K., & Beccari, S. (2017). Coupled proliferation and apoptosis maintain the rapid turnover of microglia in the adult brain. *Cell reports*, 18(2), 391-405.
- Au, N. P. B., & Ma, C. H. E. (2022). Neuroinflammation, Microglia and Implications for Retinal Ganglion Cell Survival and Axon Regeneration in Traumatic Optic Neuropathy. *Front Immunol*, 13, 860070. <https://doi.org/10.3389/fimmu.2022.860070>
- Bandopadhyay, R., Orte, C., Lawrenson, J. G., Reid, A. R., De Silva, S., & Allt, G. (2001). Contractile proteins in pericytes at the blood-brain and blood-retinal barriers. *Journal of neurocytology*, 30(1), 35-44.
- Barabas, P., Augustine, J., Fernández, J. A., McGeown, J. G., McGahon, M. K., & Curtis, T. M. (2020). Ion channels and myogenic activity in retinal arterioles. *Curr Top Membr*, 85, 187-226. <https://doi.org/10.1016/bs.ctm.2020.01.008>

- Barber, A. J., Lieth, E., Khin, S. A., Antonetti, D. A., Buchanan, A. G., & Gardner, T. W. (1998). Neural apoptosis in the retina during experimental and human diabetes. Early onset and effect of insulin. *The Journal of clinical investigation*, *102*(4), 783-791.
- Barnes, S., Grove, J. C. R., McHugh, C. F., Hirano, A. A., & Brecha, N. C. (2020). Horizontal Cell Feedback to Cone Photoreceptors in Mammalian Retina: Novel Insights From the GABA-pH Hybrid Model. *Front Cell Neurosci*, *14*, 595064. <https://doi.org/10.3389/fncel.2020.595064>
- Barouch, F. C., Miyamoto, K., Allport, J. R., Fujita, K., Bursell, S. E., Aiello, L. P., Luscinskas, F. W., & Adamis, A. P. (2000). Integrin-mediated neutrophil adhesion and retinal leukostasis in diabetes. *Invest Ophthalmol Vis Sci*, *41*(5), 1153-1158.
- Bek, T. (2017). Diameter changes of retinal vessels in diabetic retinopathy. *Current diabetes reports*, *17*, 1-7.
- Belevich, I., Joensuu, M., Kumar, D., Vihinen, H., & Jokitalo, E. (2016). Microscopy Image Browser: A Platform for Segmentation and Analysis of Multidimensional Datasets. *PLOS Biology*, *14*(1), e1002340. <https://doi.org/10.1371/journal.pbio.1002340>
- Beltramo, E., & Porta, M. (2013). Pericyte loss in diabetic retinopathy: mechanisms and consequences. *Current medicinal chemistry*, *20*(26), 3218-3225.
- Bennis, A., Gorgels, T. G., Ten Brink, J. B., van der Spek, P. J., Bossers, K., Heine, V. M., & Bergen, A. A. (2015). Comparison of Mouse and Human Retinal Pigment Epithelium Gene Expression Profiles: Potential Implications for Age-Related Macular Degeneration. *PLoS One*, *10*(10), e0141597. <https://doi.org/10.1371/journal.pone.0141597>
- Berbudi, A., Rahmadika, N., Tjahjadi, A. I., & Ruslami, R. (2020). Type 2 Diabetes and its Impact on the Immune System. *Curr Diabetes Rev*, *16*(5), 442-449. <https://doi.org/10.2174/1573399815666191024085838>
- Bergers, G., & Song, S. (2005). The role of pericytes in blood-vessel formation and maintenance. *Neuro-oncology*, *7*(4), 452-464. <https://doi.org/10.1215/S1152851705000232>
- Berson, D. M. (2007). Phototransduction in ganglion-cell photoreceptors. *Pflugers Arch*, *454*(5), 849-855. <https://doi.org/10.1007/s00424-007-0242-2>
- Bharadwaj, A. S., Appukuttan, B., Wilmarth, P. A., Pan, Y., Stempel, A. J., Chipps, T. J., Benedetti, E. E., Zamora, D. O., Choi, D., David, L. L., & Smith, J. R. (2013). Role of the retinal vascular endothelial cell in ocular disease. *Prog Retin Eye Res*, *32*, 102-180. <https://doi.org/10.1016/j.preteyeres.2012.08.004>
- Bianchi, E., Ripandelli, G., Taurone, S., Feher, J., Plateroti, R., Kovacs, I., Magliulo, G., Orlando, M. P., Micera, A., Battaglione, E., & Artico, M. (2016). Age and diabetes related changes of the retinal capillaries: An ultrastructural and immunohistochemical study. *Int J Immunopathol Pharmacol*, *29*(1), 40-53. <https://doi.org/10.1177/0394632015615592>
- Blauth, K., Banerjee, S., & Bhat, M. A. (2010). Chapter Three - Axonal Ensheatment and Intercellular Barrier Formation in Drosophila. In K. Jeon (Ed.), *International Review of Cell and Molecular Biology* (Vol. 283, pp. 93-128). Academic Press. [https://doi.org/https://doi.org/10.1016/S1937-6448\(10\)83003-5](https://doi.org/https://doi.org/10.1016/S1937-6448(10)83003-5)
- Bloom, J., Motlagh, M., & Czyz, C. N. (2024). Anatomy, Head and Neck: Eye Iris Sphincter Muscle. In *StatPearls*. StatPearls Publishing
- Copyright © 2024, StatPearls Publishing LLC.
- Bodeutsch, N., & Thanos, S. (2000). Migration of phagocytotic cells and development of the murine intraretinal microglial network: an in vivo study using fluorescent dyes. *Glia*, *32*(1), 91-101.

- Boycott, B. B., & Hopkins, J. M. (1981). Microglia in the retina of monkey and other mammals: its distinction from other types of glia and horizontal cells. *Neuroscience*, 6(4), 679-688. [https://doi.org/10.1016/0306-4522\(81\)90151-2](https://doi.org/10.1016/0306-4522(81)90151-2)
- Braunger, B. M., Leimbeck, S. V., Schlecht, A., Volz, C., Jägle, H., & Tamm, E. R. (2015). Deletion of Ocular Transforming Growth Factor β Signaling Mimics Essential Characteristics of Diabetic Retinopathy. *The American Journal of Pathology*, 185(6), 1749-1768. <https://doi.org/https://doi.org/10.1016/j.ajpath.2015.02.007>
- Bringmann, A., & Wiedemann, P. (2012). Müller glial cells in retinal disease. *Ophthalmologica*, 227(1), 1-19. <https://doi.org/10.1159/000328979>
- Brownlee, M. (2005). The pathobiology of diabetic complications: a unifying mechanism. *Diabetes*, 54(6), 1615-1625. <https://doi.org/10.2337/diabetes.54.6.1615>
- Bui, B. V., Hu, R. G., Acosta, M. L., Donaldson, P., Vingrys, A. J., & Kalloniatis, M. (2009). Glutamate metabolic pathways and retinal function. *J Neurochem*, 111(2), 589-599. <https://doi.org/10.1111/j.1471-4159.2009.06354.x>
- Campochiaro, P. A. (2015). Molecular pathogenesis of retinal and choroidal vascular diseases. *Prog Retin Eye Res*, 49, 67-81. <https://doi.org/10.1016/j.preteyeres.2015.06.002>
- Caporali, A., Martello, A., Miscianinov, V., Maselli, D., Vono, R., & Spinetti, G. (2017). Contribution of pericyte paracrine regulation of the endothelium to angiogenesis. *Pharmacology & Therapeutics*, 171, 56-64. <https://doi.org/https://doi.org/10.1016/j.pharmthera.2016.10.001>
- Carlson, E. C. (1989). Fenestrated subendothelial basement membranes in human retinal capillaries. *Invest Ophthalmol Vis Sci*, 30(9), 1923-1932.
- Carter-Dawson, L. D., & LaVail, M. M. (1979). Rods and cones in the mouse retina. I. Structural analysis using light and electron microscopy. *J Comp Neurol*, 188(2), 245-262. <https://doi.org/10.1002/cne.901880204>
- Chan-Ling, T. (1994). Glial, neuronal and vascular interactions in the mammalian retina. *Progress in Retinal and Eye Research*, 13(1), 357-389.
- Chao, P. C., Li, Y., Chang, C. H., Shieh, J. P., Cheng, J. T., & Cheng, K. C. (2018). Investigation of insulin resistance in the popularly used four rat models of type-2 diabetes. *Biomed Pharmacother*, 101, 155-161. <https://doi.org/10.1016/j.biopha.2018.02.084>
- Chen, L., Yang, P., & Curcio, C. A. (2022). Visualizing lipid behind the retina in aging and age-related macular degeneration, via indocyanine green angiography (ASHS-LIA). *Eye (Lond)*, 36(9), 1735-1746. <https://doi.org/10.1038/s41433-022-02016-3>
- Chiaverina, G., di Blasio, L., Monica, V., Accardo, M., Palmiero, M., Peracino, B., Vara-Messler, M., Puliafito, A., & Primo, L. (2019). Dynamic Interplay between Pericytes and Endothelial Cells during Sprouting Angiogenesis. *Cells*, 8(9). <https://doi.org/10.3390/cells8091109>
- Choi, S. H., Chung, M., Park, S. W., Jeon, N. L., Kim, J. H., & Yu, Y. S. (2018). Relationship between Pericytes and Endothelial Cells in Retinal Neovascularization: A Histological and Immunofluorescent Study of Retinal Angiogenesis. *Korean J Ophthalmol*, 32(1), 70-76. <https://doi.org/10.3341/kjo.2016.0115>
- Coburn, P. S., Wiskur, B. J., Miller, F. C., LaGrow, A. L., Astley, R. A., Elliott, M. H., & Callegan, M. C. (2016). Bloodstream-To-Eye Infections Are Facilitated by Outer Blood-Retinal Barrier Dysfunction. *PLoS One*, 11(5), e0154560. <https://doi.org/10.1371/journal.pone.0154560>

- Coffey, P. J., Gias, C., McDermott, C. J., Lundh, P., Pickering, M. C., Sethi, C., Bird, A., Fitzke, F. W., Maass, A., Chen, L. L., Holder, G. E., Luthert, P. J., Salt, T. E., Moss, S. E., & Greenwood, J. (2007). Complement factor H deficiency in aged mice causes retinal abnormalities and visual dysfunction. *Proc Natl Acad Sci U S A*, *104*(42), 16651-16656. <https://doi.org/10.1073/pnas.0705079104>
- Coorey, N. J., Shen, W., Chung, S. H., Zhu, L., & Gillies, M. C. (2012). The role of glia in retinal vascular disease. *Clin Exp Optom*, *95*(3), 266-281. <https://doi.org/10.1111/j.1444-0938.2012.00741.x>
- Courson, J. A., Landry, P. T., Do, T., Spehlmann, E., Lafontant, P. J., Patel, N., Rumbaut, R. E., & Burns, A. R. (2021). Serial Block-Face Scanning Electron Microscopy (SBF-SEM) of Biological Tissue Samples. *J Vis Exp*(169). <https://doi.org/10.3791/62045>
- Courtoy, P. J., & Boyles, J. (1983). Fibronectin in the microvasculature: localization in the pericyte-endothelial interstitium. *J Ultrastruct Res*, *83*(3), 258-273. [https://doi.org/10.1016/s0022-5320\(83\)90133-8](https://doi.org/10.1016/s0022-5320(83)90133-8)
- Cunha-Vaz, J. (1979). The blood-ocular barriers. *Survey of ophthalmology*, *23*(5), 279-296.
- Curcio, C. A., Johnson, M., Huang, J. D., & Rudolf, M. (2010). Apolipoprotein B-containing lipoproteins in retinal aging and age-related macular degeneration. *J Lipid Res*, *51*(3), 451-467. <https://doi.org/10.1194/jlr.R002238>
- Curtis, T. M., Gardiner, T. A., & Stitt, A. W. (2009). Microvascular lesions of diabetic retinopathy: clues towards understanding pathogenesis? *Eye (Lond)*, *23*(7), 1496-1508. <https://doi.org/10.1038/eye.2009.108>
- Deniz, S., Wersinger, E., Schwab, Y., Mura, C., Erdelyi, F., Szabó, G., Rendon, A., Sahel, J. A., Picaud, S., & Roux, M. J. (2011). Mammalian retinal horizontal cells are unconventional GABAergic neurons. *J Neurochem*, *116*(3), 350-362. <https://doi.org/10.1111/j.1471-4159.2010.07114.x>
- Derevjanik, N. L., Vinoses, S. A., Xiao, W. H., Mori, K., Turon, T., Hudish, T., Dong, S., & Campochiaro, P. A. (2002). Quantitative assessment of the integrity of the blood-retinal barrier in mice. *Invest Ophthalmol Vis Sci*, *43*(7), 2462-2467.
- Díaz-Flores, L., Gutiérrez, R., Madrid, J. F., Varela, H., Valladares, F., Acosta, E., & Martin-Vasallo, P. (2009). Pericytes. Morphofunction, interactions and pathology in a quiescent and activated mesenchymal cell niche. *Histology and histopathology*.
- Díaz-Flores, L., Jr., Gutiérrez, R., Madrid, J. F., Sáez, F. J., Valladares, F., Villar, J., & Díaz-Flores, L. (2011). Peg-and-socket junctions between smooth muscle cells and endothelial cells in femoral veins are stimulated to angiogenesis by prostaglandin E₂ and glycerols. *Histol Histopathol*, *26*(5), 623-630. <https://doi.org/10.14670/hh-26.623>
- Diniz, L. P., Matias, I., Siqueira, M., Stipursky, J., & Gomes, F. C. A. (2019). Astrocytes and the TGF- β 1 Pathway in the Healthy and Diseased Brain: a Double-Edged Sword. *Mol Neurobiol*, *56*(7), 4653-4679. <https://doi.org/10.1007/s12035-018-1396-y>
- Dodson, P. M. (2007). Diabetic retinopathy: treatment and prevention. *Diab Vasc Dis Res*, *4* Suppl 3, S9-S11. <https://doi.org/10.3132/dvdr.2007.051>
- Dore-Duffy, P., & Cleary, K. (2011). Morphology and properties of pericytes. *The Blood-Brain and Other Neural Barriers: Reviews and Protocols*, 49-68.
- Dufrane, D., van Steenberghe, M., Guiot, Y., Goebbels, R.-M., Saliez, A., & Gianello, P. (2006). Streptozotocin-induced diabetes in large animals (pigs/primates): role of GLUT2 transporter and β -cell plasticity. *Transplantation*, *81*(1), 36-45.
- Duh, E. J., Sun, J. K., & Stitt, A. W. (2017). Diabetic retinopathy: current understanding, mechanisms, and treatment strategies. *JCI Insight*, *2*(14). <https://doi.org/10.1172/jci.insight.93751>

- Eastlake, K., Banerjee, P. J., Angbohang, A., Charteris, D. G., Khaw, P. T., & Limb, G. A. (2016). Müller glia as an important source of cytokines and inflammatory factors present in the gliotic retina during proliferative vitreoretinopathy. *Glia*, *64*(4), 495-506.
- Ejaz, S., Chekarova, I., Ejaz, A., Sohail, A., & Lim, C. W. (2008). Importance of pericytes and mechanisms of pericyte loss during diabetic retinopathy. *Diabetes, Obesity and Metabolism*, *10*(1), 53-63.
- El-Asrar, A. M. A., Dralands, L., Missotten, L., Al-Jadaan, I. A., & Geboes, K. (2004). Expression of apoptosis markers in the retinas of human subjects with diabetes. *Investigative ophthalmology & visual science*, *45*(8), 2760-2766.
- Euler, T., Haverkamp, S., Schubert, T., & Baden, T. (2014). Retinal bipolar cells: elementary building blocks of vision. *Nat Rev Neurosci*, *15*(8), 507-519. <https://doi.org/10.1038/nrn3783>
- Fehér, J., Taurone, S., Spoletini, M., Biró, Z., Varsányi, B., Scuderi, G., Orlando, M. P., Turchetta, R., Micera, A., & Artico, M. (2018). Ultrastructure of neurovascular changes in human diabetic retinopathy. *Int J Immunopathol Pharmacol*, *31*, 394632017748841. <https://doi.org/10.1177/0394632017748841>
- Ferro Desideri, L., Traverso, C. E., Nicolò, M., & Munk, M. R. (2023). Faricimab for the Treatment of Diabetic Macular Edema and Neovascular Age-Related Macular Degeneration. *Pharmaceutics*, *15*(5). <https://doi.org/10.3390/pharmaceutics15051413>
- Fletcher, E. L., Jobling, A. I., Greferath, U., Mills, S. A., Waugh, M., Ho, T., de longh, R. U., Phipps, J. A., & Vessey, K. A. (2014). Studying age-related macular degeneration using animal models. *Optom Vis Sci*, *91*(8), 878-886. <https://doi.org/10.1097/oxp.0000000000000322>
- Forouhi, N. G., & Wareham, N. J. (2014). Epidemiology of diabetes. *Medicine (Abingdon)*, *42*(12), 698-702. <https://doi.org/10.1016/j.mpmed.2014.09.007>
- Frankl, A., Mari, M., & Reggiori, F. (2015). Electron microscopy for ultrastructural analysis and protein localization in *Saccharomyces cerevisiae*. *Microb Cell*, *2*(11), 412-428. <https://doi.org/10.15698/mic2015.11.237>
- Fu, Z., Sun, Y., Cakir, B., Tomita, Y., Huang, S., Wang, Z., Liu, C.-H., S. Cho, S., Britton, W., S. Kern, T., Antonetti, D. A., Hellström, A., & E.H. Smith, L. (2020). Targeting Neurovascular Interaction in Retinal Disorders. *International Journal of Molecular Sciences*, *21*(4).
- Furman, B. L. (2021). Streptozotocin-Induced Diabetic Models in Mice and Rats. *Current Protocols*, *1*(4), e78. <https://doi.org/https://doi.org/10.1002/cpz1.78>
- García, M., & Vecino, E. (2003). Role of Müller glia in neuroprotection and regeneration in the retina. *Histol Histopathol*, *18*(4), 1205-1218. <https://doi.org/10.14670/hh-18.1205>
- Gardiner, T. A., Archer, D. B., Curtis, T. M., & Stitt, A. W. (2007). Arteriolar involvement in the microvascular lesions of diabetic retinopathy: implications for pathogenesis. *Microcirculation*, *14*(1), 25-38. <https://doi.org/10.1080/10739680601072123>
- Garhöfer, G., Chua, J., Tan, B., Wong, D., Schmidl, D., & Schmetterer, L. (2020). Retinal Neurovascular Coupling in Diabetes. *J Clin Med*, *9*(9). <https://doi.org/10.3390/jcm9092829>
- Geevarghese, A., & Herman, I. M. (2014). Pericyte-endothelial crosstalk: implications and opportunities for advanced cellular therapies. *Transl Res*, *163*(4), 296-306. <https://doi.org/10.1016/j.trsl.2014.01.011>
- Gerhardt, H., & Betsholtz, C. (2003). Endothelial-pericyte interactions in angiogenesis. *Cell and tissue research*, *314*, 15-23.

- Goggin, P., Ho, E. M. L., Gnaegi, H., Searle, S., Oreffo, R. O. C., & Schneider, P. (2020). Development of protocols for the first serial block-face scanning electron microscopy (SBF SEM) studies of bone tissue. *Bone*, *131*, 115107. <https://doi.org/10.1016/j.bone.2019.115107>
- Goncalves, A., & Antonetti, D. A. (2022). Transgenic animal models to explore and modulate the blood brain and blood retinal barriers of the CNS. *Fluids and Barriers of the CNS*, *19*(1), 86. <https://doi.org/10.1186/s12987-022-00386-0>
- Goncharov, N. V., Popova, P. I., Avdonin, P. P., Kudryavtsev, I. V., Serebryakova, M. K., Korf, E. A., & Avdonin, P. V. (2020). Markers of Endothelial Cells in Normal and Pathological Conditions. *Biochem (Mosc) Suppl Ser A Membr Cell Biol*, *14*(3), 167-183. <https://doi.org/10.1134/s1990747819030140>
- Goyal, M., Bordt, A. S., Neitz, J., & Marshak, D. W. (2023). Trogocytosis of neurons and glial cells by microglia in a healthy adult macaque retina. *Sci Rep*, *13*(1), 633. <https://doi.org/10.1038/s41598-023-27453-2>
- Greenberg, A. (2009). *Primer on kidney diseases E-book*. Elsevier Health Sciences.
- Grossman, P., Kappos, L., Gensicke, H., D'Souza, M., Mohr, D. C., Penner, I. K., & Steiner, C. (2010). MS quality of life, depression, and fatigue improve after mindfulness training: a randomized trial. *Neurology*, *75*(13), 1141-1149. <https://doi.org/10.1212/WNL.0b013e3181f4d80d>
- Guo, L., Choi, S., Bikkannavar, P., & Cordeiro, M. F. (2022). Microglia: Key Players in Retinal Ageing and Neurodegeneration. *Front Cell Neurosci*, *16*, 804782. <https://doi.org/10.3389/fncel.2022.804782>
- Gupta, V., & Arevalo, J. F. (2013). Surgical management of diabetic retinopathy. *Middle East Afr J Ophthalmol*, *20*(4), 283-292. <https://doi.org/10.4103/0974-9233.120003>
- Guymer, R. H., & Campbell, T. G. (2023). Age-related macular degeneration. *Lancet*, *401*(10386), 1459-1472. [https://doi.org/10.1016/s0140-6736\(22\)02609-5](https://doi.org/10.1016/s0140-6736(22)02609-5)
- Hammes, H. P., Feng, Y., Pfister, F., & Brownlee, M. (2011). Diabetic retinopathy: targeting vasoregression. *Diabetes*, *60*(1), 9-16. <https://doi.org/10.2337/db10-0454>
- Hannibal, J., Hindersson, P., Knudsen, S. M., Georg, B., & Fahrenkrug, J. (2002). The photopigment melanopsin is exclusively present in pituitary adenylate cyclase-activating polypeptide-containing retinal ganglion cells of the retinohypothalamic tract. *J Neurosci*, *22*(1), Rc191. <https://doi.org/10.1523/JNEUROSCI.22-01-j0002.2002>
- Hartnett, M. E. (2005). *Pediatric retina*. Lippincott Williams & Wilkins.
- Hattar, S., Kumar, M., Park, A., Tong, P., Tung, J., Yau, K. W., & Berson, D. M. (2006). Central projections of melanopsin-expressing retinal ganglion cells in the mouse. *J Comp Neurol*, *497*(3), 326-349. <https://doi.org/10.1002/cne.20970>
- Hawkins, B. T., & Davis, T. P. (2005). The Blood-Brain Barrier/Neurovascular Unit in Health and Disease. *Pharmacological Reviews*, *57*(2), 173. <https://doi.org/10.1124/pr.57.2.4>
- Hayden, M. R., Sowers, J. R., & Tyagi, S. C. (2005). The central role of vascular extracellular matrix and basement membrane remodeling in metabolic syndrome and type 2 diabetes: the matrix preloaded. *Cardiovascular Diabetology*, *4*(1), 9. <https://doi.org/10.1186/1475-2840-4-9>
- Heng, L. Z., Comyn, O., Peto, T., Tadros, C., Ng, E., Sivaprasad, S., & Hykin, P. G. (2013). Diabetic retinopathy: pathogenesis, clinical grading, management and future developments. *Diabet Med*, *30*(6), 640-650. <https://doi.org/10.1111/dme.12089>
- Hogan, M. J. (1971). *Histology of the human eye: an atlas and textbook. (No Title)*, 187.

- Holländer, H., Makarov, F., Dreher, Z., van Driel, D., Chan-Ling, T. L., & Stone, J. (1991). Structure of the macroglia of the retina: sharing and division of labour between astrocytes and Müller cells. *J Comp Neurol*, 313(4), 587-603. <https://doi.org/10.1002/cne.903130405>
- Hoon, M., Okawa, H., Della Santina, L., & Wong, R. O. L. (2014). Functional Architecture of the Retina: Development and Disease. *Progress in Retinal and Eye Research*, 42, 44-84. <https://doi.org/10.1016/j.preteyeres.2014.06.003>
- Huang, H., He, J., Johnson, D. K., Wei, Y., Liu, Y., Wang, S., Luttly, G. A., Duh, E. J., Carmeliet, P., & Semba, R. D. (2015). Deletion of placental growth factor prevents diabetic retinopathy and is associated with Akt activation and HIF1 α -VEGF pathway inhibition. *Diabetes*, 64(1), 200-212.
- Hudson, N., & Campbell, M. (2021). Tight Junctions of the Neurovascular Unit. *Front Mol Neurosci*, 14, 752781. <https://doi.org/10.3389/fnmol.2021.752781>
- Ichinose, T., & Habib, S. (2022). ON and OFF Signaling Pathways in the Retina and the Visual System. *Front Ophthalmol (Lausanne)*, 2. <https://doi.org/10.3389/fopht.2022.989002>
- Ireland, A. C., & Carter, I. B. (2024). Neuroanatomy, Optic Chiasm. In *StatPearls*. StatPearls Publishing
- Copyright © 2024, StatPearls Publishing LLC.
- Isakson, B. E., Ramos, S. I., & Duling, B. R. (2007). Ca²⁺ and inositol 1,4,5-trisphosphate-mediated signaling across the myoendothelial junction. *Circ Res*, 100(2), 246-254. <https://doi.org/10.1161/01.Res.0000257744.23795.93>
- Ivanova, E., Alam, N. M., Prusky, G. T., & Sagdullaev, B. T. (2019). Blood-retina barrier failure and vision loss in neuron-specific degeneration. *JCI Insight*, 4(8).
- Janssen, S. F., van der Spek, S. J., Ten Brink, J. B., Essing, A. H., Gorgels, T. G., van der Spek, P. J., Jansonius, N. M., & Bergen, A. A. (2013). Gene expression and functional annotation of the human and mouse choroid plexus epithelium. *PLoS One*, 8(12), e83345. <https://doi.org/10.1371/journal.pone.0083345>
- Jayadev, R., & Sherwood, D. R. (2017). Basement membranes. *Curr Biol*, 27(6), R207-r211. <https://doi.org/10.1016/j.cub.2017.02.006>
- Jeon, C. J., Strettoi, E., & Masland, R. H. (1998). The major cell populations of the mouse retina. *J Neurosci*, 18(21), 8936-8946. <https://doi.org/10.1523/jneurosci.18-21-08936.1998>
- Jeremic, N., Pawloff, M., Lachinov, D., Rokitansky, S., Hasun, M., Weidinger, F., Pollreisz, A., Bogunovic, H., & Schmidt-Erfurth, U. (2024). Severity Stratification of Coronary Artery Disease Using Novel Inner Ellipse-Based Foveal Avascular Zone Biomarkers. *Invest Ophthalmol Vis Sci*, 65(12), 15. <https://doi.org/10.1167/iovs.65.12.15>
- Joussen, A. M., Poulaki, V., Mitsiades, N., Cai, W. Y., Suzuma, I., Pak, J., Ju, S. T., Rook, S. L., Esser, P., Mitsiades, C. S., Kirchhof, B., Adamis, A. P., & Aiello, L. P. (2003). Suppression of Fas-FasL-induced endothelial cell apoptosis prevents diabetic blood-retinal barrier breakdown in a model of streptozotocin-induced diabetes. *Faseb j*, 17(1), 76-78. <https://doi.org/10.1096/fj.02-0157fj>
- Kador, P. F., Wyman, M., & Oates, P. J. (2016). Aldose reductase, ocular diabetic complications and the development of topical Kinostat[®]. *Prog Retin Eye Res*, 54, 1-29. <https://doi.org/10.1016/j.preteyeres.2016.04.006>
- Karlstetter, M., Scholz, R., Rutar, M., Wong, W. T., Provis, J. M., & Langmann, T. (2015). Retinal microglia: just bystander or target for therapy? *Progress in Retinal and Eye Research*, 45, 30-57.

- Kasza, M., Meleg, J., Vardai, J., Nagy, B., Jr., Szalai, E., Damjanovich, J., Csutak, A., Ujhelyi, B., & Nagy, V. (2017). Plasma E-selectin levels can play a role in the development of diabetic retinopathy. *Graefes Arch Clin Exp Ophthalmol*, 255(1), 25-30. <https://doi.org/10.1007/s00417-016-3411-1>
- Kawamura, H., Sugiyama, T., Wu, D. M., Kobayashi, M., Yamanishi, S., Katsumura, K., & Puro, D. G. (2003). ATP: a vasoactive signal in the pericyte-containing microvasculature of the rat retina. *The Journal of physiology*, 551(3), 787-799.
- Kels, B. D., Grzybowski, A., & Grant-Kels, J. M. (2015). Human ocular anatomy. *Clin Dermatol*, 33(2), 140-146. <https://doi.org/10.1016/j.clindermatol.2014.10.006>
- Khalilgharibi, N., & Mao, Y. (2021). To form and function: on the role of basement membrane mechanics in tissue development, homeostasis and disease. *Open Biol*, 11(2), 200360. <https://doi.org/10.1098/rsob.200360>
- Kinuthia, U. M., Wolf, A., & Langmann, T. (2020). Microglia and Inflammatory Responses in Diabetic Retinopathy. *Front Immunol*, 11, 564077. <https://doi.org/10.3389/fimmu.2020.564077>
- Klaassen, I., Van Noorden, C. J., & Schlingemann, R. O. (2013). Molecular basis of the inner blood-retinal barrier and its breakdown in diabetic macular edema and other pathological conditions. *Prog Retin Eye Res*, 34, 19-48. <https://doi.org/10.1016/j.preteyeres.2013.02.001>
- Klug, N. R., Sancho, M., Gonzales, A. L., Heppner, T. J., O'Brien, R. I. C., Hill-Eubanks, D., & Nelson, M. T. (2023). Intraluminal pressure elevates intracellular calcium and contracts CNS pericytes: Role of voltage-dependent calcium channels. *Proc Natl Acad Sci U S A*, 120(9), e2216421120. <https://doi.org/10.1073/pnas.2216421120>
- Kohner, E. M. (2008). Microvascular disease: what does the UKPDS tell us about diabetic retinopathy? *Diabet Med*, 25 Suppl 2, 20-24. <https://doi.org/10.1111/j.1464-5491.2008.02505.x>
- Kolb, H. (1995). Gross Anatomy of the Eye. In H. Kolb, E. Fernandez, & R. Nelson (Eds.), *Webvision: The Organization of the Retina and Visual System*. University of Utah Health Sciences Center
- Copyright: © 2024 Webvision .
- Koss, M. C. (1999). Functional role of nitric oxide in regulation of ocular blood flow. *Eur J Pharmacol*, 374(2), 161-174. [https://doi.org/10.1016/s0014-2999\(99\)00242-3](https://doi.org/10.1016/s0014-2999(99)00242-3)
- Kovacs-Oller, T., Ivanova, E., Bianchimano, P., & Sagdullaev, B. T. (2020). The pericyte connectome: spatial precision of neurovascular coupling is driven by selective connectivity maps of pericytes and endothelial cells and is disrupted in diabetes. *Cell Discovery*, 6(1), 39. <https://doi.org/10.1038/s41421-020-0180-0>
- Kowluru, R. A., & Koppolu, P. (2002). Diabetes-induced activation of caspase-3 in retina: effect of antioxidant therapy. *Free Radical Research*, 36(9), 993-999.
- Lachin, J. M., White, N. H., Hainsworth, D. P., Sun, W., Cleary, P. A., & Nathan, D. M. (2015). Effect of intensive diabetes therapy on the progression of diabetic retinopathy in patients with type 1 diabetes: 18 years of follow-up in the DCCT/EDIC. *Diabetes*, 64(2), 631-642. <https://doi.org/10.2337/db14-0930>
- Lang, G. E. (2007). Optical coherence tomography findings in diabetic retinopathy. *Dev Ophthalmol*, 39, 31-47. <https://doi.org/10.1159/000098498>
- Lange, C. A., & Bainbridge, J. W. (2012). Oxygen sensing in retinal health and disease. *Ophthalmologica*, 227(3), 115-131. <https://doi.org/10.1159/000331418>
- Lavia, C., Mecê, P., Nassisi, M., Bonnin, S., Marie-Louise, J., Couturier, A., Erginay, A., Tadayoni, R., & Gaudric, A. (2020). Retinal Capillary Plexus Pattern and Density from Fovea to Periphery Measured in Healthy

- Eyes with Swept-Source Optical Coherence Tomography Angiography. *Sci Rep*, 10(1), 1474. <https://doi.org/10.1038/s41598-020-58359-y>
- Laws, R., Steel, D. H., & Rajan, N. (2022). Research Techniques Made Simple: Volume Scanning Electron Microscopy. *J Invest Dermatol*, 142(2), 265-271.e261. <https://doi.org/10.1016/j.jid.2021.10.020>
- Lechner, J., O'Leary, O. E., & Stitt, A. W. (2017). The pathology associated with diabetic retinopathy. *Vision Res*, 139, 7-14. <https://doi.org/10.1016/j.visres.2017.04.003>
- Lechner, J., O'Leary, O. E., & Stitt, A. W. (2017). The pathology associated with diabetic retinopathy. *Vision Research*, 139, 7-14. <https://doi.org/https://doi.org/10.1016/j.visres.2017.04.003>
- Lenzen, S. (2008). The mechanisms of alloxan- and streptozotocin-induced diabetes. *Diabetologia*, 51(2), 216-226. <https://doi.org/10.1007/s00125-007-0886-7>
- Li, G., Gao, J., Ding, P., & Gao, Y. (2024). The role of endothelial cell-pericyte interactions in vascularization and diseases. *J Adv Res*. <https://doi.org/10.1016/j.jare.2024.01.016>
- Li, J., Wang, J. J., Yu, Q., Chen, K., Mahadev, K., & Zhang, S. X. (2010). Inhibition of reactive oxygen species by Lovastatin downregulates vascular endothelial growth factor expression and ameliorates blood-retinal barrier breakdown in db/db mice: role of NADPH oxidase 4. *Diabetes*, 59(6), 1528-1538.
- Li, P., & Fan, H. (2023). Pericyte Loss in Diseases. *Cells*, 12(15). <https://doi.org/10.3390/cells12151931>
- Li, X., Lv, J., Li, J., & Ren, X. (2021). Kir4.1 may represent a novel therapeutic target for diabetic retinopathy (Review). *Exp Ther Med*, 22(3), 1021. <https://doi.org/10.3892/etm.2021.10453>
- Limb, G. A., Hickman-Casey, J., Hollifield, R. D., & Chignell, A. H. (1999). Vascular adhesion molecules in vitreous from eyes with proliferative diabetic retinopathy. *Invest Ophthalmol Vis Sci*, 40(10), 2453-2457.
- Liu, J., Han, Y. S., Liu, L., Tang, L., Yang, H., Meng, P., Zhao, H. Q., & Wang, Y. H. (2021). Abnormal Glu/mGluR(2/3)/PI3K pathway in the hippocampal neurovascular unit leads to diabetes-related depression. *Neural Regen Res*, 16(4), 727-733. <https://doi.org/10.4103/1673-5374.296418>
- Liu, L., & Liu, X. (2019). Roles of Drug Transporters in Blood-Retinal Barrier. *Adv Exp Med Biol*, 1141, 467-504. https://doi.org/10.1007/978-981-13-7647-4_10
- Lupo, G., Motta, C., Giurdanella, G., Anfuso, C. D., Alberghina, M., Drago, F., Salomone, S., & Bucolo, C. (2013). Role of phospholipases A2 in diabetic retinopathy: in vitro and in vivo studies. *Biochemical pharmacology*, 86(11), 1603-1613.
- Maarouf, N., Sancho, M., Fürstenhaupt, T., Tran, C. H., & Welsh, D. G. (2017). Structural analysis of endothelial projections from mesenteric arteries. *Microcirculation*, 24(3). <https://doi.org/10.1111/micc.12330>
- MacLeod, D. C., Strauss, B. H., de Jong, M., Escaned, J., Umans, V. A., van Suylen, R. J., Verkerk, A., de Feyter, P. J., & Serruys, P. W. (1994). Proliferation and extracellular matrix synthesis of smooth muscle cells cultured from human coronary atherosclerotic and restenotic lesions. *J Am Coll Cardiol*, 23(1), 59-65. [https://doi.org/10.1016/0735-1097\(94\)90502-9](https://doi.org/10.1016/0735-1097(94)90502-9)
- Maeda, T., Imanishi, Y., & Palczewski, K. (2003). Rhodopsin phosphorylation: 30 years later. *Prog Retin Eye Res*, 22(4), 417-434. [https://doi.org/10.1016/s1350-9462\(03\)00017-x](https://doi.org/10.1016/s1350-9462(03)00017-x)
- Mannu, G. S. (2014). Retinal phototransduction. *Neurosciences (Riyadh)*, 19(4), 275-280.
- Marshall, C. B. (2016). Rethinking glomerular basement membrane thickening in diabetic nephropathy: adaptive or pathogenic? *Am J Physiol Renal Physiol*, 311(5), F831-f843. <https://doi.org/10.1152/ajprenal.00313.2016>

- Masland, R. H. (2011). Cell populations of the retina: the Proctor lecture. *Invest Ophthalmol Vis Sci*, 52(7), 4581-4591. <https://doi.org/10.1167/iovs.10-7083>
- Masland, R. H. (2012a). The neuronal organization of the retina. *Neuron*, 76(2), 266-280. <https://doi.org/10.1016/j.neuron.2012.10.002>
- Masland, R. H. (2012b). The tasks of amacrine cells. *Vis Neurosci*, 29(1), 3-9. <https://doi.org/10.1017/s0952523811000344>
- Matuszewski, W., Baranowska-Jurkun, A., Stefanowicz-Rutkowska, M. M., Modzelewski, R., Pieczyński, J., & Bandurska-Stankiewicz, E. (2020). Prevalence of Diabetic Retinopathy in Type 1 and Type 2 Diabetes Mellitus Patients in North-East Poland. *Medicina (Kaunas)*, 56(4). <https://doi.org/10.3390/medicina56040164>
- McMahon, D. G., & Dowling, J. E. (2023). Neuromodulation: Actions of Dopamine, Retinoic Acid, Nitric Oxide, and Other Substances on Retinal Horizontal Cells. *Eye Brain*, 15, 125-137. <https://doi.org/10.2147/eb.S420050>
- Meng, C., Gu, C., He, S., Su, T., Lhamo, T., Draga, D., & Qiu, Q. (2021). Pyroptosis in the Retinal Neurovascular Unit: New Insights Into Diabetic Retinopathy [Review]. *Frontiers in Immunology*, 12. <https://doi.org/10.3389/fimmu.2021.763092>
- Metaa, M. R., & Newman, E. A. (2006). Glial cells dilate and constrict blood vessels: a mechanism of neurovascular coupling. *J Neurosci*, 26(11), 2862-2870. <https://doi.org/10.1523/jneurosci.4048-05.2006>
- Metaa, M. R., & Newman, E. A. (2007). Signalling within the neurovascular unit in the mammalian retina. *Exp Physiol*, 92(4), 635-640. <https://doi.org/10.1113/expphysiol.2006.036376>
- Mills, S. A., Jobling, A. I., Dixon, M. A., Bui, B. V., Vessey, K. A., Phipps, J. A., Greferath, U., Venables, G., Wong, V. H. Y., Wong, C. H. Y., He, Z., Hui, F., Young, J. C., Tonc, J., Ivanova, E., Sagdullaev, B. T., & Fletcher, E. L. (2021). Fractalkine-induced microglial vasoregulation occurs within the retina and is altered early in diabetic retinopathy. *Proc Natl Acad Sci U S A*, 118(51). <https://doi.org/10.1073/pnas.2112561118>
- Miyamoto, K., Hiroshiba, N., Tsujikawa, A., & Ogura, Y. (1998). In vivo demonstration of increased leukocyte entrapment in retinal microcirculation of diabetic rats. *Invest Ophthalmol Vis Sci*, 39(11), 2190-2194.
- Miyamoto, K., Khosrof, S., Bursell, S. E., Rohan, R., Murata, T., Clermont, A. C., Aiello, L. P., Ogura, Y., & Adamis, A. P. (1999). Prevention of leukostasis and vascular leakage in streptozotocin-induced diabetic retinopathy via intercellular adhesion molecule-1 inhibition. *Proc Natl Acad Sci U S A*, 96(19), 10836-10841. <https://doi.org/10.1073/pnas.96.19.10836>
- Molday, R. S., & Moritz, O. L. (2015). Photoreceptors at a glance. *J Cell Sci*, 128(22), 4039-4045. <https://doi.org/10.1242/jcs.175687>
- Monteiro, J. P., Santos, F. M., Rocha, A. S., Castro-de-Sousa, J. P., Queiroz, J. A., Passarinha, L. A., & Tomaz, C. T. (2015). Vitreous humor in the pathologic scope: insights from proteomic approaches. *Proteomics Clin Appl*, 9(1-2), 187-202. <https://doi.org/10.1002/prca.201400133>
- Moran, E. P., Wang, Z., Chen, J., Sapieha, P., Smith, L. E., & Ma, J. X. (2016). Neurovascular cross talk in diabetic retinopathy: Pathophysiological roles and therapeutic implications. *Am J Physiol Heart Circ Physiol*, 311(3), H738-749. <https://doi.org/10.1152/ajpheart.00005.2016>
- Moutray, T., Evans, J. R., Lois, N., Armstrong, D. J., Peto, T., & Azuara-Blanco, A. (2018). Different lasers and techniques for proliferative diabetic retinopathy. *Cochrane Database Syst Rev*, 3(3), Cd012314. <https://doi.org/10.1002/14651858.CD012314.pub2>

- Nagata, M., Katz, M. L., & Robison, W. G., Jr. (1986). Age-related thickening of retinal capillary basement membranes. *Invest Ophthalmol Vis Sci*, 27(3), 437-440.
- Naggert, A., Collin, G. B., Wang, J., Krebs, M. P., & Chang, B. (2022). A mouse model of cone photoreceptor function loss (cpfl9) with degeneration due to a mutation in *Gucy2e*. *Front Mol Neurosci*, 15, 1080136. <https://doi.org/10.3389/fnmol.2022.1080136>
- Nathan, D. M., Genuth, S., Lachin, J., Cleary, P., Crofford, O., Davis, M., Rand, L., & Siebert, C. (1993). The effect of intensive treatment of diabetes on the development and progression of long-term complications in insulin-dependent diabetes mellitus. *N Engl J Med*, 329(14), 977-986. <https://doi.org/10.1056/nejm199309303291401>
- Netter, F. H. (2014). *Atlas of human anatomy, Professional Edition E-Book: including NetterReference. com Access with full downloadable image Bank*. Elsevier health sciences.
- Newman, E., & Reichenbach, A. (1996). The Müller cell: a functional element of the retina. *Trends Neurosci*, 19(8), 307-312. [https://doi.org/10.1016/0166-2236\(96\)10040-0](https://doi.org/10.1016/0166-2236(96)10040-0)
- Newman, E. A. (2015). Glial cell regulation of neuronal activity and blood flow in the retina by release of gliotransmitters. *Philosophical transactions of the Royal Society of London. Series B, Biological sciences*, 370(1672), 20140195. <https://doi.org/10.1098/rstb.2014.0195>
- Noda, K., Nakao, S., Ishida, S., & Ishibashi, T. (2012). Leukocyte adhesion molecules in diabetic retinopathy. *J Ophthalmol*, 2012, 279037. <https://doi.org/10.1155/2012/279037>
- Noell, W. (1965). *Biochemistry of the Retina. Supplement of Experimental Eye Research*. Academic Press, London.
- Nusinovici, S., Rim, T. H., Li, H., Yu, M., Deshmukh, M., Quek, T. C., Lee, G., Chong, C. C. Y., Peng, Q., Xue, C. C., Zhu, Z., Chew, E. Y., Sabanayagam, C., Wong, T. Y., Tham, Y. C., & Cheng, C. Y. (2024). Application of a deep-learning marker for morbidity and mortality prediction derived from retinal photographs: a cohort development and validation study. *Lancet Healthy Longev*, 5(10), 100593. [https://doi.org/10.1016/s2666-7568\(24\)00089-8](https://doi.org/10.1016/s2666-7568(24)00089-8)
- O'Hare, M., Esquivia, G., McGahon, M. K., Hombrebueno, J. M. R., Augustine, J., Canning, P., Edgar, K. S., Barabas, P., Friedel, T., Cincolà, P., Henry, J., Mayne, K., Ferrin, H., Stitt, A. W., Lyons, T. J., Brazil, D. P., Grieve, D. J., McGeown, J. G., & Curtis, T. M. (2022). Loss of TRPV2-mediated blood flow autoregulation recapitulates diabetic retinopathy in rats. *JCI Insight*, 7(18). <https://doi.org/10.1172/jci.insight.155128>
- O'Neal, T. B., & Luther, E. E. (2024). Retinitis Pigmentosa. In *StatPearls*. StatPearls Publishing
- Copyright © 2024, StatPearls Publishing LLC.
- Ochs, M., Mayhew, T. M., & Knabe, W. (2000). To what extent are the retinal capillaries ensheathed by Müller cells? A stereological study in the tree shrew *Tupaia belangeri*. *J Anat*, 196 (Pt 3)(Pt 3), 453-461. <https://doi.org/10.1046/j.1469-7580.2000.19630453.x>
- Orlidge, A., & D'Amore, P. A. (1987). Inhibition of capillary endothelial cell growth by pericytes and smooth muscle cells. *J Cell Biol*, 105(3), 1455-1462. <https://doi.org/10.1083/jcb.105.3.1455>
- Ornelas, S., Berthiaume, A. A., Bonney, S. K., Coelho-Santos, V., Underly, R. G., Kremer, A., Guérin, C. J., Lippens, S., & Shih, A. Y. (2021). Three-dimensional ultrastructure of the brain pericyte-endothelial interface. *J Cereb Blood Flow Metab*, 41(9), 2185-2200. <https://doi.org/10.1177/0271678x211012836>

- Paik, S.-G., Fleischer, N., & Shin, S.-i. (1980). Insulin-dependent diabetes mellitus induced by subdiabetogenic doses of streptozotocin: obligatory role of cell-mediated autoimmune processes. *Proceedings of the National Academy of Sciences*, 77(10), 6129-6133.
- Palczewski, K. (2012). Chemistry and biology of vision. *J Biol Chem*, 287(3), 1612-1619. <https://doi.org/10.1074/jbc.R111.301150>
- Patel, J. I., Hykin, P. G., Gregor, Z. J., Boulton, M., & Cree, I. A. (2005). Angiopoietin concentrations in diabetic retinopathy. *The British Journal of Ophthalmology*, 89(4), 480.
- Peirson, S. N., Brown, L. A., Potheary, C. A., Benson, L. A., & Fisk, A. S. (2018). Light and the laboratory mouse. *J Neurosci Methods*, 300, 26-36. <https://doi.org/10.1016/j.jneumeth.2017.04.007>
- Peppiatt, C. M., Howarth, C., Mobbs, P., & Attwell, D. (2006). Bidirectional control of CNS capillary diameter by pericytes. *Nature*, 443(7112), 700-704. <https://doi.org/10.1038/nature05193>
- Powner, M. B., Gillies, M. C., Tretiach, M., Scott, A., Guymer, R. H., Hageman, G. S., & Fruttiger, M. (2010). Perifoveal müller cell depletion in a case of macular telangiectasia type 2. *Ophthalmology*, 117(12), 2407-2416. <https://doi.org/10.1016/j.ophtha.2010.04.001>
- Powner, M. B., Scott, A., Zhu, M., Munro, P. M., Foss, A. J., Hageman, G. S., Gillies, M. C., & Fruttiger, M. (2011). Basement membrane changes in capillaries of the ageing human retina. *Br J Ophthalmol*, 95(9), 1316-1322. <https://doi.org/10.1136/bjo.2011.204222>
- Rakieten, N., Rakieten, M. L., & Nadkarni, M. V. (1963). Studies on the diabetogenic action of streptozotocin (NSC-37917). *Cancer Chemother Rep*, 29, 91-98.
- Rangasamy, S., McGuire, P. G., & Das, A. (2012). Diabetic retinopathy and inflammation: novel therapeutic targets. *Middle East Afr J Ophthalmol*, 19(1), 52-59. <https://doi.org/10.4103/0974-9233.92116>
- Rangasamy, S., McGuire, P. G., Franco Nitta, C., Monickaraj, F., Oruganti, S. R., & Das, A. (2014). Chemokine mediated monocyte trafficking into the retina: role of inflammation in alteration of the blood-retinal barrier in diabetic retinopathy. *PLoS One*, 9(10), e108508. <https://doi.org/10.1371/journal.pone.0108508>
- Rangasamy, S., Srinivasan, R., Maestas, J., McGuire, P. G., & Das, A. (2011). A potential role for angiopoietin 2 in the regulation of the blood-retinal barrier in diabetic retinopathy. *Investigative ophthalmology & visual science*, 52(6), 3784-3791.
- Reddy, K. N., Locke, M. A., Wagner, S. C., Zablotowicz, R. M., Gaston, L. A., & Smeda, R. J. (1995). Chlorimuron ethyl sorption and desorption kinetics in soils and herbicide-desiccated cover crop residues. *Journal of Agricultural and Food Chemistry*, 43(10), 2752-2757. <https://doi.org/10.1021/jf00058a038>
- Regus-Leidig, H., & Brandstätter, J. H. (2012). Structure and function of a complex sensory synapse. *Acta Physiol (Oxf)*, 204(4), 479-486. <https://doi.org/10.1111/j.1748-1716.2011.02355.x>
- Reichenbach, A., & Bringmann, A. (2013). New functions of Müller cells. *Glia*, 61(5), 651-678. <https://doi.org/10.1002/glia.22477>
- Ren, J., Zhang, S., Pan, Y., Jin, M., Li, J., Luo, Y., Sun, X., & Li, G. (2022). Diabetic retinopathy: Involved cells, biomarkers, and treatments. *Front Pharmacol*, 13, 953691. <https://doi.org/10.3389/fphar.2022.953691>
- Rhodin, J. A. G. (1968). Ultrastructure of mammalian venous capillaries, venules, and small collecting veins. *Journal of ultrastructure research*, 25(5-6), 452-500.
- Riazi-Esfahani, H., Ahmadi, A., Sadeghi, R., Mirghorbani, M., Ghassemi, F., Zarei, M., Khojasteh, H., Bayan, N., Faghihi, H., Khalili Pour, E., & Mirshahi, A. (2024). Evaluation of Foveal Vasculature by Optical

- Coherence Tomography Angiography after Pan-Retinal Photocoagulation versus Intravitreal Anti-VEGF Injections. *J Ophthalmic Vis Res*, 19(3), 313-323. <https://doi.org/10.18502/iov.v19i3.13622>
- Ribatti, D., Nico, B., & Crivellato, E. (2011). The role of pericytes in angiogenesis. *Int J Dev Biol*, 55(3), 261-268. <https://doi.org/10.1387/ijdb.103167dr>
- Romeo, G., Liu, W.-H., Asnaghi, V., Kern, T. S., & Lorenzi, M. (2002). Activation of nuclear factor- κ B induced by diabetes and high glucose regulates a proapoptotic program in retinal pericytes. *Diabetes*, 51(7), 2241-2248.
- Roorda, A., & Williams, D. R. (1999). The arrangement of the three cone classes in the living human eye. *Nature*, 397(6719), 520-522. <https://doi.org/10.1038/17383>
- Rousseau, S., Houle, F., Landry, J., & Huot, J. (1997). p38 MAP kinase activation by vascular endothelial growth factor mediates actin reorganization and cell migration in human endothelial cells. *Oncogene*, 15(18), 2169-2177.
- Roy, S., & Kim, D. (2021). Retinal capillary basement membrane thickening: Role in the pathogenesis of diabetic retinopathy. *Progress in Retinal and Eye Research*, 82, 100903. <https://doi.org/https://doi.org/10.1016/j.preteyeres.2020.100903>
- Roy, S., & Kim, D. (2021). Retinal capillary basement membrane thickening: Role in the pathogenesis of diabetic retinopathy. *Prog Retin Eye Res*, 82, 100903. <https://doi.org/10.1016/j.preteyeres.2020.100903>
- Ruberti, J. W., Curcio, C. A., Millican, C. L., Menco, B. P., Huang, J. D., & Johnson, M. (2003). Quick-freeze/deep-etch visualization of age-related lipid accumulation in Bruch's membrane. *Invest Ophthalmol Vis Sci*, 44(4), 1753-1759. <https://doi.org/10.1167/iovs.02-0496>
- Rübsam, A., Parikh, S., & Fort, P. E. (2018). Role of Inflammation in Diabetic Retinopathy. *Int J Mol Sci*, 19(4). <https://doi.org/10.3390/ijms19040942>
- Ruiz-Torres, M. P., Pérez-Rivero, G., Rodríguez-Puyol, M., Rodríguez-Puyol, D., & Díez-Marqués, M. L. (2006). The leukocyte-endothelial cell interactions are modulated by extracellular matrix proteins. *Cell Physiol Biochem*, 17(5-6), 221-232. <https://doi.org/10.1159/000094127>
- Rungger-Brändle, E., Dosso, A. A., & Leuenberger, P. M. (2000). Glial reactivity, an early feature of diabetic retinopathy. *Investigative ophthalmology & visual science*, 41(7), 1971-1980.
- Santos, A. R., Lopes, M., Santos, T., Reste-Ferreira, D., Marques, I. P., Yamaguchi, T. C. N., Miranda, T., Mendes, L., Martinho, A. C. V., Pearce, L., & Cunha-Vaz, J. (2024). Intraretinal Microvascular Abnormalities in Eyes with Advanced Stages of Nonproliferative Diabetic Retinopathy: Comparison Between UWF-FFA, CFP, and OCTA-The RICHARD Study. *Ophthalmol Ther*. <https://doi.org/10.1007/s40123-024-01054-2>
- Santos, A. R., Ribeiro, L., Bandello, F., Lattanzio, R., Egan, C., Frydkjaer-Olsen, U., García-Arumí, J., Gibson, J., Grauslund, J., Harding, S. P., Lang, G. E., Massin, P., Midea, E., Scanlon, P., Aldington, S. J., Simão, S., Schwartz, C., Ponsati, B., Porta, M., . . . Simó, R. (2017). Functional and Structural Findings of Neurodegeneration in Early Stages of Diabetic Retinopathy: Cross-sectional Analyses of Baseline Data of the EUROCONDOR Project. *Diabetes*, 66(9), 2503-2510. <https://doi.org/10.2337/db16-1453>
- Santos, A. R., Ribeiro, L., Bandello, F., Lattanzio, R., Egan, C., Frydkjaer-Olsen, U., García-Arumí, J., Gibson, J., Grauslund, J., Harding, S. P., Lang, G. E., Massin, P., Midea, E., Scanlon, P., Aldington, S. J., Simão, S., Schwartz, C., Ponsati, B., Porta, M., . . . Retinopathy, f. t. E. C. f. t. E. T. o. D. (2017). Functional and Structural Findings of Neurodegeneration in Early Stages of Diabetic Retinopathy: Cross-sectional Analyses of Baseline Data of the EUROCONDOR Project. *Diabetes*, 66(9), 2503-2510. <https://doi.org/10.2337/db16-1453>

- Sasaki, M., Ozawa, Y., Kurihara, T., Kubota, S., Yuki, K., Noda, K., Kobayashi, S., Ishida, S., & Tsubota, K. (2010). Neurodegenerative influence of oxidative stress in the retina of a murine model of diabetes. *Diabetologia*, *53*(5), 971-979. <https://doi.org/10.1007/s00125-009-1655-6>
- Savige, J., Liu, J., DeBuc, D. C., Handa, J. T., Hageman, G. S., Wang, Y. Y., Parkin, J. D., Vote, B., Fassett, R., Sarks, S., & Colville, D. (2010). Retinal basement membrane abnormalities and the retinopathy of Alport syndrome. *Invest Ophthalmol Vis Sci*, *51*(3), 1621-1627. <https://doi.org/10.1167/iovs.08-3323>
- Schafer, D. P., Lehrman, E. K., Kautzman, A. G., Koyama, R., Mardinly, A. R., Yamasaki, R., Ransohoff, R. M., Greenberg, M. E., Barres, B. A., & Stevens, B. (2012). Microglia sculpt postnatal neural circuits in an activity and complement-dependent manner. *Neuron*, *74*(4), 691-705.
- Schnitzer, J. (1988). Astrocytes in mammalian retina. *Progress in retinal research*, *7*, 209-231.
- Schröder, S., Palinski, W., & Schmid-Schönbein, G. W. (1991). Activated monocytes and granulocytes, capillary nonperfusion, and neovascularization in diabetic retinopathy. *Am J Pathol*, *139*(1), 81-100.
- Schubert, T., Huckfeldt, R. M., Parker, E., Campbell, J. E., & Wong, R. O. (2010). Assembly of the outer retina in the absence of GABA synthesis in horizontal cells. *Neural Dev*, *5*, 15. <https://doi.org/10.1186/1749-8104-5-15>
- Shen, W., Li, S., Chung, S. H., & Gillies, M. C. (2010). Retinal vascular changes after glial disruption in rats. *J Neurosci Res*, *88*(7), 1485-1499. <https://doi.org/10.1002/jnr.22317>
- Sheng, X., Zhang, C., Zhao, J., Xu, J., Zhang, P., Ding, Q., & Zhang, J. (2024). Microvascular destabilization and intricated network of the cytokines in diabetic retinopathy: from the perspective of cellular and molecular components. *Cell & Bioscience*, *14*(1), 85. <https://doi.org/10.1186/s13578-024-01269-7>
- Shepro, D., & Morel, N. M. (1993). Pericyte physiology. *Faseb j*, *7*(11), 1031-1038. <https://doi.org/10.1096/fasebj.7.11.8370472>
- Shukla, U. V., & Tripathy, K. (2023). Diabetic Retinopathy. In *StatPearls*. StatPearls Publishing
- Copyright © 2023, StatPearls Publishing LLC.
- Simó, R., & Hernández, C. (2014). Neurodegeneration in the diabetic eye: new insights and therapeutic perspectives. *Trends in Endocrinology & Metabolism*, *25*(1), 23-33. <https://doi.org/https://doi.org/10.1016/j.tem.2013.09.005>
- Simó, R., Stitt, A. W., & Gardner, T. W. (2018). Neurodegeneration in diabetic retinopathy: does it really matter? *Diabetologia*, *61*(9), 1902-1912. <https://doi.org/10.1007/s00125-018-4692-1>
- Sohn, E. H., van Dijk, H. W., Jiao, C., Kok, P. H., Jeong, W., Demirkaya, N., Garmager, A., Wit, F., Kucukevciloglu, M., van Velthoven, M. E., DeVries, J. H., Mullins, R. F., Kuehn, M. H., Schlingemann, R. O., Sonka, M., Verbraak, F. D., & Abramoff, M. D. (2016). Retinal neurodegeneration may precede microvascular changes characteristic of diabetic retinopathy in diabetes mellitus. *Proc Natl Acad Sci U S A*, *113*(19), E2655-2664. <https://doi.org/10.1073/pnas.1522014113>
- Sorrentino, F. S., Allkabet, M., Salsini, G., Bonifazzi, C., & Perri, P. (2016). The importance of glial cells in the homeostasis of the retinal microenvironment and their pivotal role in the course of diabetic retinopathy. *Life Sci*, *162*, 54-59. <https://doi.org/10.1016/j.lfs.2016.08.001>
- Starke, R. D., Ferraro, F., Paschalaki, K. E., Dryden, N. H., McKinnon, T. A., Sutton, R. E., Payne, E. M., Haskard, D. O., Hughes, A. D., Cutler, D. F., Laffan, M. A., & Randi, A. M. (2011). Endothelial von Willebrand factor regulates angiogenesis. *Blood*, *117*(3), 1071-1080. <https://doi.org/10.1182/blood-2010-01-264507>

- Stetler-Stevenson, W. G. (1996). Dynamics of matrix turnover during pathologic remodeling of the extracellular matrix. *Am J Pathol*, *148*(5), 1345-1350.
- Stitt, A. W., Anderson, H. R., Gardiner, T. A., & Archer, D. B. (1994). Diabetic retinopathy: quantitative variation in capillary basement membrane thickening in arterial or venous environments. *Br J Ophthalmol*, *78*(2), 133-137. <https://doi.org/10.1136/bjo.78.2.133>
- Stone, J., & Dreher, Z. (1987). Relationship between astrocytes, ganglion cells and vasculature of the retina. *Journal of Comparative Neurology*, *255*(1), 35-49.
- Stratman, A. N., Schwindt, A. E., Malotte, K. M., & Davis, G. E. (2010). Endothelial-derived PDGF-BB and HB-EGF coordinately regulate pericyte recruitment during vasculogenic tube assembly and stabilization. *Blood*, *116*(22), 4720-4730. <https://doi.org/10.1182/blood-2010-05-286872>
- Suzuki, Y., Nakazawa, M., Suzuki, K., Yamazaki, H., & Miyagawa, Y. (2011). Expression profiles of cytokines and chemokines in vitreous fluid in diabetic retinopathy and central retinal vein occlusion. *Jpn J Ophthalmol*, *55*(3), 256-263. <https://doi.org/10.1007/s10384-011-0004-8>
- Tang, L., Xu, G. T., & Zhang, J. F. (2023). Inflammation in diabetic retinopathy: possible roles in pathogenesis and potential implications for therapy. *Neural Regen Res*, *18*(5), 976-982. <https://doi.org/10.4103/1673-5374.355743>
- Timpl, R., Rohde, H., Robey, P. G., Rennard, S. I., Foidart, J. M., & Martin, G. R. (1979). Laminin—a glycoprotein from basement membranes. *Journal of Biological Chemistry*, *254*(19), 9933-9937. [https://doi.org/https://doi.org/10.1016/S0021-9258\(19\)83607-4](https://doi.org/https://doi.org/10.1016/S0021-9258(19)83607-4)
- Tomita, Y., Lee, D., Tsubota, K., Negishi, K., & Kurihara, T. (2021). Updates on the Current Treatments for Diabetic Retinopathy and Possibility of Future Oral Therapy. *J Clin Med*, *10*(20). <https://doi.org/10.3390/jcm10204666>
- Trevino, T. N., & Lutz, S. E. (2022). Matrix proteins plug a hole: How pericytes suppress blood brain barrier transcytosis. *Neuron*, *110*(10), 1601-1603. <https://doi.org/10.1016/j.neuron.2022.04.011>
- Trost, M., Blattner, A. C., & Lehner, C. F. (2016). Regulated protein depletion by the auxin-inducible degradation system in *Drosophila melanogaster*. *Fly (Austin)*, *10*(1), 35-46. <https://doi.org/10.1080/19336934.2016.1168552>
- Tsai, W. S., Thottarath, S., Gurudas, S., Pearce, E., Yamaguchi, T. C. N., & Sivaprasad, S. (2024). A Comparison of Optical Coherence Tomography Angiography Metrics and Artifacts on Scans of Different Sizes in Diabetic Macular Ischemia. *Am J Ophthalmol*, *269*, 303-314. <https://doi.org/10.1016/j.ajo.2024.09.012>
- Uckermann, O., Wolf, A., Kutzera, F., Kalisch, F., Beck-Sickingher, A. G., Wiedemann, P., Reichenbach, A., & Bringmann, A. (2006). Glutamate release by neurons evokes a purinergic inhibitory mechanism of osmotic glial cell swelling in the rat retina: activation by neuropeptide Y. *J Neurosci Res*, *83*(4), 538-550. <https://doi.org/10.1002/jnr.20760>
- van der Wijk, A. E., Vogels, I. M. C., van Veen, H. A., van Noorden, C. J. F., Schlingemann, R. O., & Klaassen, I. (2018). Spatial and temporal recruitment of the neurovascular unit during development of the mouse blood-retinal barrier. *Tissue Cell*, *52*, 42-50. <https://doi.org/10.1016/j.tice.2018.03.010>
- van Dijk, H. W., Kok, P. H., Garvin, M., Sonka, M., Devries, J. H., Michels, R. P., van Velthoven, M. E., Schlingemann, R. O., Verbraak, F. D., & Abràmoff, M. D. (2009). Selective loss of inner retinal layer thickness in type 1 diabetic patients with minimal diabetic retinopathy. *Invest Ophthalmol Vis Sci*, *50*(7), 3404-3409. <https://doi.org/10.1167/iovs.08-3143>
- van Rossum, D., & Hanisch, U.-K. (2004). Microglia. *Metabolic brain disease*, *19*, 393-411.

- von Tell, D., Armulik, A., & Betsholtz, C. (2006). Pericytes and vascular stability. *Experimental cell research*, 312(5), 623-629.
- Wakui, S., Furusato, M., Nikaido, T., Yokota, K., Sekiguchi, J., Ohmori, K., Kano, Y., & Ushigome, S. (1990). Ultrastructural localization of fibronectin and laminin in human granulation tissue in relation to capillary development. *Cell Struct Funct*, 15(4), 201-210. <https://doi.org/10.1247/csf.15.201>
- Wakui, S., Furusato, M., Ohshige, H., & Ushigome, S. (1993). Endothelial-pericyte interdigitations in rat subcutaneous disc implanted angiogenesis. *Microvasc Res*, 46(1), 19-27. <https://doi.org/10.1006/mvre.1993.1032>
- Wang, W., & Lo, A. C. Y. (2018). Diabetic Retinopathy: Pathophysiology and Treatments. *Int J Mol Sci*, 19(6). <https://doi.org/10.3390/ijms19061816>
- Weinreb, R. N., Aung, T., & Medeiros, F. A. (2014). The pathophysiology and treatment of glaucoma: a review. *Jama*, 311(18), 1901-1911. <https://doi.org/10.1001/jama.2014.3192>
- Weir, G. C., Marselli, L., Marchetti, P., Katsuta, H., Jung, M. H., & Bonner-Weir, S. (2009). Towards better understanding of the contributions of overwork and glucotoxicity to the beta-cell inadequacy of type 2 diabetes. *Diabetes Obes Metab*, 11 Suppl 4, 82-90. <https://doi.org/10.1111/j.1463-1326.2009.01113.x>
- Welling, L. W., & Grantham, J. J. (1972). Physical properties of isolated perfused renal tubules and tubular basement membranes. *J Clin Invest*, 51(5), 1063-1075. <https://doi.org/10.1172/jci106898>
- Wilkinson-Berka, J. L., & Miller, A. G. (2008). Update on the treatment of diabetic retinopathy. *ScientificWorldJournal*, 8, 98-120. <https://doi.org/10.1100/tsw.2008.25>
- Winkler, E. A., Bell, R. D., & Zlokovic, B. V. (2011). Central nervous system pericytes in health and disease. *Nature neuroscience*, 14(11), 1398-1405.
- Wisniewska-Kruk, J., Hoeben, K. A., Vogels, I. M. C., Gaillard, P. J., Van Noorden, C. J. F., Schlingemann, R. O., & Klaassen, I. (2012). A novel co-culture model of the blood-retinal barrier based on primary retinal endothelial cells, pericytes and astrocytes. *Experimental Eye Research*, 96(1), 181-190. <https://doi.org/https://doi.org/10.1016/j.exer.2011.12.003>
- Wolf, S. A., Boddeke, H., & Kettenmann, H. (2017). Microglia in physiology and disease. *Annual review of physiology*, 79, 619-643.
- Wong, T. Y., & Mitchell, P. (2007). The eye in hypertension. *Lancet*, 369(9559), 425-435. [https://doi.org/10.1016/s0140-6736\(07\)60198-6](https://doi.org/10.1016/s0140-6736(07)60198-6)
- Wu, D. M., Kawamura, H., Sakagami, K., Kobayashi, M., & Puro, D. G. (2003). Cholinergic regulation of pericyte-containing retinal microvessels. *American Journal of Physiology-Heart and Circulatory Physiology*, 284(6), H2083-H2090.
- Yan, W., Laboulaye, M. A., Tran, N. M., Whitney, I. E., Benhar, I., & Sanes, J. R. (2020). Mouse Retinal Cell Atlas: Molecular Identification of over Sixty Amacrine Cell Types. *J Neurosci*, 40(27), 5177-5195. <https://doi.org/10.1523/jneurosci.0471-20.2020>
- Ye, X. D., Laties, A. M., & Stone, R. A. (1990). Peptidergic innervation of the retinal vasculature and optic nerve head. *Invest Ophthalmol Vis Sci*, 31(9), 1731-1737.
- Yildirim, A., Russell, J., Yan, L. S., Senchenkova, E. Y., & Granger, D. N. (2012). Leukocyte-dependent responses of the microvasculature to chronic angiotensin II exposure. *Hypertension*, 60(6), 1503-1509. <https://doi.org/10.1161/hypertensionaha.112.198465>

- Yin, D., Tao, J., Lee, D. D., Shen, J., Hara, M., Lopez, J., Kuznetsov, A., Philipson, L. H., & Chong, A. S. (2006). Recovery of islet beta-cell function in streptozotocin- induced diabetic mice: an indirect role for the spleen. *Diabetes*, 55(12), 3256-3263. <https://doi.org/10.2337/db05-1275>
- Younes, M. S., Steele, H. D., Robertson, E. M., & Bencosme, S. A. (1965). Correlative light and electron microscope study of the basement membrane of the human ectocervix. *American Journal of Obstetrics and Gynecology*, 92(2), 163-171.
- Yuuki, T., Kanda, T., Kimura, Y., Kotajima, N., Tamura, J., Kobayashi, I., & Kishi, S. (2001). Inflammatory cytokines in vitreous fluid and serum of patients with diabetic vitreoretinopathy. *J Diabetes Complications*, 15(5), 257-259. [https://doi.org/10.1016/s1056-8727\(01\)00155-6](https://doi.org/10.1016/s1056-8727(01)00155-6)
- Zhang, J., Li, P., Zhao, G., He, S., Xu, D., Jiang, W., Peng, Q., Li, Z., Xie, Z., & Zhang, H. (2022). Mesenchymal stem cell-derived extracellular vesicles protect retina in a mouse model of retinitis pigmentosa by anti-inflammation through miR-146a-Nr4a3 axis. *Stem Cell Research & Therapy*, 13(1), 1-22.

